China sets its sights high in space science *p. 342*

Cospeciation of primates and microbiota *pp. 350 & 380*

Understanding key factors for Zika control *p. 353*

Science

$15
22 JULY 2016
sciencemag.org

AAAS

COMPLEX DESIGN

Building with engineered proteins *pp. 338 & 389*

CONTENTS

22 JULY 2016 • VOLUME 353 • ISSUE 6297

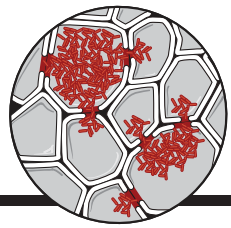

346
Unchecked march of a plant pathogen

331

NEWS

IN BRIEF

328 News at a glance

IN DEPTH

331 VAGINAL MICROBIOME AFFECTS HIV RISK
Unusual bacteria in vagina help explain high infection rates in South African women *By J. Cohen*

332 AFRICAN HIV/TUBERCULOSIS INSTITUTES MERGE
Major charities back creation of Africa Health Research Institute to tackle South African epidemics *By J. Cohen*

333 TO SAVE CARIBOU, ALBERTA WANTS TO FENCE THEM IN
Controversial proposal envisions the construction of a massive, predator-free pen *By W. Cornwall*

334 DO GENOMIC CONFLICTS DRIVE EVOLUTION?
Clashes between the cell's two genomes—mitochondrial and nuclear—could shape the tree of life *By E. Pennisi*

335 WILD BIRD COMES WHEN HONEY HUNTERS CALL FOR HELP
Honeyguides understand specific human signal *By E. Pennisi*
▸ REPORT P. 387

336 HUGE STATUE SUGGESTS EARLY RISE FOR BUDDHISM
Reclining sage in Pakistan may be world's oldest monumental Buddha *By A. Lawler*

337 A LICHEN MÉNAGE À TROIS
Genomic and imaging studies of lichen add a third symbiotic partner to the textbook pair *By E. Pennisi*
▸ REPORT BY T. SPRIBILLE *ET AL.* 10.1126/science.aaf8287

FEATURES

338 RULES OF THE GAME
By deciphering the rules of protein structure, David Baker has learned how to one-up nature and design new medicines and materials *By R. F. Service*
▸ REPORT P. 389; VIDEO

342 RED STAR RISING
A fusillade of missions has thrust China into the upper echelon of space science *By D. Normile*

345 Who's missing from this picture?
By D. Normile

342

INSIGHTS

PERSPECTIVES

346 CAN APULIA'S OLIVE TREES BE SAVED?
An introduced plant pathogen proves difficult to contain in southern Italy
By R. P. P. Almeida

348 IS TRICLOSAN HARMING YOUR MICROBIOME?
Studies on the effects of a widely used antimicrobial reach conflicting results
By A. L. Yee and J. A. Gilbert
▸ PODCAST

350 HOMINID SUPERORGANISMS
Ancient microbial symbionts cospeciated with hominids
By J. A. Segre and N. Salafsky
▸ REPORT P. 380

351 DEMYSTIFYING THE DEMISE OF PATERNAL MITOCHONDRIAL DNA
A process that eliminates organelle DNA during sexual reproduction is identified
By A. M. van der Bliek
▸ REPORT P. 394

355

POLICY FORUM

353 COUNTERING THE ZIKA EPIDEMIC IN LATIN AMERICA
Epidemic dynamics are key and data gaps must be addressed
By N. M. Ferguson et al.

BOOKS *ET AL.*

355 THE GRID
By G. Bakke, reviewed by C. Howe

356 THE GREAT INVENTION
By E. Masood, reviewed by N. G. Mankiw

Science Staff 326
New Products 405
Science Careers 406

Published by AAAS

CONTENTS

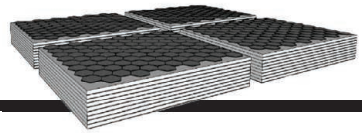

364
A graphene/polycarbonate composite

22 JULY 2016 • VOLUME 353 • ISSUE 6297

LETTERS

357 **324 MILLION MINORITIES**
By S. de Lacalle

357 **MISREPRESENTING *A. FISHER V. U. TEXAS***
By S. H. Hurlbert

357 **RESPONSE**
By S. J. Gates Jr.

357 **MINORITIES AND BIAS: THE BIG PICTURE**
By L. Aponte-Soto

358 **TECHNICAL COMMENT ABSTRACTS**

RESEARCH

IN BRIEF

359 From *Science* and other journals

REVIEW

362 **HIV-1 CURE**
Latency reversal and viral clearance to cure HIV-1 *D. M. Margolis* et al.
REVIEW SUMMARY; FOR FULL TEXT: dx.doi.org/10.1126/science.aaf6517

RESEARCH ARTICLE

363 **SYNTHETIC BIOLOGY**
Synthetic recombinase-based state machines in living cells *N. Roquet* et al.
RESEARCH ARTICLE SUMMARY; FOR FULL TEXT: dx.doi.org/10.1126/science.aad8559

REPORTS

364 **COMPOSITES**
Layered and scrolled nanocomposites with aligned semi-infinite graphene inclusions at the platelet limit *P. Liu* et al.

368 **METALLURGY**
A lightweight shape-memory magnesium alloy *Y. Ogawa* et al.

371 **QUANTUM GASES**
Observation of the Efimovian expansion in scale-invariant Fermi gases *S. Deng* et al.

374 **PHYSICS**
Electron microscopy of electromagnetic waveforms *A. Ryabov and P. Baum*

377 **WATER RESOURCES**
Connections between groundwater flow and transpiration partitioning *R. M. Maxwell and L. E. Condon*

380 **MICROBIOME**
Cospeciation of gut microbiota with hominids *A. H. Moeller* et al.
▸ PERSPECTIVE P. 350

383 **MEMORY RESEARCH**
Competition between engrams influences fear memory formation and recall *A. J. Rashid* et al.

387 **BEHAVIORAL ECOLOGY**
Reciprocal signaling in honeyguide-human mutualism *C. N. Spottiswoode* et al.
▸ NEWS STORY P. 335

389 **PROTEIN DESIGN**
Accurate design of megadalton-scale two-component icosahedral protein complexes *J. B. Bale* et al.
▸ NEWS STORY P. 338

394 **MITOCHONDRIA**
Mitochondrial endonuclease G mediates breakdown of paternal mitochondria upon fertilization *Q. Zhou* et al.
▸ PERSPECTIVE P. 351

399 **CANCER IMMUNOTHERAPY**
Cdk5 disruption attenuates tumor PD-L1 expression and promotes antitumor immunity *R. D. Dorand* et al.

DEPARTMENTS

327 **EDITORIAL**
Science advice for Europe
By James Wilsdon

418 **WORKING LIFE**
Alternatives within academia
By Nathan L. Vanderford

ON THE COVER

Computationally designed, 120-subunit icosahedral protein nanoparticles (yellow, dimers; blue, trimers; green, pentamers). Combinations of these shapes result in a kaleidoscopic array of self-assembling protein complexes, each of which rivals the size of a small viral capsid. Protein assemblies like these could form the basis for a new generation of biomolecular machines with structures and functions that are customizable for particular applications. See pages 338 and 389.
*Illustration: Valerie Altounian/*Science, *based on design models provided by J. Bale*

SCIENCE (ISSN 0036-8075) is published weekly on Friday, except the last week in December, by the American Association for the Advancement of Science, 1200 New York Avenue, NW, Washington, DC 20005. Periodicals mail postage (publication No. 484460) paid at Washington, DC, and additional mailing offices. Domestic individual membership and subscription (51 issues): $165 ($74 allocated to subscription). Domestic institutional subscription (51 issues): $1522; Foreign postage extra: Mexico, Caribbean (surface mail) $55; other countries (air assist delivery) $89. First class, airmail, student, and emeritus rates on request. Canadian rates with GST available upon request, GST #1254 88122. Publications Mail Agreement Number 1069624. **Printed in the U.S.A.**
Change of address: Allow 4 weeks, giving old and new addresses and 8-digit account number. **Postmaster:** Send change of address to AAAS, P.O. Box 96178, Washington, DC 20090–6178. **Single-copy sales:** $15.00 current issue, $20.00 back issue prepaid includes surface postage; bulk rates on request. *Science* is indexed in the *Reader's Guide to Periodical Literature* and in several specialized indexes.

Published by AAAS

353 (6297)
(July 22, 2016)
Science **353** (6297), 327-418.

Editor's Summary

Science (print ISSN 0036-8075; online ISSN 1095-9203) is published weekly, except the last week in December, by the American Association for the Advancement of Science, 1200 New York Avenue NW, Washington, DC 20005.

Science
AAAS
1200 New York Avenue, NW, Washington, DC 20005
Clarendon House, Clarendon Road, Cambridge, UK CB2 8FH

SUBSCRIPTION SERVICES For change of address, missing issues, new orders and renewals, and payment questions: 866-434-AAAS (2227) or 202-326-6417, FAX 202-842-1065. Mailing addresses: AAAS, P.O. Box 96178, Washington, DC 20090-6178 or AAAS Member Services, 1200 New York Avenue, NW, Washington, DC 20005

INSTITUTIONAL SITE LICENSES 202-326-6730 **REPRINTS:** Author Inquiries 800-635-7181 **COMMERCIAL INQUIRIES** 803-359-4578 **PERMISSIONS** 202-326-6765, permissions@aaas.org **AAAS Member Services** 202-326-6417 or http://membercentral.aaas.org/discounts

INFORMATION FOR AUTHORS See pages 624 and 625 of the 5 February 2016 issue or access www.sciencemag.org/authors/science-information-authors

EDITORIAL

Science advice for Europe

On 23 July, exactly 1 month after Britain's momentous decision to leave the European Union, around 4500 scientists and friends of science will assemble in Manchester, UK, for the opening of the EuroScience Open Forum (ESOF), Europe's largest interdisciplinary research conference. The vote for Britain's exit ("Brexit")—with worrying repercussions for European science and wider society—and questions about the plans of the new UK Prime Minister Theresa May, will inevitably cast a shadow over proceedings. But as Jerzy Langer, chair of ESOF's program committee, argues, the meeting has now acquired a sharper purpose: to demonstrate at a time of acute uncertainty that "we, the scientists, are one big family, whose rules and values extend beyond political and geographic borders."

Concern about the implications of Brexit for science has focused primarily on the obstacles it may pose to continued collaboration and free movement of researchers across Europe. However, the dense web of connections between British and European science extends into many other areas, including science policy and the provision of evidence and expert advice to decision-makers.

One example is the European Commission's Scientific Advice Mechanism (SAM), announced last year by Carlos Moedas, the Commissioner for Research, Science and Innovation. After an open nomination process, a high-level group of seven advisers was appointed and began its work in January 2016. Supported by a Brussels secretariat, the SAM will also procure advice from networks of national academies and learned societies across Europe.

The SAM's first two projects—on CO_2 emissions from light-duty vehicles; and digital identities and cybersecurity—are well advanced, and on target to release findings before the end of 2016. It also recently published an explanatory note on the safety and risks of the herbicide glyphosate, which remains a vexed issue in Europe.

Henrik Wegener, inaugural chair of the SAM's high-level group, has emphasized the need for it to work in an independent, transparent, and consultative way. In support of this goal, its next meeting will take place at ESOF, providing a first opportunity for the wider research community to engage with the SAM's work. A summit meeting this September of the International Network for Government Science Advice will be hosted in Brussels by the European Commission, at which the SAM will play a prominent role.

"... a strong focus on science policy... is more important than ever."

These are still early days for the SAM. It has met just twice, and its initial priorities were proposed by Brussels policy-makers. It is envisaged that the SAM will soon begin to work in both reactive and proactive ways, and the high-level group has developed a long list of potential topics and questions where it could make a meaningful contribution to European Union (EU) decision-making. How it strikes a balance between independence and policy relevance, and how far it gets drawn into the more contested terrain between evidence, policy, and politics, remain to be seen.

Even before Brexit, the ESOF meeting intended a strong focus on science policy. In the present climate, this is more important than ever. The vocal dismissal of evidence and expertise during what some described as the UK's "post-fact" referendum on the EU raises the possibility of a reversal of progress toward more evidence-informed decision-making. There is a risk that such a trend will spread to other fields and become more prominent in European political discourse, and that the research community will adopt overly defensive or dismissive positions.

Argument and analysis of events over the past month will be prominent at ESOF, but answers are likely to require a more searching period of reflection. Hopefully, the SAM can provide one arena through which these debates move forward within Britain, across Europe, and beyond.

–James Wilsdon

James Wilsdon is professor of research policy at the University of Sheffield, UK, and vice-chair of the International Network for Government Science Advice. Email: j.wilsdon@sheffield.ac.uk

10.1126/science.aah5584

NEWS

> “My list of excuses for not getting more articles out this summer was just blown to pieces #ObamaJAMA”

University of Georgia, Athens, education anthropologist @RolfStraubhaar, tweeting about U.S. President Barack Obama’s recently published paper on health care reform in *The Journal of the American Medical Association*.

IN BRIEF

Fiery Cross Reef in the South China Sea is part of China’s contentious island-building efforts.

U.N. sea ruling flags habitat loss

A panel under the United Nations Convention on the Law of the Sea last week eviscerated China’s claim to about 90% of the South China Sea, handing a major victory to the Philippines, which had asked for the arbitration. The tribunal also declared that China’s attempts to turn reefs in the disputed waters into islands through reclamation had “caused severe harm to the coral reef environment” and failed to protect “the habitat of depleted, threatened, or endangered species” as required by the convention. China refused to participate in the arbitration, and its foreign ministry says the country “neither accepts nor recognizes” the ruling. Marine scientists note that the South China Sea’s troubles go beyond island building. At a 12 July symposium at the Center for Strategic and International Studies in Washington, D.C., researchers described an impending fishery collapse due to overfishing, which threatens the 100 million people who depend on the sea for food and livelihoods. They urged South China Sea nations to make the sea a protected area under joint management.

AROUND THE WORLD

Whales win court victory

SAN FRANCISCO, CALIFORNIA | The U.S. Navy has not adequately protected whales and other marine mammals from being hurt by low-frequency sonar, a federal appeals court ruled last week. In 2012, the National Marine Fisheries Service (NMFS) issued a 5-year permit that allowed the Navy to incidentally harm up to 31 whales and 25 pinnipeds each year with the sonar, used to detect ships and submarines. The Natural Resources Defense Council and other groups sued, charging that NMFS had not followed the Marine Mammal Protection Act. On 15 July, a three-judge panel of the Ninth U.S. Circuit Court of Appeals agreed, noting that NMFS had not analyzed whether its mitigation plans—in particular designating quiet areas—would lead to the smallest practical amount of harm. The district court will now determine how the Navy should better protect marine mammals.

PHOTO: CSIS ASIA MARITIME TRANSPARENCY INITIATIVE/DIGITALGLOBE

Published by AAAS

Canadian peer-review reversal

OTTAWA | Canada's scientific community last week forced the Canadian Institutes of Health Research (CIHR) into a partial retreat from a controversial introduction of online peer review. CIHR President Alain Beaudet's move to do away with face-to-face meetings of peer-review panels prompted an open letter of protest to federal Health Minister Jane Philpott last month, which more than 1300 scientists signed. At a 13 July meeting convened at Philpott's request, Beaudet met with roughly 50 practicing scientists and agreed to a "hybrid" peer-review system: An online review process will cull roughly 60% of grants from consideration, but the surviving 40% of proposals will be subject to face-to-face peer review to determine actual competition winners. In the next few weeks, a working group will be convened to iron out details, including the size and membership of the face-to-face expert panels. **http://scim.ag/Canadareview**

DNA sequencer bound for space

CAPE CANAVERAL, FLORIDA | Among the more than 2000 kilograms of supplies sent barreling toward the International Space Station (ISS) this week was an unprecedented bit of cargo: a thumb drive–sized DNA sequencer. SpaceX's Dragon cargo craft delivered the device, produced by Oxford Nanopore Technologies, to NASA researchers hoping to perform the first attempts at genetic testing in orbit. Until now, DNA samples collected aboard the ISS had to be returned to Earth for analysis. The scientists plan to use the sequencer to identify microbes aboard the spacecraft, more quickly diagnose diseases in astronauts, and explore whether spaceflight introduces permanent genetic changes in humans and other organisms. They also see the project as a preliminary test of how such a device might work when affixed to a future Mars rover.

Ancient papyrus revealed

CAIRO | Six of the oldest known papyri in Egypt are now on public display. Last week, Cairo's Egyptian Museum unveiled an exhibition of the 4500-year-old documents, part of a larger collection of 30 papyri that were found in 2013 inside caves in the ancient Red Sea port of Wadi al-Jarf. They were written in the fourth dynasty of King Khufu, for whom the Great Pyramid of Giza was built as a tomb. The papyri contain information in neat hieroglyphs about the lives of pyramid workers, the transportation of building materials along the Nile River, and inventories of food and supplies like sheep.

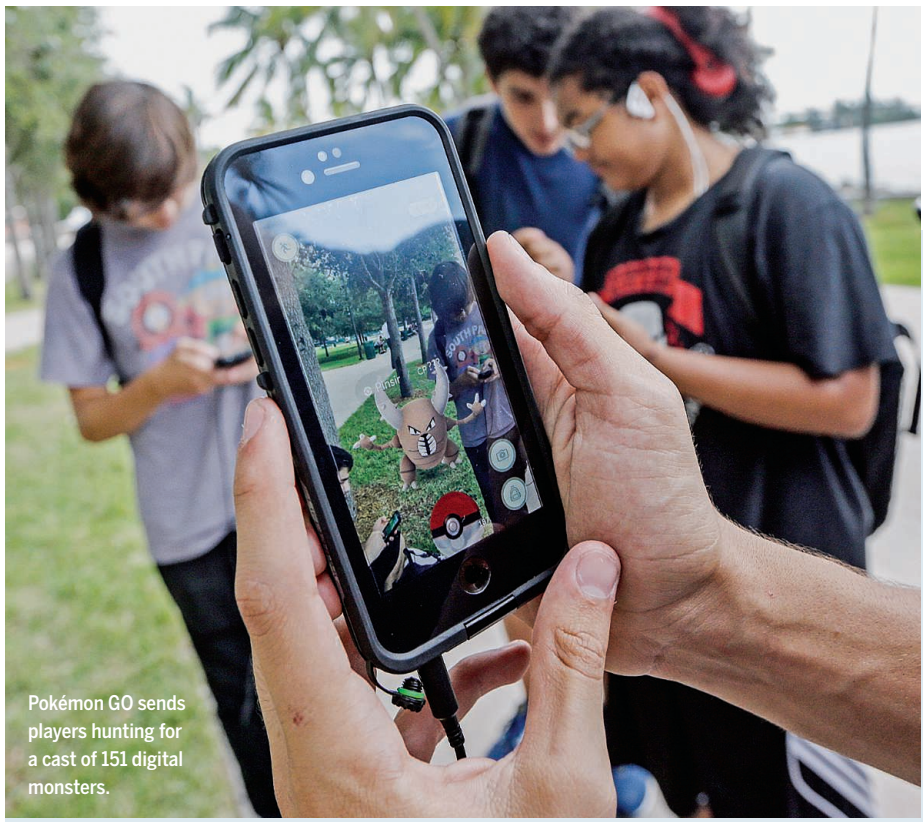

Pokémon GO sends players hunting for a cast of 151 digital monsters.

Pokémon invade iconic science centers

The viral sensation Pokémon GO, a free-to-play mobile game from the Pokémon Company, has sent millions of players out scouring their neighborhoods for rare Pokémon—digital monsters the franchise has been creating since 1996. The app uses a phone's camera to overlay Pokémon with the real world, and turns certain locations into supply outposts (Pokéstops) and competition grounds (Gyms). Those sites have included a few scientific landmarks. "The Mathias Lab is overrun," tweeted researchers at the Smithsonian Environmental Research Center in Edgewater, Maryland, after a Pokémon invasion last week. Staff at the Arizona Science Center in Phoenix identified a Caterpie—a large, caterpillarlike Pokémon—near an exhibition on giant insects. And a physicist working at the Large Hadron Collider (LHC) at CERN, the European particle physics laboratory near Geneva, Switzerland, found that the A Toroidal LHC Apparatus detector, used to identify and study new particles, is actually a Pokéstop. However, a solemn tweet from the International Space Station noted that there are no Pokémon to be captured in space. **http://scim.ag/Pokemonspots**

A papyrus from the collection of King Khufu, on display for the first time in Cairo.

NEWSMAKERS

U.K. science minister stays

The research community in the United Kingdom is relieved that science and universities minister **Jo Johnson** has kept his job during a massive shakeup of the government cabinet. Theresa May became prime minister after last month's referendum to leave the European Union, which has created great uncertainty about

PHOTOS: (TOP TO BOTTOM) AP PHOTO/ALAN DIAZ, FILE; AP PHOTO/AMR NABIL

Published by AAAS

the future of research in the United Kingdom. The tumult continued last week as a raft of senior ministers were fired and hired. As part of the reshuffling, May separated science and higher education into two departments. Johnson, who has been in the job for a year, will now report to both. His split brief makes the best of the shakeup, says Sarah Main of the Campaign for Science and Engineering in London, because Johnson will be able to advocate for keeping the research and university sectors closely connected. http://scim.ag/UKsciminister

FINDINGS

Women deterred by calculus

A first encounter with college calculus is more likely to discourage women than men from pursuing a major in a science, technology, engineering, and mathematics (STEM) field, according to a study last week in *PLOS ONE*. Researchers surveyed 2266 students at 129 2- and 4-year U.S. undergraduate colleges and universities taking Calculus I courses in the fall of 2010. Women were, on average, 1.5 times more likely to say they'd forgo Calculus II—required for most STEM majors—compared with male students with the same background and course experience. Women also expressed less confidence than men in their math abilities and were more likely to cite a poor understanding of the material as their reason for stopping.

A survey suggests low confidence disproportionately drives women to abandon calculus.

Memory from single atoms

In a feat of data storage, researchers have used a scanning tunneling microscope (STM) to store information at the atomic scale. The work, published this week in *Nature Nanotechnology*, uses chlorine atoms evaporated atop a copper surface, which assemble themselves into a gridlike pattern. Researchers used the STM to move individual atoms around, encoding a series of 0s and 1s into a 12x12 array of rectangular blocks. By precisely controlling the spots missing a chlorine atom, they encoded various writings, including physicist Richard Feynman's prescient 1959 lecture on a new age of nanotechnology. Reading and writing data this way is still painfully slow, but the research shows it's possible to store as much as 62.5 terabytes of data per 6.5 square centimeters—500 times better than today's hard disk technology.

BY THE NUMBERS

104

New exoplanets discovered by NASA's Kepler satellite and unveiled this week—3 years after the craft was deemed broken beyond repair.

11,676

Number of Amazonian tree species in a new inventory compiled from collections dating back to 1707 (*Scientific Reports*).

91%

Drop in dengue cases in the last year reported by the U.K. firm Oxitec in parts of Piracicaba, Brazil, where its genetically modified mosquitoes were released, versus 52% in areas using conventional mosquito control.

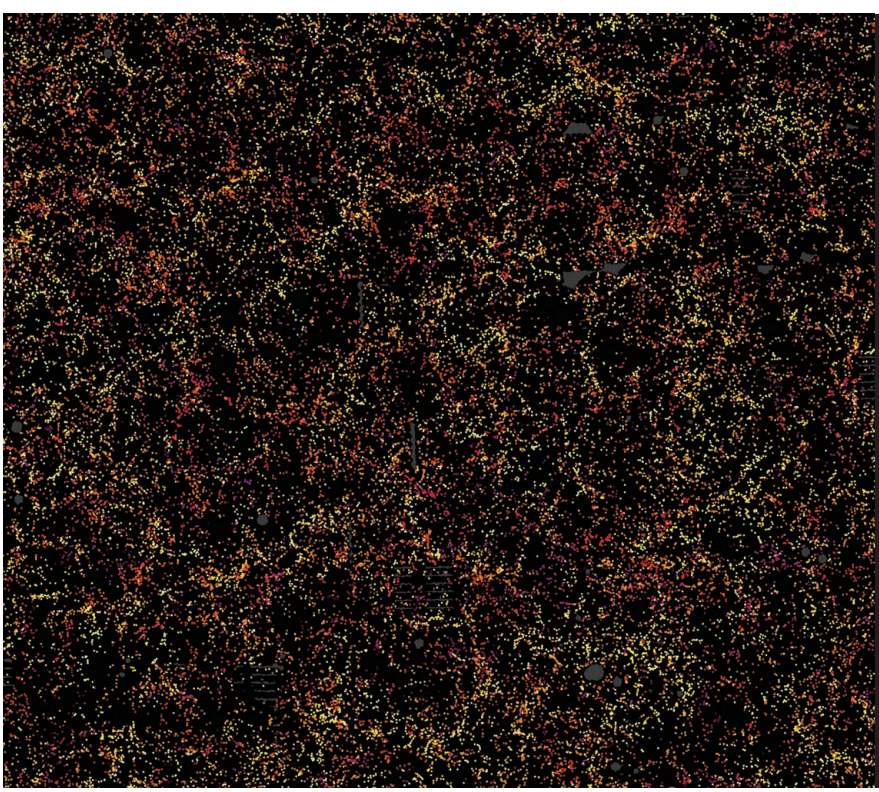

A spattering of galaxies

Scientists from the Sloan Digital Sky Survey III have created the largest 3D map of the universe to date, pinpointing 1.2 million galaxies in a wedge of space 6 billion light-years wide, 4.5 billion light-years tall, and 500 million light-years deep. The map helps probe the mysterious dark energy that's speeding up the expansion of the universe. Both the distribution of the galaxies and ripples in the afterglow of the big bang—the cosmic microwave background—carry the imprint of soundwaves called baryon acoustic oscillations that zipped through the soup of subatomic particles that filled the infant universe. So comparing the two helps trace the universe's expansion history. Papers describing the results have been submitted to the *Monthly Notices of the Royal Astronomical Society*.

A slice through a 3D map of 1.2 million galaxies, depicted as specks color-coded by distance from Earth.

IMAGES: (TOP TO BOTTOM) © BLEND IMAGES/ALAMY STOCK PHOTO; DANIEL EISENSTEIN/SDSS-III

Published by AAAS

In April, Bongekile Sokhela was hospitalized with AIDS in KwaZulu-Natal province in South Africa.

PHOTO: WILLIAM BRANGHAM

INFECTIOUS DISEASE

Vaginal microbiome affects HIV risk

Unusual bacteria in vagina help explain high infection rates in South African women

By **Jon Cohen**, *in Durban, South Africa*

The makeup of a woman's vaginal microbiome strongly influences her susceptibility to HIV infection, suggest studies presented at the 21st International AIDS Conference here this week. The microbiome may also explain why pre-exposure prophylaxis (PrEP)—giving anti-HIV drugs to prevent infection—works better in men than in women. These findings have particular relevance here in South Africa's KwaZulu-Natal province, which has perplexingly high levels of HIV infection in teenage girls and young women.

"It's a really important insight into why young women in Africa are getting infected at such high rates," says Douglas Kwon, an immunologist at Massachusetts General Hospital in Boston, who has studied the vaginal microbiome and HIV.

The new findings come from follow-up studies of women in a PrEP trial of a vaginal gel containing the anti-HIV drug tenofovir. Conducted by the Centre for the AIDS Programme of Research in South Africa (CAPRISA) based here, the trial took place in a region where 66% of 30-year-old women are infected. The CAPRISA team made headlines in 2010 by showing that the gel reduced a woman's risk of infection by 44%. But many wondered why the gel wasn't more effective—and indeed it failed in a later trial.

The more provocative of the two new studies compared the vaginal microflora in 49 women who became infected during the trial with that of 70 who remained HIV negative. A previous study of women in this trial had shown that those with increased genital tract inflammation were more likely to become infected. Vaginal biopsies suggest a reason: Inflammation brings more of HIV's favorite target, CD4 white blood cells, to the mucosal surface. And in a separate study of women in KwaZulu-Natal, Kwon and colleagues reported last year that inflammation in the vagina is linked to a decrease in *Lactobacillus*, which creates an acidic environment inhospitable to many pathogens. As the researchers noted but could not explain, *Lactobacillus* dominated in the vaginas of only 37% of the women, compared with 90% of U.S. white women.

Until now, however, no one had clearly linked specific vaginal microbiomes to an increased risk of HIV infection. "Now we have actual data," says CAPRISA's director, epidemiologist Salim Abdool Karim.

The data come from a massive effort to identify bacterial species on vaginal swabs from the women in the CAPRISA tenofovir gel study. By extracting thousands of bacterial ribosomal RNAs from each swab, Ian Lipkin's lab at Columbia University identified a total of 1368 species.

One relatively rare species, *Prevotella bivia*, stood out. Women whose vaginal microbiome included more than 1% of *P. bivia* had the highest levels of genital inflammation and the highest likelihood of becoming infected. These women had markedly reduced levels of *Lactobacilli*, and the researchers showed that *P. bivia* itself releases an inflammation-promoting compound called lipopolysaccharide. Women with more than 1% *P. bivia* were nearly 13 times more likely to become infected by HIV than those with less.

In the second study, of vaginal washings from 688 women in the CAPRISA trial, Adam Burgener from the Public Health Agency of Canada in Winnipeg and Nichole Klatt of the University of Washington, Seattle, showed that the vaginal microbiome can directly interfere with PrEP. The tenofovir gel protected only 18% of the women whose microbiome contained less than 50% *Lactobacilli*. The efficacy jumped to 61% when the *Lactobacillus* proportion was above 50%. In the lab, the researchers found that drug levels drop by half in the presence of *Gardnerella*, a genus that flourishes when *Lactobacilli* are scarce. "*Gardnerella* gobbles it up," Karim says.

Anthony Fauci, head of the U.S. National Institute of Allergy and Infectious Diseases in Bethesda, Maryland, says these findings open the possibility of manipulating the vaginal microbiome with antibiotics or beneficial microbes. "If this pans out, it seems like a relatively low-tech way to make an impact on whether you get infected or not," Fauci says.

Kwon cautions that efforts to manipulate the microbiome to treat inflammatory diseases of the gut have had limited success. But Fauci is more optimistic. The vaginal vault has far less susceptible tissue than the gut, he points out. "You're talking inches rather than feet," he says. "This is an interesting issue that needs to be pursued." ■

The Africa Centre for Population Health will merge with another powerhouse research institution.

PHOTO: B. GILBERT/WELLCOME TRUST

PUBLIC HEALTH

African HIV/tuberculosis institutes merge

Major charities back creation of Africa Health Research Institute to tackle South African epidemics

By **Jon Cohen**, *in Durban, South Africa*

As the International AIDS Conference kicked off here this week, two of South Africa's most prominent biomedical research institutions announced that they will marry and merge resources to attack the raging coepidemic of tuberculosis (TB) and HIV in the region. The new Africa Health Research Institute, backed by the deep-pocketed U.K.-based Wellcome Trust and the equally flush U.S.-based Howard Hughes Medical Institute (HHMI), will connect basic research to population-level studies and clinical trials. "This is something very strong," says Bruce Walker, an immunologist and HHMI investigator at Massachusetts General Hospital in Boston.

Many fundamental questions remain about why HIV spreads so fiercely in South Africa, which has more infected people than any other country in the world. South Africa also has a huge burden of TB, caused by a mycobacterium that thrives in an HIV-compromised immune system, and badly needs both better diagnostics and more effective treatments to combat widespread multidrug-resistant TB strains. The new institute promises to attack these overlapping problems—both at their worst in the province of KwaZulu-Natal, where the institute resides—with a unique combination of high-powered basic research and biological samples, such as blood and lung tissue, from tens of thousands of people who have carefully documented health histories. "We've got significant funding and significant expertise and it really has a huge potential," says virologist Deenan Pillay, who will head the new institute.

It will also provide a solid home for two institutions that have faced uncertain futures. One partner in the merger is the KwaZulu-Natal Research Institute for Tuberculosis and HIV (K-RITH), which HHMI created in 2008 at the suggestion of Walker. The idea was to create a strong basic research institution at the heart of the HIV/TB coepidemic that would bring in world-class researchers and train a new generation of African scientists. HHMI spent $40 million building a state-of-the-art biomedical facility, including a biosafety level 3 lab that can handle dangerous pathogens. "In terms of facilities, I don't think there's any place that comes close in sub-Saharan Africa," Walker says.

But K-RITH ran into trouble soon after it opened its doors in 2012. Its first director, William Bishai, a TB investigator from Johns Hopkins School of Medicine in Baltimore, Maryland, ended up resigning a year later after HHMI, which emphasizes "fundamental research," told him not to pursue clinical trials. HHMI feared that trials would divert from its mission and also could make the philanthropy vulnerable to lawsuits, says developmental geneticist Dennis McKearin, an HHMI administrator based here, who ran K-RITH after Bishai left.

Several others familiar with the episode told *Science* that HHMI also had concerns that Bishai inappropriately used its funds to pursue clinically related projects. Bishai confirms that there were tensions but says he did nothing wrong and is "very proud" of how he ran K-RITH. "Why put in $100 million to study TB and HIV and put the right hand in a sling and prevent it from reaching out to the patients?" he asks.

The other partner in this new union, the Africa Centre for Population Health, has gone through upheavals as well. Established by the Wellcome Trust in 1996 in Somkhele, about 235 kilometers north of Durban, it has focused on observational studies that track HIV's spread through communities, creating elegant spatial epidemiological maps. It has also led clinical studies of mother-to-child transmission of HIV and the impact of antiretroviral treatment on AIDS prevention.

But in 2013, the Wellcome Trust brought in Pillay, a clinical virologist from University College London, to head the center, a leadership change that signaled a desire to conduct more research that directly helped the local community. "One of the reasons I became director of the Africa Centre in 2013 was the wish of the Wellcome Trust as the main funder to see a very different scientific agenda," Pillay says. "There's been increasing pressure and need for the Africa Centre not just to observe the epidemic, but to do something about it. How long can you be producing bloody maps?"

Barry Bloom, a TB researcher at Harvard T.H. Chan School of Public Health in Boston, says Pillay effectively rescued the Africa Centre. "The sense I got from Deenan and others is that if he didn't take the job, Wellcome would have shut the place down," he says. Bloom, a former HHMI investigator who has chaired the scientific advisory board for K-RITH, is optimistic Pillay will also be successful at the combined insitute. "Deenan has the insight and the enthusiasm to pull together the basic research and the clinical studies."

The Wellcome Trust, which, unlike HHMI, strongly supports clinical trials, has promised the new institution $50 million over the next 5 years in a renewable grant. HHMI, for its part, plans to give it a total of $80 million (in addition to the building) by 2018, after which it plans to cut back its contribution, McKearin says.

This is the first time the two organizations have collaborated on a global health institution. "Bringing together HHMI and the Wellcome Trust into funding this unified institution is a great match," McKearin says. "It would be very difficult to even imagine a better outcome." ■

CONSERVATION

To save caribou, Alberta wants to fence them in

Controversial proposal envisions the construction of a massive, predator-free pen

By **Warren Cornwall**

The Little Smoky caribou herd of western Alberta province is among the most imperiled in Canada, its few dozen animals threatened by oil and gas development, logging, and hungry wolves. Soon, the herd could also become a high-profile test case for a controversial plan to save some of Canada's woodland caribou from extinction: herding them into pens enclosing 100 square kilometers or more and ringed with electric fences, and killing or removing every predator inside.

The massive, predator-free pen proposed for the Little Smoky animals last month by Alberta's government is "a Noah's Ark strategy, and it's desperate. But these are desperate times," says Mark Hebblewhite, a wildlife biologist at the University of Montana, Missoula.

But some caribou advocates are skeptical that the expensive pens will work. They also fear that the strategy, which the energy industry has helped fund, will undermine efforts to curb habitat destruction, the main cause of caribou decline. The thinking is that "if industry is willing to invest in these sorts of activities, then you give them license to trash the rest of the boreal forest," says biologist Chris Johnson of the University of Northern British Columbia, Prince George, in Canada.

The woodland caribou *(Rangifer tarandus)* inhabits a vast swath of northern Canada, from the Yukon to Newfoundland and Labrador. But the modern era hasn't been kind to the gentle, reclusive creatures, which sport distinctive upsweeping antlers. The leveling of old growth forests through logging, road building, and seismic mapping of oil and gas deposits has created habitat more suitable to moose and deer. Those animals compete with caribou and have attracted wolves that also hunt caribou when the chance arises. Of 51 herds of boreal caribou, a type of woodland caribou that includes the Little Smoky, just 14 are self-sustaining, according to a 2012 federal report. The Little Smoky herd's roughly 80 animals is well below historic levels; one study estimated the herd shrank by 35% just from 2000 to 2006.

To protect caribou populations, officials in Alberta and elsewhere have launched wolf killing operations, which have drawn public opposition. In the Little Smoky range, hunters killed 841 wolves between 2005 and 2012, reducing the winter population by nearly half each year. The caribou population stabilized, but a 2014 study found that there was no evidence the wolf hunt was helping the herd increase.

Alberta's new plan for reviving the Little Smoky herd, released in early June, calls for a range of actions, including new restrictions on logging and drilling, as well as a push to reforest thousands of kilometers of old seismic lines by 2022. It also includes an unprecedented government endorsement of the penning strategy, which has been tested on much smaller scales in neighboring British Columbia, with mixed results.

For Stan Boutin, an ecologist at the University of Alberta, Edmonton, the plan offers a chance to try an idea he has been pursuing for 5 years. He envisions building a fence 2.5 to 3 meters high, laced with electrified wires, and then killing or removing any wolves, bears, and other predators inside. The enclave would hold 20 or more female caribou, along with a handful of males. As the fenced population grows, biologists would release surplus animals, supplementing the herd outside. One estimate puts the cost at $15 million over 10 years.

"The fence in some ways is a necessary evil," Boutin says. But it could be more politically palatable than the wolf kills, he says, "and I guess I'm opting to say that this is less evil than a full-fledged, ongoing wolf-control program." It's not clear, however, that the enclosure would lead the government to lay down its guns, others note. Alberta's plan calls for continued wolf killing.

Alberta officials are accepting comments on their plan through 5 August, and critics are urging the government to drop the penning project and shield more land from development. "Our concern is that the government is allocating money to this flashy experiment at the [expense] of actual protection," says Alison Ronson, executive director of the Northern Alberta chapter of the Canadian Parks and Wilderness Society in Edmonton.

But if fencing moves forward and is successful, promoters say the approach could be used elsewhere—including in the oil sands region of northern Alberta, the heart of Canada's oil industry. "There certainly are opportunities other than Little Smoky," says Scott Grindal, a senior environmental coordinator with ConocoPhillips Canada in Calgary, which is part of an industry group that has funded fencing research.

Alberta's government says it wants to issue recovery plans for all its caribou herds by the end of 2017. If fencing becomes widespread, caribou biologist Johnson says, it would mark a "transformational change in how we see the conservation of caribou." ■

Caribou cows and calves were released from an experimental pen in British Columbia in Canada on 15 July.

PHOTO: WILDLIFE INFOMETRICS INC.

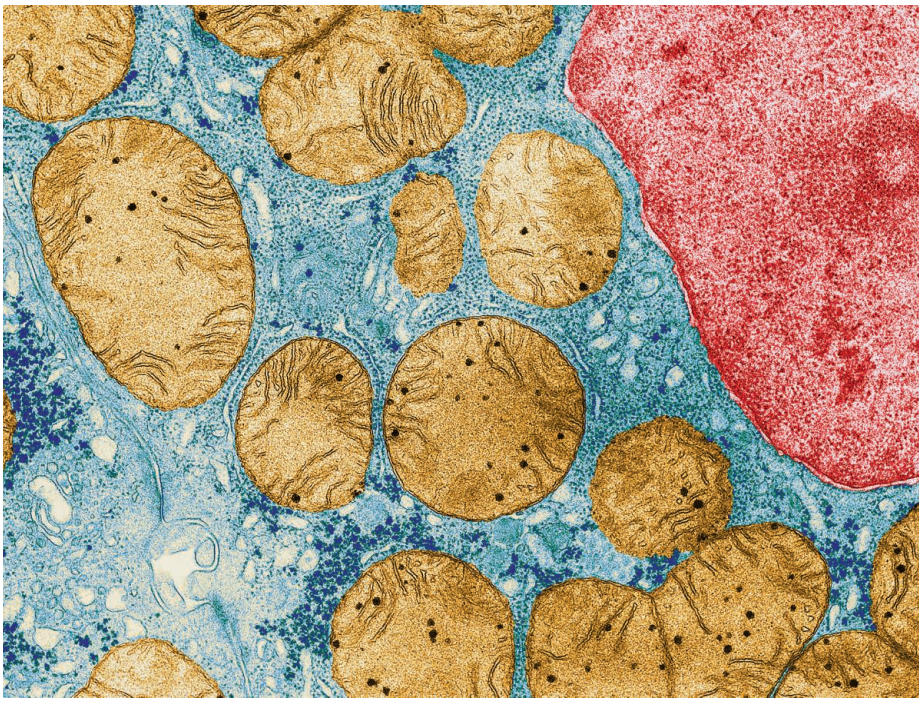

Genes in the nucleus (red) must evolve with genes in the mitochondria (gold) for a cell to stay healthy.

EVOLUTIONARY BIOLOGY

Do genomic conflicts drive evolution?

Clashes between the cell's two genomes—mitochondrial and nuclear—could shape the tree of life

By **Elizabeth Pennisi**

Two billion years ago, an early cell swallowed an energy-producing microbe, giving birth to the mitochondria that are the hallmarks of all eukaryotes, from protists to people. Evolutionary biologists now think that was just the start of the influence that the cell's "powerhouses" have on the tree of life. Mitochondria, which typically exist by the scores in a eukaryotic cell, have their own set of genes, which can replicate and mutate faster than the cell's better known complement in the nucleus. Yet both genomes code for proteins and other molecules that have to work together in the mitochondria. Researchers are now finding hints that conflicts between nuclear and mitochondrial genes could play a major role in evolution.

At the Evolution 2016 meeting in Austin last month, biologists suggested that out-of-sync nuclear and mitochondrial genomes may explain many biological puzzles—from why some female birds prefer the reddest mates to the evolution of new species in both plants and animals. "These interacting genomes are really underappreciated as mechanisms that drive evolutionary processes," says Geoff Hill of Auburn University in Alabama.

Mitochondria are crowded with interacting proteins that churn out energy-packed adenosine triphosphate (ATP) molecules, which provide 90% of the fuel for a eukaryotic cell. Over time, many genes coding for the proteins in the ATP pathway, as well as other genes essential for mitochondrial function, shifted into the cell's nucleus, leaving just 13 protein-coding genes in animals' mitochondria. (Plants have much bigger mitochondrial genomes, containing two to three times as many protein-coding genes.) To keep the ATP pathway working properly, the genes in the nucleus and mitochondria have to produce proteins that remain compatible.

Vivid colors drive sexual selection in birds—and may signal mitochondrial fitness.

And that's not easy, because each mitochondrion replicates many times over before the cell completes a single division. As a result, mutations naturally accumulate faster in mitochondrial DNA (mtDNA) than they do in the nuclear genome. "It's like what happens when one dance partner starts going at a different beat," explains Daniel Sloan, an evolutionary biologist at Colorado State University, Fort Collins.

Some researchers had assumed that any mismatches that result from the disparate mutation rates are simply weeded out through a process called purifying selection. But others suspect there's more to the story, pointing to evidence that natural selection boosts mutation rates in the nucleus, apparently to keep up with mitochondrial evolution.

Sloan and his postdoc Justin Havird, for example, assessed mutation rates in *Silene*, a group of flowering plants in which some species have slow-evolving mitochondrial genomes—a feature of most plants—whereas others have mitochondrial genomes that evolve two orders of magnitude faster, as in many animals. The plants with rapid mtDNA mutations also had a fast evolutionary rate in their nucleus, Sloan and Havird reported—and the speed-up was seen only in nuclear genes that code for mitochondrial proteins. How the plants selectively speed up mutation remains a mystery, Havird notes.

Felipe Barreto saw a similar speed-up in small crustaceans called copepods, which he studied as a postdoc with Ron Burton, an evolutionary biologist at the Scripps Institution of Oceanography in San Diego, California. Barreto found that as in the *Silene* plants, the mutation rates of certain nucleus-encoded proteins are faster than others, although in the copepods the speed-up was not limited to proteins involved in mitochondrial energy production. He also found signs of fast evolution in nuclear genes for proteins that become part of the mitochondrial ribosome or interact with mtDNA or RNA, he said at the meeting. "Across multiple different functional pathways, you can find evidence of coevolution,"

says Barreto, who is now at Oregon State University, Corvallis.

Some researchers speculate that the impact of mitochondria on evolution goes well beyond spurring faster mutation in the nucleus. Burton, for example, thinks that mismatches between nuclear and mtDNA can help isolate populations, possibly setting them on a path toward diverging into two different species. When he mated copepods from separate tidepools, whose mitochondrial and nuclear genomes had been coevolving along different trajectories, he found that the offspring of the mismatched parents were less viable, a first step in reproductive isolation.

Auburn's Hill suggests that some species may even alert prospective mates to the health of their mitochondria, driving sexual selection. In 2013, he proposed that variations in the redness of male finches, a trait well known to be under sexual selection, may reflect differences in mitochondrial function due to genomic incompatibility. At the meeting, he reported circumstantial evidence: In the finches, the enzyme that makes red pigment may concentrate in the mitochondria, possibly to produce the pigment inside the organelle. He thinks that the redness of the feathers is a signal of mitochondrial fitness and hence the compatibility of the birds' mitochondrial and nuclear genomes.

Testing the idea by gauging genomic compatibility in male finches of different rednesses is difficult. But working with Burton, Hill has found that in copepods, which also produce a red pigment, color and compatibility do vary together.

A possible connection between mitochondria and sexual selection "is a provocative and exciting idea," Sloan says. But David Rand, an evolutionary biologist at Brown University, is skeptical that the interplay between mitochondrial and nuclear DNA has as broad an influence on evolution as others suggest. The evidence "is not in line with the enthusiasm out there," he says.

The enthusiasts, however, are going further. In the September 2015 issue of *Bioessays*, Havird and Damian Dowling and Matthew Hall from Monash University, Clayton, in Australia, proposed the biggest role yet for genomic incompatibility: spurring the evolution of sex. The trio argued that the mixing and matching of genomes that takes place during sexual reproduction might help nuclear genes keep pace with the rapidly accumulating changes in an mtDNA. For all these reasons, Sloan says, how eukaryotes deal with the genomic mismatch at the heart of the cell is "one of the coolest and most important biological questions out there." ■

PHOTO: CLAIRE N. SPOTTISWOODE

ANIMAL BEHAVIOR

Wild bird comes when honey hunters call for help

Honeyguides understand specific human signal

By **Elizabeth Pennisi**

Of all the relationships between people and wild animals, few are more heartwarming than that of African honey hunters and a starling-sized bird called the greater honeyguide. Flitting and calling, the bird leads the way to a bee nest and feasts on the wax left after the hunters have raided it. A study on p. 387 now shows that this mutualistic relationship is even tighter than it seemed, with the bird recognizing and responding to specific calls from its human partners.

The work, by evolutionary biologist Claire Spottiswoode and her collaborators, "is the first to provide clear and direct evidence that honeyguides respond to specialized human signals … and that the birds associate those signals with potential benefits," says John Thompson, an evolutionary biologist at the University of California, Santa Cruz. "The honeyguide literally understands what the human is saying," adds Stuart West, an evolutionary biologist at the University of Oxford in the United Kingdom. "It suggests that the honeyguide and human behavior have coevolved in response to each other."

A Yao honey hunter with a feathered friend.

Spottiswoode, who is at the University of Cambridge in the United Kingdom and the University of Cape Town in South Africa, first became fascinated with honeyguides at age 11. She had heard a talk by Kenyan ornithologist Hussein Isack, who had followed honey hunters and found that the birds really do lead people to honey. In the new work, she teamed up with Keith and Colleen Begg, conservation biologists who work at the Niassa National Reserve in Mozambique. They began by quantifying Isack's discovery, showing that when guided by the bird, Yao honey hunters in Mozambique find nests 75% of the time.

The trio went on to study how the honeyguide responds to people. The Yao summon the bird with a "trill-grunt" call—one that is reserved for attracting honeyguides, according to 20 hunters Spottiswoode interviewed. In 72 trials, the team played back one of three sounds—the hunter's usual trill-grunt, a ring-necked dove's song, or an unrelated Yao call—and tracked the birds' responses. They were "elegantly simple controlled experiments," West says.

In response to the proper call, the birds guided 66% of the time, and 81% of those forays led to a nest. Guiding occurred half as often or less in response to other calls, and nest finding was much less likely, the team reports. The pattern makes evolutionary sense: By saving their efforts for calls that indicate a willing human partner, the birds run a better chance of ending up with a bonanza of tasty beeswax.

Brian Wood, an anthropologist at Yale University who has studied honey hunters, says the Hadza, a hunter-gatherer group in Tanzania, summon honeyguides with a different signal, a melodious whistle. He expects that the Tanzanian birds, too, discriminate the call from other sounds and respond specifically to it.

It's unclear how young birds learn to recognize the hunters' calls, given another peculiarity of honeyguide behavior: Like cuckoos, they lay their eggs in the nests of other species, which means that young honeyguides don't have an opportunity to learn from their biological parents. There may be little time left to solve this and other puzzles, as age-old lifestyles like honey hunting vanish. "The historical connections between humans and wild animals are becoming altered at unprecedented rates," Thompson says, and "the possibility of studying these kinds of relationships in any historically meaningful way are decreasing quickly." ■

ARCHAEOLOGY

Huge statue suggests early rise for Buddhism

Reclining sage in Pakistan may be world's oldest monumental Buddha

By **Andrew Lawler**, *in Cardiff, U.K.*

At first, archaeologists excavating at the sprawling Buddhist complex of Bhamala Stupa, north of Islamabad, thought they were digging up yet another stone wall. But when excavation director Abdul Samad examined the feature closely in January 2015, he realized that he was instead looking at the shattered remains of a massive statue—a monumental reclining Buddha that stretched more than 15 meters, the length of a shipping container.

That was surprise enough. But Samad, director general of the regional archaeology office of Khyber Pakhtunkhwa province in Pakistan, got another surprise when radiocarbon dates on wood from the collapsed ceiling and the supports within nearby statues came back at 240 C.E. to 390 C.E. That's several centuries before Buddhists were thought to have created the massive sculptures common in temples across Asia. The date startled art historians meeting here earlier this month at the European Association for South Asian Archaeology and Art. "If the chronology is right, then this would be the earliest evidence of a monumental Buddhist sculpture," said Anna Filigenzi, an art historian at the University of Naples Federico II in Italy.

Big statues have big implications, because they require wealthy patrons and rulers to fund their creation. Much of the power and wealth in that era came from international trade on what is now called the Silk Road. "Why do statues and buildings suddenly become monumental?" asked Marion Frenger, a University of Bonn in Germany art historian. "This shows a change in the relationship between Buddhism and political power."

The reclining Buddha represents the sage—thought to have lived around the fifth century B.C.E.—in a fatal illness as he prepared to enter nirvana. The statue extended across nearly the entire length of a building that once had numerous other terra cotta statues attached to its walls. The figures were largely destroyed in antiquity by treasure hunters, says Jonathan Mark Kenoyer, an archaeologist at the University of Wisconsin, Madison, who has worked with Samad; only the outline and a foot of the reclining Buddha remain intact. But some of the hundreds of pieces uncovered in the dig (funded in part by the U.S. Department of State to encourage Pakistan-India scientific collaboration) are still flecked with white paint and gold leaf, hinting at their former grandeur.

Other giant Buddhas, such as those in India and the Bamiyan Buddhas in nearby Afghanistan, which were destroyed by the Taliban in 2001 (*Science*, 8 November 2002, p. 1204), were generally built starting in the sixth century C.E. Giant reclining statues only became common around the seventh century C.E. in what is now northern Pakistan and eastern Afghanistan. The statues at Bhamala Stupa could be 4 centuries older.

Archaeologists laid out blocks from the outsized Buddha statue, which was smashed long ago.

PHOTO: J. M. KENOYER, COURTESY OF THE DIRECTORATE OF ARCHAEOLOGY

Just when Buddhism in this region began to expand from a religious tradition into an economic and political powerhouse capable of producing such a monumental sculpture has been controversial, in part because texts from the early centuries C.E. are scarce. It is known that the era began with the Kushan Empire, a cosmopolitan society in which the central Asian elite drank from Egyptian glasses and wore Chinese silks, used Greek as the standard language for administering their vast realm, and adopted Buddhism.

But by the middle of the third century, the empire began to disintegrate. The White Huns, a nomadic people from the east who favored Zoroastrianism and a branch of Hinduism, overwhelmed the nascent Buddhist culture by the fifth century and laid waste to hundreds of monasteries around Bhamala Stupa, according to texts and scattered archaeological remains. Historians long thought that this invasion halted the spread of Buddhism. But the dates of the giant Buddha suggest that the White Huns instead supported Buddhism, Filigenzi says.

"This is about a ruler showing off his power and prestige," Frenger says, though no one can be sure just which ruler. Monumental sculptures served to draw pilgrims from afar, she adds, and therefore produced revenues as well as veneration. "These were images of worship, not just for decoration," she says.

Recent excavations at sites like Mes Aynak in nearby Afghanistan indicate that monasteries were also critical centers for activity from agriculture to mining, as well as places for pilgrims and merchants to pray and rest (*Science*, 14 September 2012, p. 1279). The monasteries "functioned not just as providers of hospitality, but produced food, and functioned in some way as banks," Frenger says.

Some researchers aren't convinced that all this began as early as Samad suggests. "It's an extremely important find," said the University of Vienna's Deborah Klimburg-Salter. "But we don't know yet if these radiocarbon dates are accurate. It could be old wood," from trees that captured radiocarbon long before they were felled. Kenoyer, however, says the sampled timbers came from relatively small, young trees.

Samad stands by the dates, and says that he expects even earlier dates to emerge because the first samples were taken from the most recent levels in the building. In the meantime, he intends to continue excavations. Given the scant funds for archaeology in Pakistan, Samad hopes to attract tourists to admire the impressive ruins. If he succeeds, then after almost 2 millennia Bhamala Stupa may again draw pilgrims and spur prosperity. ■

A newly disovered yeast partner may explain the unusual compounds found in many lichens.

PHOTOS: TIM WHEELER

SYMBIOSIS

A lichen ménage à trois

Genomic and imaging studies of lichen add a third symbiotic partner to the textbook pair

By **Elizabeth Pennisi**

Lichen isn't much to look at—often just a gray, yellow-green, or garish orange crust on rock or bark. Yet lichens cover up to 6% of Earth's surface, by one estimate, and play a major role in breaking down rock into soil. Now, modern genomics is revealing these humble organisms to be startlingly complex.

For some 140 years, scientists have understood lichens to be a symbiosis between a fungus, which provides a physical structure and supplies moisture, and a photosynthesizing alga or cyanobacterium, which produces nutrients. But this week a research team reports online in *Science* that many are instead a threesome, with two fungi in the mix.

The role of the second fungus, a yeast, is uncertain, and some lichen aficionados aren't convinced it is a true symbiotic partner. But others say it's time to "throw the textbook understanding out of the window," as Toby Kiers, an evolutionary biologist at Vrije University Amsterdam, puts it. Biologists are only just beginning to understand how the twosome might work; "A third partner just complicates things even more," says Pierre-Luc Chagnon, an ecologist at the University of Alberta, Edmonton, in Canada.

Slow-growing and tightly bound to their substrates, lichens have been hard to cultivate in the lab, making it difficult to extract and analyze their DNA. To tackle this challenge, Toby Spribille, now at the University of Graz in Austria, collaborated with John McCutcheon, a genomicist at the University of Montana, Missoula, who specializes in insect-microbial partnerships. He convinced McCutcheon to apply his genomics techniques to two local lichens that grow as thick, hairy masses from tree branches, hoping their DNA would be easier to purify than that of soil-based lichens.

Spribille, McCutcheon, and their colleagues gathered 15 samples and initially analyzed just part of their genetic material, looking for differences in gene activity that might distinguish the two types of lichens. They found none, so Spribille analyzed the full array of genetic material isolated from the lichens. The results showed a lot of active genes from what turned out to be a second fungus, a yeast belonging to a group called Basidiomycota. One of the two lichens—a yellow, toxic variety called *Bryoria tortuosa*—had much higher yeast-gene activity than the other, brown variety, *B. fremontii*, suggesting to the team that the yeast might explain the differences.

Spribille checked with Swedish colleagues working on a chartreuse lichen from their nation, and a genomic analysis showed that it, too, had a yeast partner—as did 52 lichen genera from six continents, he and his colleagues found in follow-up DNA studies. "This is not a single oddity," Kiers says. "We're looking at a global phenomenon."

One reason mycologists overlooked it for so long is that the yeast cells are hard to see, unlike the two known lichen partners. But Spribille and his colleagues developed a way to label yeast with fluorescent tags and eventually spotted the cells embedded in a starch layer coating the lichen's wall-like microstructure. Lichens often contain unusual compounds, which have mystified scientists—the yellow *Bryoria*, for example, is packed with crystals of a toxin called vulpinic acid. Spribille and his colleagues think the third, previously silent yeast partner is responsible for the mystery chemicals, either directly making them or stimulating the other fungus to do so. "Lichen has been studied quite extensively, but every time we start looking more in depth we find other layers of complexity," says François Lutzoni, a lichenologist at Duke University in Durham, North Carolina.

Still, the mere presence of the yeast doesn't prove it is an essential participant in the lichen symbiosis; some lichens were already known to comprise more than two organisms, after all. Certain varieties contain both a green alga and a cyanobacterium as well as the fungus, and many lichens host species of bacteria. By the same token, "Whether these yeasts play any role in the lichen symbiosis remains to be seen," says Thorsten Lumbsch, a mycologist at the Field Museum of Natural History in Chicago, Illinois. Lumbsch says scientists must establish that the yeast exchanges nutrients or interacts in some other way with the other fungus and the alga.

Spribille and his colleagues agree, but to date they have been stymied by the challenge of isolating and growing the yeast in the lab, nevermind reconstituting the lichen as well. So instead, they are sequencing the entire genomes of all three partners and will look for evidence of gene transfer among the trio and of metabolic pathways that require proteins from multiple partners. "Until the function of the yeast is fully understood, there will be debate as to whether this is a true symbiont or not," Kiers concludes. But regardless, "this paper is a game-changer not only for lichen research but also for the field of symbiosis more generally." ■

RULES OF THE GAME

By deciphering the rules of protein structure, David Baker has learned how to one-up nature and design new medicines and materials

By **Robert F. Service**, *in Seattle, Washington*

David Baker appreciates nature's masterpieces. "This is my favorite spot," says the Seattle native, admiring the views from a terrace at the University of Washington (UW) here. To the south rises Mount Rainier, a 4400-meter glacier-draped volcano; to the west, the white-capped Olympic Mountain range.

But head inside to his lab and it's quickly apparent that the computational biochemist is far from satisfied with what nature offers, at least when it comes to molecules. On a low-slung coffee table lie eight toy-sized, 3D-printed replicas of proteins. Some resemble rings and balls, others tubes and cages—and none existed before Baker and his colleagues designed and built them. Over the last several years, with a big assist from the genomics and computer revolutions, Baker's team has all but solved one of the biggest challenges in modern science: figuring out how long strings of amino acids fold up into the 3D proteins that form the working machinery of life. Now, he and colleagues have taken this ability and turned it around to design and then synthesize unnatural proteins intended to act as everything from medicines to materials.

Already, this virtuoso proteinmaking has yielded an experimental HIV vaccine, novel proteins that aim to combat all strains of the influenza viruses simultaneously, carrier molecules that can ferry reprogrammed DNA into cells, and new

PHOTO: © RICH FRISHMAN

David Baker shows off models of some of the unnatural proteins his team has designed and made.

enzymes that help microbes suck carbon dioxide out of the atmosphere and convert it into useful chemicals. On p. 389, Baker's team and collaborators report making cages that assemble themselves from as many as 120 designer proteins, which could open the door to a new generation of molecular machines.

If the ability to read and write DNA spawned the revolution of molecular biology, the ability to design novel proteins could transform just about everything else. "Nobody knows the implications," because it has the potential to impact dozens of different disciplines, says John Moult, a protein-folding expert at the University of Maryland, College Park. "It's going to be totally revolutionary."

Baker is by no means alone in this pursuit. Efforts to predict how proteins fold, and use that information to fashion novel versions, date back decades. But today he leads the charge. "David has really inspired the field," says Guy Montelione, a protein structure expert at Rutgers University, New Brunswick, in New Jersey. "That's what a great scientist does."

BAKER, 53, DIDN'T START OUT with any such vision. Though both his parents were professors at UW—in physics and atmospheric sciences—Baker says he wasn't drawn to science growing up. As an undergraduate at Harvard University, Baker tried studying philosophy and social studies. That was "a total waste of time," he says now. "It was a lot of talk that didn't necessarily add content." Biology, where new insights can be tested and verified or discarded, drew him instead, and he pursued a Ph.D. in biochemistry. During a postdoc at the University of California, San Francisco, when he was studying how proteins move inside cells, Baker found himself captivated instead by the puzzle of how they fold. "I liked it because it's getting at something fundamental."

In the early 1960s, biochemists at the U.S. National Institutes of Health (NIH) recognized that each protein folds itself into an intrinsic shape. Heat a protein in a solution and its 3D structure will generally unravel. But the NIH group noticed that the proteins they tested refold themselves as soon as they cool, implying that their structure stems from the interactions between different amino acids, rather than from some independent molecular folding machine inside cells. If researchers could determine the strength of all those interactions, they might be able to calculate how any amino acid sequence would assume its final shape. The protein-folding problem was born.

One way around the problem is to determine protein structures experimentally, through methods such as x-ray crystallography and nuclear magnetic resonance (NMR) spectroscopy. But that's slow and expensive. Even today, the Protein Data Bank, an international repository, holds the structures of only roughly 110,000 proteins out of the hundreds of millions or more thought to exist.

Knowing the 3D structures of those other proteins would offer biochemists vital insights into each molecule's function, such as whether it serves to ferry ions across a cell membrane or catalyze a chemical reaction. It would also give chemists valuable clues to designing new medicines. So, instead of waiting for the experimentalists, computer modelers such as Baker have tackled the folding problem with computer models.

They've come up with two broad kinds of folding models. So-called homology models compare the amino acid sequence of a target protein with that of a template—a protein with a similar sequence and a known 3D structure. The models adjust their prediction for the target's shape based on the differences between its amino acid sequence and that of the template. But there's a major drawback: Today's experimental structures can only serve as templates for about half of all proteins—despite costly efforts to perform industrial-scale x-ray crystallography and NMR spectroscopy.

Templates were even scarcer more than 2 decades ago, when Baker accepted his first faculty position at UW. That prompted him to pursue a second path, known as ab initio modeling, which calculates the push and pull between neighboring amino acids to predict a structure. Baker also set up a biochemistry lab to study amino acid interactions, in order to improve his models.

Early on, Baker and Kim Simons, one of his first students, created an ab initio folding program called Rosetta, which broke new ground by scanning a target protein for short amino acid stretches that typically fold in known patterns and using that information to help pin down the molecule's overall 3D configuration. Rosetta required such extensive computations that Baker's team quickly found themselves outgrowing their computer resources at UW.

Seeking more computing power, they created a crowdsourcing extension called Rosetta@home, which allows people to contribute idle computer time to crunching the calculations needed to survey all the likely protein folds. Later, they added a video game extension called Foldit, allowing remote users to apply their instinctive protein-folding insights to guide Rosetta's search. The approach has spawned an international community of more than 1 million users and nearly two dozen related software packages that do everything from designing novel proteins to predicting the way proteins interact with DNA.

"The most brilliant thing David has done is build a community," says Neil King, a former Baker postdoc, now an investigator at UW's Institute for Protein Design (IPD). Some 400 active scientists continually update and improve the Rosetta software. The program is free for academics and nonprofit users, but there's a $40,000 fee for large companies. Proceeds are plowed back into research and an annual party called RosettaCon in Leavenworth, Washington, where attendees mix mountain hikes and scientific talks.

Despite this success, Rosetta was limited. The software was often accurate at predicting structures for small proteins, fewer than 100 amino acids in length. Yet, like other ab initio programs, it struggled with larger proteins. Several years ago, Baker began to doubt that he or anyone else would ever manage to solve most protein structures. "I wasn't sure whether I would get there."

Now, he says, "I don't feel that way anymore."

WHAT CHANGED HIS OUTLOOK was a technique first proposed in the 1990s by com-

putational biologist Chris Sander, then with the European Molecular Biology Laboratory in Heidelberg, Germany, and now with Harvard. Those were the early days of whole genome sequencing, when biologists were beginning to decipher the entire DNA sequences of microbes and other organisms. Sander and others wondered whether gene sequences could help identify pairs of amino acids that, although distant from each other on the unfolded proteins, have to wind up next to each other after the protein folds into its 3D structure.

Sander reasoned that the juxtaposition of those amino acids must be crucial to a protein's function. If a mutation occurs, changing one of the amino acids so that it no longer interacts with its partner, the protein might no longer work, and the organism could suffer or die. But if both neighboring amino acids are mutated at the same time, they might continue to interact, and the protein might work as well or even better.

The upshot, Sander proposed, was that certain pairs of amino acids necessary to a protein's structure would likely evolve together. And researchers would be able to read out that history by comparing the DNA sequences of genes from closely related proteins in different organisms. Whenever such DNA revealed pairs of amino acids that appeared to evolve in lockstep, it would suggest that they were close neighbors in the folded protein. Put enough of those constraints on amino acid positions into an ab initio computer model, and the program might be able to work out a protein's full 3D structure.

Unfortunately, Sander says, his idea "was a little ahead of its time." In the 1990s, there weren't enough high-quality DNA sequence data from enough similar proteins to track coevolving amino acids.

By the early part of this decade, however, DNA sequences were flooding in thanks to new gene-sequencing technology. Sander had also teamed up with Debora Marks at Harvard Medical School in Boston to devise a statistical algorithm capable of teasing out real coevolving pairs from the false positives that plagued early efforts. In a 2011 article in *PLOS ONE*, Sander, Marks, and colleagues reported that the coevolution technique could constrain the position of dozens of pairs of amino acids in 15 proteins—each from a different structural family—and work out their 3D shapes. Since then, Sander and Marks have shown that they can decipher the structure of a wide variety of proteins for which there are no homology templates. "It has changed the protein-folding game," Sander says.

IT CERTAINLY DID SO FOR BAKER. When he and colleagues realized that scanning genomes offered new constraints for Rosetta's ab initio calculations, they seized the opportunity. They were already incorporating constraints from NMR and other techniques. So they rushed to write a new software program, called Gremlin, to automatically compare gene sequences and come up with all the likely coevolving amino acid pairs. "It was natural for us to put them into Rosetta," Baker says.

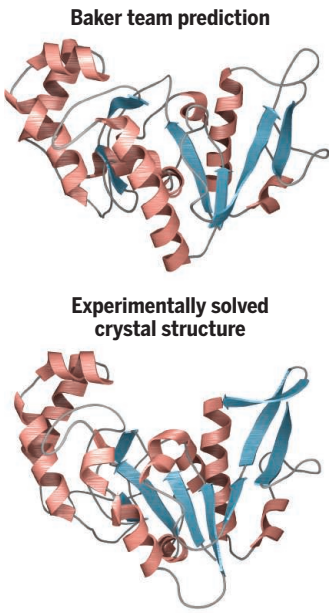

In a protein-folding competition, Baker's team stunned judges by almost matching the actual structure.

The results have been powerful. Rosetta was already widely considered the best ab initio model. Two years ago, Baker and colleagues used their combined approach for the first time in an international protein-folding competition, the 11th Critical Assessment of protein Structure Prediction (CASP). The contest asks modelers to compute the structures of a suite of proteins for which experimental structures are just being worked out by x-ray crystallography or NMR. After modelers submit their predictions, CASP's organizers reveal the actual experimental structures. One submission from Baker's team, on a large protein known as T0806, came back nearly identical to the experimental structure. Moult, who heads CASP, says the judge who reviewed the predicted structure immediately fired off an email to him saying "either someone solved the protein-folding problem, or cheated."

"We didn't [cheat]," Sergey Ovchinnikov, a grad student in Baker's lab, says with a chuckle.

The implications are profound. Five years ago, ab initio models had determined structures for just 56 proteins of the estimated 8000 protein families for which there are no templates. Since then, Baker's team alone has added 900 and counting, and Marks believes the approach will already work for 4700 families. With genome sequence data now pouring into scientific databases, it will likely only be a couple years before protein-folding models have enough coevolution data to solve structures for nearly any protein, Baker and Sander predict. Moult agrees. "I have been waiting 10 years for a breakthrough," he says. "This seems to me a breakthrough."

For Baker, it's only the beginning. With Rosetta's steadily improving algorithms and ever-greater computing power, his team has in essence mastered the rules for folding—and they've begun to use that understanding to try to one-up nature's creations. "Almost everything in biomedicine could be impacted by an ability to build better proteins," says Harvard synthetic biologist George Church.

Baker notes that for decades researchers pursued a strategy he refers to as "Neandertal protein design," tweaking the genes for existing proteins to get them to do new things. "We were limited by what existed in nature. ... We can now short-cut evolution and design proteins to solve modern-day problems."

TAKE MEDICINES, such as drugs to combat the influenza virus. Flu viruses come in many strains that mutate rapidly, which makes it difficult to find molecules that can knock them all out. But every strain contains a protein called hemagglutinin that helps it invade host cells, and a portion of the molecule, known as the stem, remains similar across many strains. Earlier this year, Baker teamed up with researchers at the Scripps Research Institute in San Diego, California, and elsewhere to develop a novel protein that would bind to the hemagglutinin stem and thereby prevent the virus from invading cells.

The effort required 80 rounds of designing the protein, engineering microbes to make it, testing it in the lab, and reworking the structure. But in the 4 February issue of *PLOS ONE*, the researchers reported that when they administered their final creation to mice and then injected them with a normally lethal dose of flu virus, the rodents were protected. "It's more effective than 10 times the dose of Tamiflu," an antiviral drug currently on the market, says Aaron Chevalier, a former Baker Ph.D. student who now works at a Seattle biotech company called Virvio that is trying to commercialize the protein as a universal antiflu drug.

Another potential addition to the medicine cabinet: a designer protein that chops

ILLUSTRATIONS: V. ALTOUNIAN/*SCIENCE*

up gluten, the infamous substance in wheat and other grains that people with Celiac disease or gluten sensitivity have trouble digesting. Ingrid Swanson Pultz began crafting the gluten-breaker even before joining Baker's lab as a postdoc and is now testing it in animals and working with IPD to commercialize the research. And those self-assembling cages that debut this week could one day be filled with drugs or therapeutic snippets of DNA or RNA that can be delivered to disease sites throughout the body.

The potential of these unnatural proteins isn't limited to medicines. Baker, King, and their colleagues have also attached up to 120 copies of a molecule called green fluorescent protein to the new cages, creating nanolanterns that could aid research by lighting up as they move through tissues.

Church says he believes that designer proteins might soon rewrite the biology inside cells. In a paper last year in *eLife*, he, Baker, and colleagues designed proteins to bind to either a hormone or a heart disease drug inside cells, and then regulate the activity of a DNA-cutting enzyme, Cas9, that is part of the popular CRISPR genome-editing system. "The ability to design sensors [inside cells] is going to be big," Church says. The strategy could allow researchers or physicians to target the powerful gene-editing system to a specific set of cells—those that are responding to a hormone or drug. Biosensors could also make it possible to switch on the expression of specific genes as needed to break down toxins or alert the immune cells to invaders or cancer.

Baker's lab is abuzz with other projects. Last year, his group and collaborators reported engineering into bacteria a completely new metabolic pathway, complete with a designer protein that enabled the microbes to convert atmospheric carbon dioxide into fuels and chemicals. Two years ago, they unveiled in *Science* proteins that spontaneously arrange themselves in a flat layer, like interlocking tiles on a bathroom floor. Such surfaces may lead to novel types of solar cells and electronic devices.

In perhaps the most thought-provoking project, Baker's team has designed proteins to carry information, imitating the way DNA's four nucleic acid letters bind and entwine in the genetic molecule's famed double helix (*Science*, 6 May, p. 680). For now, these protein helixes can't convey genetic information that cells can read. But they symbolize something profound: Protein designers have shed nature's constraints and are now only limited by their imagination. "We can now build a whole new world of functional proteins," Baker says. ■

Cracking the folding problem

Each protein is made up of a long chain of amino acids that folds into a precise 3D structure, which determines the protein's function. It has been difficult to experimentally determine many such structures, so scientists have tried to predict them from the amino acid sequence. To do so, they must pin down the rules that govern how an amino acid chain will naturally fold.

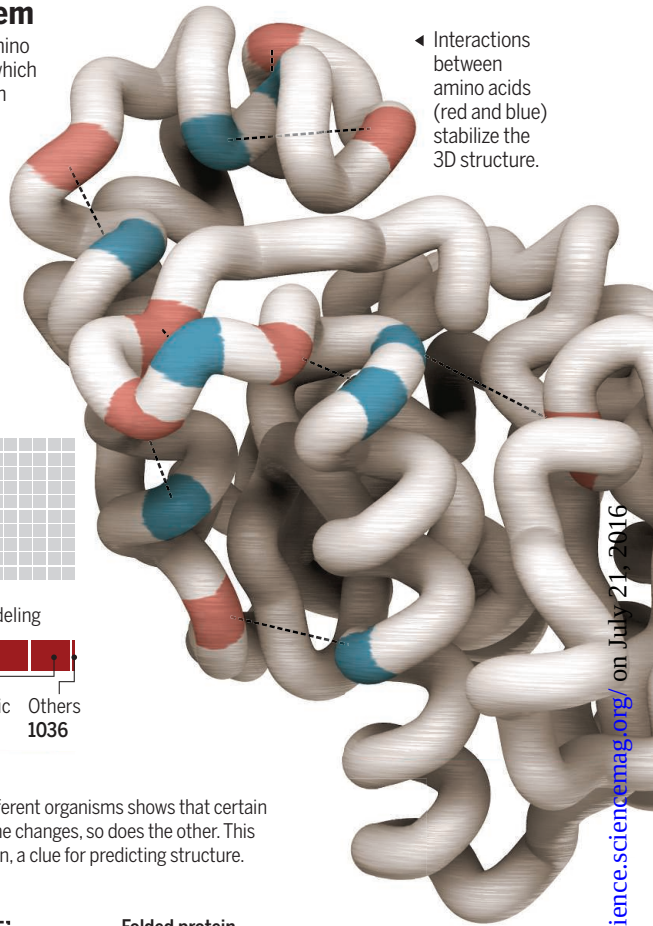

◀ Interactions between amino acids (red and blue) stabilize the 3D structure.

A scarcity of structures

X-ray crystallography and other techniques have determined the structures of only a fraction of proteins, though these can be used to model others.

Proteins in nature

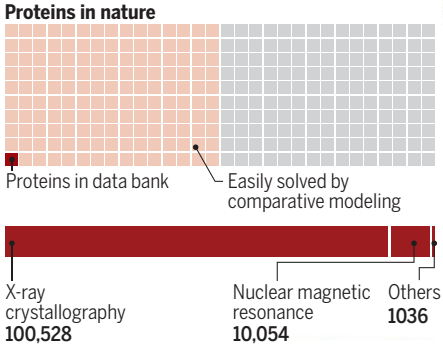

Clues from genome sequences

Comparing the DNA of similar proteins from different organisms shows that certain pairs of amino acids evolve in tandem—when one changes, so does the other. This suggests they are neighbors in the folded protein, a clue for predicting structure.

Amino acid sequences

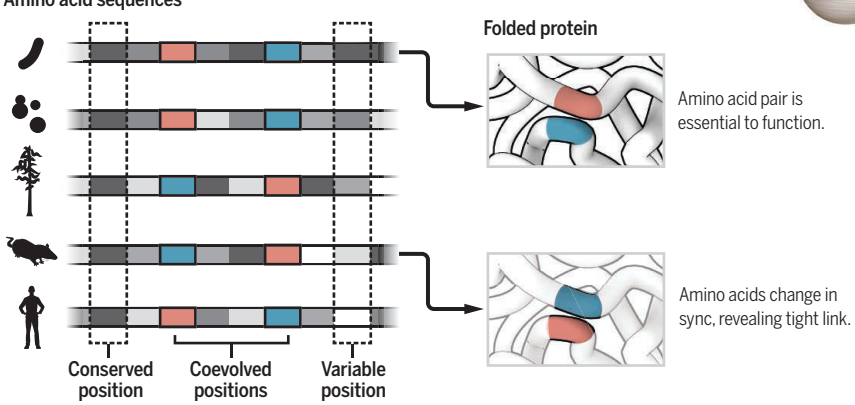

A protein for every purpose

The ability to predict how an amino acid sequence will fold—and hence how the protein will function—opens the way to designing novel proteins that can catalyze specific chemical reactions or act as medicines or materials. Genes for these proteins can be synthesized and inserted into microbes, which build the proteins.

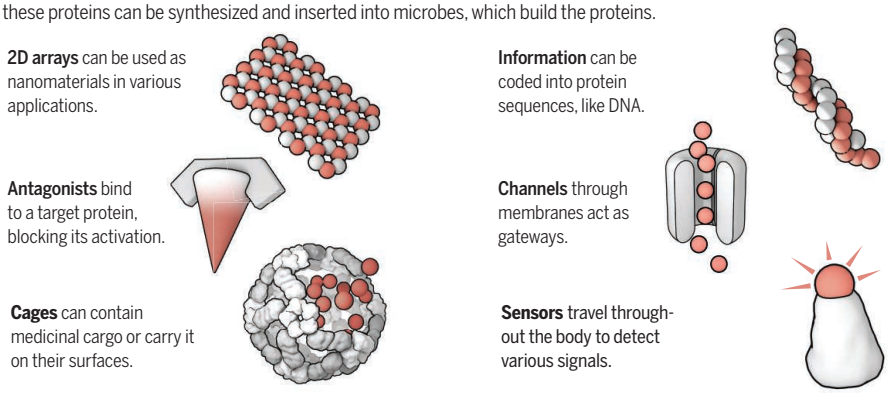

CREDITS: (ILLUSTRATIONS) V. ALTOUNIAN/*SCIENCE*; (DATA) SERGEY OVCHINNIKOV/BAKER'S LAB

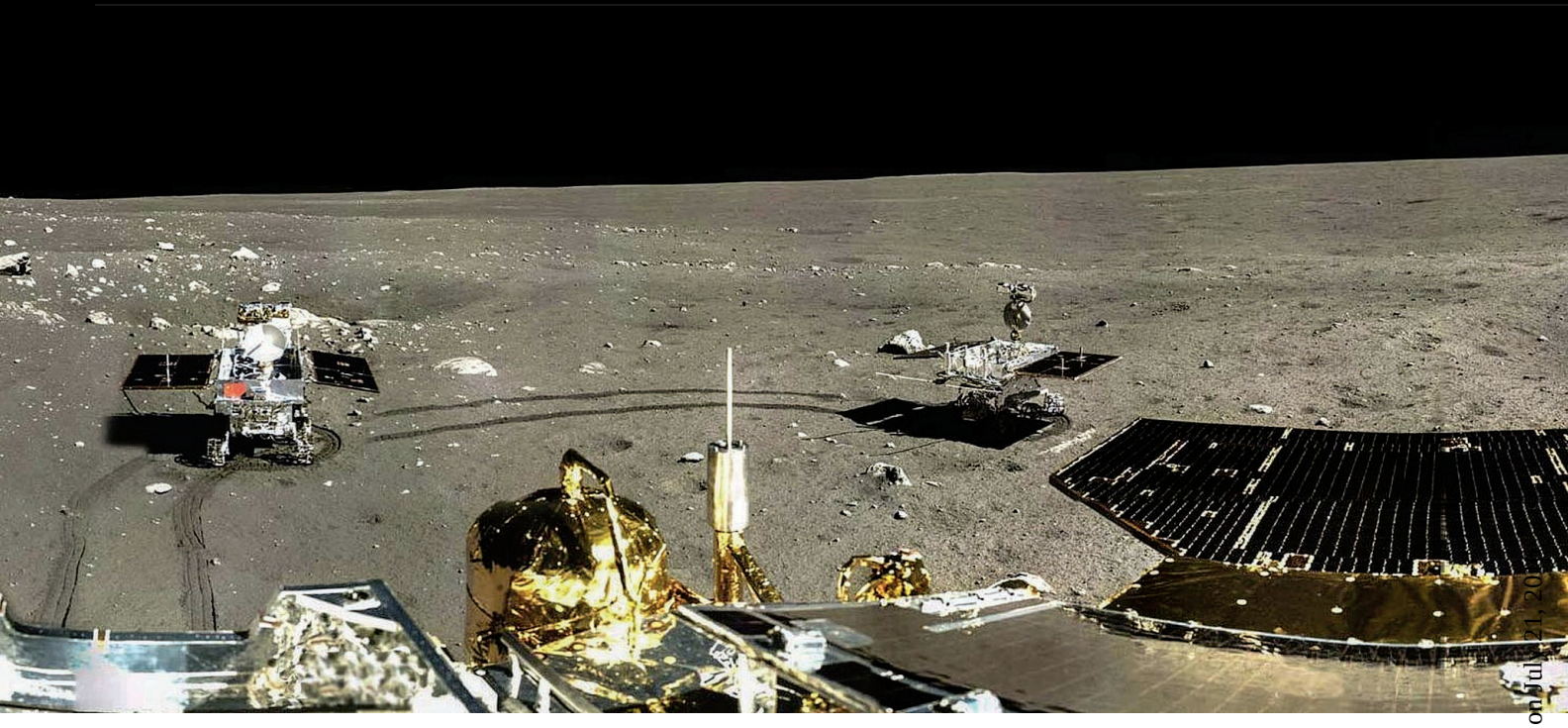

RED STAR RISING

A fusillade of missions has thrust China into the upper echelon of space science

By **Dennis Normile**, *in Beijing*

China's military launches unnerve its rivals, and its human space flights impress the world. But a launch planned for next month has riveted an unusual audience: quantum physicists. The Quantum Experiments at Space Scale (QUESS) aims to test a bedrock principle of quantum mechanics by generating pairs of photons in a state called entanglement, in which measuring the polarity of one photon instantly determines the outcome of a measurement on the other, no matter how far away—what Einstein famously called "spooky action at a distance." Entanglement is well established at close range. But to push the limits, QUESS will transmit one photon in each entangled pair to a receiver in Delingha, in western China, and the other to Lijiang, 1200 kilometers to the southeast.

The experiment is not only a milestone test of quantum mechanics, but a symbol of China's ambitions in space science. Led by Pan Jian-Wei, a physicist at the University of Science and Technology of China in Hefei, QUESS is "very significant," says Nicolas Gisin, a quantum physicist at the University of Geneva in Switzerland. Not only because it is expected to extend the distance record for entanglement, Gisin says, but because the techniques that Pan's team has developed to generate, capture, and identify single photons "open new possibilities both for fundamental experiments and for applications."

China's space science launches are now coming thick and fast. Three missions bracket QUESS, including two that promise valuable x-ray observations: the Dark Matter Particle Explorer (DAMPE), launched last December to look for signs of dark matter particles annihilating in the distant universe, and the Hard X-ray Modulation Telescope (HXMT), slated for launch this December or January. HXMT will survey the cosmos for black holes and other high-energy objects. Another cluster of four missions is slated for launch starting in 2020. And China's lunar exploration program, although closely bound up with its ambitions for human spaceflight, is also yielding path-breaking science.

Wu Ji, director of the Chinese Academy of Sciences's (CAS's) National Space Science Center (NSSC) here, would prefer a more measured pace. Four missions within a year "is too much," he says, but the fusillade reflects the flow of funding. China's space scientists were poor cousins of colleagues in the manned space program until CAS won governmental support in 2011 for a 10-year Strategic Priority Program on Space Science. The initiative provided $450 million over the first 5 years, leaving the newly formed NSSC scrambling to plan, design, and launch four missions at once. A roughly equal dollop is promised for the second 5 years, just getting underway—leaving NSSC with the task, once again, of developing multiple missions in parallel before the money runs dry. "This is

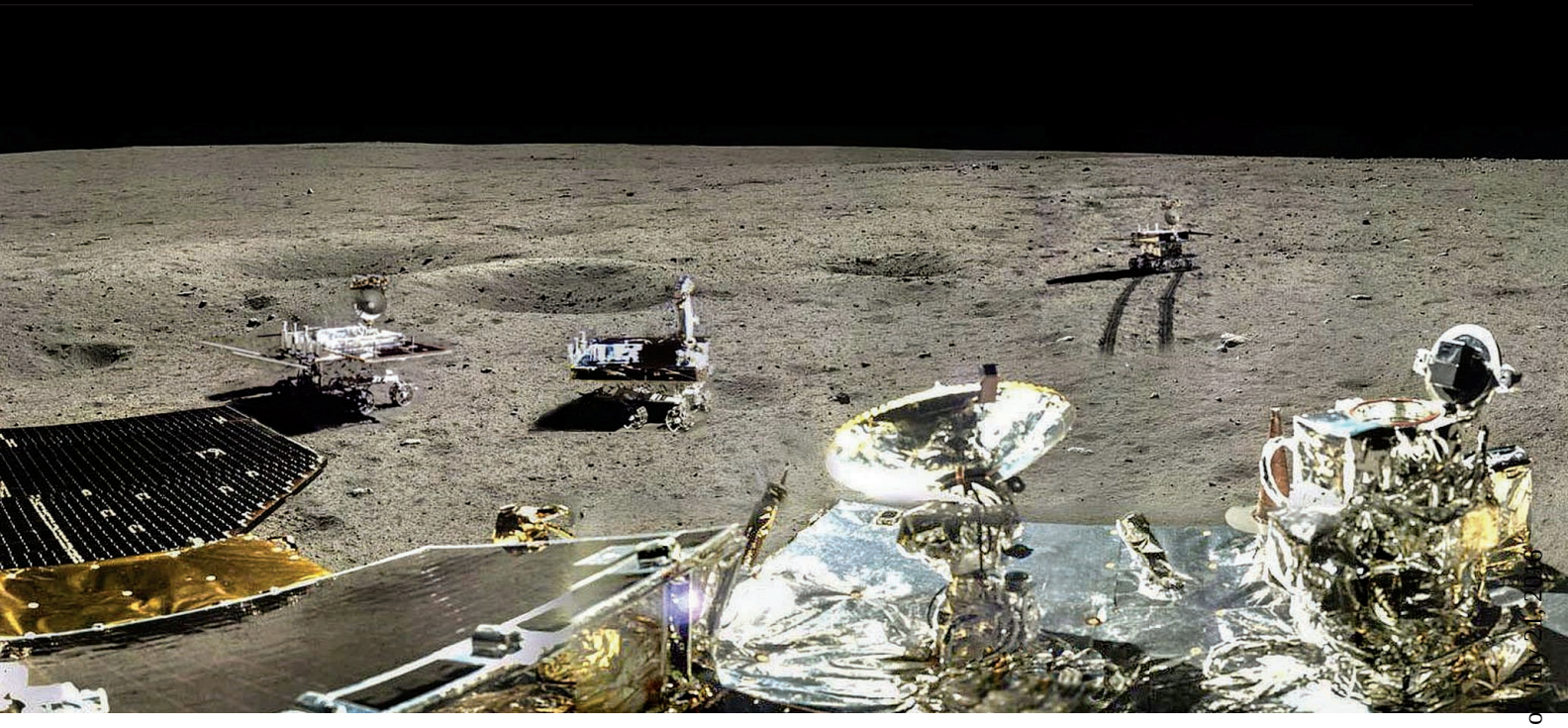

Panorama of the Chang'e-3 landing site after the Yutu rover rolled out onto the moon's surface in late 2013.

not a sustainable way to have a science program," Wu says.

Yet China deserves high marks for doing a lot in space with little, observers say. China's overall spending on space is "a smallish fraction" of NASA's $19.3 billion budget, says John Logsdon, an expert on China's space program at The George Washington University in Washington, D.C. Despite the limited resources, says Chris Carr, a space plasma physicist at Imperial College London, "China is certainly stepping out on its own with its own ideas of what it wants to do and confidence in its scientific capabilities."

China only got into the space science race 15 years ago, with a mission to study the magnetosphere—the plasma bubble that shields Earth from the solar wind. Double Star was designed to complement the European Space Agency's (ESA's) Cluster mission: four satellites orbiting in close formation launched in 2000 to get a fine-grained, 3D picture of the magnetosphere. The two Double Star satellites, launched in 2003 and 2004, with one in a polar orbit and the other circling above the equator, added big picture context to Cluster's localized view, says Carr, who collaborated with China on the mission. The coordinated measurements led to insights into the interaction between the solar wind and the magnetosphere, including how the disturbances that generate the aurora begin, and how solar flares can drastically compress the magnetosphere, sometimes exposing satellites to damaging radiation. Even though Double Star officially ended in 2007, when one of the spacecraft re-entered Earth's atmosphere and burned up, researchers are still mining the data, with more than 2300 peer-reviewed papers and counting, Carr says.

Meanwhile, science has become increasingly important for China's lunar exploration program, which is run by the China National Space Administration (CNSA) in Beijing. The Chinese Lunar Exploration Program, or Chang'e, missions, named after a Chinese moon goddess, started with a lunar orbiter in 2007. The latest, Chang'e-3, comprised a lander and rover that touched down in December 2013—the first lunar landing since a Soviet sample return mission in 1976. Chang'e-3 carried an instrument suite to probe the moon's geology and soil and an ultraviolet telescope to test the feasibility of making astronomical observations from the moon.

At a mission control center in Beijing, space science chief Wu Ji gives an update on the Dark Matter Particle Explorer after its launch last December.

An apparent electrical circuit failure left the rover, named Yutu, immobile 6 weeks into its 3-month mission after it traveled 114 meters. Nevertheless, Chang'e-3 fulfilled its mission and is now "working overtime," gathering scientific data while engineers assess component durability, says Wu Weiren, Chang'e program chief designer for CNSA.

Chang'e-3 scientists were out to "complement and deepen humankind's scientific understanding of the moon," says Li Chunlai, deputy director-general of CAS's National Astronomical Observatories in Beijing, which advised on the mission's science. One example is the rover's ground-penetrating radar, which mapped layers of regolith, or lunar "soil," and subsurface lava flows. The mapping revealed a "more complex geological history than we had thought," Long Xiao of the China University of Geosciences, Wuhan, and colleagues wrote in *Science* (13 March 2015, p. 1226). David Kring, a geologist at the Center for Lunar Science and Exploration in Houston, Texas, calls the radar's performance "spectacular."

Kring and others are even more excited about upcoming Chang'e missions. In the second half of next year, Chang'e-5 is slated to land on the moon, collect surface rocks and drill 2 meters into the regolith for samples, and then return to Earth. The lunar landing will probably be

PHOTOS: (TOP TO BOTTOM) CNSA/CHINANEWS/KEN KRAMER/MARCO DI LORENZO; XINHUA/JIN LIWANG

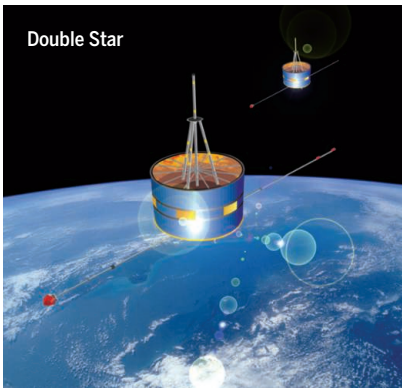

Loftier ambitions

China set out on its space science journey in 2004 with Double Star, a joint mission with Europe. Now, it is carrying out four missions in a little more than a year starting last December, including a highly anticipated quantum spacecraft set to launch next month. Another clutch of science missions is planned for 2020. China's lunar program, meanwhile, is evolving from technology demonstration to exploration.

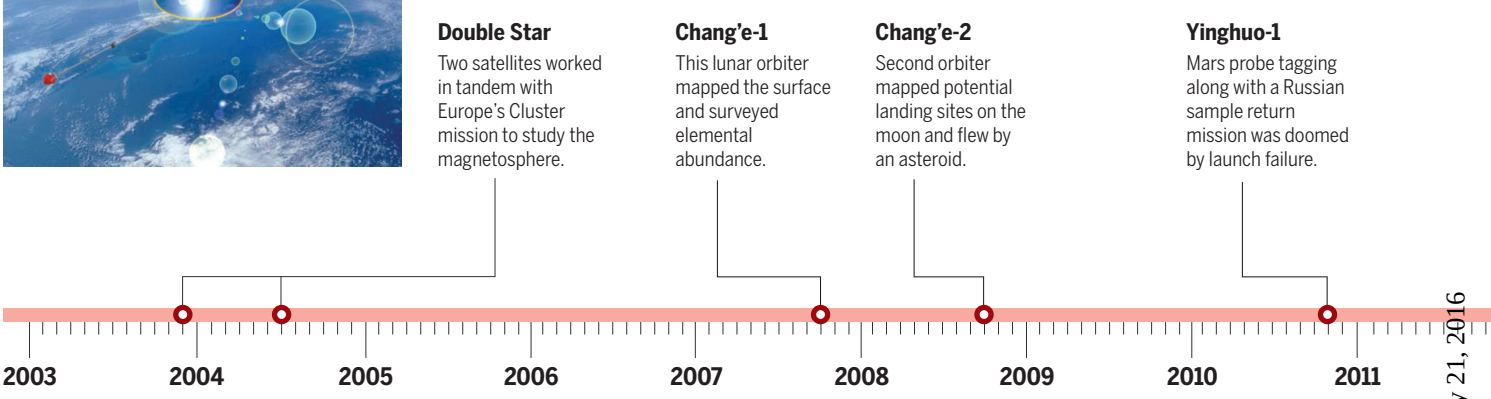

somewhere on the Ocean of Storms, a vast basaltic plain on the moon's western near side. The CNSA team is looking for a landing site that will produce "maximum scientific results," Wu says.

Then, in 2018, Chang'e-4 will attempt the first landing on the far side of the moon. Kring predicts the probe will yield a bonanza of findings on the moon's early days that could shed light on how planets throughout the solar system accreted material and formed crusts. Chang'e-4 will also investigate the promise of the moon's far side—sheltered from Earth's glare and radio emissions—as a base for astronomical observations. Russian, Swedish, and Dutch groups are contributing to the payloads, and a team from Luxembourg is developing a small lander that will separate from Chang'e-4 and touch down on the moon's near side.

Then it will be on to Mars, with a 2020 mission comprising an orbiter, lander, and rover, says Tian Yulong, CNSA's secretary general. The scientific objectives will cover topography, geology, and environment, Tian says. The data will aid planning for a crewed mission to Mars, but are likely to advance basic science as well.

CNSA has had the luxury of steady funding. Until recently, space science missions had to scrape by, except for Double Star, which got one-off funding through CNSA. Pan, for instance, used money leftover from other projects to initiate QUESS. When CAS launched the 10-year space science program, NSSC took over missions already in the works, including QUESS, DAMPE, and HXMT.

For the next set of missions, NSSC picked three winners based on scientific impact, or "how many papers it will generate," and influence, judged by how many researchers want the promised data, Wu Ji says. A joint NSSC-ESA program chose the fourth mission.

All four missions are now planned for 2020. One satellite will look down at Earth to capture simultaneous measurements of soil moisture, ocean salinity, water in snow packs, atmospheric water vapor, and precipitation. Called the Water Cycle Observation Mission, it is China's maiden contribution to global Earth observation efforts. "We're

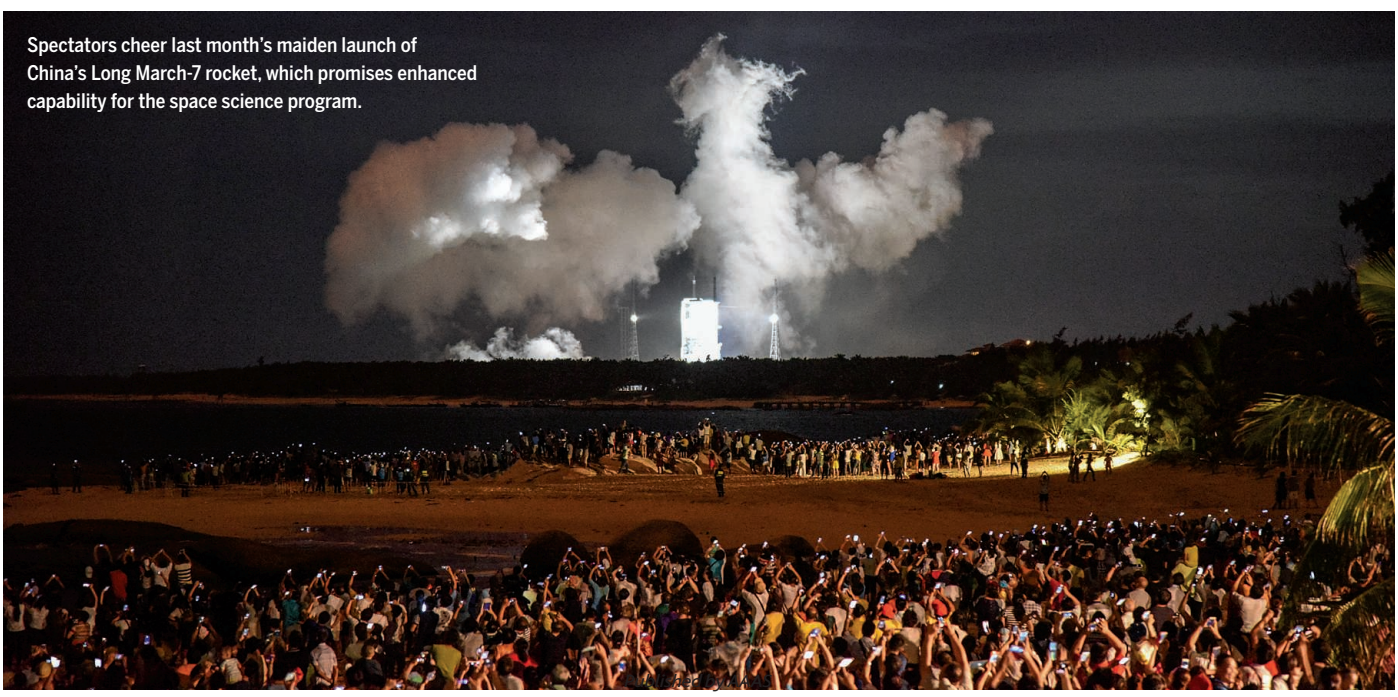

Spectators cheer last month's maiden launch of China's Long March-7 rocket, which promises enhanced capability for the space science program.

PHOTOS: (TOP TO BOTTOM) ESA; VISUAL CHINA GROUP VIA GETTY IMAGES

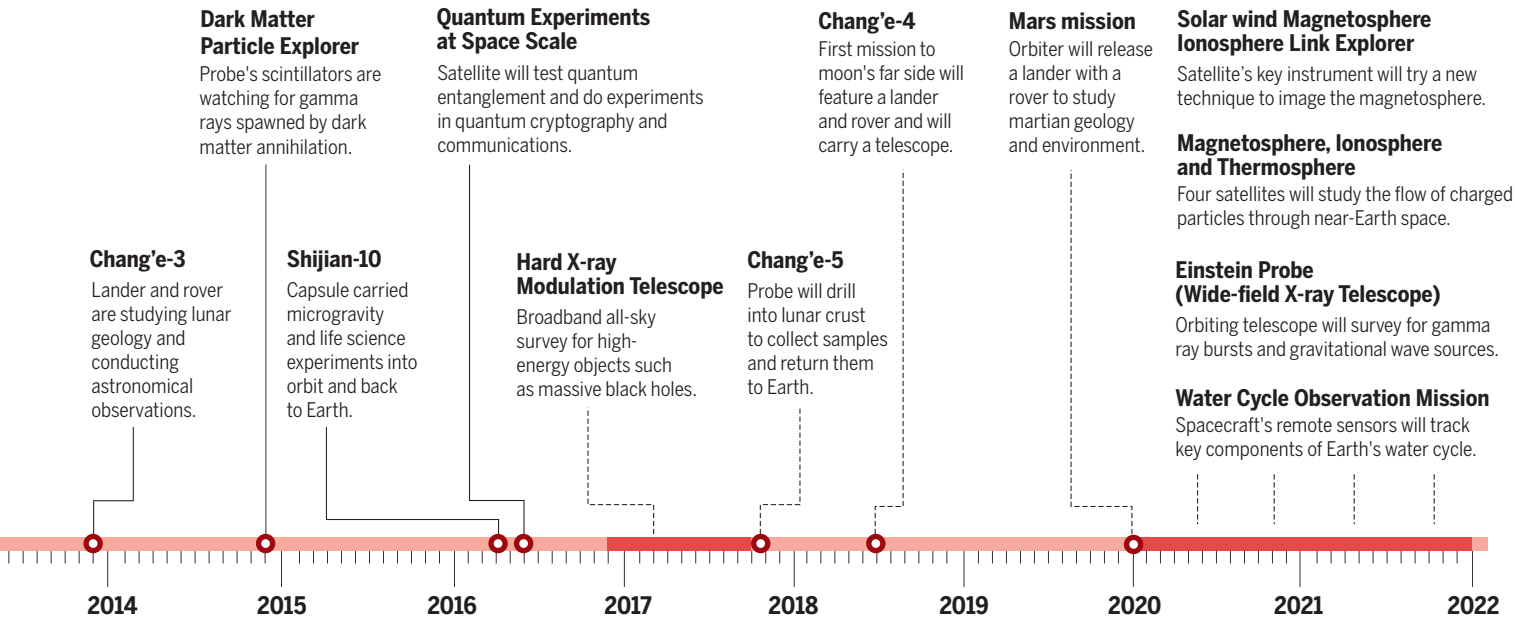

TIMELINE DATA SOURCE: NSSC AND CNSA

all eager to see it succeed," says Jeff Dozier, a hydrologist at the University of California, Santa Barbara. Current satellites can't capture data on water in its multiple forms, which makes hydrological modeling difficult, says lead scientist Shi Jiancheng of CAS's Institute of Remote Sensing and Digital Earth in Beijing.

The mission with ESA, to study x-rays generated when the solar wind slams into neutral particles above the magnetosphere, is taking "a jump forward into unknown territory, rather than doing something just a little bit better," says David Sibeck, a space physicist at NASA's Goddard Space Flight Center in Greenbelt, Maryland, who will help analyze the data. The mission, the Solar wind Magnetosphere Ionosphere Link Explorer (SMILE), could lead to strategies to mitigate the impact of space weather on communications infrastructure. Sibeck says that many teams, including his Goddard group, wanted to probe the x-ray phenomenon, but SMILE will get first crack.

Wu Ji worries that such ambitions will be difficult to sustain after funding runs out in 2020. Although annual funding would be a step in the right direction, a longer term hope is to unite China's space efforts under a civilian agency similar to NASA and ESA. As a possible step in that direction, CNSA's Tian says his agency is developing a 10-year road map for scientific missions, drawing input from CAS, the science ministry, and universities.

In the meantime, space scientists in other countries are applauding China's rise—and in some cases envying it. As Sibeck says of SMILE, "We would like to have done it ourselves." ■

Who's missing from this picture?

By **Dennis Normile**

As China's ambitions in space science soar, other space powers are eager to join forces with it. But one country has been absent from the burgeoning science cooperation: the United States.

Every year since 2011, powerful Republican members of the U.S. House of Representatives, concerned about China's human rights record and fearing industrial espionage, have inserted language into NASA's appropriations legislation that bars the agency from using the funding for any bilateral activities "with China or any Chinese-owned company" (*Science*, 29 April 2011, p. 521). NASA officials can meet Chinese counterparts only under certain conditions.

"The calculation comes down to whether the benefits of civil cooperation are great enough to outweigh the risks of helping China's military capabilities," says John Logsdon, an expert on China's space program at The George Washington University in Washington, D.C. The answer so far has been a resounding no.

Other countries see cooperation with China in a different light. European and Russian researchers are contributing to China's lunar program and virtually all the space science missions. Last year, the European Space Agency (ESA) officially designated China as a key partner, along with the United States and Russia, says Karl Bergquist, an ESA international relations administrator in Paris.

U.S. scientists can sidestep the ban by finding non-NASA funding or by concentrating on data analysis. But the restriction on closer cooperation "is frustrating to the community," says Jeff Dozier, a hydrologist and remote sensing specialist at the University of California, Santa Barbara. NASA administrator Charles Bolden in Washington, D.C., has also urged that it be relaxed.

But there is dogged opposition to any easing of the restrictions. Representative John Culberson (R–TX), chairman of the House committee that crafts the annual appropriations bill, told *Science* that he believes the existing language should be toughened because NASA "must keep the Chinese out of the U.S. space program."

"Do we still need American technologies? The answer is clearly no," scoffs China National Space Administration Secretary General Tian Yulong in Beijing. "The purpose of any cooperation with the U.S.," he says, "would be to realize joint objectives for the benefit of human society." ■

ECOLOGY

Can Apulia's olive trees be saved?

An introduced plant pathogen proves difficult to contain in southern Italy

By **Rodrigo P. P. Almeida**

On 21 October 2013, the Italian phytosanitary service notified the European Commission (EC) that the plant pathogen *Xylella fastidiosa* had been detected in olive trees near Gallipoli, a tourist destination in Italy's southern region of Apulia (*1*). This xylem-limited bacterium is spread by insect vectors and causes disease in crops such as grapevines, citrus, coffee, and almond; various ornamentals; and trees such as oaks, elms, and sycamores. Because of the risks of *X. fastidiosa* being introduced, established, and spread throughout Europe, this species is a regulated quarantine pest. Yet, *X. fastidiosa* has been left unchecked and has marched northward, leaving destruction in its wake (see the photo) (*2*). The establishment of *X. fastidiosa* in Italy has been an agricultural, environmental, political, and cultural disaster.

The threat of *X. fastidiosa* to European and Mediterranean agriculture, forests, and ecosystems goes beyond specific crops such as grapevines or citrus. The current host range of this bacterium includes more than 300 plant species (*3*). Most of these species support some degree of pathogen multiplication without expressing symptoms. Susceptible hosts infected with *X. fastidiosa* often show disease symptoms only after months or years, although epidemics can spread fast and be devastating.

A phylogenetic study has shown that the genotype in Italy was likely introduced via contaminated plant material from Costa Rica (*3*). Several *X. fastidiosa*–infected coffee plants from Costa Rica have been intercepted at European ports since 2014, supporting this hypothesis (*4*). As a response, the EC in February 2014 approved European Union (EU) emergency measures aimed at preventing the introduction and spread of *X. fastidiosa*. Since May 2015, the import of coffee plants from Costa Rica and Honduras into the EU has been forbidden. Limiting the introduc-

Department of Environmental Science, Policy and Management, University of California, Berkeley, Berkeley, CA 94720, USA. Email: rodrigoalmeida@berkeley.edu

PHOTO: ANTONIO GUARIO

Irreplaceable trees. In this aerial view of an olive grove in the Salento peninsula, *X. fastidiosa*–infected trees show intermediate disease symptoms. Efforts to contain the pathogen's spread by cutting down infected trees have been hampered by local opposition.

tion of insect vectors is considered an easier task, but this is not possible for *X. fastidiosa* because any xylem-sap–sucking insect species can be a potential vector. Europe has few sharpshooter leafhopper species, the most important group of vectors in the Americas. However, various endemic spittlebug species (froghoppers) are also potential vectors of *X. fastidiosa* (*3*).

Trade is an important pathway in the introduction of plant pests and pathogens (*5*), and *X. fastidiosa*–infected plant material has likely been introduced via European ports on a regular basis. Given that biological and environmental conditions in Europe support *X. fastidiosa* infection, the question arises why the pathogen has not been reported previously. One possible explanation is that limited surveillance efforts missed previous introductions. Monitoring was one component of the EU emergency measures. After the French authorities started a systematic monitoring program for *X. fastidiosa* in 2014, they found 250 distinct infected areas in Corsica and several in the French Riviera. However, no disease epidemic has yet been noted in France, and the genotype of *X. fastidiosa* differs from that found in Italy.

Control efforts of *X. fastidiosa* diseases in Brazil and the United States, where most economic losses due to this pathogen occur, rely on a combination of insect population suppression and removal of infected plant material. Initial management efforts in Italy and France were expected to follow legally binding EC decisions. These include elimination of infected plant material and other susceptible hosts within 100 meters, the use of treatments to suppress vector populations, and surveillance of a larger area surrounding each location where infected material has been found. France is following these regulations, but they have not been implemented in Italy.

Eradication of *X. fastidiosa* requires early diagnosis and a small infected area, and is no longer feasible in Apulia. The role of olive trees in pathogen spread remains to be quantified, but they serve as a source of inoculum to spittlebug vectors (see the figure). Information required to manage the epidemic in Italy is being generated, such as new evidence of olive varietal tolerance to *X. fastidiosa* (*6*). But it remains unclear how long it takes for plants to develop symptoms after infection. A March 2016 report by the European Food Safety Authority indicates that it takes 12 to 14 months for small olive plants to show disease symptoms after artificial infection with *X. fastidiosa* in greenhouses (*7*). This is relevant because vectors may acquire *X. fastidiosa* from an infected host prior to developing symptoms. Eliminating diseased trees may thus have limited impact on containing the pathogen. Instead, removing infected yet asymptomatic plants surrounding sick trees may be key to controlling disease spread. It is likely that the epidemic is more prevalent than suggested by symptomatic trees, and the pathogen may already be present north of the current containment line.

Local environmentalists and politicians have challenged EC decisions and have used lawsuits to block attempts to manage the epidemic (*2*). Their efforts to protect olive trees by blocking containment strategies have, however, only exacerbated the problem. Public distrust of science and scientists has led to conspiracy theories that have permeated local society, further hampering control efforts. In retrospect, social turmoil should have been expected given the prominent role of olive trees in Apulian culture. Olive trees are tightly linked to its people; it is their heritage, an indivisible part of who they are. In addition, ubiquitous olive trees are a key attraction of an economically important tourism industry, provide income to rural communities, and are a keystone species in the ecosystem. The EC aims to address the threats of *X. fastidiosa* as a plant pathogen, demanding management and containment measures. But the reality to Apulians is different: Cutting down their olive trees means destroying the physical embodiment of their families and history. Here, the disease is killing irreplaceable trees, including those planted to mark the births of family members for generations. The harm to Apulian culture and society is perhaps beyond quantification.

Reconciling technical and political differences will be key to limiting the impact of *X. fastidiosa* to Apulia and Europe at large.

It remains to be seen whether a 9 June 2016 ruling of the European Court of Justice, determining that EC-mandated control measures were legal, will be accepted locally. Implementation of the ruling would suggest that there is hope in limiting pathogen spread, but time is running out for the olive trees in Apulia. The reluctance of political leaders to quickly take required but unpopular decisions, in addition to a judicial system slow in responding to an emergency, are likely responsible for the current lack of substantial action in controlling the epidemic. There has also been limited local political support for scientists, who are unable to freely seek answers to important epidemiological questions because of restrictions on field experimentation; even disease monitoring has been blocked (*8*).

The introduction of plant pathogens and pests is a growing risk to ecosystems and societies (*9*), but not a new one. The potato famine in Ireland, blight of American chestnut in the USA, and grapevine phylloxera in France are examples of diseases and pests that have reshaped landscapes and cultures. Swift management strategies can lead to eradication or effective containment and long-term sustainable solutions. Global strategies to manage emerging disease and pest problems may be required, as have been proposed for planted forests (*10*). International trade regulations represent an opportunity to limit the introduction of novel pests, but the relationship between trade and biological invasions may need to be better explored (*11*), and control of the pathogen at the source rather than destination may be more effective.

An important lesson from the *X. fastidiosa* epidemic is that strategies to manage diseases of socially important plants must go beyond technical solutions and incorporate social, economic, political, and cultural components. In the case of *X. fastidiosa* in Italy, implementation has been the bottleneck as these diverse stakeholders did not cooperate. Models for such cooperative structures have been proposed (*12*). Rapid reaction time is key to success in managing outbreaks, unfortunately building trust among stakeholders to solve environmental problems often requires years. ■

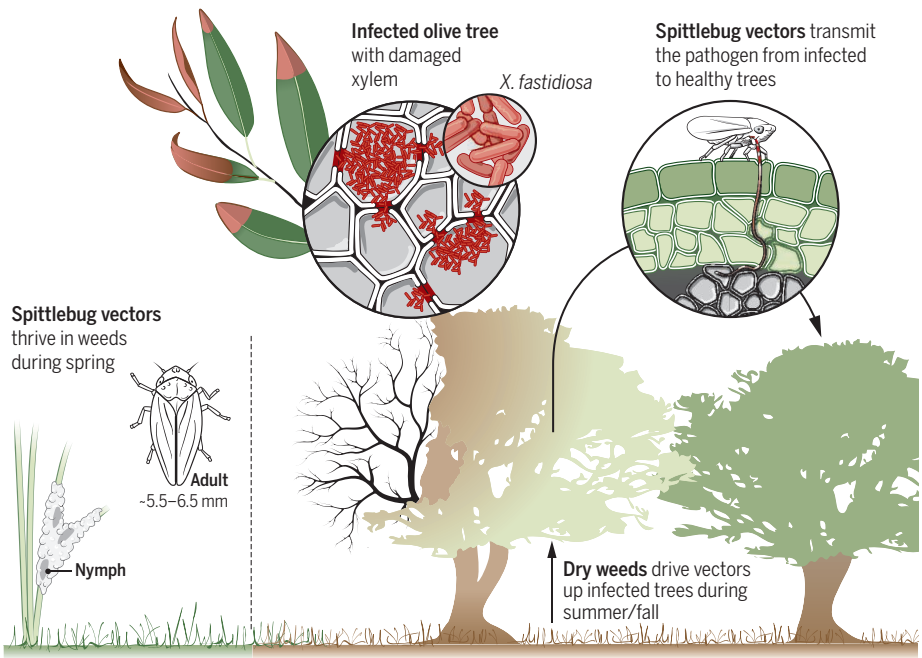

Pathogen spread. The epidemiology of *X. fastidiosa* infecting olive trees in Apulia is still poorly understood. The prevailing hypothesis proposes that olive trees are the main pathogen inoculum source, and that tree-to-tree *X. fastidiosa* spread occurs once insect vectors move to trees from drying ground vegetation.

GRAPHIC: K. SUTLIFF/*SCIENCE*

REFERENCES

1. E. Stokstad, *Science* **348**, 620 (2015).
2. A. Abbott, *Nature* 10.1038/nature.2015.19078 (2015).
3. European Food Standards Authority (EFSA) Panel on Plant Health, *EFSA J.* **13**, 3989 (2015).
4. EFSA, *EFSA J.* **13**, 4061 (2015).
5. European and Mediterranean Plant Protection Organization (EPPO), EPPO technical document no. 1061 (2012).
6. A. Giampetruzzi, *BMC Genomics* **17**, 475 (2016).
7. M. Saponari *et al.*, EFSA supporting publication 2016:EN-1013 (2016).
8. A. Abbott, *Nature* **533**, 299 (2016).
9. I. L. Boyd, *Science* **342**, 823 (2013).
10. M. J. Wingfield, *Science* **349**, 832 (2015).
11. D. R. Paini *et al.*, *Proc. Natl. Acad. Sci. U.S.A.* **113**, 7575 (2016).
12. P. Mills, *Phil. Trans. R. Soc. B.* **366**, 2035 (2011).

10.1126/science.aaf9710

MICROBIOME

Is triclosan harming your microbiome?

Studies on the effects of a widely used antimicrobial reach conflicting results

By **Alyson L. Yee**[1,2,3] *and* **Jack A. Gilbert**[2]

Antibacterial soaps were originally used only in hospitals, but since the 1990s, their use has expanded into households. Antimicrobial chemicals are now found in many soaps, wipes, hand gels, cutting boards, detergents, cosmetics, and toothpastes, as well as toys and plastics. One of the most common antibacterials, triclosan [5-chloro-2-(2,4-dichlorophenoxy)phenol], is found in ~75% of antibacterial soaps (*1*). In 2008, it was detected in ~75% of urine samples in the United States (*2*). There are concerns that triclosan use contributes to the development of antibiotic resistance and may adversely affect human health. Partial bans exist in the European Union and the U.S. state of Minnesota (*3*, *4*). However, recent studies exploring triclosan's effect on the microbiome have given conflicting results.

Triclosan works by inhibiting the final step of the bacterial fatty acid synthesis pathway. At low concentrations it stops microbial growth, but at high concentrations it is bactericidal. Bacterial resistance to triclosan is readily obtained in the laboratory, but it is not clear that resistance is widespread in the environment. A 10-year study of triclosan exposure found no change in the antibiotic tolerance of methicillin-resistant *Staphylococcus aureus* or *Pseudomonas aeruginosa* (*5*). However, in a recent report, prolonged treatment with triclosan produced clinical resistance to ampicillin and/or ciprofloxacin in *S. aureus* and *Escherichia coli* (*6*).

To explore the effectiveness of triclosan, Kim *et al.* (*7*) recently compared the bactericidal effects of plain and triclosan-containing soaps under conditions that mimic

[1]*Committee on Microbiology, University of Chicago, Chicago, IL 60637, USA.* [2]*Department of Surgery, University of Chicago, Chicago, IL 60637, USA.* [3]*Medical Scientist Training Program, University of Chicago, Chicago, IL 60637, USA. Email: gilbertjack@uchicago.edu*

handwashing. They found no differences in the soaps' ability to reduce bacterial abundance during a brief (20 s) exposure. The exposure time may have been too short to see an effect, or soap surfactants may have reduced triclosan's activity. Triclosan is bactericidal in water-based solution with 24 hours of exposure.

Exposure to antimicrobial compounds can disrupt the community of microorganisms that colonize the human body. Perturbations in the microbiota have been linked to a wide array of diseases and metabolic disorders, including obesity, inflammatory bowel disease (IBD), irritable bowel syndrome (IBS), and behavioral and metabolic disorders. However, it remains unclear whether triclosan can disrupt the microbiome to such an extent that it influences health and well-being (*8*).

To elucidate the effect of triclosan on the microbiome, Gaulke *et al.* exposed adult zebrafish to high oral doses of triclosan over the course of 7 days (*9*). This acute exposure resulted in changes in community structure, interaction networks, and an increase in triclosan resistance. However, the microbiome of fish exposed for only 4 days with 3 days of no exposure was no different from that of the control fish. This observation suggests either resilience to temporary disturbance or that changes are reversible.

Narrowe *et al.* studied the effects of triclosan exposure on the microbiome of fathead minnows (*10*). They used environmentally relevant doses of triclosan in the fishes' habitat, which led to substantial shifts in the microbiome, which again recovered after triclosan was removed. However, in a study of riverine biofilms, Lawrence *et al.* found that even after the removal of triclosan, the microbiome remained disrupted (*11*).

To explore the effects of triclosan on human microbiota, Poole *et al.* gave seven volunteers personal products (toothpaste, hard and liquid soap, and dish soap) containing triclosan to use at will for 4 months; the same volunteers then switched to 4 months of products without triclosan. A second group started with non-triclosan products and then switched to the triclosan products (*12*). Urinary concentrations of triclosan were higher in all volunteers during the triclosan period, but the composition of the stool, molar, or incisor microbiomes did not change, nor were there changes in serum endocrine markers.

There are a few possible explanations for the disparities among these studies. In both the zebrafish and minnow studies, the fish were exposed to triclosan for much longer durations than those generally experienced by humans. The fish consumed triclosan in food or were immersed in triclosan, whereas humans typically encounter the compound in products such as soap and toothpaste that are rinsed off immediately. It is also possible that triclosan exposure is so ubiquitous, starting as early as prenatal exposure, that the human microbiota has already adapted. Even in the human trial with periods of no triclosan, the compound was still detectable in urine, although at lower concentrations (*12*).

Future research should explore the role of dose, timing, and route of triclosan exposure. Humans are exposed to triclosan transiently and in small doses, but the presence of triclosan in surface, ground, and drinking water indicates its potential to persist and accumulate in the environment (*5*). Triclosan is readily absorbed through the skin and gastrointestinal tract, but in humans, it tends to be applied topically and is thus not subject to metabolic alteration in the gastrointestinal tract, whereas this may have been the case in the fish studies. Therefore, it is important to determine whether the metabolic by-products of triclosan also affect the structure of the microbiota.

It is also possible that prenatal, perinatal, and postnatal triclosan exposure is more detrimental than adult exposure. Cox *et al.* have suggested that there are key developmental windows during which microbiome perturbations can leave lasting impacts on neurological and immune development (*13*). Hu *et al.* recently showed that the adolescent rat microbiota are more vulnerable to chemical perturbation than that of adult rats (*14*). They administered oral doses of triclosan sufficient to recapitulate observed human urinary levels and found substantial differences between the microbiota of triclosan-exposed and control adolescent rats. These changes were attenuated in adult rats, implying that low-dose postnatal exposure to triclosan may modulate microbiota composition but that the microbiota may recover.

Triclosan and disinfectants containing other antimicrobials are used even more frequently and in higher concentrations in hospitals than in the home. Given that more than 98% of infants are delivered in hospitals and that infants are particularly naïve to microbes, their microbiota is vulnerable at this developmental stage. Thus, triclosan should be investigated for its potential to perturb microbial community assembly and succession. ■

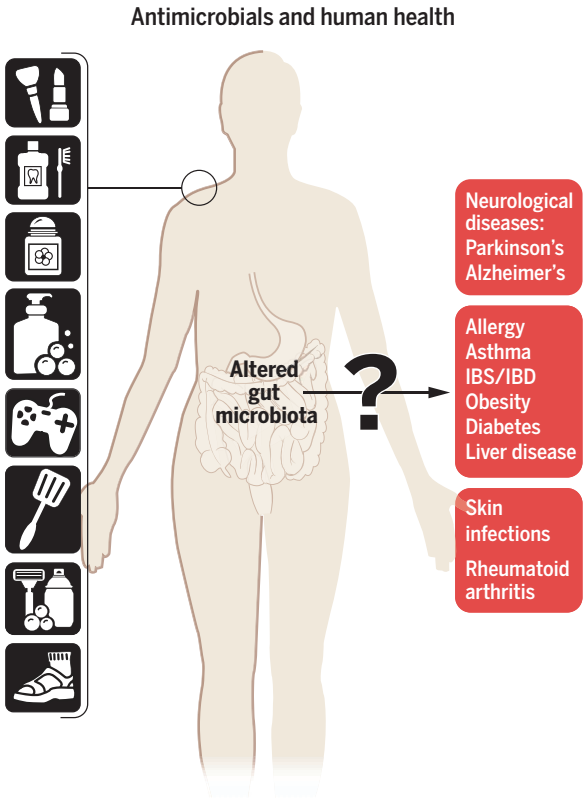

Uncertain effects. The antimicrobial compound triclosan, found in many soaps and other household products, can change the gut microbiota of fish and rats. It remains unclear whether such effects occur in humans and, if so, what the health effects are.

GRAPHIC: N. CARY/*SCIENCE*

REFERENCES

1. U.S. Food and Drug Administration, "FDA Taking Closer Look at 'Antibacterial' Soap" (December 2013); www.fda.gov/downloads/ForConsumers/ConsumerUpdates/UCM378615.pdf.
2. A. M. Calafat, X. Ye, L.-Y. Wong, J. A. Reidy, L. L. Needham, *Environ. Health Perspect.* **116**, 303 (2008).
3. Triclosan, White Paper prepared by the Alliance for the Prudent Use of Antibiotics (APUA), January 2011; www.tufts.edu/med/apua/consumers/personal_home_21_4240495089.pdf.
4. J. Marty, F. Hawj, J. A. Hoffman, C. A. Eaton, B. Scalze, Minnesota Senate Bill 2192 (2014).
5. G. S. Dhillon *et al.*, *Int. J. Environ. Res. Public Health* **12**, 5657 (2015).
6. R. Wesgate, P. Grasha, J.-Y. Maillard, *Am. J. Infect. Control* **44**, 458 (2016).
7. S. A. Kim, H. Moon, K. Lee, M. S. Rhee, *J. Antimicrob. Chemother.* **70**, 3345 (2015).
8. M. A. Adgent, W. J. Rogan, *Environ. Res.* **142**, 66 (2015).
9. C. A. Gaulke, C. L. Barton, S. Proffitt, R. L. Tanguay, T. J. Sharpton, *PLOS ONE* **11**, e0154632 (2016).
10. A. B. Narrowe *et al.*, *Microbiome* **3**, 6 (2015).
11. J. R. Lawrence *et al.*, *Aquat. Toxicol.* **161**, 253 (2015).
12. A. C. Poole *et al.*, *mSphere* **1**, e00056-15 (2016).
13. L. M. Cox *et al.*, *Cell* **158**, 705 (2014).
14. J. Hu *et al.*, *Microbiome* **4**, 26 (2016).

10.1126/science.aag2698

EVOLUTION

Hominid superorganisms

Ancient microbial symbionts cospeciated with hominids

By **Julia A. Segre**[1] *and* **Nick Salafsky**[2]

Mutualistic symbiotic relationships are those in which both species benefit; for example, the vivid colors of coral reefs come from symbiotic algae that provide their living coral hosts with nutrients and oxygen through photosynthesis in exchange for protection. A similar mutualistic relationship exists between gut-dwelling bacteria and their animal hosts (*1*). It remains unclear, however, to what degree symbiosis has shaped host-microbial interactions and coevolution. On page 380 of this issue, Moeller *et al.* show that gut bacterial strains cospeciated with hominids (apes and humans) over the past 15 million years (*2*). These findings set the stage for exploring the evolutionary processes that underlie the symbiotic relationship between hominids and their gut-dwelling microbes.

Moeller *et al.* obtained fecal samples from wild chimpanzees (*Pan troglodytes*) from Tanzania, wild bonobos (*P. paniscus*) from the Democratic Republic of the Congo, wild gorillas (*Gorilla gorilla*) from Cameroon, and humans (*Homo sapiens*) from the United States. They use DNA gyrase, subunit B (*gyrB*)—a single-copy, protein-coding gene in bacterial genomes that evolves at a moderate rate (*3*)—as a marker to assess strain diversity of Bifidobacteriaceae, Bacteroidaceae, and Lachnospiraceae in the gut of humans, chimpanzees, bonobos, and gorillas. This relatively constant *gyrB* molecular clock data allows them to compare the timing of speciation of gut bacterial communities with the known speciation patterns of their hominid hosts.

For different species of Bacteroidaceae, Moeller *et al.* explore the phylogenetic relatedness of closely related strains from the feces of the hominids. Taking the most commonly related *gyrB* sequence from each hominid, the authors calculate the most recent common ancestor and show that bonobo- and chimpanzee-associated strains are most closely related to each other and together form a sister clade to the gorilla and human clades.

This phylogenetic relationship among hominid-associated Bacteroidaceae strains mirrors the host evolutionary topology. For most genera of Bacteroidaceae, the dominant pattern of diversification is hominid-microbial parallel cospeciation, but the authors also report small anomalies. For example, some Bacteroidaceae lineages are absent from either humans or gorillas, representing lost microbial diversity. Bifidobacteriaceae strain phylogeny more or less mirrors that seen for Bacteroidaceae lineages, but Lachnospiraceae strains show evidence for transfer between host species, perhaps because Lachnospiraceae can survive as spores and can thus more readily disperse and transfer among host species. Thus, different evolutionary pressures and forces may shape both host and microbial community members.

To corroborate their findings, the authors also reanalyzed ribosomal sequence data from chimpanzees and gorillas that live together in regions of Cameroon. They found no sequences that were 100% identical, again suggesting that distinct strains coevolved with their hosts. Conversely, to explore if geographic separation might foster diversification within a species, they show that bacterial lineages differ between humans in Malawi and the United States.

Based solely on the sequence divergence of gut bacteria, the authors date the split between humans and chimpanzees at 5.3 million years ago (Ma), in agreement with estimates based on host mitochondrial genomes but slightly later than estimates based on nuclear genomes. They calculate the human-gorilla split at 15.6 Ma, older than estimates based on mitochondrial genomes but within the range of estimates based on nuclear genomes (see the figure).

In addition to corroborating patterns of hominid speciation, the findings of this research potentially lay the groundwork for exploring the genetic basis of symbiotic cospeciation. Regions of the bacterial genomes that are evolving faster than the *gyrB* baseline clock presumably encode genes under positive selection pressure, similar to regions in the human nuclear genome under positive selection because they are involved in language or tool usage (*4*).

A possible caveat to these microbial evolutionary findings is that selective forces may have changed more dramatically in the past century. For example, recent loss of habitat and ensuing geographic isolation of African wild apes may have affected their gut microbe diversity dramatically, much as antibiotic usage may affect human microbial communities (*5*). Close proximity to human communities, researchers, and tourists may also have affected ape microbiomes, either directly or indirectly by introducing disease agents.

Given Moeller *et al.*'s evidence that ancient microbial symbionts cospeciated with hominids, an outstanding functional question is the genetic basis of both the host and microbial side of this symbiosis. At what level does this genetic evolution occur? One could easily imagine a scenario in which an individual ape has a heritable trait

Evidence for cospeciation

Moeller *et al.* (*2*) demonstrate that Bacteroidaceae (Bact.) and Bifidobacteriaceae (Biff.) strains, shown as hues of the same color, cospeciated with their hosts. This suggests that symbiosis may be an evolutionary force. Speciation dates based on (*2*, *10*).

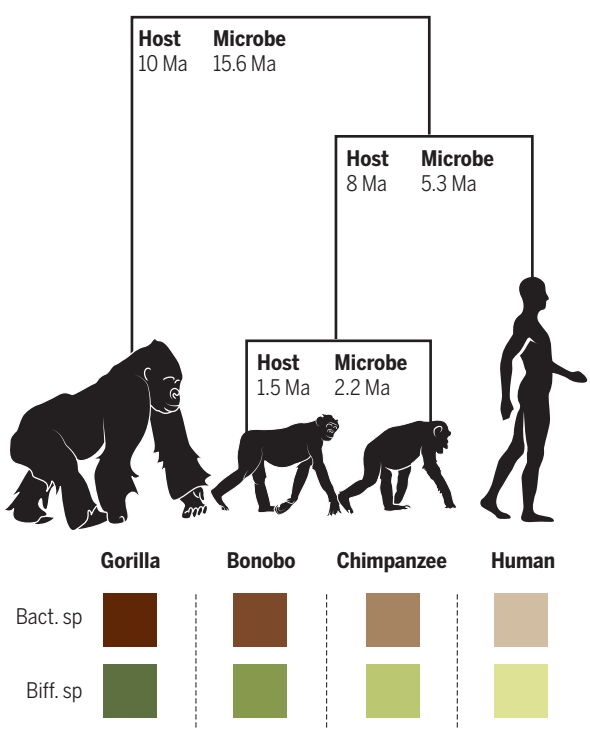

GRAPHIC: K. SUTLIFF/*SCIENCE*

[1]*Microbial Genomics Section, Translational and Functional Genomics Branch, National Human Genome Research Institute, Bethesda, MD 20892, USA.* [2]*Foundations of Success, Bethesda, MD 20816, USA. Email: jsegre@nhgri.nih.gov*

that provides modest positive selection for a gut-dwelling strain with the capacity to extract slightly greater energy from a key food source.

It is also possible, however, that the selection pressure could in some cases operate at higher levels (*6*). An individual host's microbiome is not automatically inherited by its offspring. Although gut microbial communities are assembled anew in each individual, preliminary studies suggest that some strains are inherited from parents or siblings and then maintained for years or decades (*7*). Stochastic forces must also shape these microbial communities on an individual level, given that even monozygotic twins share only a limited set of microbial taxa (*8*). However, in the context of microbial sharing through some form of grooming or ingestion of small quantities of feces, the benefit could extend more widely. In a clinical setting, molecular analysis of fecal microbiota transplants between humans has shown that conspecific donor strains are more likely to durably colonize (*9*). Thus, a symbiotic advantage conferred by a microbial strain to an individual might extend to a larger subgroup of the population.

Similarly, across time, if a group of animals are forced to move to a new area and/or eat alternative foods during periodic times of hardship, there may be a selective advantage to retaining "bet-hedging" microbial community diversity across the animal population. Thus, although symbiosis is often experimentally considered as a single microbial strain conferring a singular benefit to a host, with this baseline data, one could also begin to explore evolutionary signatures of symbioses that extend from microbial strains to communities and from individual animals to animal populations.

Moeller *et al.*'s study once again underscores that hominids are multispecies superorganisms. It opens the door to investigations of the genetic features upon which fundamental host-microbiome symbiotic relationships are based. ■

REFERENCES

1. M. A. Fischbach, J. A. Segre, *Cell* **164**, 1288 (2016).
2. A. H. Moeller *et al.*, *Science* **353**, 380 (2016).
3. A. Caro-Quintero, H. Ochman, *Genome Biol. Evol.* **7**, 3416 (2015).
4. P. C. Sabeti *et al.*, *Nature* **449**, 913 (2007).
5. M. J. Blaser, *Science* **352**, 544 (2016).
6. E. J. van Opstal, S. R. Bordenstein, *Science* **349**, 1172 (2015).
7. J. J. Faith, J.-F. Colombel, J. I. Gordon, *Proc. Natl. Acad. Sci. U.S.A.* **112**, 633 (2015).
8. J. K. Goodrich *et al.*, *Cell* **159**, 789 (2014).
9. S. S. Li *et al.*, *Science* **352**, 586 (2016).
10. K. E. Langergraber *et al.*, *Proc. Natl. Acad. Sci. U.S.A.* **109**, 15716 (2012).

10.1162/science.aag2788

GENETICS

Demystifying the demise of paternal mitochondrial DNA

A process that eliminates organelle DNA during sexual reproduction is identified

By **Alexander M. van der Bliek**

The vast majority of genes in sexually reproducing eukaryotes can recombine during the production of gametes. This reshuffling generates new genotypes that may provide selective advantages. However, reshuffling does not occur among the few genes in the genomes of cytoplasmic organelles (chloroplasts and mitochondria). Instead, these organelles are almost always transmitted through maternal inheritance (*1*). Why is this phenomenon widespread and how is it achieved? On page 394 of this issue, Zhou *et al.* (*2*) solve part of this puzzle by identifying the enzyme that degrades sperm mitochondrial DNA after fertilization.

"...paternal mitochondria contain a 'self-destruct button' that is activated by fertilization."

Mammalian sperm mitochondria were once depicted as simply being lost, along with the rest of the sperm tail, upon fusion of the sperm's head region with an oocyte during fertilization, but this assumption proved to be wrong. Vertebrate sperm mitochondria are transferred to the oocyte during fertilization, just like paternal mitochondria in other organisms with widely differing sperm structures. In the worm *Caenorhabditis elegans*, for example, the spermatozoids are amoeboid cells that fuse in their entirety with an oocyte during fertilization (see the figure). However, paternal mitochondria, across species, are eliminated during fertilization. Thus, there must be an evolutionarily conserved mechanism that facilitates this removal.

The story gained momentum with the realization that organelles, such as mitochondria, can be selectively destroyed by autophagy. In this complex cellular process, cytoplasmic components, including entire organelles, are encapsulated by a so-called "isolation membrane," followed by fusion with lysosomes and wholesale degradation by lysosomal proteases and lipases (*3*). The removal of mitochondria by autophagy (called "mitophagy") can be restricted to an individual mitochondrion that shows a loss of membrane potential. It can also be used more globally to remove all mitochondria from a cell—for example, during maturation of mammalian red blood cells. *C. elegans* paternal mitochondria are removed by mitophagy quickly after fertilization (*4, 5*). A common autophagy adapter protein called light chain 3 (LC3) (LGG-1 in *C. elegans*) accumulates on paternal mitochondria, consistent with degradation through a canonical autophagy pathway. Paternal mitochondria are presumably marked in some way for degradation, distinguishing them from maternal mitochondria. *Drosophila* sperm degrade most of their mitochondrial DNA prior to fertilization (*6*), but *Drosophila* and mouse embryos also show selective mitophagy of paternal mitochondria after fertilization, consistent with a common mechanism for maternal inheritance (*5, 7*).

Initial triggers for degrading the paternal mitochondria are unknown. Zhou *et al.* helped address this question by showing that paternal mitochondria quickly lose inner membrane integrity after fertilization. Surprisingly, mitochondrial endonuclease G (ENDOG), encoded by the *CED-3 protease suppressor-6* (*cps-6*) gene in *C. elegans,* is required for rapid degradation of paternal mitochondrial DNA after fertilization. The *Drosophila* homolog of CPS-6/ENDOG acts during sperm maturation (*6*), but in *C. elegans*, this protein acts before autophagosomes fuse with lysosomes, as mutations in *cps-6* lead to an accumulation of autophagy intermediates in the embryo.

Several conclusions can be drawn from these data. One is that internal breakdown precedes autophagy, which implies that paternal mitochondria contain a "self-destruct button" that is activated by fertilization. Simply tagging paternal mito-

David Geffen School of Medicine at UCLA, Los Angeles, CA 90095, USA. Email: avan@mednet.ucla.edu

Self-destruct button?

Paternal mitochondrial DNA, across species, is eliminated during fertilization, as illustrated below for the worm *C. elegans*. A model for the underlying mechanism involves disruption of paternal mitochondrial membranes.

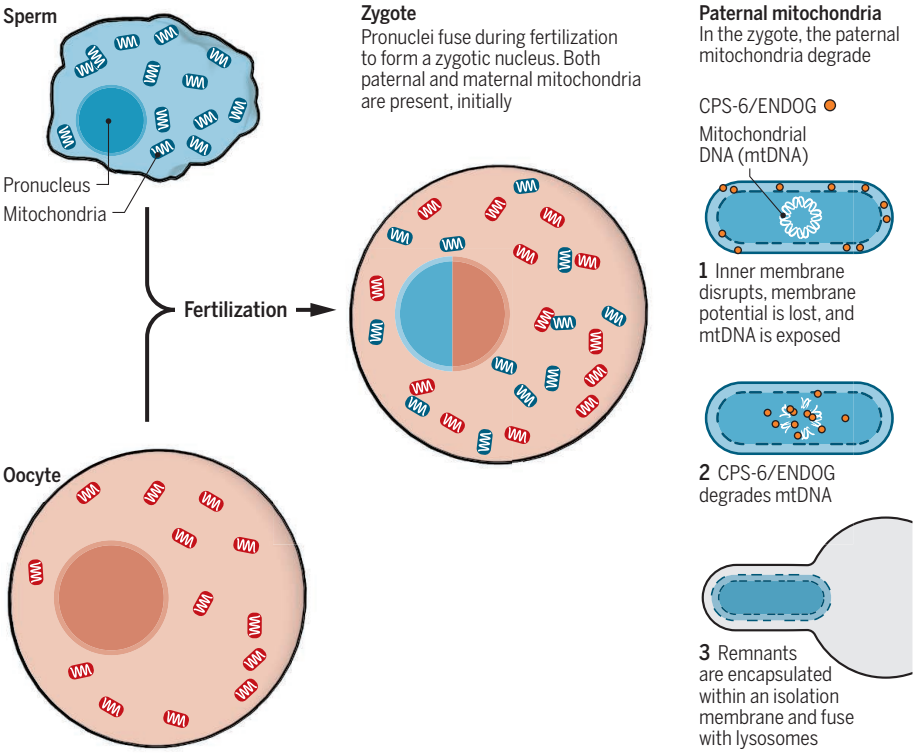

chondria with degradation markers, such as ubiquitin, is not enough to explain this mystery. Some unique feature of paternal mitochondria might actively disrupt their inner membranes when these organelles are exposed to oocyte cytoplasm. Another conclusion is that degradation of mitochondrial DNA by CPS-6/ENDOG accelerates mitochondria destruction by autophagy, even though their inner membranes are already disrupted and lysosomes have their own endonucleases. The extra precautions to degrade paternal mitochondrial DNA suggest that this step is critical for embryogenesis. Indeed, Zhou *et al.* show that deletions in *cps-6* slow cell division during embryogenesis and cause embryonic lethality in crosses with strains containing heterologous mitochondrial DNA. These results highlight the importance of eliminating paternal mitochondrial DNA.

CPS-6/ENDOG was first identified as a critical factor for programmed cell death (apoptosis) (*8*). It normally resides in the mitochondrial intermembrane space, but is released into the cytosol during apoptosis to degrade nuclear DNA. Likewise, cytochrome c is an integral part of the mitochondrial electron transport chain, but is released from the mitochondrial intermembrane space during apoptosis to activate caspases (*9*). Other apoptosis factors that are released from the mitochondrial intermembrane space during apoptosis, such as apoptosis-inducing factor–1 (AIF-1), most likely also have a normal housekeeping function. CPS-6/ENDOG thus joins a growing list of dual-function mitochondrial proteins with a role in normal growth and development as well as in apoptosis.

A model arising from the findings of Zhou *et al.* is that soon after fertilization, morphological disruptions of paternal mitochondrial membranes occur. This presumably exposes mitochondrial DNA to the CPS-6/ENDOG endonuclease in the intermembrane space. The authors also observed concomitant loss of mitochondrial membrane potential, consistent with holes in the mitochondrial inner membrane. Loss of membrane potential activates the mitophagy machinery, so how paternal mitochondrial inner membranes are disrupted becomes of paramount importance. Conversely, it is unclear whether CPS-6/ENDOG affects mitophagy in other developmental stages or cell types, and whether it also functions when restricted to the mitochondrial intermembrane space. Could it, for example, be a guardian against mitochondrial DNA that might inadvertently escape from the mitochondrial matrix through occasional breaches in the mitochondrial membranes?

Maternal inheritance has a broader societal impact than one might expect from the small number of genes encoded by mitochondria and chloroplasts. Subtle mutations in human mitochondrial DNA can provide selective advantages, such as cold tolerance, suggested by tracing extensive lineages of human migration with mitochondrial DNA (*1*). These seemingly innocuous changes in mitochondrial DNA can alter nuclear gene expression through cross-talk between genomes in the nucleus and mitochondria (*10*). Such interaction could explain the incompatibility with paternal mitochondria that was observed by Zhou *et al.* in genetic crosses with *C. elegans cps-6* mutants.

An awareness of the interplay between mitochondrial and nuclear genes might influence our understanding of mutations in mitochondrial DNA that cause debilitating diseases, including those that affect optic nerves, muscles, and metabolism (*1*). U.S. and UK science and ethics panels gave limited approval to preventing these diseases by in vitro fertilization with nuclear transfer using genetic material from three parents: sperm from the father, an oocyte nucleus from the mother, and oocyte cytoplasm from a second female with healthy mitochondrial DNA. Recent experiments to test the effectiveness of this approach have, however, uncovered difficulties with heteroplasmy (heterogeneous population of mitochondrial DNA) (*11*). Small amounts of residual mutant mitochondrial DNA sometimes compromise the larger population of healthy mitochondrial DNA through genetic drift (*12*). Further mechanistic studies of mitochondrial inheritance may help solve this problem. ■

REFERENCES AND NOTES

1. D. C. Wallace, D. Chalkia, *Cold Spring Harb. Perspect. Biol.* **5**, a021220 (2013).
2. Q. Zhou *et al.*, *Science* **353**, 394 (2016).
3. R. J. Youle, D. P. Narendra, *Nat. Rev. Mol. Cell Biol.* **12**, 9 (2011).
4. M. Sato, K. Sato, *Science* **334**, 1141 (2011).
5. S. Al Rawi *et al.*, *Science* **334**, 1144 (2011).
6. S. Z. DeLuca, P. H. O'Farrell, *Dev. Cell* **22**, 660 (2012).
7. Y. Politi *et al.*, *Dev. Cell* **29**, 305 (2014).
8. J. Parrish *et al.*, *Nature* **412**, 90 (2001).
9. C. Wang, R. J. Youle, *Annu. Rev. Genet.* **43**, 95 (2009).
10. U. Cagin, J. A. Enriquez, *Int. J. Biochem. Cell Biol.* **63**, 10 (2015).
11. L. A. Hyslop *et al.*, *Nature* **534**, 383 (2016).
12. M. Yamada *et al.*, *Cell Stem Cell* **18**, 749 (2016).

ACKNOWLEDGMENTS

A.M.v.d.B. is funded by NIH grant U01 GM 109764.

10.1126/science.aah4131

GRAPHIC: V. ALTOUNIAN/*SCIENCE*

POLICY FORUM

EPIDEMIOLOGY

Countering the Zika epidemic in Latin America

Epidemic dynamics are key and data gaps must be addressed

By **Neil M. Ferguson,[1] Zulma M. Cucunubá,[1]* Ilaria Dorigatti,[1]* Gemma L. Nedjati-Gilani,[1]* Christl A. Donnelly,[1] Maria-Gloria Basáñez,[1] Pierre Nouvellet,[1] Justin Lessler[2]**

As evidence grew for a causal link between Zika infection and microcephaly and other serious congenital anomalies (*1*), the World Health Organization (WHO) declared the Latin American Zika epidemic a public health emergency of international concern in February 2016 (*2*). The speed of spread [see the figure, top, and the supplementary materials (SM)] has made effective public health responses challenging. Immediate responses have included vector control (*3*) and advice to delay pregnancy in a few countries (*4*), followed by an extended recommendation to all affected countries by WHO in June 2016. These have merits but are likely to have limited effectiveness (*5*) and may interact antagonistically. Fuller understanding of dynamics and drivers of the epidemic is needed to assess longer-term risks to prioritize interventions.

Three key factors determine the scale and speed of spread of an emerging infection in a naïve population and the risk of longer-term endemicity. The first is the transmissibility of the infection, characterized by the reproduction number, R, the average number of secondary infections caused by a typical index case ($R < 1$ stops an epidemic). We provide time-varying estimates of R for Latin American countries where surveillance data are available (see the figure, top chart, and the SM). Country-level trends hide subnational heterogeneity (see SM), which likely reflects geographic variation in vector habitat and climate-driven variation in vector density and competence (*6*).

The generation time (T_g, the time between sequential rounds of infection; see SM) is the second key factor that determines the time scale of disease invasions. Taking estimates of R and T_g, we used a stochastic spatial model of Zika transmission (see SM) to illustrate dynamics of the epidemic and possible future waves of transmission (see the figure, center chart). We expect the current epidemic to be largely over in 3 years, with seasonal oscillations in incidence caused by variation in mosquito populations and transmissibility. Herd immunity will likely then cause a delay of more than a decade until further large epidemics are possible.

> ***"[C]ross-reactivity with dengue is a particular concern…and might increase …long-term endemicity…"***

The large-scale connectivity of human populations is the third key factor. Human mobility determines the chance an infection present in one location will be introduced elsewhere. Although the seeding of infection in Brazil was a chance event (*7*), once a full-blown epidemic was under way, export of infections across the Americas was inevitable and rapid and led to the widespread epidemics which unfolded from May 2015 onward (see SM).

Modeling gives insight into how the age distribution of infection will evolve over time—of particular relevance given the risk of congenital Zika syndrome and microcephaly. During the initial epidemic, we would expect all ages to be equally affected unless exposure and/or susceptibility vary substantially with age. The mean age of infection would then fall in future epidemics, given the immunity acquired by older people through past exposure. However, our analysis suggests that this effect is unlikely to be sufficient to prevent ongoing and substantial risk to pregnant women in future Zika epidemics (see the figure, age distribution insets, and the SM). This conclusion is supported by analysis of historical Zika seroprevalence data (*8*).

WHAT SHOULD POLICY-MAKERS DO?

Advising against pregnancy has been criticized for being infeasible for many women—especially long term (*4*). Our analysis (see the figure, spatial variation insets) suggests that, at the provincial scale, the timing of epidemic seeding is unpredictable but that the duration of the first wave of transmission is typically <6 months. However, in some locations, the timing of virus introduction can interact with seasonality of transmissibility to extend a local epidemic over two transmission seasons. If recommendations to delay pregnancy were tuned to the local context, in many areas they could be kept in place for a shorter time—making adherence more feasible while retaining potential risk-reduction benefits. Local optimization of control or risk-reduction measures requires timely availability of high-quality geographically stratified surveillance data.

Enhanced vector control is potentially beneficial, but it is critical to set realistic expectations. Evidence (*8*, *9*) suggests that traditional insecticide-based control is rarely sufficiently effective to stop dengue epidemics. Effectiveness would need to be considerably higher to stop the first epidemic of a new virus in a naïve population. But vector control with limited effectiveness could—if sustained—reduce attack rates seen in the initial epidemic (see SM). Modeling suggests downsides, however. The epidemic may last longer, which might make it harder for women to adhere to recommendations delaying pregnancy. Also, the epidemic will overshoot the herd-immunity threshold by less than if interventions had not been introduced—leaving a smaller proportion of the population immune and reducing the delay until new births allow population susceptibility to again reach levels that allow sustained endemic transmission (see the figure, bottom chart, and the SM).

What is the likelihood that the virus will become endemic or that sporadic epidemics will occur with sufficient regularity to pose an equivalent risk? Our analysis suggests that once the current epidemic is over, herd immunity will lead to a delay of at least a decade before large epidemics may recur (see SM). This prediction has caveats. The delay to resumption of transmission might be substantially reduced by high levels of spatiotemporal heterogeneity in exposure risk (not accounted for in our model) or by transient reductions in transmission caused by interventions or population behavior change. Also, our model makes the conservative assumption that flavivirus transmissibility in Latin America has not been anomalously high in the past 2 or 3 years (e.g., due to cli-

[1]*MRC Centre for Outbreak Analysis and Modelling, School of Public Health, Imperial College London, London W2 1PG UK.* [2]*Johns Hopkins Bloomberg School of Public Health, Department of Epidemiology, Baltimore, MD 21205 USA. *These authors contributed equally. Email: neil.ferguson@imperial.ac.uk*

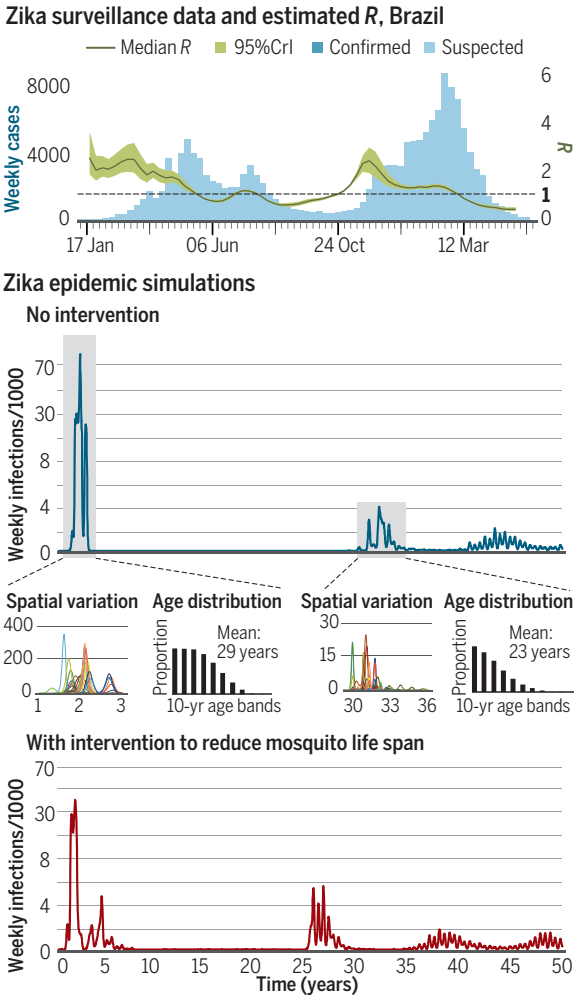

Zika transmission dynamics. (**Top**) Publicly available surveillance data on weekly suspected and laboratory-confirmed Zika cases in Brazil 2015–16 overlaid with estimates of *R* [running 5-week average (green) shown, centered on the middle week]. *R* = 1 threshold shown as dashed line. See SM for other countries and sources, estimation methods, and weekly infections. (**Center** and **bottom**) Typical simulated time series of Zika weekly infection incidence in a population of 600 million for two scenarios: no interventions (blue line) and with interventions that decrease mosquito life span by 20% for 1 year during the initial epidemic (red line). Incidence is plotted on a nonlinear scale to allow later epidemics to be resolved clearly. (Insets) (left) Incidence dynamics in the 20 spatial regions being modeled and (right) the age distribution of infections, for the first two epidemic periods without interventions. Full details are provided in the SM.

matic conditions) and so predicts that the virus will eventually become endemic. This does not imply predictable annual epidemics in all regions but rather that sustained transmission would be expected somewhere in the continent every year—akin to what is seen for individual dengue serotypes today. However, if Zika transmissibility is strongly modulated by longer-term climatic variation (such as El Niño), the virus may not be able to sustain endemic transmission, resulting in more sporadic, but larger-scale, epidemics when reseeding of infection coincides with favorable conditions for transmission. Last, we have assumed a constant risk of reseeding of the infection into the human population; if a sylvatic reservoir for Zika is established in the Americas (*8*, *10*), background levels of human exposure may increase.

A more precise assessment of long-term risks requires key data gaps to be filled. We need to measure the extent of (and geographic variation in) herd immunity in populations that have experienced recent Zika epidemics. Studies should not be restricted to Latin America. Currently, we cannot assess whether Asia is at risk of a major Zika epidemic—or why the scale of transmission in Latin America has been so much greater than anything previously seen. Multiple hypotheses have been proposed (*8*) but cannot yet be tested: immunological enhancement from prior exposure to dengue, El Niño–driven climate effects, viral evolution, and regional genetic differences in *Aedes aegypti* populations. Although data are currently limited (*11*), cross-reactivity with dengue is a particular concern, as our analysis indicates both cross-protection and enhancement could shorten the time until epidemics can reoccur and might increase the chances of long-term endemicity (see SM). Age-structured seroprevalence surveys are a priority, with assays that can distinguish exposure to Zika from exposure to other flaviviruses. Such surveys allow estimation of variation in exposure with time and age, of interactions with other flaviviruses, and of overall transmissibility (*8*). Long-term cohort studies can provide longitudinal data on individual variation in exposure and clinical and immunological outcomes.

The traditional model for vaccine and antiviral efficacy trials used for endemic diseases poses challenges for emerging infections with sporadic and unpredictable epidemics. Although phase I safety studies do not require active transmission, efficacy studies do. Our analysis suggests that there is limited time to initiate such studies in the current epidemic before incidence may be insufficient to measure impacts. Given the unpredictable timing and intensity of Zika outbreaks, future efficacy trials may need to be preapproved in a large number of potential sites then rapidly initiated in particular sites once local transmission has been detected. Efficacy studies for vaccines may need to recruit and vaccinate participants now and follow up for a longer period than is typical. Active case detection in multiple sites over a long time would be prohibitively expensive, so study protocols need to be adaptive—e.g., start active surveillance in a site only when Zika transmission is detected, even if the outbreak occurs several years after vaccination took place. Evaluating rare end points, such as microcephaly, poses particular difficulties and requires very large scale trials if undertaken in advance of an epidemic, or the risks associated with using a novel vaccine in pregnant women must be accepted if undertaken in the face of an epidemic.

Like Ebola, Zika is a public health crisis in which policy-makers have had to make decisions in the presence of enormous uncertainty. In such contexts, it is natural to reach for policies that mirror those used previously. However, Zika and Ebola epidemiology and thus policy options differ fundamentally. The current epidemic is not containable; at best, interventions can mitigate its health impacts. More optimistically, the natural dynamics of the epidemic are now likely to give a multiyear window to develop new interventions before further large-scale outbreaks occur. ■

REFERENCES AND NOTES

1. S. Cauchemez *et al.*, *Lancet* **387**, 2125 (2016).
2. World Health Organization, "WHO Director-General summarizes the outcome of the Emergency Committee regarding clusters of microcephaly and Guillain-Barré syndrome" (WHO, Geneva, 2016); http://bit.ly/HealthEmergency.
3. WHO, "Mosquito (vector) control emergency response and preparedness for Zika virus" (WHO, Geneva, 2016); http://bit.ly/ZikaEmergencyPrepar.
4. C. Schuck-Paim *et al.*, *PLOS ONE* **7**, e41918 (2012).
5. N. K. Tepper *et al.*, *Morb. Mortal. Wkly. Rep.* **65**, 311 (2016).
6. M. A. Johansson, F. Dominici, G. E. Glass, *PLOS Negl. Trop. Dis.* **3**, e382 (2009).
7. N. R. Faria *et al.*, *Science* **352**, 345 (2016).
8. J. Lessler *et al.*, *Science* 10.1126/science.aaf8160 (2016).
9. N. L. Achee *et al.*, *PLOS Negl. Trop. Dis.* **9**, e0003655 (2015).
10. D. Musso, D. J. Gubler, *Clin. Microbiol. Rev.* **29**, 487 (2016).
11. W. Dejnirattisai *et al.*, *Nat. Immunol.* 10.1038/ni.3515 (2016).

ACKNOWLEDGMENTS

The authors acknowledge funding from the UK Medical Research Council; the UK National Institute for Health Research under the Health Protection Research Unit initiative; National Institute of Allergy and Infectious Diseases and National Institute of General Medical Sciences, NIH, under the Models of Infectious Disease Agent Study (MIDAS) initiative; the European Union Framework 7 PREDEMICS project; the Bill and Melinda Gates Foundation; and Imperial College's Junior Research Fellowship program. Views expressed are not necessarily those of the funders.

SUPPLEMENTARY MATERIALS

www.sciencemag.org/content/353/6297/353/suppl/DC1

Published online 14 July 2016
10.1126/science.aag0219

The electric power grid, hailed as the world's largest machine, is all but invisible to most Americans.

PHOTO: © WASHINGTON STOCK PHOTO/ALAMY STOCK PHOTO

The Grid
The Fraying Wires Between Americans and Our Energy Future
Gretchen Bakke
Bloomsbury, 2016. 384 pp.

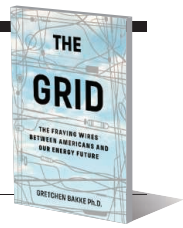

INFRASTRUCTURE

Power to the people

A cultural history of the U.S. power grid reveals the system's current failings and its potential

By **Cymene Howe**

We have all seen them. Some of us even have them: a mangle of cords leading to our TVs, Xboxes, iPhone chargers, and that homely lamp that we can't let go. These knotted bodies of wires hint at the exponentially more complex system of which they are a part. In *The Grid: The Fraying Wires Between Americans and Our Energy Future*, Gretchen Bakke dives deep into the history of the electric power grid. Bakke, a cultural anthropologist, also shows how the social sciences help us understand infrastructure and technological management as deeply social qualities.

The American electric grid is the largest machine in the world. But bigger is not necessarily better. Huge infrastructures tend to last a long time and yet often fail to keep pace with the way we live our lives. While other technological innovations sprint ahead of social change, when it comes to deeply institutionalized systems, we often neglect urgent maintenance and delay critical upgrades.

Our grid is a technological system. But it is also prone to the fragility of biological systems, unpredictable meteorological phenomena, and the vagaries of legal and bureaucratic decisions. Ironically, this massive machine is often vanquished by overgrown trees and overzealous squirrels.

The United States has more outage minutes than any other developed nation. Blackouts are getting longer and are expected to increase with the erratic weather associated with global climate change.

Despite legislation that effectively equates the two from a market standpoint, electricity, Bakke writes, is not a banana. It is a unique commodity that, once produced, must be used in a millisecond. However, even though the grid must be everywhere at once, local authorities are now also faced with integrating variable electricity, as derived from renewable sources like wind or solar—a tall order for an aging system.

Untangling the grid means looking to its past. In *The Grid,* we learn about the early electric turf wars and the triumph of AC power over DC. Bakke reveals that San Francisco actually hosted the first operational grid in 1879, a full 17 years before the better-known Niagara Falls plant went live. She also shows how Niagara's 19th-century renewable hydropower paved the way for the accelerated use of fossil fuels. (The Niagara plant made aluminum manufacturing profitable, which, in turn, facilitated the rise of the automobile and the airplane.)

In the 20th century, utility companies promoted the idea of endless growth and energy consumption, but Jimmy Carter encouraged us to dial down the thermostat and put on a sweater instead. His 1978 National Energy Act and, later, the Energy Policy Act, which deregulated the electricity industry, forever changed its business model. In the past, utility companies made money by generating and selling electricity. Now they earn profits by transporting power and trading it as a commodity. This leads to a conundrum: Companies can't upgrade existing technology without putting themselves out of business, but they also can't afford not to.

The Grid is full of rich detail across a wide range of energy-related topics. We hear about the woman who, worried about undue surveillance of her activities, pulled a gun on a utility worker sent to swap her analog meter for a smart one, and we learn how wires are "smartened" to transmit information as well as electricity. Microgrids (local grids that can operate autonomously), nanogrids (microgrids that serve a single building or entity), and "soft energy technologies" (simple, efficient, renewable energy devices) all appear, along with their possibilities and limitations. We glimpse Powerwalls (home batteries that charge via solar panels) and cars that act as distributed storage for electricity generated by the wind or sun.

One of the book's most surprising revelations is the commonality shared by stereotypical "off-the-grid" communities—hippie collectives and militia survivalists—and the U.S. military. Like these groups, the military needs to have power in gridless places.

One estimate that Bakke cites says that fully 70% of gasoline used in military field operations currently goes toward transporting other gasoline around. However, in the next 5 years, the military will more than double its use of (partly) renewable sourced microgrids—a major step forward.

At times, especially early on in the book, renewable energy sources are cast as forces that threaten to upset the grid, which could be read by some as a reason to cling to carbon. However, the book ultimately makes very clear that the frailty of our grid calls for a revolutionary retooling of this grand machine.

The reviewer is at the Department of Anthropology, Rice University, Houston, TX 77521, USA. Email: cymene@rice.edu

10.1126/science.aaf9323

ECONOMICS

The GDP and its discontents

Can a single number ever really capture all of what matters about a society?

By **N. Gregory Mankiw**

Other things equal, would you prefer more income or less? Unless you are one of the lucky few who have reached satiation, you would probably prefer more. A higher income would allow you to buy more of whatever it is you happen to enjoy: books, video games, fine dining, etc. That more income is better than less is almost axiomatic.

For much the same reason, when macroeconomists study the economy as a whole, the most important statistic in their toolbox is gross domestic product (GDP), which measures a society's total income and its total expenditure on newly produced goods and services. This profoundly important measure is the focus of Ehsan Masood's new book, *The Great Invention: The Story of GDP and the Making (and Unmaking) of the Modern World*.

During the Great Depression of the 1930s, at the request of policy-makers, economists including Simon Kuznets and Richard Stone began drawing together a variety of disparate data sources to summarize the state of the economy in a single number. Given the complexity of modern society, it was a Herculean task. Kuznets and Stone would go on to win Nobel Prizes in 1971 and 1984, respectively, for their efforts.

Masood devotes most of the book to a discussion of the outsized influence that GDP has come to bear on policy. In the view of Masood and a number of other critics of GDP, there are too many things that this metric leaves out.

One of the missing elements is inequality. For example, a society in which 10 people earn $20,000 a year and 2 earn $200,000 has the same GDP as one in which all 12 people earn $50,000. Yet no one would view those economies as equivalent.

Income inequality is one of several factors not accounted for in a country's GDP.

Also omitted are quality-of-life factors that are not reflected in monetary measures. Two nations can have the same GDP per person, but if one nation has greater literacy and longer life expectancy, most would agree that we should rank that one higher than the other.

A third element missing from GDP is the environment: If an economy produces its income by dirtying the air and water or threatening endangered species, it would make sense that those costs should be debited when gauging a nation's overall prosperity.

The reviewer is at the Department of Economics, Harvard University, Cambridge, MA 02138, USA. Email: ngmankiw@harvard.edu

The Great Invention
The Story of GDP and the Making (and Unmaking) of the Modern World
Ehsan Masood
Pegasus Books, 2016. 255 pp.

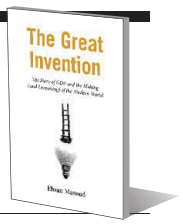

Masood expresses great admiration for those who have tried to transcend GDP by developing more inclusive measures. The United Nations, for example, has introduced a human development index, which is essentially a weighted average of income per person, literacy, and life expectancy. Similarly, some "ecological economists" have tried to add to GDP an imputed dollar value of the benefits we derive from a healthy environment. Most radically, the nation of Bhutan has focused its attention on "gross national happiness," which is less a metric than a philosophy that asserts that policy should be attuned to spiritual values and not just to the material standard of living.

So, what do mainstream economists make of these efforts? (Disclosure: I am one of them.) We tend to have three reactions. First, we agree that GDP is an incomplete gauge of well-being. Second, we point out that although it is far from perfect, GDP does, in fact, correlate with many nonmonetary features of society that people care about. Higher-income nations can, for instance, afford more schooling and better health care. Third, we are skeptical that any single statistic can capture everything, but we tend to believe that national leaders are usually smart enough not to focus on a single statistic when choosing among alternative policies.

Let's return to your personal situation. You prefer more income to less, but remember that pesky phrase "other things equal." You might turn down a pay hike if it required taking a dangerous or unpleasant job. You might choose not to increase your income by working longer hours if it meant spending less time with your family. To make the right decisions, you don't need one number that somehow incorporates your income, your job's attributes, and the quality of your family relations. Producing such a measure would require many questionable judgments, and having one in hand would not make it any easier to face life's inevitable trade-offs.

The same is true of GDP. It is a key gauge of national prosperity, but no single statistic can capture everything that matters about a society. Masood is on the wrong track when he yearns for a single new metric that will supersede the current measure. But his highly readable book is a useful reminder of what GDP is and what it isn't.

10.1126/science.aaf9800

PHOTO: ANDREW HOLBROOKE/GETTY IMAGES

LETTERS

Edited by **Jennifer Sills**

324 million minorities

IN HIS EDITORIAL "Einstein v. Roberts" (25 March, p. 1371), S. J. Gates Jr. describes how minorities can add to the creative scientific process by bringing a different perspective. He misses the point.

Minorities bring their own perspective to every aspect of life, not just physics, and their views, insights, and approaches have the same value—no more, no less—as those of the rest of the population. We must continue to ask what unique perspectives each group brings to each field of investigation. By asking this question, the answer will become obvious: It is not about minorities; it is about recognizing the value of every individual. Trying to remedy the victimization of minorities by isolating them as different only results in the reversed victimization of nonminorities, and the social conflict never ends. Let's start a new trend: Let's agree that the United States is home to 324 million minorities. That is my challenge.

Sonsoles de Lacalle

Department of Biomedical Sciences, Ohio University, Athens, OH 45701, USA. Email: delacall@ohio.edu

10.1126/science.aaf8874

Misrepresenting A. Fisher v. U. Texas

IN HIS EDITORIAL "Einstein v. Roberts" (25 March, p. 1371), University of Maryland Physics Professor S. J. Gates Jr. recounts two anecdotes. In one, an African-American student provides a key insight that allows a group of students to solve a math problem. In the other, Gates relates his own success to his "idiosyncratic framing of problems." In neither case does Gates provide evidence that it was his or the student's racial background that was responsible for their success or contributions to society. For all the reader knows, the "uniqueness" of their ideas was the result of an experience and had nothing to do with their race.

Given that Gates is writing in support of the University of Texas in the current *A. Fisher v. University of Texas* Supreme Court case concerning race-based affirmative action programs, one further statement of his is especially misleading. Referring to his own long ago admission as a student to MIT, he says, "If MIT had been legally bound then to admissions based solely on test scores, I would never have been admitted." In fact, no college or university has ever based admissions "solely on test scores." It is wrong for Gates to imply otherwise and to imply that this is the issue currently before the Supreme Court.

Stuart H. Hurlbert

Department of Biology, San Diego State University, San Diego, CA 92182, USA. Email: hurlbert@mail.sdsu.edu

10.1126/science.aaf9588

Response

DE LACALLE MAY be surprised to learn that I agree with her. I lived diversity long before I knew the word. I have benefitted from extraordinary mentoring by many individuals, most of them European-American men. I continue to appreciate the contributions of each such individual mentor, including my collaborators, postdocs, and research students. I have not lived a life that permitted the internalization of a victimization perspective.

Affirmative action should never be used to reward the demonstrably less-qualified over the more so. Comparing different candidates, it is scientifically impossible to precisely measure the merit or potential of each individual. We should admit this and, within such narrow limits, work to eliminate unfair privilege (*1*).

Hurlbert objects to my anecdotes, which I included to illustrate a well-researched fact: Diversity can catalyze enhanced creativity and innovation in a number of circumstances, including classrooms (*2*). Students have few opportunities to experience this change of perspective in the absence of broadly diverse classrooms.

Hurlbert also claims that universities do not base admissions solely on test scores. The University of Texas automatically admits applicants in the top 10% of their high school class (*3*). These students comprise 75% of the freshman class. Ms. Fisher, the plaintiff in the Supreme Court case, was not in the top 10% and was thus evaluated under a holistic review involving an Academic Index (AI) based on class rank, grades, SAT scores, and a personal achievement score of six factors (*4*). Of the factors, "special circumstances" assesses seven attributes, including race, to provide context and shed light on the applicant's relevant personal qualities. Based on UT's Supreme Court brief, even with a perfect Personal Achievement Score, Ms. Fisher would not have been admitted. Technically, Hurlbert is correct that the University of Texas does not consider test scores alone. Practically, test scores are weighted so heavily, even for the 25% of admissions slots filled by students outside the top 10% of their high school class, that other factors become trivial.

The recent Supreme Court ruling in *A. Fisher v. University of Texas* aligns well with the ethical foundation I proposed (*1*) over 20 years ago. These principles have now been judged to support practices sanctioned by the constitution.

Sylvester James Gates Jr.

Department of Physics, University of Maryland, College Park, MD 20740, USA. Email: gatess@physics.umd.edu

REFERENCES

1. S. J. Gates Jr., *The Scientist* **9**, 12 (1995).
2. Scott E. Page, *The Difference: How the Power of Diversity Creates Better Groups, Firms, Schools and Societies* (Princeton Univ. Press, 2007).
3. Texas Admissions, Admissions decisions (https://admissions.utexas.edu/apply/decisions).
4. Texas Admissions, Freshman Application Review (https://admissions.utexas.edu/apply/decisions/freshman-review).

10.1126/science.aag2134

Minorities and bias: The big picture

THE RECENT NATIONAL Institutes of Health (NIH) announcement about the launch of three "experimental interventions" to determine whether there is bias in the NIH grant process is a step in the right direction (J. Mervis, "In effort to understand continuing racial disparities, NIH to test for bias in study sections," *ScienceInsider*, 9 June). However, grants are only one part of the greater bias that scholars of color encounter in their academic careers.

The opportunity to address this bias begins with improving representation in academia. Black professors account for about 5% of full-time faculty in higher education (*1*). Latino and Native Americans

are also woefully underrepresented in academia (*2*). Expanding representation would build a more robust peer network that scholars of color can turn to with questions about grant proposals, tenure, and other professional development needs.

Academics of color also have competing demands on time (*3*, *4*), such as serving on more committees or additional mentoring requests. Although mentoring students is a positive outcome of having a diverse faculty—research shows that all students do better on campuses with a higher representation of minority professors (*5*)—this demand still takes time away from research.

Finally, there is the problem of gaining tenure. Researchers often face a lack of respect from the science community and their students, which leads to a trickle-down effect across their department. Because they aren't seen as qualified candidates, they are often passed over for tenure (*6*). It's a reason we lose so many researchers of color to the private sector where their skills are welcomed as more marketable and profitable.

Lisa Aponte-Soto

New Connections, Philadelphia, PA 19102, USA.
Email: Laponte-soto@Equalmeasure.org

REFERENCES

1. The Journal of Blacks in Higher Education, Black Faculty in Higher Education: Still Only a Drop in the Bucket (www.jbhe.com/features/55_blackfaculty.html).
2. National Center for Education Statistics, Fast Facts (https://nces.ed.gov/fastfacts/display.asp?id=61).
3. A. Harvey Wingfield, "The plight of the black academic," *The Atlantic* (2015); www.theatlantic.com/business/archive/2015/12/the-plight-of-the-black-academic/420237/.
4. B. Baez, *Higher Ed*. **39**, 363 (2000).
5. E. Fine, J. Handelsman, "Benefits and challenges of diversity in academic settings" (WISELI, 2010); https://wiseli.engr.wisc.edu/docs/Benefits_Challenges.pdf.
6. R. E. Zambrana, "Brief Summary: Understanding the relationship between work stress and U.S. research institutions' failure to retain underrepresented minority (URM) faculty" (University of Maryland, 2015); www.crge.umd.edu/Documents/URM/Brief%20Summary%20of%20SFS%20FINAL%20August%2028%202015%20%281%29.pdf.

10.1126/science.aah3713

TECHNICAL COMMENT ABSTRACTS

Comment on "A histone acetylation switch regulates H2A.Z deposition by the SWR-C remodeling enzyme"

Feng Wang, Anand Ranjan, Debbie Wei, Carl Wu

Watanabe *et al.* (Reports, 12 April 2013, p. 195) study the yeast SWR1/SWR-C complex responsible for depositing the histone variant H2A.Z by replacing nucleosomal H2A with H2A.Z. They report that reversal of H2A.Z replacement is mediated by SWR1 and related INO80 on an H2A.Z nucleosome carrying H3K56Q. Using multiple assays and reaction conditions, we find no evidence of such reversal of H2A.Z exchange.

Full text at http://dx.doi.org/10.1126/science.aad5921

Response to Comment on "A histone acetylation switch regulates H2A.Z deposition by the SWR-C remodeling enzyme"

Shinya Watanabe and Craig L. Peterson

Wang *et al.* report a failure to reproduce our biochemical observation that the INO80C and SWR1C/SWR1/SWR-C chromatin remodeling enzymes catalyze replacement of nucleosomal H2A.Z with H2A when the substrate contains H3-K56Q. They point to technical problems with our dimer exchange assay. In response, we have recapitulated our findings using a mobility shift assay that was developed and employed by Wang and colleagues.

Full text at http://dx.doi.org/10.1126/science.aad6398

TECHNICAL COMMENT

CHROMATIN

Comment on "A histone acetylation switch regulates H2A.Z deposition by the SWR-C remodeling enzyme"

Feng Wang,[1] Anand Ranjan,[2] Debbie Wei,[1] Carl Wu[1,2]*

Watanabe *et al*. (Reports, 12 April 2013, p. 195) study the yeast SWR1/SWR-C complex responsible for depositing the histone variant H2A.Z by replacing nucleosomal H2A with H2A.Z. They report that reversal of H2A.Z replacement is mediated by SWR1 and related INO80 on an H2A.Z nucleosome carrying H3K56Q. Using multiple assays and reaction conditions, we find no evidence of such reversal of H2A.Z exchange.

Histone variant H2A.Z is deposited in chromatin by the adenosine triphosphate (ATP)–dependent chromatin remodeling complex SWR1/SRCAP/Tip60. Budding yeast SWR1 (also called SWR-C) catalyzes unidirectional, stepwise replacement of two histone H2A-H2B dimers on the canonical nucleosome with H2A.Z-H2B dimers (*1*–*4*). Watanabe *et al*. reported that histone exchange in the reverse direction—the replacement of nucleosomal H2A.Z-H2B with H2A-H2B dimers—is mediated by SWR1 and the related INO80 complex on nucleosomes harboring the histone H3K56Q substitution, a mimic of H3K56 acetylation (*5*). We find no evidence of such reverse activity for SWR1 or INO80.

We used three methods to detect histone exchange. In an electrophoretic mobility shift assay (EMSA) (*3*), replacement of nucleosomal H2A-H2B or H2A.Z-H2B with histone dimers bearing a 3xFlag tag gives a mobility shift of the mononucleosome band on nondenaturing polyacrylamide gel electrophoresis (PAGE), one shift per 3xFlag (Fig. 1). On the $(H2A.Z\text{-}H2B\text{-}H3K56Q\text{-}H4)_2$ (ZQ) nucleosome, SWR1 catalyzed no exchange of H2A.Z-H2B for the H2A-H2B-3xFlag dimer (A-Flag). This was true under the reaction conditions of Watanabe *et al*. (*5*) (Buffer I) or Ranjan *et al*. (*3*) (Buffer II) (Fig. 1, A and B), but the same dimers could be nonenzymatically exchanged by salt gradient dialysis (Fig. 1C). As previously established on the canonical H2A nucleosome containing wild type histone H3K56 (AK nucleosome), SWR1 catalyzed ATP-dependent exchange of the H2A-H2B dimer for H2A.Z-H2B-3xFlag (Z-Flag) (44% exchange, Buffer I; 58% exchange, Buffer II) (Fig. 1, A and B). These results obtained by F.W. were confirmed by A.R. (Fig. 1D).

Watanabe *et al*. detected histone exchange indirectly by Western blotting after native PAGE (*1*, *5*). We found no evidence for reversal of H2A.Z exchange when the PAGE gel of Fig. 1D was processed for Western blot-chemiluminescence imaging (Fig. 1E). To eliminate the possibility of tag interference, we used a fluorescently labeled histone dimer free of epitope tags for histone exchange. SWR1 mediated no incorporation of Cy3-labeled H2A-H2B (A-Cy3) on the ZQ nucleosome but substantial ATP-dependent incorporation of Cy3-labeled H2A.Z-H2B (Z-Cy3) on the AK nucleosome in Buffer I and Buffer II (Fig. 1, F and G).

The INO80 complex mediated no exchange of nucleosomal H2A.Z-H2B for H2A-H2B-3xFlag on a centrally positioned ZQ nucleosome (Fig. 2A), whereas INO80 displayed its known histone octamer sliding activity from one end of a long-linker nucleosome to the mobility-retarded central position (Fig. 2B). This absence of H2A.Z reverse exchange demonstrated by F.W. (Fig. 2A) was confirmed by A.R. using EMSA (Fig. 1D) and Western blot-chemiluminescence (Fig. 1E). Furthermore, contrary to the report of Watanabe *et al*. (*5*), we detected no reversal of H2A.Z exchange using SWR1 complex purified from a Swc2Δ strain, which is deficient for the major DNA- and H2A.Z-binding component of SWR1 (*3*, *6*) (Fig. 2C).

The source of these discrepancies is unclear, but it is not due to the use of different affinity tags for enzyme purification, as INO80 from the Peterson laboratory also showed no reversal of H2A.Z exchange in our hands. It is unlikely to be due to different nucleosome preparations, as two reconstitution procedures gave the same results (Figs. 1, A and B, and 2D). Under the same buffer conditions and enzyme-substrate concentrations, we find no evidence for their claim of 30% nucleosomal H2A.Z exchange for H2A, within the detection limits of quantitative EMSA (~0.03% H2A-H2B-3xFlag) (Fig. 2E) or Western blot-chemiluminescence.

Watanabe *et al*. cite reduced promoter occupancy in vivo by H2A.Z in the H3K56Q yeast strain as evidence consistent with SWR1-mediated reverse H2A.Z exchange on the ZQ nucleosome. Although we observed no reverse exchange, we detected ~two-fold lower H2A.Z exchange in the forward direction on the AQ nucleosome (Fig. 2F), consistent with their in vitro observations (*5*). Because steady-state H2A.Z occupancy is a function of deposition and eviction pathways, the lower forward H2A.Z exchange could suffice to explain reduced H2A.Z occupancy for the H3K56Q strain.

Our findings conflict with Peterson and colleagues' claims of reversal of H2A.Z exchange by SWR1 and INO80. Irreproducibility of their findings despite use of three detection modalities compels consideration of other mechanisms for H2A.Z eviction.

Experimental procedures were as follows: Preparation of nucleosomes, SWR1-Flag or INO80-Flag complexes, and H2A/H2A.Z-H2B dimers was as published (*1*, *3*, *7*). DNA purity of nucleosomes were reconstituted by our laboratory protocol in Fig. 2G. Histone exchange assays were as published (*2*, *5*, *8*, *9*).

Recombinant yeast histones were purified individually following the Tsukiyama Laboratory (http://research.fhcrc.org/content/dam/stripe/tsukiyama/files/Protocols/expression.pdf) or copurified as a dimer (H2A-H2B) (*7*). Nucleosomes were reconstituted by mixing yeast histones and unlabeled or Cy5-labeled 208 base pairs (bp) Widom 601 DNA (31N30) or Cy5-N60 DNA, followed by salt gradient dialysis according to Luger *et al*. (*10*). Cy5-labeled reconstituted nucleosomes were subsequently treated with λ DNA (1 μg λ DNA per 4 pmol 601 DNA, incubated for ~2 hours at 4°C) to bind residual unincorporated histones and purified by 5 to 20% sucrose gradient sedimentation (100 μl to 150 μl sample load per 4.8 ml sucrose gradient, Beckman SW55Ti rotor, 30,000 rpm, 17.1 hours, 5°C) following Ranjan *et al*. (*3*). Purity of nucleosome fractions was confirmed by EMSA and SYBR Green I staining (Fig. 2G). Alternatively, the λ DNA treatment was omitted, and nucleosomes were used directly or purified on a sucrose gradient as above (Fig. 2D). Yeast histones H2A, H2A.Z, H2A.Z-K121C, H2B (for H2A.Z-K121C-H2B), and H2B-3xFlag proteins were expressed individually in *Escherichia coli*, except for coexpression of H2A-K120C-H2B. Cell pastes for H2A/Z and H2B (or H2B-3xFlag) were resuspended and mixed before sonication and histone dimer purification using an established protocol (*7*). H2A-K120C-H2B and H2A.Z-K121C-H2B were labeled with Cy3 following a protocol modified from Joo and Ha (*11*).

[1]Laboratory of Biochemistry and Molecular Biology, Center for Cancer Research, National Cancer Institute, Building 37, Room 6114, Bethesda, MD 20892, USA. [2]Janelia Research Campus, Howard Hughes Medical Institute, 19700 Helix Drive, Ashburn, VA 20147, USA.
*Corresponding author. Email: wuc@janelia.hhmi.org

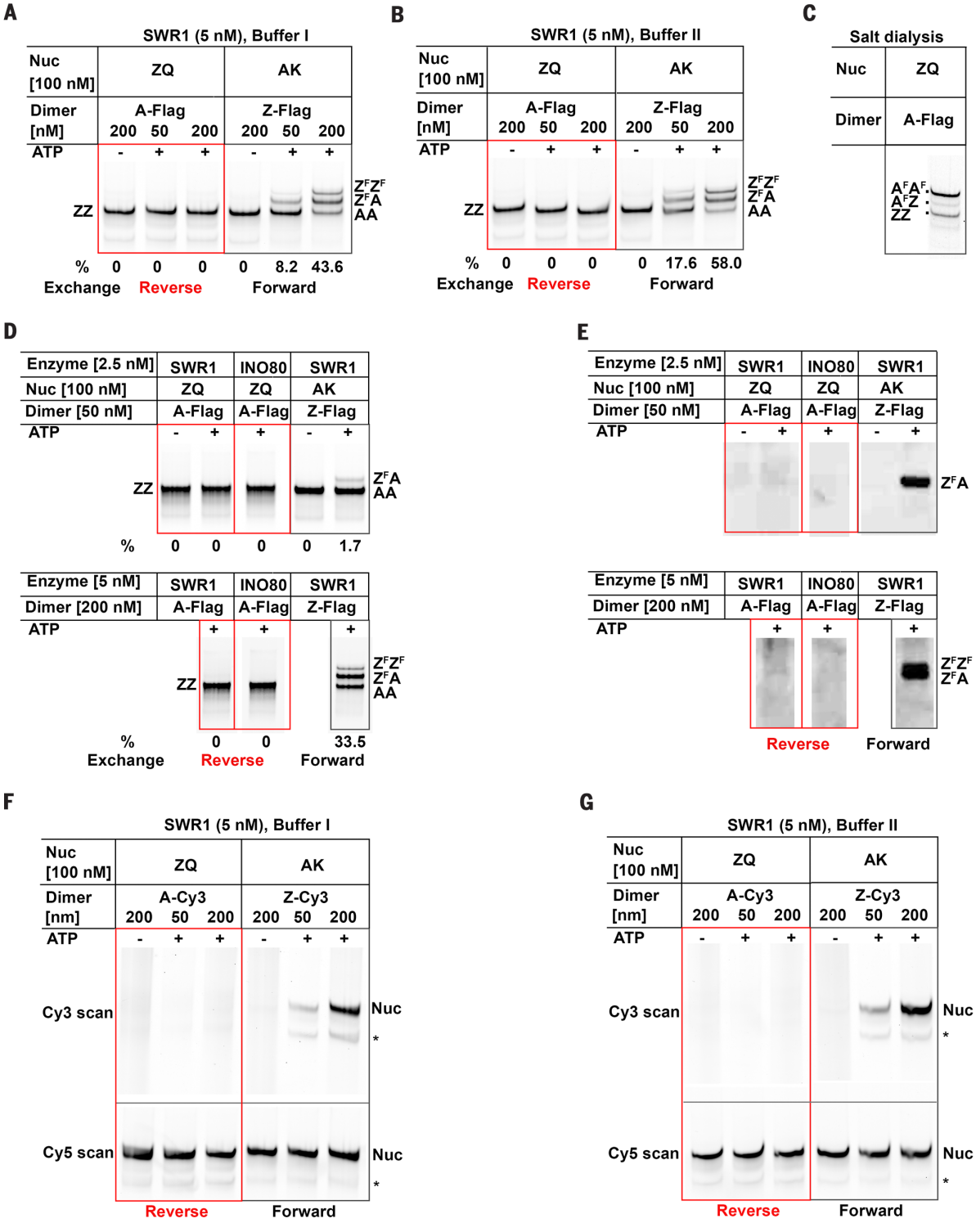

Fig. 1. Histone exchange by SWR1. (**A**) EMSA shows Cy5-DNA (208 bp) (*12*) nucleosome products (*3*) of forward and reverse H2A.Z exchange. Typical 10-µl reaction contains 1 mM ATP, at 30°C for 1 hour in Buffer I [70 mM NaCl, 10 mM Tris-HCl (pH8.0), 5 mM $MgCl_2$, 0.1 mg/ml bovine serum albumin (BSA), and 1 mM dithiothreitol (DTT)]. A 4-µl stop solution (1 mg/ml salmon sperm DNA, 50 mM EDTA, 5 mM ATPγS) was added before loading on 6% native mini-PAGE gel in 0.5X tris-borate EDTA, followed by Cy5 scanning. Forward reaction % replacement = %AZ band/2 + %ZZ band. (**B**) As in (A), using Buffer II (20 mM HEPES-KOH pH 7.6, 0.3 mM EDTA, 0.28 mM EGTA, 4% glycerol, 0.014% NP40, 0.8 mM DTT, 56 mM KCl, 5.6 mM $MgCl_2$, 80 µg/ml BSA, and protease inhibitors). (**C**) EMSA nucleosome markers harboring two H2A.Z-H2B (ZZ), one H2A-H2B-3xFlag plus one H2A.Z-H2B (A^FZ), and two H2A-H2B-3xFlag dimers (A^FA^F), produced by salt gradient dialysis after adding A-Flag dimer to the ZQ nucleosome reconstitution mixture. (**D**) Nucleosomes after forward and reverse H2A.Z exchange by SWR1 and INO80. (**E**) Anti-Flag Western blot-chemiluminescence of the nondenaturing PAGE gels in (D) (*2*, *5*). (**F**) As in (A), except for H2A-K121C-Cy3-H2B dimer (A-Cy3) or H2A.Z-K120C-Cy3-H2B (Z-Cy3). *, may be an asymmetrically positioned nucleosome. (**G**) As in (F) using Buffer II.

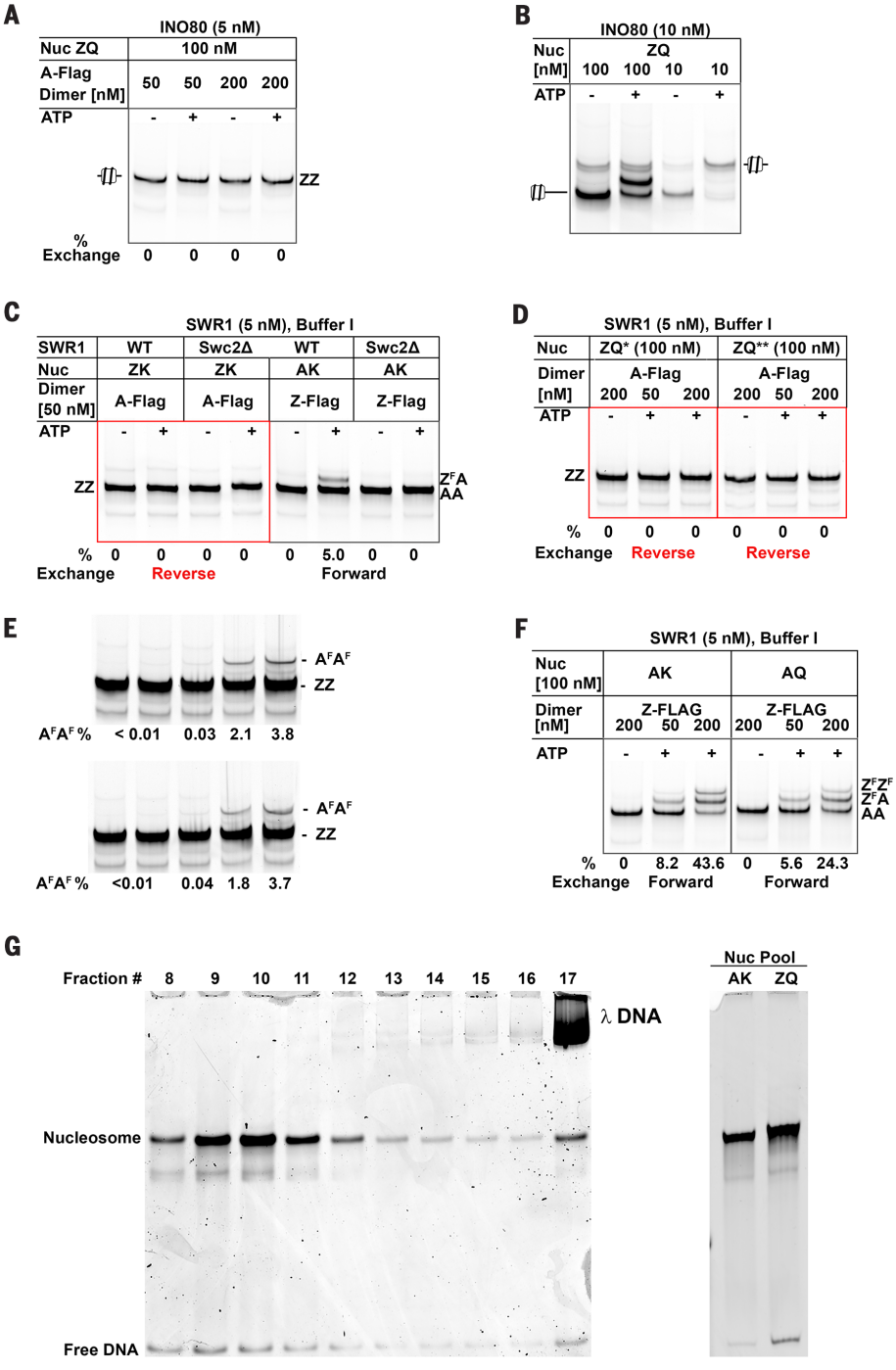

Fig. 2. Analysis of INO80 and SWR1 activities. (**A**) Nucleosome products of H2A.Z exchange by INO80, as in Fig. 1A. (**B**) Histone octamer sliding (*13*) of end-positioned ZQ nucleosome (60-bp linker) in Buffer I at 30°C for 1 hour. (**C**) SWR1 (Swc2Δ) mutant exhibits neither reverse nor forward H2A.Z exchange, as in Fig. 1A. (**D**) Nucleosomes after reverse H2A.Z exchange by SWR1, as in Fig. 1A, except that ZQ nucleosomes were reconstituted with no subsequent λ DNA treatment, and with (*) and without (**) sucrose gradient purification. (**E**) H2A.Z (ZZ) nucleosomes (Fig. 1A), mixed with increasing amounts of nucleosomes bearing A-Flag dimers produced by salt dialysis (Fig. 1C). % band intensities (Cy-5) of A^FA^F nucleosome over A^FA^F + ZZ nucleosome indicated. (**F**) Forward H2A.Z exchange by SWR1 on AK and AQ nucleosomes, as in Fig. 1A. (**G**) EMSA and SYBR Green I DNA stain of purified nucleosomes in sucrose gradient fractions.

REFERENCES AND NOTES

1. E. Luk *et al.*, *Cell* **143**, 725–736 (2010).
2. G. Mizuguchi *et al.*, *Science* **303**, 343–348 (2004).
3. A. Ranjan *et al.*, *Cell* **154**, 1232–1245 (2013).
4. A. Ranjan *et al.*, *eLife* **4**, e06845 (2015).
5. S. Watanabe, M. Radman-Livaja, O. J. Rando, C. L. Peterson, *Science* **340**, 195–199 (2013).
6. W.-H. Wu *et al.*, *Nat. Struct. Mol. Biol.* **12**, 1064–1071 (2005).
7. G. Mizuguchi, H. Xiao, J. Wisniewski, M. M. Smith, C. Wu, *Cell* **129**, 1153–1164 (2007).
8. G. Mizuguchi, W.-H. Wu, S. Alami, E. Luk, *Methods Enzymol.* **512**, 275–291 (2012).
9. M. Papamichos-Chronakis, S. Watanabe, O. J. Rando, C. L. Peterson, *Cell* **144**, 200–213 (2011).
10. K. Luger, T. J. Rechsteiner, T. J. Richmond, *Methods Enzymol.* **304**, 3–19 (1999).
11. C. Joo, T. Ha, *Cold Spring Harb. Protoc.* **2012**, 1009–1012 (2012).
12. B. Dorigo *et al.*, *Science* **306**, 1571–1573 (2004).
13. X. Shen, *Methods Enzymol.* **377**, 401–412 (2003).

ACKNOWLEDGMENTS

We thank S. Watanabe and C. Peterson for an INO80 sample and our colleagues for helpful comments. This work was supported by the Intramural Research Program of the Center for Cancer Research, National Cancer Institute, and by the Janelia Research Campus, Howard Hughes Medical Institute.

6 October 2015; accepted 10 June 2016
10.1126/science.aad5921

TECHNICAL RESPONSE

CHROMATIN

Response to Comment on "A histone acetylation switch regulates H2A.Z deposition by the SWR-C remodeling enzyme"

Shinya Watanabe and Craig L. Peterson*

Wang *et al*. report a failure to reproduce our biochemical observation that the INO80C and SWR1C/SWR1/SWR-C chromatin remodeling enzymes catalyze replacement of nucleosomal H2A.Z with H2A when the substrate contains H3-K56Q. They point to technical problems with our dimer exchange assay. In response, we have recapitulated our findings using a mobility shift assay that was developed and employed by Wang and colleagues.

SWR1C and INO80C are two yeast members of the INO80 subfamily of remodelers (*1*). Whereas SWR1C promotes replacement of nucleosomal H2A/H2B dimers with H2A.Z/H2B in an adenosine triphosphate (ATP)–dependent reaction (*2*), we reported that INO80C catalyzes the reverse dimer exchange reaction, replacing H2A.Z/H2B dimers with H2A/H2B (*3*–*5*). A role for INO80C in removal of H2A.Z is consistent with global disruption of H2A.Z localization in yeast strains lacking INO80C (*3*). Furthermore, we found that this reverse reaction was stimulated when nucleosomes contained acetylated lysine 56 of histone H3 (H3-K56Ac) or a substitution of H3-K56 for glutamine (H3-K56Q) (*5*). Strikingly, H3-K56Q or H3-K56Ac switched the substrate specificity of SWR1C, inhibiting H2A.Z deposition while promoting exchange of H2A.Z with H2A (*5*). Furthermore, H3-K56Q altered the adenosine triphosphatase (ATPase) properties of SWR1C. Normally, the ATPase activity of SWR1C is activated by H2A nucleosomes and further stimulated by free H2A.Z/H2B dimers. However, we found that H3-K56Q allowed both H2A and H2A.Z nucleosomes to fully stimulate ATPase activity, and the enzyme was insensitive to histone dimers (*5*). These ATPase data support the observation of altered substrate specificity for dimer exchange activity.

In their Comment, Wu and colleagues used three gel-based assays to monitor dimer exchange by SWR1C and INO80C [Wang *et al*. (*6*)]. Although their assays detected H2A.Z deposition by SWR1C, they did not observe the reverse reaction by either SWR1C or INO80C. Interestingly, they did observe inhibition of H2A.Z deposition by H3-K56Q, similar to our previous results (*5*). They suggest that interpretation of our published results may be confounded by technical problems with our dimer exchange assay. Our assay involves incubation of remodelers with recombinant yeast mononucleosomes and recombinant yeast H2A/H2B or H2A.Z/H2B dimers (*3*). Reaction products are electrophoresed on polyacrylamide gel electrophoresis (PAGE) to separate mononucleosome products from free histones or other non-nucleosomal products. Nucleosome integrity is monitored by Western blot for H3 or by visualizing DNA with ethidium bromide, and dimer exchange is assayed by Western blot. To avoid aggregation by free histone dimers, the concentration of free dimers is titrated for each experiment. With this assay, we found that all dimer exchange activities are strongly ATP- and enzyme concentration–dependent (*3*, *4*, *5*, *7*). Furthermore, in side-by-side comparisons, INO80C catalyzed the reverse reaction (replacement of H2A.Z with H2A), but the SWI/SNF remodeler was inactive (*3*). Likewise, SWR1C catalyzed the reverse reaction with H2A.Z/H3-K56Ac or H2A.Z/H3-K56Q nucleosomes but not with an unmodified substrate (*5*). All results have been confirmed numerous times with independent enzyme, histone, and nucleosome preparations. Wu and colleagues suggest that our results may be influenced by a failure to stop reactions with excess DNA, although they acknowledge that this cannot explain the ATP dependence (or enzyme specificity) of our results. The altered ATPase parameters of SWR1C with H3-K56Q nucleosomes cannot be explained by the specifics of the exchange assay.

To eliminate the possibility that our particular assay might have influenced results, we performed reactions using the direct electrophoretic mobility shift assay (EMSA) assay developed and employed by Wu and colleagues (*8*). Given the time frame allowed for our response, we have focused on INO80C. In their EMSA assay, the substrate is a fluorescently labeled mononucleosome, and dimer exchange is monitored by incorporation of a 3xFlag-tagged histone dimer, which causes a shift in mobility on PAGE. Using this assay, and an H2A.Z/H3-K56Q nucleosome, we confirmed that INO80C catalyzes incorporation of 3xFlag-tagged H2A (Fig. 1). Importantly, this dimer exchange reaction was ATP-dependent, and the amount of product increased with increasing enzyme concentration and time of incubation (Fig. 1). Interestingly, the reaction appears to favor replacement of both H2A.Z/H2B dimers, because the slower migrating species

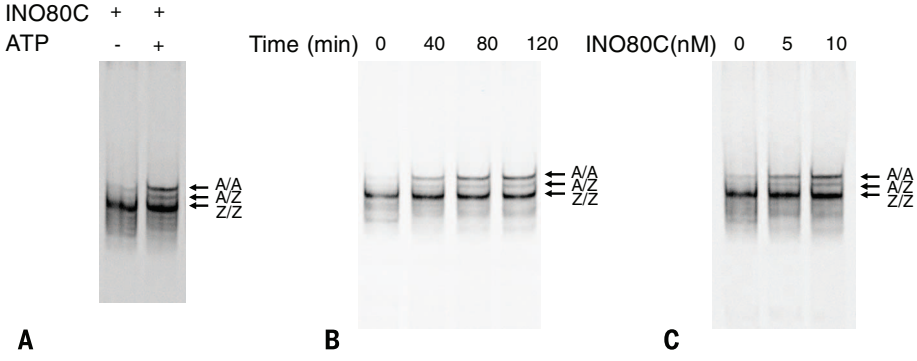

Fig. 1. Histone exchange by INO80C. EMSA shows Cy5-DNA (200 base pairs) of yeast H2A.Z/H3-K56Q mononucleosomes reconstituted on centrally located 601 nucleosome positioning sequence. Arrows indicate nucleosomes containing two H2A.Z/H2B dimers (Z/Z), one 3xFlag-H2A/H2B dimer (A/Z), or two 3xFlag-H2A/H2B dimers (A/A). Migration of each species was confirmed by assembly of "marker" nucleosomes created by reconstitution with H3/H4 tetramers and mixtures of H2A.Z/H2B and 3xFlag-H2A/H2B dimers. (**A**) INO80C catalyzes "reverse" dimer exchange. Reactions contained 10 nM INO80C, 100 nM H2A.Z/H3-K56Q nucleosomes, and 100 nM 3xFlag-H2A/H2B dimers. ATP (2 mM) was added as indicated. Reactions incubated 2 hours at 30°C in buffer [70 mM NaCl/10 mM Tris-HCl (pH8.0)/5 mM $MgCl_2$/0.1 mg/ml bovine serum albumin/1 mM dithiothreitol] ± 2 mM ATP as indicated. Stop solution (1 mg/ml salmon sperm DNA/50% glycerol) was added before loading on 6% native PAGE gel in 0.5X tris-borate EDTA, followed by Cy5 scanning on GE Typhoon imager. (**B**) Reactions as in (A) but samples incubated with 2 mM ATP for indicated times. (**C**) Reactions as in (A) and samples contained indicated amounts of INO80C with 2 mM ATP.

Program in Molecular Medicine, University of Massachusetts Medical School, Worcester, MA 01605, USA.
*Corresponding author. Email: craig.peterson@umassmed.edu

accumulates at low enzyme concentrations and at early time points. Thus, using either our Western blot assay or the direct EMSA assay, INO80C catalyzes replacement of H2A.Z/H2B with H2A/H2B on an H2A.Z/H3-K56Q substrate.

At present it is not clear why the Wu group is unable to detect the reverse dimer exchange reaction, even when using the same assay. As they note, the differing results do not appear to be due to different methods of purifying enzymes, nor does the problem appear to be due to differences with recombinant histone dimers, as H2A/H2B dimers provided by the Wu group were functional in our hands. The only remaining variables are histone octamers and nucleosome reconstitutions. We find that yeast H2A.Z and H2A.Z/K56Q octamers do not reconstitute efficiently and that great care has to be taken to ensure that octamers do not contain free histone tetramers or dimers. The success of these dimer exchange reactions is highly sensitive to the quality and concentrations of both the reconstituted nucleosome and free dimers. The only clear solution is to continue to share reagents until the source of the technical problem is identified.

The differing results obtained with gel-based assays for histone dimer exchange reactions reinforce the need for more sophisticated, solution-based assays that monitor each of the steps in the exchange reaction. Indeed, a previous fluorescence resonance energy transfer–based study suggested that the ATP-dependent steps of dimer exchange may occur quite rapidly and that formation of a product that is detectable by PAGE occurs on a much slower time scale (*9*). We anticipate that application of such methods will not only define the detailed mechanism of dimer exchange by INO80 subfamily members but that these more quantitative tools will enhance the reproducibility of data obtained among groups.

Experimental procedures were as follows: Purification of recombinant histones, reconstitution of mononucleosomes, preparation of yeast histone dimers, and purification of INO80C-TAP were as published (*3*, *5*, *10*). Exchange assays were performed as published (*3*, *5*).

REFERENCES AND NOTES

1. C. B. Gerhold, S. M. Gasser, *Trends Cell Biol.* **24**, 619–631 (2014).
2. G. Mizuguchi *et al.*, *Science* **303**, 343–348 (2004).
3. M. Papamichos-Chronakis, S. Watanabe, O. J. Rando, C. L. Peterson, *Cell* **144**, 200–213 (2011).
4. S. Watanabe *et al.*, *Nat. Commun.* **6**, 7108 (2015).
5. S. Watanabe, M. Radman-Livaja, O. J. Rando, C. L. Peterson, *Science* **340**, 195–199 (2013).
6. F. Wang, A. Ranjan, D. Wei, C. Wu, *Science* **353**, 358 (2016).
7. C. Jeronimo, S. Watanabe, C. D. Kaplan, C. L. Peterson, F. Robert, *Mol. Cell* **58**, 1113–1123 (2015).
8. A. Ranjan *et al.*, *Cell* **154**, 1232–1245 (2013).
9. C. E. Rowe, G. J. Narlikar, *Biochemistry* **49**, 9882–9890 (2010).
10. K. Luger, T. J. Rechsteiner, T. J. Richmond, *Methods Enzymol.* **304**, 3–19 (1999).

ACKNOWLEDGMENTS

We thank C. Wu and colleagues for reagents and communicating results before publication. This work was supported by NIH R37-GM049650.

10.1126/science.aad6398

REVIEW SUMMARY

HIV-1 CURE

Latency reversal and viral clearance to cure HIV-1

David M. Margolis,* J. Victor Garcia, Daria J. Hazuda, Barton F. Haynes

BACKGROUND: A central challenge to emerging efforts to cure HIV infection is the persistence of quiescent but replication-competent proviral genomes in resting $CD4^+$ T lymphocytes and, to an unknown extent, in other cell populations. Targeted approaches are sought to reverse latency, induce viral antigen expression within formerly latently infected cells, and use immune clearance mechanisms to eradicate persistent infection. Small-molecule HIV latency-reversing agents (LRAs) capable of modulating pathways that control HIV-1 latency are the first tools to be studied in this effort. However, despite the successful reversal of latency, the only clinical interventions to date producing a significant decrease in the viral reservoir involved bone marrow transplantation. Moreover, whether the HIV-1 RNA expression induced by LRAs leads to durable viral protein presentation on the surface of infected cells sufficient to allow immune mediated clearance is unknown. Because multiple mechanisms are involved in maintaining the transcriptional silence of HIV-1, a combination of LRAs may be necessary to effectively perturb persistent HIV-1 infection. Defining the cells that harbor persistent HIV-1 is technically challenging, burdening the development of antilatency therapy. Last, immune interventions designed to clear persistently infected cells have yet to be combined with LRAs in a successful, coordinated therapeutic strategy.

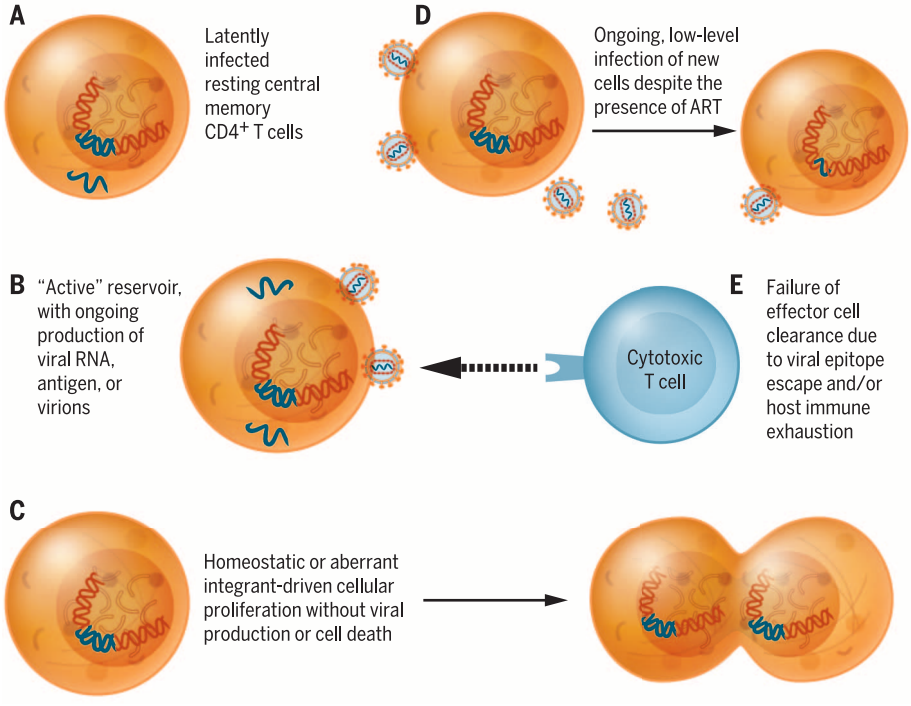

HIV latency. Potential obstacles to HIV eradication. (**A**) True virological and transcriptional latency, with little HIV RNA expression, and no detectable HIV antigen presentation. (**B**) So-called "active latency" with ongoing production of HIV RNA and antigen. (**C**) Proliferation of latently infected cells, driven by homeostatic forces, or by dysregulation of the host gene program by a viral integrant, without viral production. (**D**) The possibility that de novo infection occurs despite effective ART. (**E**) Failure of immune clearance owing to viral epitope escape or host immune exhaustion.

ON OUR WEBSITE

Read the full article at http://dx.doi.org/10.1126/science.aaf6517

ADVANCES: Histone deacetylase (HDAC) inhibitors have been the most widely investigated LRAs, inducing cell-associated HIV-1 RNA in four clinical studies. The complex nature of the mechanisms that restrict HIV-1 expression of the population of latent integrated proviruses suggests the hypothesis that combinations of agents could more effectively disrupt latency. Numerous in vitro studies support this hypothesis, but thus far, only one animal model study used several LRAs; although results appeared promising, the effect of this combination was not directly assessed.

A study of latently infected cells obtained from $HIV\text{-}1^+$ donors on antiretroviral therapy revealed that instantaneous reversal of latency across all cells harboring integrated proviruses may be challenging and suggests that effective LRA strategies will likely need to be delivered serially over time. This study also illustrates the limitations of assessing the persistence of latent infection via HIV-1 RNA expression because a majority of such RNA transcripts are defective and therefore irrelevant. New approaches,such as novel techniques that can quantitate the frequency of rare cells in a large population that are capable of expressing viral antigen, may surmount this challenge.

Other recent efforts have examined the obstacles to clearance of persistent, latent infection. For example, the latent reservoir harbors viral mutant subspecies that have previously escaped the extant antiviral immune response. Tissue sanctuaries that may be poorly accessed by the cytotoxic T lymphocyte (CTL) response have been described, as has the potential for some LRAs to interfere with CTL activity. Whether the extent of antigen presentation induced by the current generation of LRAs is sufficient to allow targeting and clearance of infected cells remains unknown.

OUTLOOK: Although the challenges of latent HIV-1 infection are daunting, the stability of the latent pool over years of antiviral therapy gives hope that an effective perturbation of the homeostasis that maintains the latent pool may allow substantial depletion, and eventually eradication, of persistent infection. The steady advances in animal models of HIV-1 latency, tools for the assessment of persistent infection, LRAs to disrupt latency, and emerging immunotherapeutics to clear persistently infected cells suggest that the first effective combination studies may be close at hand. Such studies will likely represent progress toward the goal of HIV-1 cure while also revealing new challenges to be overcome. ■

Author affiliations are available in the full article online.
*Corresponding author. Email: dmargo@med.unc.edu
Cite this article as D. M. Margolis *et al.*, *Science* **353**, aaf6517 (2016). DOI: 10.1126/science.aaf6517

REVIEW

HIV-1 CURE

Latency reversal and viral clearance to cure HIV-1

David M. Margolis,[1,2]* J. Victor Garcia,[2] Daria J. Hazuda,[3] Barton F. Haynes[4]

Research toward a cure for human immunodeficiency virus type 1 (HIV-1) infection has joined prevention and treatment efforts in the global public health agenda. A major approach to HIV eradication envisions antiretroviral suppression, paired with targeted therapies to enforce the expression of viral antigen from quiescent HIV-1 genomes, and immunotherapies to clear latent infection. These strategies are targeted to lead to viral eradication—a cure for AIDS. Paired testing of latency reversal and clearance strategies has begun, but additional obstacles to HIV eradication may emerge. Nevertheless, there is reason for optimism that advances in long-acting antiretroviral therapy and HIV prevention strategies will contribute to efforts in HIV cure research and that the implementation of these efforts will synergize to markedly blunt the effect of the HIV pandemic on society.

The human immunodeficiency virus (HIV) has been a major burden on society since the virus emerged over 30 years ago. But in less than 2 decades, a remarkable investment and the resultant scientific progress across the biomedical research enterprise and the pharmaceutical industry produced the spectacular success that is now modern antiretroviral therapy (ART) (*1*). These advances transformed HIV infection from a fatal disease into a manageable chronic illness. The global implementation of ART and HIV prevention efforts are now showing signs of blunting the HIV pandemic (*2*).

Despite these successes, the stigma of HIV infection and its long-term societal and resource costs remain a substantial challenge. Suppressive, lifelong antiviral therapy alone cannot be the final solution to the HIV pandemic, and thus, recent efforts have focused on interventions that can yield a drug-free remission of HIV infection or even its cure. Drug-free immune control of chronic HIV infection may exact a toll on the host, and many may prefer the complex goal of HIV eradication. At the individual level, ART provides substantial long-term health benefits, and so compared with other foreseeable goals such as drug-free immune control of chronic HIV infection, perhaps only the challenging goal of HIV eradication may be acceptable to some. A number of diverse and novel approaches aimed at finding a cure for HIV are being explored, and encouraging advances have emerged.

[1]University of North Carolina HIV Cure Center, Department of Medicine, and Center for AIDS Research, University of North Carolina at Chapel Hill School of Medicine, Chapel Hill, NC, USA. [2]Department of Microbiology and Immunology, University of North Carolina at Chapel Hill School of Medicine, Chapel Hill, NC, USA. [3]Merck Research Laboratories, White Horse Junction, PA, USA. [4]Duke Human Vaccine Institute, Department of Medicine, and Department of Immunology, Duke University School of Medicine, Durham, NC, USA.
*Corresponding author. Email: dmargo@med.unc.edu

The challenge at hand is considerable and is well illustrated both by a singular success and several failures. In the case of Timothy Brown, the Berlin patient, it seems that a series of complex clinical events after the transplantation of CCR5-deficient cells innately resistant to HIV infection led to the complete clearance of infected cells (*3*, *4*). Although limited studies did not detect latently infected cells in the Boston patients after stem cell transplantation (*5*), or in the Mississippi child (*6*) treated with potent antiretroviral therapy in the first hours of life, the absence of a durable and potent anti-HIV immune response may have allowed viral rebound. There is little doubt that a considerable and sustained effort will be needed in both basic and translational research to transform these clinical anecdotes into therapeutic approaches that are safe and effective enough to be deployed broadly against the HIV pandemic.

The beginnings of HIV cure research

The initiation of efforts to develop therapeutic strategies to clear HIV infection has led to advances overcoming the obstacles to viral eradication and has illuminated new challenges. Proviral latency—the persistence of quiescent but replication-competent proviral genomes in resting $CD4^+$ T lymphocytes, and to an unknown extent in other cell populations such as myeloid cells—is a central problem for curative strategies (*7*). A central approach to this problem envisions targeted approaches to reverse latency so that viral antigen is expressed by a formerly latently infected cell and becomes vulnerable to immune clearance mechanisms. Further, such viral clearance mechanisms may require therapeutic or immunomodulatory enhancement strategies such as reversal of anti–HIV-1 effector cell exhaustion.

Host cell–mediated molecular mechanisms maintain the quiescence of HIV-1 gene expression in infected resting $CD4^+$T lymphocytes, and these mechanisms are potential therapeutic targets for disrupting latency (Fig. 1). One well-defined mechanism contributing to maintenance of latency is the recruitment of histone deacetylases (HDACs) to the HIV promoter in the long terminal repeat (LTR), mediating the formation of a repressive chromatin environment that inhibits LTR transcription and viral production (*8*–*13*). The relevance of this mechanism has been validated in resting $CD4^+$ T cells obtained from ART-treated, aviremic, HIV-infected individuals (*10*, *11*, *14*, *15*–*19*). The potent HDAC inhibitor, vorinostat induces HIV chromatin acetylation and promoter expression in cell lines and elicits virus production ex vivo from the resting $CD4^+$ T cells of HIV-infected patients on suppressive ART. This effect is achieved without cellular activation, up-regulation of HIV coreceptors, or de novo HIV infection, all of which could increase the number of infected cells in the host (*20*, *21*). Direct proof-of-concept of latency reversal has also been achieved in clinical studies, in which increases in cell-associated HIV-1 RNA production and/or plasma viremia was observed after in vivo administration of the HDAC inhibitors vorinostat, panobinostat, or romidepsin (*22*–*25*)—and in one study, the drug disulfiram (*26*)—to ART-suppressed patients. However, thus far none of these interventions alone has been found to reduce the frequency of latently infected cells.

Although these data are encouraging, challenges for the effective implementation of so-called "latency-reversing agents" (LRAs) have emerged. Several studies have suggested that LRAs, at least when tested after a single drug exposure in vitro, may disrupt latency in only a subset of the population of latently infected cells (*27*, *28*). On the basis of these in vitro studies, combinatorial LRA strategies are widely assumed to be needed to effectively and comprehensively purge the pool of replication-competent, integrated, persistent HIV. Concepts include combining HDAC inhibitors with histone methylation inhibitors (*29*), and protein kinase C (PKC) agonists with HDAC inhibitors or bromodomain (BRD) inhibitors (*30*). Toll-like receptor agonists, whose mechanism of action as an LRA is not yet fully defined (*31*, *32*), have appeared promising in nonhuman primate studies. Human trials to test these concepts are in development.

More problematic for the discovery and development of new LRAs is the challenge that the preclinical models used for their study respond in diverse ways to signals known to reverse latency (*33*). Further, assays using cells from HIV^+, ART-treated patients may not fully recapitulate the complexity of latency in vivo (*34*) because a single pulse of maximal mitogenic activation in vitro does not disrupt latency in all infected cells. This surprising observation suggested that there might be absolute limitations to the effectiveness of a single exposure to even the most potent LRAs. Although serial stimulation in vitro induces expression of a larger proportion of the latently infected population over time (*35*), the challenge of

developing single or combinatorial therapies that safely disrupt latency in all infected cells over a clinically tractable period of time may be considerable. An additional complication is the recent appreciation that the majority of species of cell-associated HIV RNA expressed in latently infected cells contains substantial mutations and deletions, largely because of the action of APOBECs (apolipoprotein B mRNA editing enzyme, catalytic polypeptide-like), a family of cytidine deaminase proteins that efficiently restrict HIV expression (*36*). Therefore, although the detection of HIV RNA within these cells reveals past infection, many viral genomes detected by means of RNA expression are replication-incompetent. The predominance of defective HIV DNA genomes (*37*) and incompetent HIV RNA transcripts (*34*) pose a challenge for investigators wishing to quantify the latent reservoir and evaluate strategies to deplete it.

Replication-competent HIV can be measured by using the quantitative viral outgrowth assay (QVOA). Although QVOA can measure the frequency of truly latent proviral infection in cohorts of stably treated patients, as documented by independent studies carried out over more than 2 decades (*38*, *39*), the output represents a minimal estimate of the frequency of persistent, latent HIV infection (*34*). This leaves investigators in a conundrum: Measures of integrated HIV DNA vastly overestimate the frequency of true latent HIV infection, as do (to a lesser extent) measures of cell-associated HIV RNA, whereas the QVOA underestimates the size of the latent reservoir.

We suggest that these problems could be circumvented by the development and implementation of more sensitive tools that could assess latency reversal at the level of viral protein production, or the presentation of viral antigen to the immune system. Cells that are capable of expressing viral proteins are more relevant than cells that simply contain replication-defective HIV DNA genomes or or express HIV RNA transcripts. Such cells are likely to be more frequent and more easily assayed than those that produce functional virions. This is perhaps the most relevant metric by which to evaluate latency reversal because the current goal of latency reversal is to create targets for immune-based clearance.

The calculus of viral persistence: Forces that drive the decay of the latent reservoir

Because latent, persistent HIV infection was described within the resting $CD4^+$ memory T cell, viral quiescence was initially thought to derive principally from the quiescent cellular state of the host T cell, an environment unfavorable to HIV expression (*40*–*43*). Over the next decade, studies of HIV transcriptional regulation did not refute that view but modified it, as several specific cellular mechanisms were described that served to enforce proviral quiescence (*44*). Some cellular mechanisms that enforce proviral latency have now become the rational targets of latency-reversing agents, seeking to inhibit these silencing mechanisms and allow expression of latent provirus (*45*, *46*).

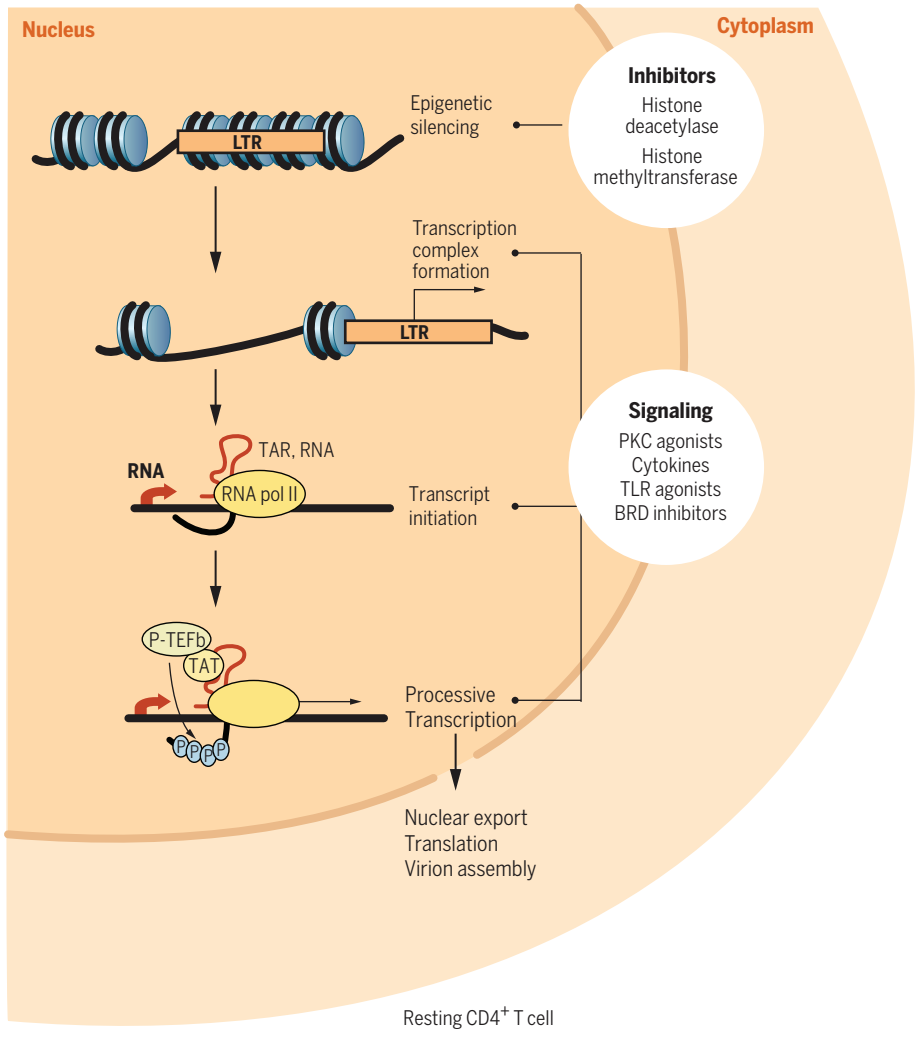

Fig. 1. HIV latency. Cellular pathways that enforce HIV latency are targets for LRAs. The escape of the integration provirus from the latent state is restricted at several levels: epigenetic silencing of the proviral promoter, transcription complex formation, transcript initiation, and transcription complex processivity. Examples of inhibitors and inducers currently under study as potential LRAs are displayed.

However, recent findings have reignited the debate around two additional mechanisms that could contribute to the persistence of replication-competent provirus: cellular proliferation and ongoing viral replication. HIV-infected patients on long-term ART have now been found to have identical HIV sequences integrated at the same position in the host genome in multiple cells, suggesting that the infected cells had descended from an identical clone via cellular proliferation (*47*, *48*). However, the replication-competence of these proliferating clones remains in question. One study found that all of 75 integrated genomes that were fully sequenced contained lethal mutations or deletions and were replication-incompetent (*49*). However, this finding should be replicated and expanded because even a small fraction of proliferating but replication-competent HIV genomes could contribute substantially to viral persistence.

The contribution of other cell populations that sequester HIV in a quiescent state and persist for years despite ongoing ART also requires further examination. Latent infection can be established in vivo in naïve and transitional CD4 T cells, stem memory T cells, and γ-δ T cells (*50*–*54*). But the durability of these potential reservoirs in vivo is not understood. Similarly, whereas it is clear that various myeloid cell populations can be infected during untreated HIV viremia (*54*), the contribution of the persistence of latent infection in these populations to the HIV reservoir in ART-suppressed patients is unclear (*55*, *56*).

Last, the potential contribution of residual virus replication and spread, despite ongoing ART, to HIV persistence remains controversial. Multiple controlled studies of ART intensification have found that additional inhibitors of entry, reverse transcription, integration, and viral protease function had no effect on low-level viremia, arguing that low-level viremia was generated by chronically infected cells and not by ongoing

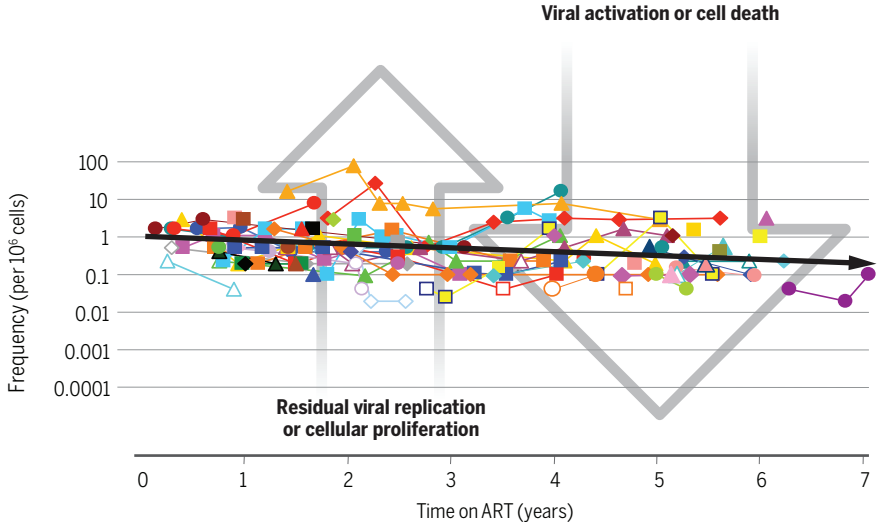

Fig. 2. Persistent, latent infection of memory CD4 cells decays slowly over time. Residual HIV replication and proliferation of latently infected cells might increase the frequency of latent infection, but these forces must be slightly outweighed by those that naturally deplete latent infection because a slow decay of latent infection is uniformly seen in stably treated patients. The goal of antilatency therapy is to effectively accelerate the clearance of persistent infection across all reservoirs of persistent infection. This data, collected over 10 years ago (*35*), has recently been precisely reproduced in a contemporary patient cohort using improved ART (*36*). [Adapted by permission from Macmillan Publishers, *Nature Med.* 2003.]

rounds of replication (*57*–*63*). However, in several studies that added an integrase inhibitor to ART-suppressed patients, transient changes in forms of HIV 2-LTR DNA and/or reductions in immune activation were seen, potentially because of ongoing replication (*64*, *65*). HIV sequence evolution might be expected in treated patients in whom replication was ongoing. One study reported this within lymph node tissue in patients treated for 6 months (*66*), a relatively short period of time after initiating ART, but other studies found no evidence of evolution in plasma or tissues in participants in whom durable suppression of viremia had been established for years (*67*, *68*).

Regardless of the final adjudication of these issues, the overall calculus of persistent infection is clear: Once durable and suppressive ART is implemented, all measures of persistent HIV infection are either stable or decay slowly over time. Therefore, although any new persistent infections founded by cellular proliferation or residual replication on a daily basis have the potential to increase the number of latently infected cells, this contribution is apparently slightly outweighed by the number of cells that reactivate or die and leave the quiescent pool on a daily basis (Fig. 2). If this were not the case, the frequency of latent infection would increase over time.

Although not the only possible approach to eradicate HIV infection, the tools are now at hand to implement latency-reversal strategies that create a window of vulnerability within the pool of latently infected cells. LRAs must be implemented effectively in combination with immunotherapeutic approaches that can clear HIV-infected cells that present viral proteins in the context of latency reversal. Such combination eradication approaches, even if only modestly effective, should result in substantial, measurable, and reproducible depletion of persistent infection, the next major step in the development of HIV eradication strategies.

Current approaches to clearance of persistent HIV infection after latency reversal

The clearance of residual HIV infection in the context of prolonged suppression of viral replication by ART is a major challenge for the immune system and for immunotherapeutics. The targets for clearance are rare populations of cells, induced to express HIV proteins in quantities that are likely to be limited, for which the duration and kinetics of antigen presentation are unknown. Further, these cell populations may be widely distributed across anatomical compartments, and in many patients, the HIV-specific immune response may have waned in the absence of recent antigen exposure and/or may be dysfunctional or depleted owing to the effects of HIV infection on the immune system. Although CD8 T cells are highly effective in targeting and clearing virus-infected cells, and in HIV infection contribute to control of viremia, Deng *et al*. highlighted the widespread prevalence of CD8 T cell escape mutations in viral genomes found in the resting CD4 T cell reservoir (*69*). However, within these subjects, CD8 cells capable of targeting other epitopes that lacked mutations were detectable in all patients after peptide stimulation. This suggests that although HIV can rapidly evade the immune system in the setting of unchecked viremia, HIV-infected individuals on ART possess effector cell populations that may be capable of clearing viral species within the latent reservoir.

It is also important to consider the effects of agents used to reverse latency on the various host immune mechanisms that are required to recognize and clear the infected cells. The window of vulnerability induced by latency-reversing agents must be judged not only by the extent of antigen expression within the latent reservoir of ART-suppressed, HIV-infected individuals, but by the ability of immune mediators to act after LRA exposure. One in vitro study suggested that romidepsin and panobinostat—two HDAC inhibitors, the leading class of LRAs—might inhibit the HIV-specific T cell response and thereby reduce the ability of the immune system to clear infection after the reversal of latency (*70*). But in this study and two others using autologous cells from aviremic, HIV-infected patients on ART, the antiviral activity of effector cells was unaffected by exposure to the HDAC inhibitor vorinostat (*71*, *72*). Data from an ongoing study of pulsatile vorinostat therapy given several times a week revealed no evidence that vorinostat exposure reduced the ability of $CD8^+$ T cells or natural killer cells to recognize and clear latently infected cells induced to express HIV ex vivo (*73*, *74*). Similarly, Søgaard (*25*) found that three weekly doses of romidepsin failed to measurably blunt the HIV-specific T cell response in vivo. Nevertheless, the possibility that, because of the very nature of their cellular targets, LRAs may affect immune function and therefore clearance of infected cells in which latency has been reversed, is an important issue that must be systematically assessed.

However, although LRAs can be selected for minimal impact on the immune response, in many individuals on stable, suppressive ART, the low frequency of HIV-specific $CD8^+$ T cell responses may be insufficient to clear the latent reservoir (*75*). As described above, this deficiency may be related to $CD8^+$ T cell escape mutations archived in the latent reservoir that arose before the implementation of ART (*69*, *76*–*78*) and/or to the dysfunctional, or "exhausted," state of the HIV-specific T cell seen in chronic infection (*79*). Thus, strategies to strengthen HIV-specific T cell immune responses may be needed.

A number of therapeutic HIV-1 vaccines that might fill this need have been tested, including whole inactivated virus, recombinant proteins or viruses, DNA vectors, or dendritic cell presentation of autologous antigens (*80*–*84*). Some vaccines improved HIV-specific immune responses (*85*), but none to date has allowed sustained ART interruption. However, in such studies the vaccine-induced immune response is asked to fully restrain all HIV replication in the absence of ART, an as-yet unmet milestone. However, for the goal of eradication in the setting of ongoing ART and antilatency therapies, the bar may be much lower because viral replication and therefore viral escape is blocked in the presence of ART.

Further, a small number of vaccine trials have measured the impact of the vaccine on the size of the latent reservoir and seen either no sustained impact on the reservoir (*86*) or, at best, a small,

transient decline in the frequency of replication-competent latent infection (87), below a threshold predicted to be clinically relevant (38). This is most likely due to the lack of viral expression in latently infected cells, making these reservoirs insensitive to any immune response (7).

Last, such vaccines have not yet been tested for specific characteristics that may be critical to allow effective clearance of persistent HIV infection: recognition of relevant epitopes in the context of infection emerging from the latent state; reduction of low-level viremia that persists during ART; or decrease in the frequency of latently infected cells (88, 89). These endpoints should be considered in future studies as well as use of those HIV-preventive vaccines that have induced the greatest level of HIV-specific $CD8^+$ cytotoxic T lymphocyte (CTL) in man (90). Vaccines that induce T cell responses against conserved viral epitopes may contribute to the ability to clear persistent HIV (91–94). Recent data have demonstrated that attenuated cytomegalovirus (CMV)–vectored SIV genes can induce CD8 CTL, which might eradicate SIV-infected CD4 T cells, as 50% of macaques appeared cured of acute infection (95, 96). A portion of CMV-induced CD8 T cells recognize SIV-infected CD4 T cells atypically via major histocompatibility complex class II and human lymphocyte antigen E, potentially representing a new approach to the clearance of retroviral infection (96, 97). Understanding the mechanisms of atypical CD8 T cell killing of retroviral-infected CD4 T cells and validation of the safety and efficacy of CMV-vectored approaches in humans is needed.

Antibodies that can specifically direct immune clearance of HIV-infected cells are a new area of HIV cure research. Cocktails of broadly neutralizing antibodies derived from HIV-infected individuals can bind to virions and virus-infected CD4 T cells and may be useful tools for curative strategies (98, 99). Other non-neutralizing HIV antibodies have been isolated that selectively target virus-infected CD4 T cells. Engineering of these Env-targeting antibodies into bispecific antibodies or chimeric dual-affinity retargeting antibodies (DARTS) that can target CD8 effector cells to HIV-infected CD4 T cells is a promising new strategy (72, 100, 101). Novel immune-augmenting strategies, such as adjunctive treatment with immune checkpoint inhibitors, might reawaken an extant but exhausted or diminished immune response and facilitate clearance of viral reservoirs (102).

Testing latency reversal and clearance

Although informative studies of latency reversal and clearance strategies can be executed in ex vivo tissue culture models, a full analysis of curative strategies must be performed in animal model studies and human clinical trials. Like all HIV-infected cells, latently infected cells exist predominantly in tissues, and some anatomic compartments may differ in drug penetrance or in the access of components of the cellular and humoral immune response. Therefore, comprehensive studies of latency reversal and clearance strategies require extensive tissue monitoring and sampling that is both practically and ethically untenable in human studies. Although it is fortunate that both humanized mouse models and nonhuman primate models have recently been advanced so that infection and ART can be reliably used, both models could benefit from further optimization in order to address the most relevant questions related to HIV cure research.

Novel humanized mice models such as the bone marrow–liver-thymus (BLT) mouse, the T cell–only mouse (ToM), and the recently described Myeloid-only mouse (MoM) serve effectively in this capacity (54, 103). Humanized BLT mice exhibit systemic human reconstitution, including in the brain, gut, and vaginal mucosa, with a complete and functional human immune system. By virtue of only having human T cells, ToM allow for the investigation of latency purely in this important compartment. In both of these models, HIV establishes a chronic, lifelong infection from which latently infected cells can be isolated after suppression of viremia ART (104, 105). Similarly, the availability of a model devoid of human T cells but with a full complement of myeloid cells (MoM) allows for the investigation of the contribution of macrophages to HIV latency and persistence in the complete absence of human T cells. The utility of humanized mice for the in vivo analysis of LRAs and clearance strategies has been demonstrated (99, 103, 106). BLT and ToM mice allow (i) the evaluation of different types of highly relevant viruses for infection, (ii) the analysis of latency and persistence by virtually all human cell types that are targets of HIV infection in both the periphery and tissues, (iii) the evaluation of new and established antiretroviral drug interventions, and (iv) the evaluation of novel induction and killing approaches (106). Other humanized mouse models have been successfully used to evaluate broadly neutralizing antibodies and combination induction therapy, with encouraging results (99, 107, 108). In addition, because humanized mice represent a complex system featuring virtually all cell types that are important for adaptive immune responses, they can be useful for the in vivo evaluation of novel approaches to curing HIV that are based on biological molecules as well as gene and cell therapies.

Pathogenic models of SIV infection in the rhesus macaque have also been used in HIV cure research, following the formulation of ART similar in composition, safety, and efficacy to those that have been used in humans. ART regimens now consistently suppress SIV viremia to levels below detection (less than three copies per milliliter of plasma) of the most sensitive assays, thus reaching viral suppression comparable with that in HIV-infected humans (109–111). The availability of such sensitive viral detection assays in both animal models may now allow the field to address critical questions in the context of ongoing ART in vivo.

Thus, human testing of latency reversal and clearance strategies is needed. In selected settings, experimental agents that have already advanced to human testing in venues such as oncology may be more rapidly brought forward for proof-of concept studies in man. But initial evaluation of novel agents or combinations will still likely require testing in animal models. Where exhaustive analysis of tissue is needed, animal models will continue to be integral to research advances, although when possible, immune tissues in human clinical trials should be examined. For example, specialized structures in lymph nodes called lymphoid follicles are enriched for viral infection, and CTL responses have recently been shown to be restricted at these sites (112). The ability of diverse eradication strategies to deliver effectors to such potential sanctuaries can be carefully tested only in such in vivo models.

Conclusion: The synergies of cure and prevention

Research toward HIV eradication began with the success of ART, followed closely by the description of latent, persistent infection. The daunting problem of proviral latency and the failure of initial eradication efforts (113) led to a long hiatus in such efforts, but these were renewed after the report of an HIV cure in the Berlin patient (3) and the initial description of a LRA (22). The next major advance will likely be the demonstration, outside of the context of bone marrow transplantation, of substantial depletion of persistent infection when effective LRAs are appropriately paired with a viral clearance strategy that delivers active effector cells to the sites of induced viral expression. Years of longitudinal measurements have suggested a benchmark for such trials: a decrease by a factor of at least 6 of the frequency of replication-competent HIV within the resting $CD4^+$ T cell reservoir after an intervention, a decline that is rarely seen on ART alone. Such a depletion of latent infection shown by means of QVOA would be expected to correlate with a depletion of the total replication-competent latent reservoir, a meaningful step toward the goal of HIV eradication (38). Already, the decades of investment in the development of a prophylactic HIV vaccine and other preventive strategies have paid unexpected dividends; this research pipeline provides key knowledge and research tools needed to implement effective HIV clearance strategies.

However, it is very likely that additional advances will be needed to allow durable remission of viremia in the absence of ART or, eventually, eradication of HIV infection. This challenge is poignantly illustrated by the case of the "Mississippi child," in whom ART was interrupted after treatment for the first 18 months of life, and a remission of viremia lasted 27 months before a robust viral rebound mimicking primary infection (6). In this child, the viral reservoir was too small to measure, and aviremia in the absence of an HIV-specific immune response presumably was maintained by the intrinsic quiescence of latently infected cells.

This scenario also suggests a third intervention that should be added after therapeutic

disruption of HIV latency and clearance of cellular reservoirs of persistent infection: protection against viral rebound and new HIV infection. As the field of HIV vaccine development moves forward, prophylactic vaccines should be deployed as the last step in an HIV latency reversal and clearance strategy, both to prevent viral rebound that might emanate from rare latently infected cells that have survived the initial rounds of latency reversal and clearance, and to protect against new HIV infection in this at-risk patient population. The prevention of reinfection is an important public health measure, given the substantial health care investment likely to be needed to achieve durable remission or cure of HIV infection.

The past 5 years have seen a substantial new investment in HIV cure research from governments, foundations, and industry. Advances and new insights into the nature of the problem have marked the founding of this new field of endeavor. Key insights into the diverse and complex biology of persistent HIV infection have been made. A diverse portfolio of LRAs is under study, and a pipeline for the development, testing, and validation of new agents now exists. A variety of approaches to imbue an effective anti–HIV-1 response to mediate viral clearance are under study, and some are entering clinical testing. Clearly much work and many challenges lie ahead, but if novel scientific insights can be brought to bear in clinically effective ways, the era marked by the benefits of ART may be followed by one in which ART is no longer a lifelong necessity. And as HIV vaccine science contributes to efforts to eradicate persistent HIV infection, the fields of HIV prevention, treatment, and cure will create the tools to move us toward a world without AIDS.

REFERENCES AND NOTES

1. S. Broder, The development of antiretroviral therapy and its impact on the HIV-1/AIDS pandemic. *Antiviral Res.* **85**, 1–18 (2010). doi: 10.1016/j.antiviral.2009.10.002; pmid: 20018391
2. UNAIDS, 2015. Countries adopt UNAIDS Fast-Track Strategy to double number of people on life-saving HIV treatment by 2020; www.unaids.org/en/resources/presscentre/pressreleaseandstatementarchive/2015/november/20151124_LocationPopulation.
3. G. Hütter *et al*., Long-term control of HIV by CCR5 Delta32/Delta32 stem-cell transplantation. *N. Engl. J. Med.* **360**, 692–698 (2009). doi: 10.1056/NEJMoa0802905; pmid: 19213682
4. S. A. Yukl *et al*., Challenges in detecting HIV persistence during potentially curative interventions: A study of the Berlin patient. *PLOS Pathog.* **9**, e1003347 (2013). doi: 10.1371/journal.ppat.1003347; pmid: 23671416
5. T. J. Henrich *et al*., Antiretroviral-free HIV-1 remission and viral rebound after allogeneic stem cell transplantation: Report of 2 cases. *Ann. Intern. Med.* **161**, 319–327 (2014). doi: 10.7326/M14-1027; pmid: 25047577
6. K. Luzuriaga *et al*., Viremic relapse after HIV-1 remission in a perinatally infected child. *N. Engl. J. Med.* **372**, 786–788 (2015). doi: 10.1056/NEJMc1413931; pmid: 25693029
7. N. M. Archin, J. M. Sung, C. Garrido, N. Soriano-Sarabia, D. M. Margolis, Eradicating HIV-1 infection: Seeking to clear a persistent pathogen. *Nat. Rev. Microbiol.* **12**, 750–764 (2014). doi: 10.1038/nrmicro3352; pmid: 25402363
8. F. Romerio, M. N. Gabriel, D. M. Margolis, Repression of human immunodeficiency virus type 1 through the novel cooperation of human factors YY1 and LSF. *J. Virol.* **71**, 9375–9382 (1997). pmid: 9371597
9. J. J. Coull *et al*., The human factors YY1 and LSF repress the human immunodeficiency virus type 1 long terminal repeat via recruitment of histone deacetylase 1. *J. Virol.* **74**, 6790–6799 (2000). doi: 10.1128/JVI.74.15.6790-6799.2000; pmid: 10888618
10. J. J. Coull *et al*., Targeted derepression of the human immunodeficiency virus type 1 long terminal repeat by pyrrole-imidazole polyamides. *J. Virol.* **76**, 12349–12354 (2002). doi: 10.1128/JVI.76.23.12349-12354.2002; pmid: 12414976
11. L. Ylisastigui *et al*., Polyamides reveal a role for repression in latency within resting T cells of HIV-infected donors. *J. Infect. Dis.* **190**, 1429–1437 (2004). doi: 10.1086/423822; pmid: 15378435
12. G. He, D. M. Margolis, Counterregulation of chromatin deacetylation and histone deacetylase occupancy at the integrated promoter of human immunodeficiency virus type 1 (HIV-1) by the HIV-1 repressor YY1 and HIV-1 activator Tat. *Mol. Cell. Biol.* **22**, 2965–2973 (2002). doi: 10.1128/MCB.22.9.2965-2973.2002; pmid: 11940654
13. C. Van Lint, S. Emiliani, M. Ott, E. Verdin, Transcriptional activation and chromatin remodeling of the HIV-1 promoter in response to histone acetylation. *EMBO J.* **15**, 1112–1120 (1996). pmid: 8605881
14. L. Ylisastigui, N. M. Archin, G. Lehrman, R. J. Bosch, D. M. Margolis, Coaxing HIV-1 from resting CD4 T cells: Histone deacetylase inhibition allows latent viral expression. *AIDS* **18**, 1101–1108 (2004). doi: 10.1097/00002030-200405210-00003; pmid: 15166525
15. S. A. Williams *et al*., NF-kappaB p50 promotes HIV latency through HDAC recruitment and repression of transcriptional initiation. *EMBO J.* **25**, 139–149 (2006). doi: 10.1038/sj.emboj.7600900; pmid: 16319923
16. K. Imai, T. Okamoto, Transcriptional repression of human immunodeficiency virus type 1 by AP-4. *J. Biol. Chem.* **281**, 12495–12505 (2006). doi: 10.1074/jbc.M511773200; pmid: 16540471
17. G. Jiang, A. Espeseth, D. J. Hazuda, D. M. Margolis, c-Myc and Sp1 contribute to proviral latency by recruiting histone deacetylase 1 to the human immunodeficiency virus type 1 promoter. *J. Virol.* **81**, 10914–10923 (2007). doi: 10.1128/JVI.01208-07; pmid: 17670825
18. C. Marban *et al*., Recruitment of chromatin-modifying enzymes by CTIP2 promotes HIV-1 transcriptional silencing. *EMBO J.* **26**, 412–423 (2007). doi: 10.1038/sj.emboj.7601516; pmid: 17245431
19. R. Pearson *et al*., Epigenetic silencing of human immunodeficiency virus (HIV) transcription by formation of restrictive chromatin structures at the viral long terminal repeat drives the progressive entry of HIV into latency. *J. Virol.* **82**, 12291–12303 (2008). doi: 10.1128/JVI.01383-08; pmid: 18829756
20. N. M. Archin *et al*., Expression of latent HIV induced by the potent HDAC inhibitor suberoylanilide hydroxamic acid. *AIDS Res. Hum. Retroviruses* **25**, 207–212 (2009). doi: 10.1089/aid.2008.0191; pmid: 19239360
21. X. Contreras *et al*., Suberoylanilide hydroxamic acid reactivates HIV from latently infected cells. *J. Biol. Chem.* **284**, 6782–6789 (2009). doi: 10.1074/jbc.M807898200; pmid: 19136668
22. N. M. Archin *et al*., Administration of vorinostat disrupts HIV-1 latency in patients on antiretroviral therapy. *Nature* **487**, 482–485 (2012). doi: 10.1038/nature11286; pmid: 22837004
23. J. H. Elliott *et al*., Activation of HIV transcription with short-course vorinostat in HIV-infected patients on suppressive antiretroviral therapy. *PLOS Pathog.* **10**, e1004473 (2014). doi: 10.1371/journal.ppat.1004473; pmid: 25393648
24. T. A. Rasmussen *et al*., Panobinostat, a histone deacetylase inhibitor, for latent-virus reactivation in HIV-infected patients on suppressive antiretroviral therapy: A phase 1/2, single group, clinical trial. *Lancet HIV* **1**, e13–e21 (2014). pmid: 26423811
25. O. S. Søgaard *et al*., The Depsipeptide Romidepsin Reverses HIV-1 Latency In Vivo. *PLOS Pathog.* **11**, e1005142 (2015). doi: 10.1371/journal.ppat.1005142; pmid: 26379282
26. J. H. Elliott *et al*., Short-term administration of disulfiram for reversal of latent HIV infection: A phase 2 dose-escalation study. *Lancet HIV* **2**, e520–e529 (2015). doi: 10.1016/S2352-3018(15)00226-X; pmid: 26614966
27. A. R. Cillo *et al*., Quantification of HIV-1 latency reversal in resting CD4$^+$ T cells from patients on suppressive antiretroviral therapy. *Proc. Natl. Acad. Sci. U.S.A.* **111**, 7078–7083 (2014). doi: 10.1073/pnas.1402873111; pmid: 24706775
28. C. K. Bullen, G. M. Laird, C. M. Durand, J. D. Siliciano, R. F. Siliciano, New ex vivo approaches distinguish effective and ineffective single agents for reversing HIV-1 latency in vivo. *Nat. Med.* **20**, 425–429 (2014). doi: 10.1038/nm.3489; pmid: 24658076
29. M. K. Tripathy, M. E. McManamy, B. D. Burch, N. M. Archin, D. M. Margolis, H3K27 demethylation at the proviral promoter sensitizes latent HIV to the effects of vorinostat in ex vivo cultures of resting CD4$^+$ T cells. *J. Virol.* **89**, 8392–8405 (2015). doi: 10.1128/JVI.00572-15; pmid: 26041287
30. G. Darcis *et al*., An in-depth comparison of latency-reversing agent combinations in various in vitro and ex vivo HIV-1 latency models identified bryostatin-1$^+$JQ1 and ingenol-B$^+$JQ1 to potently reactivate viral gene expression. *PLOS Pathog.* **11**, e1005063 (2015). doi: 10.1371/journal.ppat.1005063; pmid: 26225566
31. J. B. L. S. Whitney, C. E. Osuna, S. Sanisetty, T. L. Barnes, P. T. Hraber, T. Cihlar, R. Geleziunas, J. Hesselgesser, "Treatment with a TLR7 agonist induces transient viremia in SIV-infected ART-suppressed monkeys," abstract 2015, Conference on Retroviruses and Opportunistic Infections, Seattle, WA, 23–26 February 2015.
32. C. L. Novis *et al*., Reactivation of latent HIV-1 in central memory CD4$^+$ T cells through TLR-1/2 stimulation. *Retrovirology* **10**, 119 (2013). doi: 10.1186/1742-4690-10-119; pmid: 24156240
33. C. A. Spina *et al*., An in-depth comparison of latent HIV-1 reactivation in multiple cell model systems and resting CD4$^+$ T cells from aviremic patients. *PLOS Pathog.* **9**, e1003834 (2013). doi: 10.1371/journal.ppat.1003834; pmid: 24385908
34. Y. C. Ho *et al*., Replication-competent noninduced proviruses in the latent reservoir increase barrier to HIV-1 cure. *Cell* **155**, 540–551 (2013). doi: 10.1016/j.cell.2013.09.020; pmid: 24243014
35. N. C. A. Hosmane, R. F. Siliciano, "Multiple rounds of T-cell activation induce additional HIV-1 from the latent reservoir," abstract, Conference on Retroviruses and Opportunistic Infections, Seattle, WA, 23–26 February 2015.
36. M. H. Malim, APOBEC proteins and intrinsic resistance to HIV-1 infection. *Philos. Trans. R. Soc. Lond. B Biol. Sci.* **364**, 675–687 (2009). doi: 10.1098/rstb.2008.0185; pmid: 19038776
37. S. Eriksson *et al*., Comparative analysis of measures of viral reservoirs in HIV-1 eradication studies. *PLOS Pathog.* **9**, e1003174 (2013). doi: 10.1371/journal.ppat.1003174; pmid: 23459007
38. A. M. Crooks *et al*., Precise quantitation of the latent HIV-1 reservoir: Implications for eradication strategies. *J. Infect. Dis.* **212**, 1361–1365 (2015). doi: 10.1093/infdis/jiv218; pmid: 25877550
39. J. D. Siliciano *et al*., Long-term follow-up studies confirm the stability of the latent reservoir for HIV-1 in resting CD4$^+$ T cells. *Nat. Med.* **9**, 727–728 (2003). doi: 10.1038/nm880; pmid: 12754504
40. T. W. Chun *et al*., Quantification of latent tissue reservoirs and total body viral load in HIV-1 infection. *Nature* **387**, 183–188 (1997). doi: 10.1038/387183a0; pmid: 9144289
41. D. Finzi *et al*., Latent infection of CD4$^+$ T cells provides a mechanism for lifelong persistence of HIV-1, even in patients on effective combination therapy. *Nat. Med.* **5**, 512–517 (1999). doi: 10.1038/8394; pmid: 10229227
42. T. W. Chun *et al*., In vivo fate of HIV-1-infected T cells: Quantitative analysis of the transition to stable latency. *Nat. Med.* **1**, 1284–1290 (1995). doi: 10.1038/nm1295-1284; pmid: 7489410
43. J. K. Wong *et al*., Recovery of replication-competent HIV despite prolonged suppression of plasma viremia. *Science* **278**, 1291–1295 (1997). doi: 10.1126/science.278.5341.1291; pmid: 9360926
44. J. Karn, U. Mbonye, Control of HIV latency by epigenetic and non-epigenetic mechanisms. *Curr. HIV Res.* **9**, 554–567 (2011). doi: 10.2174/157016211798998736; pmid: 22211660
45. M. S. Dahabieh, E. Battivelli, E. Verdin, Understanding HIV latency: The road to an HIV cure. *Annu. Rev. Med.* **66**, 407–421 (2015). doi: 10.1146/annurev-med-092112-152941; pmid: 25587657
46. K. M. Barton, B. D. Burch, N. Soriano-Sarabia, D. M. Margolis, Prospects for treatment of latent HIV. *Clin. Pharmacol. Ther.* **93**, 46–56 (2013). doi: 10.1038/clpt.2012.202; pmid: 23212106
47. T. A. Wagner *et al*., Proliferation of cells with HIV integrated into cancer genes contributes to persistent infection.

Science **345**, 570–573 (2014). doi: 10.1126/science.1256304; pmid: 25011556
48. F. Maldarelli *et al*., Specific HIV integration sites are linked to clonal expansion and persistence of infected cells. *Science* **345**, 179–183 (2014). doi: 10.1126/science.1254194; pmid: 24968937
49. L. B. Cohn *et al*., HIV-1 integration landscape during latent and active infection. *Cell* **160**, 420–432 (2015). doi: 10.1016/j.cell.2015.01.020; pmid: 25635456
50. N. Chomont *et al*., HIV reservoir size and persistence are driven by T cell survival and homeostatic proliferation. *Nat. Med.* **15**, 893–900 (2009). doi: 10.1038/nm.1972; pmid: 19543283
51. N. Soriano-Sarabia *et al*., Quantitation of replication-competent HIV-1 in populations of resting CD4+ T cells. *J. Virol.* **88**, 14070–14077 (2014). doi: 10.1128/JVI.01900-14; pmid: 25253353
52. N. Soriano-Sarabia *et al*., Peripheral Vγ9Vδ2 T Cells Are a Novel Reservoir of Latent HIV Infection. *PLOS Pathog.* **11**, e1005201 (2015). doi: 10.1371/journal.ppat.1005201; pmid: 26473478
53. M. J. Buzon *et al*., HIV-1 persistence in CD4+ T cells with stem cell-like properties. *Nat. Med.* **20**, 139–142 (2014). doi: 10.1038/nm.3445; pmid: 24412925
54. J. B. Honeycutt *et al*., Macrophages sustain HIV replication in vivo independently of T cells. *J. Clin. Invest.* **126**, 1353–1366 (2016). doi: 10.1172/JCI84456; pmid: 26950420
55. Q. J. Sattentau, M. Stevenson, Macrophages and HIV-1: An unhealthy constellation. *Cell Host Microbe* **19**, 304–310 (2016). doi: 10.1016/j.chom.2016.02.013; pmid: 26962941
56. C. R. Avalos *et al*., Quantitation of productively infected monocytes and macrophages of simian immunodeficiency virus-infected macaques. *J. Virol.* **90**, 5643–5656 (2016). doi: 10.1128/JVI.00290-16
57. R. T. Gandhi *et al*., No evidence for decay of the latent reservoir in HIV-1-infected patients receiving intensive enfuvirtide-containing antiretroviral therapy. *J. Infect. Dis.* **201**, 293–296 (2010). doi: 10.1086/649569; pmid: 20001856
58. R. T. Gandhi *et al*., No effect of raltegravir intensification on viral replication markers in the blood of HIV-1-infected patients receiving antiretroviral therapy. *J. Acquir. Immune Defic. Syndr.* **59**, 229–235 (2012). doi: 10.1097/QAI.0b013e31823fd1f2; pmid: 22083073
59. S. M. Hammer *et al*., A randomized, placebo-controlled trial of abacavir intensification in HIV-1-infected adults with virologic suppression on a protease inhibitor-containing regimen. *HIV Clin. Trials* **11**, 312–324 (2010). doi: 10.1310/hct1105-312; pmid: 21239359
60. D. McMahon *et al*., Short-course raltegravir intensification does not reduce persistent low-level viremia in patients with HIV-1 suppression during receipt of combination antiretroviral therapy. *Clin. Infect. Dis.* **50**, 912–919 (2010). doi: 10.1086/650749; pmid: 20156060
61. J. B. Dinoso *et al*., Treatment intensification does not reduce residual HIV-1 viremia in patients on highly active antiretroviral therapy. *Proc. Natl. Acad. Sci. U.S.A.* **106**, 9403–9408 (2009). doi: 10.1073/pnas.0903107106; pmid: 19470482
62. A. Vallejo *et al*., The effect of intensification with raltegravir on the HIV-1 reservoir of latently infected memory CD4 T cells in suppressed patients. *AIDS* **26**, 1885–1894 (2012). doi: 10.1097/QAD.0b013e3283584521; pmid: 22992577
63. A. R. Cillo *et al*., Virologic and immunologic effects of adding maraviroc to suppressive antiretroviral therapy in individuals with suboptimal CD4$^+$ T-cell recovery. *AIDS* **29**, 2121–2129 (2015). doi: 10.1097/QAD.0000000000000810; pmid: 26544577
64. M. J. Buzón *et al*., HIV-1 replication and immune dynamics are affected by raltegravir intensification of HAART-suppressed subjects. *Nat. Med.* **16**, 460–465 (2010). doi: 10.1038/nm.2111; pmid: 20228817
65. J. M. Llibre *et al*., Treatment intensification with raltegravir in subjects with sustained HIV-1 viraemia suppression: A randomized 48-week study. *Antivir. Ther.* **17**, 355–364 (2012). doi: 10.3851/IMP1917; pmid: 22290239
66. R. Lorenzo-Redondo *et al*., Persistent HIV-1 replication maintains the tissue reservoir during therapy. *Nature* **530**, 51–56 (2016). doi: 10.1038/nature16933; pmid: 26814962
67. M. F. Kearney *et al*., Lack of detectable HIV-1 molecular evolution during suppressive antiretroviral therapy. *PLOS Pathog.* **10**, e1004010 (2014). doi: 10.1371/journal.ppat.1004010; pmid: 24651464
68. L. Josefsson *et al*., The HIV-1 reservoir in eight patients on long-term suppressive antiretroviral therapy is stable with few genetic changes over time. *Proc. Natl. Acad. Sci. U.S.A.* **110**, E4987–E4996 (2013). doi: 10.1073/pnas.1308313110; pmid: 24277811
69. K. Deng *et al*., Broad CTL response is required to clear latent HIV-1 due to dominance of escape mutations. *Nature* **517**, 381–385 (2015). doi: 10.1038/nature14053; pmid: 25561180
70. R. B. Jones *et al*., Histone deacetylase inhibitors impair the elimination of HIV-infected cells by cytotoxic T-lymphocytes. *PLOS Pathog.* **10**, e1004287 (2014). doi: 10.1371/journal.ppat.1004287; pmid: 25122219
71. J. A. Sung *et al*., Expanded cytotoxic T-cell lymphocytes target the latent HIV reservoir. *J. Infect. Dis.* **212**, 258–263 (2015). doi: 10.1093/infdis/jiv022; pmid: 25589335
72. J. A. Sung *et al*., Dual-affinity re-targeting proteins direct T cell-mediated cytolysis of latently HIV-infected cells. *J. Clin. Invest.* **125**, 4077–4090 (2015). doi: 10.1172/JCI82314; pmid: 26413868
73. C. Garrido, N. Soriano-Sarabia, B. Allard, K. Sholtis, N. M. Archin, D. M. Margolis, 2016. "Clinical administration of vorinostat increases NK cell capacity to produce IFN-γ," abstract, Conference on Retroviruses and Opportunistic Infections, Boston, MA, 22–25 February 2015.
74. G. Clutton, N. Archin, Y. Xu, D. M. Margolis, N. Goonetilleke, "Differential effects of HIV latency-reversing agents on T cell phenotype and function: Implications for HIV cure," abstract, Seventh International Workshop on HIV Persistence during Therapy, Miami, FL, 8–11 December 2015.
75. L. Shan *et al*., Stimulation of HIV-1-specific cytolytic T lymphocytes facilitates elimination of latent viral reservoir after virus reactivation. *Immunity* **36**, 491–501 (2012). doi: 10.1016/j.immuni.2012.01.014; pmid: 22406268
76. J. Papuchon *et al*., Resistance mutations and CTL epitopes in archived HIV-1 DNA of patients on antiviral treatment: Toward a new concept of vaccine. *PLOS ONE* **8**, e69029 (2013). doi: 10.1371/journal.pone.0069029; pmid: 23874854
77. M. K. Liu *et al*., Vertical T cell immunodominance and epitope entropy determine HIV-1 escape. *J. Clin. Invest.* **123**, 380–393 (2013). pmid: 23221345
78. A. J. Ritchie *et al*., Recombination-mediated escape from primary CD8$^+$ T cells in acute HIV-1 infection. *Retrovirology* **11**, 69 (2014). doi: 10.1186/s12977-014-0069-9; pmid: 25212771
79. N. R. Klatt, N. Chomont, D. C. Douek, S. G. Deeks, Immune activation and HIV persistence: Implications for curative approaches to HIV infection. *Immunol. Rev.* **254**, 326–342 (2013). doi: 10.1111/imr.12065; pmid: 23772629
80. F. García, A. León, J. M. Gatell, M. Plana, T. Gallart, Therapeutic vaccines against HIV infection. *Hum. Vaccin. Immunother.* **8**, 569–581 (2012). doi: 10.4161/hv.19555; pmid: 22634436
81. B. Autran *et al*., Greater viral rebound and reduced time to resume antiretroviral therapy after therapeutic immunization with the ALVAC-HIV vaccine (vCP1452). *AIDS* **22**, 1313–1322 (2008). doi: 10.1097/QAD.0b013e3282fdce94; pmid: 18580611
82. M. L. Robb, J. H. Kim, Shot in the HAART: Vaccine therapy for HIV. *Lancet Infect. Dis.* **14**, 259–260 (2014). doi: 10.1016/S1473-3099(13)70331-1; pmid: 24525315
83. A. S. Fauci, H. D. Marston, Toward an HIV vaccine: A scientific journey. *Science* **349**, 386–387 (2015). doi: 10.1126/science.aac6300; pmid: 26206922
84. A. S. Fauci, M. A. Marovich, C. W. Dieffenbach, E. Hunter, S. P. Buchbinder, Immunology. Immune activation with HIV vaccines. *Science* **344**, 49–51 (2014). doi: 10.1126/science.1250672; pmid: 24700849
85. J. P. Casazza *et al*., Therapeutic vaccination expands and improves the function of the HIV-specific memory T-cell repertoire. *J. Infect. Dis.* **207**, 1829–1840 (2013). doi: 10.1093/infdis/jit098; pmid: 23482645
86. C. Andrés *et al*., HIV-1 reservoir dynamics after vaccination and antiretroviral therapy interruption are associated with dendritic cell vaccine-induced T cell responses. *J. Virol.* **89**, 9189–9199 (2015). doi: 10.1128/JVI.01062-15; pmid: 26109727
87. D. Persaud *et al*., Effect of therapeutic HIV recombinant poxvirus vaccines on the size of the resting CD4$^+$ T-cell latent HIV reservoir. *AIDS* **25**, 2227–2234 (2011). doi: 10.1097/QAD.0b013e32834cdaba; pmid: 21918423
88. H. N. Kløverpris *et al*., Early antigen presentation of protective HIV-1 KF11Gag and KK10Gag epitopes from incoming viral particles facilitates rapid recognition of infected cells by specific CD8$^+$ T cells. *J. Virol.* **87**, 2628–2638 (2013). doi: 10.1128/JVI.02131-12; pmid: 23255798
89. A. Balamurugan *et al*., HIV-1 gag cytotoxic T lymphocyte epitopes vary in presentation kinetics relative to HLA class I downregulation. *J. Virol.* **87**, 8726–8734 (2013). doi: 10.1128/JVI.01040-13; pmid: 23740989
90. T. Hanke, Conserved immunogens in prime-boost strategies for the next-generation HIV-1 vaccines. *Expert Opin. Biol. Ther.* **14**, 601–616 (2014). doi: 10.1517/14712598.2014.885946; pmid: 24490585
91. M. Rolland *et al*., HIV-1 conserved-element vaccines: Relationship between sequence conservation and replicative capacity. *J. Virol.* **87**, 5461–5467 (2013). doi: 10.1128/JVI.03033-12; pmid: 23468488
92. B. Ondondo *et al*., Novel conserved-region T-cell mosaic vaccine with high global HIV-1 coverage is recognized by protective responses in untreated infection. *Mol. Ther.* **24**, 832–842 (2016). doi: 10.1038/mt.2016.3; pmid: 26743582
93. G. Hancock *et al*., Identification of effective subdominant anti-HIV-1 CD8$^+$ T cells within entire post-infection and post-vaccination immune responses. *PLOS Pathog.* **11**, e1004658 (2015). doi: 10.1371/journal.ppat.1004658; pmid: 25723536
94. B. Mothe *et al*., Definition of the viral targets of protective HIV-1-specific T cell responses. *J. Transl. Med.* **9**, 208 (2011). doi: 10.1186/1479-5876-9-208; pmid: 22152067
95. S. G. Hansen *et al*., Immune clearance of highly pathogenic SIV infection. *Nature* **502**, 100–104 (2013). doi: 10.1038/nature12519; pmid: 24025770
96. S. G. Hansen *et al*., Cytomegalovirus vectors violate CD8$^+$ T cell epitope recognition paradigms. *Science* **340**, 1237874 (2013). doi: 10.1126/science.1237874; pmid: 23704576
97. S. G. Hansen *et al*., Broadly targeted CD8□ T cell responses restricted by major histocompatibility complex E. *Science* **351**, 714–720 (2016). pmid: 26797147
98. K. E. Stephenson, D. H. Barouch, Broadly neutralizing antibodies for HIV eradication. *Curr. HIV/AIDS Rep.* **13**, 31–37 (2016). doi: 10.1007/s11904-016-0299-7; pmid: 26841901
99. A. Halper-Stromberg *et al*., Broadly neutralizing antibodies and viral inducers decrease rebound from HIV-1 latent reservoirs in humanized mice. *Cell* **158**, 989–999 (2014). doi: 10.1016/j.cell.2014.07.043; pmid: 25131989
100. D. D. Sloan *et al*., Targeting HIV reservoir in infected CD4 T cells by dual-affinity re-targeting molecules (DARTs) that bind HIV envelope and recruit cytotoxic T cells. *PLOS Pathog.* **11**, e1005233 (2015). doi: 10.1371/journal.ppat.1005233; pmid: 26539983
101. A. Pegu *et al*., Activation and lysis of human CD4 cells latently infected with HIV-1. *Nat. Commun.* **6**, 8447 (2015). doi: 10.1038/ncomms9447; pmid: 26485194
102. G. M. Chew *et al*., TIGIT marks exhausted T Cells, correlates with disease progression, and serves as a target for immune restoration in HIV and SIV infection. *PLOS Pathog.* **12**, e1005349 (2016). doi: 10.1371/journal.ppat.1005349; pmid: 26741490
103. J. V. Garcia, In vivo platforms for analysis of HIV persistence and eradication. *J. Clin. Invest.* **126**, 424–431 (2016). doi: 10.1172/JCI80562; pmid: 26829623
104. P. W. Denton *et al*., Generation of HIV latency in humanized BLT mice. *J. Virol.* **86**, 630–634 (2012). doi: 10.1128/JVI.06120-11; pmid: 22013053
105. J. B. Honeycutt *et al*., HIV-1 infection, response to treatment and establishment of viral latency in a novel humanized T cell-only mouse (TOM) model. *Retrovirology* **10**, 121 (2013). doi: 10.1186/1742-4690-10-121; pmid: 24156277
106. P. W. Denton *et al*., Targeted cytotoxic therapy kills persisting HIV infected cells during ART. *PLOS Pathog.* **10**, e1003872 (2014). doi: 10.1371/journal.ppat.1003872; pmid: 24415939
107. J. A. Horwitz *et al*., HIV-1 suppression and durable control by combining single broadly neutralizing antibodies and antiretroviral drugs in humanized mice. *Proc. Natl. Acad. Sci. U.S.A.* **110**, 16538–16543 (2013). doi: 10.1073/pnas.1315295110; pmid: 24043801
108. F. Klein *et al*., HIV therapy by a combination of broadly neutralizing antibodies in humanized mice. *Nature* **492**, 118–122 (2012). doi: 10.1038/nature11604; pmid: 23103874
109. G. Q. Del Prete, J. D. Lifson, Considerations in the development of nonhuman primate models of combination antiretroviral therapy for studies of AIDS virus suppression, residual virus, and curative strategies. *Curr Opin HIV AIDS* **8**, 262–272 (2013). pmid: 23698559

110. G. Q. Del Prete *et al*., Elevated plasma viral loads in romidepsin-treated simian immunodeficiency virus-infected rhesus macaques on suppressive combination antiretroviral therapy. *Antimicrob. Agents Chemother.* **60**, 1560–1572 (2015). doi: 10.1128/AAC.02625-15; pmid: 26711758
111. G. Q. Del Prete *et al*., Short communication: Comparative evaluation of coformulated injectable combination antiretroviral therapy regimens in simian immunodeficiency virus-infected rhesus macaques. *AIDS Res. Hum. Retroviruses* **32**, 163–168 (2016). doi: 10.1089/aid.2015.0130; pmid: 26150024
112. Y. Fukazawa *et al*., B cell follicle sanctuary permits persistent productive simian immunodeficiency virus infection in elite controllers. *Nat. Med.* **21**, 132–139 (2015). doi: 10.1038/nm.3781; pmid: 25599132
113. J. M. Prins *et al*., Immuno-activation with anti-CD3 and recombinant human IL-2 in HIV-1-infected patients on potent antiretroviral therapy. *AIDS* **13**, 2405–2410 (1999). doi: 10.1097/00002030-199912030-00012; pmid: 10597782

ACKNOWLEDGMENTS

The authors thank N. Goonetilleke for valuable input. D.M.M. and B.F.H. have filed patent application PCT/US2015/053027 related to dual-affinity retargeting antibodies. Work in the authors' laboratories was supported by the National Institutes of Health grants U19-AI096113 to D.M.M., UM1-AI10064 for the Duke Center for HIV/AIDS Vaccine Immunology-Immunogen Discovery to B.F.H., RO1-AI111899 and RO1-MH108179 to J.V.G, and P30-AI50410 to the University of North Carolina Center for AIDS Research. We thank all the HIV$^+$ participants in our studies for their critical contributions to this research.

10.1126/science.aaf6517

RESEARCH ARTICLE SUMMARY

SYNTHETIC BIOLOGY

Synthetic recombinase-based state machines in living cells

Nathaniel Roquet, Ava P. Soleimany, Alyssa C. Ferris, Scott Aaronson, Timothy K. Lu*

INTRODUCTION: Living systems execute regulatory programs and exhibit specific phenotypes depending on the identity and timing of chemical signals, but general strategies for mimicking such behaviors with artificial genetic programs are lacking. Synthetic circuits that produce outputs only depending on simultaneous combinations of inputs are limited in their scale and their ability to recognize dynamics because they do not uniquely detect or respond to temporally ordered inputs. To address these limitations, we developed and experimentally validated a framework for implementing state machines that record and respond to all identities and orders of gene regulatory events in living cells.

RATIONALE: We built recombinase-based state machines (RSMs) that use input-driven recombinases to manipulate DNA registers made up of overlapping and orthogonal pairs of recombinase recognition sites. Specifically, chemical inputs express recombinases that can perform two types of irreversible operations on a register: excision if their recognition sites are aligned, or inversion if their recognition sites are anti-aligned. The registers are designed to adopt a distinct DNA sequence ("state") for every possible "permuted substring" of inputs—that is, every possible combination and ordering of inputs. The state persists even when inputs are removed and may be read with sequencing or by polymerase chain reaction. Using mathematical analysis to determine how the structure of a RSM relates to its scalability, we found that incorporating multiple orthogonal pairs of recognition sites per recombinase allows a RSM to outperform combinational circuits in scale.

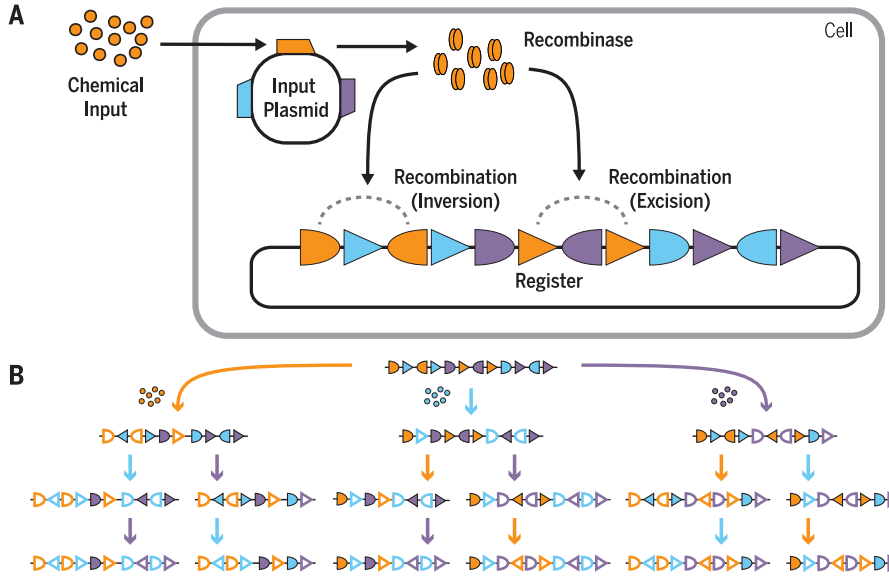

Summary of a three-input, 16-state RSM. (**A**) The RSM mechanism. A chemical input induces the expression of a recombinase (from a gene on the input plasmid) that modifies a DNA register made up of overlapping and orthogonal recombinase recognition sites. Distinct recombinases can be controlled by distinct inputs. These recombinases each target multiple orthogonal pairs of their cognate recognition sites (shown as triangles and half-ovals) to catalyze inversion (when the sites are anti-aligned) or excision (when the sites are aligned). (**B**) The register is designed to adopt a distinct DNA state for every identity and order of inputs. Three different inputs—orange, blue, and purple—are represented by colored arrows, each of which expresses a distinct recombinase. Unrecombined recognition sites are shaded; recombined recognition sites are outlined.

Genetic parts (made up of promoters, terminators, and genes) may be interleaved into RSM registers to implement gene regulation programs capable of expressing unique combinations of genes in each state. In addition, we provide a computational tool that accepts a user-specified two-input multigene regulation program and returns corresponding registers that implement it. This searchable database enables facile creation of RSMs with desired behaviors without requiring detailed knowledge of gene circuit design.

ON OUR WEBSITE

Read the full article at http://dx.doi.org/10.1126/science.aad8559

RESULTS: We built two-input, five-state RSMs and three-input, 16-state RSMs capable of recording every permuted substring of their inputs. We tested the RSMs in *Escherichia coli* and used Sanger sequencing to measure performance. For the two-input, five-state RSM, at least 97% of cells treated with each permuted substring of inputs adopted their expected state. For the three-input, 16-state RSM, at least 88% of cells treated with each permuted substring of inputs adopted their expected state, although we observed 100% for most treatment conditions.

We used these two- and three-input RSMs to implement gene regulation programs by interleaving genetic parts into their registers. For the two-input, five-state system, we designed registers for various gene regulation programs using our computational database and search function. Four single-gene regulation programs and one multigene regulation program (which expressed a different set of fluorescent reports in each state) were successfully implemented in *E. coli*, with at least 94% of cells adopting their expected gene expression profile when treated with each permuted substring of inputs. Lastly, we successfully implemented two different three-input, 16-state gene regulation programs; one of these—a three-input passcode switch—performed with at least 97% of cells adopting the expected gene expression behavior.

CONCLUSION: Our work presents a powerful framework for implementing RSMs in living cells that are capable of recording and responding to all identities and orders of a set of chemical inputs. Depending on desired applications, the prototypical inducible systems used here to drive the RSMs can be replaced by sensors that correspond to desired input signals or gene regulation events. We anticipate that the integration of RSMs into complex living systems will transform our capacity to understand and engineer them. ■

The list of author affiliations is available in the full article online.
*Corresponding author. Email: timlu@mit.edu
Cite this article as N. Roquet *et al.*, *Science* 353, aad8559 (2016). DOI: 10.1126/science.aad8559

RESEARCH ARTICLE

SYNTHETIC BIOLOGY

Synthetic recombinase-based state machines in living cells

Nathaniel Roquet,[1,2,3,4] Ava P. Soleimany,[1,2,3] Alyssa C. Ferris,[1,2,3,5] Scott Aaronson,[3] Timothy K. Lu[1,2,3,4,6,*]

State machines underlie the sophisticated functionality behind human-made and natural computing systems that perform order-dependent information processing. We developed a recombinase-based framework for building state machines in living cells by leveraging chemically controlled DNA excision and inversion operations to encode states in DNA sequences. This strategy enables convenient readout of states (by sequencing and/or polymerase chain reaction) as well as complex regulation of gene expression. We validated our framework by engineering state machines in *Escherichia coli* that used one, two, or three chemical inputs to control up to 16 DNA states. These state machines were capable of recording the temporal order of all inputs and performing multi-input, multi-output control of gene expression. We also developed a computational tool for the automated design of gene regulation programs using recombinase-based state machines. Our scalable framework should enable new strategies for recording and studying how combinational and temporal events regulate complex cell functions and for programming sophisticated cell behaviors.

State machines are systems that exist in any of a number of states, in which transitions between states are controlled by inputs (*1*). The next state of a given state machine is determined not only by a particular input, but also by its current state. This state-dependent logic can be used to produce outputs that are dependent on the order of inputs, unlike in combinational logic circuits wherein the outputs are solely dependent on the current combination of inputs. Figure 1 depicts a state machine that enters a different state for each permuted substring of two inputs A and B, by which we refer to each distinct combination and ordering of those two inputs: {no input, A only, B only, A followed by B (A → B), B followed by A (B → A)}.

Synthetic state machines that record and respond to sequences of signaling and gene regulatory events within a cell could be transformative tools in the study and engineering of complex living systems. For example, in human development, progenitor cells differentiate into specific cell types with disparate functions determined by the timing and order of transcription factor (TF) activation (*2*, *3*). This information has allowed researchers to program human stem cells into differentiated cells (*4*, *5*), and conversely, reprogram differentiated cells into stem cells by means of exogenous, sequential TF activation (*6*, *7*). However, the temporal organization of TF cascades that drive different cell lineages remains largely unknown. State machines that record and actuate gene expression in response to the order of TF activation in individual cells would be useful for understanding and modulating these differentiation processes.

Such state machines may also improve our understanding of disease progression, which can also depend on the appearance and order of extracellular and intracellular factors. For example, in cancer, the temporal order of genetic mutations in a tumor can determine its phenotype (*8*). Similarly, in both somatic diseases and pathogenic infections, preadaptation of disease cells to different environmental conditions may affect the way the cells behave and respond to drug treatments (*9*–*12*). Integrating state machines into disease models and subsequently analyzing the history of cells that survive treatment would be useful for understanding how disease progression affects therapeutic response.

Despite their potential to transform the understanding and engineering of biological systems, complex functional state machines have yet to be implemented in living cells because of a lack of scalable and generalizable frameworks (*13*). Oishi *et al.* proposed a theoretical CRISPR interference-based strategy for building state machines in living cells, in which state is encoded epigenetically (*14*). In contrast, we developed a scalable recombinase-based strategy for implementing state machines in living cells, in which a given state is encoded in a particular DNA sequence. The direct storage of state information in the DNA sequence ensures that it is maintained stably and with minimal burden to the cell. Recombinases have been used to implement switches (*15*–*19*), chemical pulse counters (*20*), Boolean logic gates integrated with memory (*21*, *22*), and temporal logic (*23*). We used them to implement scalable state machines, such as those that can distinguish among all possible permuted substrings of a set of inputs with unique gene expression outputs. We refer to our state machine implementations as recombinase-based state machines (RSMs).

Recombinase-based state machine parts and operations

In a RSM, inputs are defined by chemical signals, and state is defined by the DNA sequence within a prescribed region of DNA, termed the register. Chemical signals mediate state transitions by inducing the expression of large serine recombinases that catalyze recombination events on the register, thereby changing the state. Specifically, each recombinase recognizes a cognate pair of DNA recognition sites on the register, *attP* (derived from a phage) and *attB* (derived from its bacterial host), and carries out a recombination reaction between them, yielding *attL* and *attR* sites (made up of conjoined halves of *attB* and *attP*) (*24*, *25*). In the absence of extra cofactors, this reaction is irreversible (fig. S1 and text S1) (*26*–*28*). Each site in a cognate *attB*-*attP* pair has a matching central dinucleotide that determines its polarity (*29*, *30*). If the two sites are anti-aligned (oriented with opposite polarity) on the register, then the result of their recombination is the inversion of the DNA between them (Fig. 2A and fig. S2A). Alternatively, if the two sites are aligned (oriented with the same polarity) on the register, then the result of their recombination is the excision of the DNA between them (Fig. 2B and fig. S2B). DNA segments that are excised from the register are assumed to be lost because of a lack of origin of replication.

When there are multiple inputs to a RSM, they can each drive distinct recombinases that operate only on their own *attB*-*attP* pairs. At least 25 (putatively orthogonal) large serine recombinases have been described and tested in the literature (*18*, *25*), and bioinformatics mining can be used to discover even more (*18*). Recognition sites for

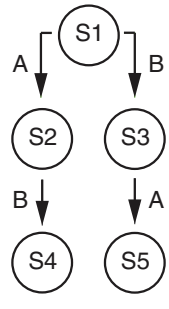

Fig. 1. Example of a state machine. Nodes represent states; arrows represent transitions between states mediated by inputs. Each of the possible permuted substrings of the two inputs A and B generates a unique state.

[1]Synthetic Biology Group, Research Laboratory of Electronics, Massachusetts Institute of Technology, Cambridge, MA 02139, USA. [2]Synthetic Biology Center, Department of Biological Engineering, Massachusetts Institute of Technology, Cambridge, MA 02139, USA. [3]Department of Electrical Engineering and Computer Science, Massachusetts Institute of Technology, Cambridge, MA 02139, USA. [4]Biophysics Program, Harvard University, Boston, MA 02115, USA. [5]Biochemistry Program, Wellesley College, Wellesley, MA 02481, USA. [6]Center for Microbiome Informatics and Therapeutics, Massachusetts Institute of Technology, Cambridge, MA 02139, USA.
*Corresponding author. Email: timlu@mit.edu

multiple recombinases may be arranged in several different ways on the register. If *attB-attP* pairs from different recombinases are nested or overlapping, then the operation of one recombinase can affect the operation of subsequent recombinases—either by rearranging the relative orientation of their *attB* and *attP* sites or by excising one or both sites in a pair from the register—thereby precluding any type of downstream operation on these sites. For example, if we consider the initial register design in Fig. 2C, applying input B → A leads to a unique DNA sequence, but applying A → B leads to the same DNA sequence we would expect if we only applied A, because the A-driven recombinase excises a site for the B-driven recombinase.

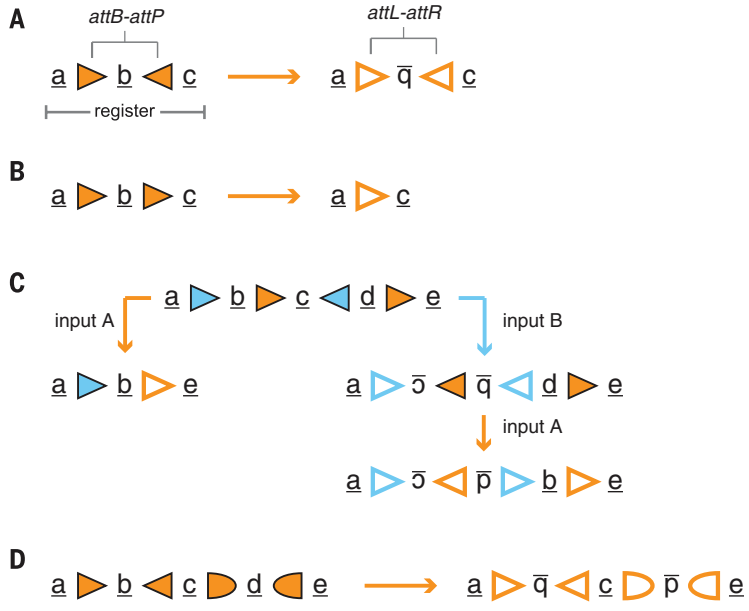

Fig. 2. Rules of recombination on a register. The register is depicted as an array of underscored alphabet symbols (arbitrary DNA) and shape symbols (recognition sites). (**A**) If sites in an *attB-attP* pair are anti-aligned, then the DNA between them is inverted during recombination. (**B**) If sites in an *attB-attP* pair are aligned, then the DNA between them is excised during recombination. (**C**) Multiple inputs can drive distinct recombinases that operate on their own *attB-attP* pairs. In this example, input A drives the orange recombinase and input B drives the blue recombinase. (**D**) Multiple orthogonal *attB-attP* pairs for a given recombinase can be placed on a register. Here, distinct shapes denote two pairs of *attB-attP*. Up to six orthogonal and directional *attB-attP* pairs can be created per large serine recombinase (*31*). Figure S2 gives more detail on the recombination reactions shown here.

We measure the "information capacity" of a RSM by the number of distinct states it can access, and hence the number of permuted substrings of inputs it can distinguish. Given the noncommutative nature of recombinase operations on a register, one might naïvely believe that the information capacity of RSMs would behave like $N!$ for N inputs. But if a RSM is designed such that each input-driven recombinase only has one *attB-attP* pair on the register, the information capacity of the RSM never exceeds 2^N, which is the result we would expect if recombinase operations were commutative (Box 1 and text S2). To circumvent this information bottleneck, registers must be designed with multiple orthogonal *attB-attP* pairs per recombinase. Orthogonal *attB-attP* pairs for a large serine recombinase can be engineered by mutating the central dinucleotide of each site in the native *attB-attP* pair (*29*–*31*). Pairs of sites with the same central dinucleotide sequence should recombine, but they should not recombine if the central dinucleotide sequences do not match (Fig. 2D and fig. S2C).

Building a two-input, five-state RSM

To implement a RSM that enters a different state (five in total) for every permuted substring of two inputs, it was sufficient to use two orthogonal *attB-attP* pairs for one recombinase and one *attB-attP* pair for the other recombinase. Figure 3A shows the RSM design and a detailed representation of its state diagram. This RSM is composed of two plasmids: an input plasmid and an output plasmid. The input plasmid, at a high copy number, expresses two large serine recombinases, BxbI and TP901, from the anhydrotetracycline (ATc)–inducible P_{LtetO} promoter and the arabinose (Ara)–inducible P_{BAD} promoter, respectively. The output plasmid, at a single copy number, contains the register that is modified by the recombinases expressed from the input plasmid.

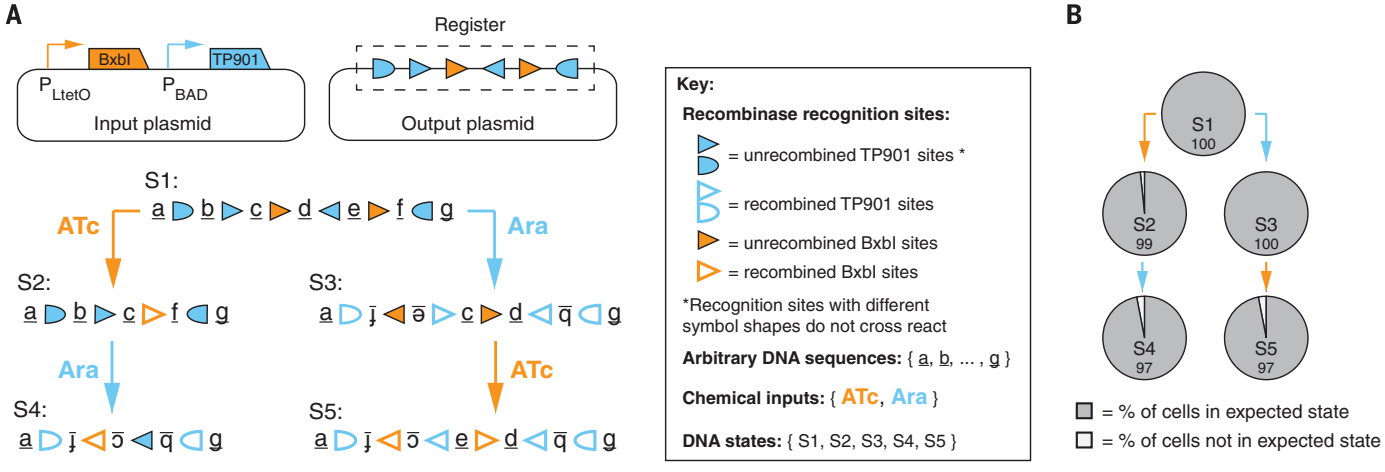

Fig. 3. Designing and validating a two-input, five-state RSM. (**A**) The two plasmids used to implement the RSM (top) and a detailed state diagram demonstrating the resulting register for each permuted substring of the two inputs (ATc and Ara; bottom). (**B**) The performance of the RSM in *E. coli*. Nodes represent populations of cells induced with permuted substrings of the inputs ATc (orange arrow) and Ara (blue arrow). Cultures were treated with saturating concentrations of each input (ATc, 250 ng/ml; Ara, 1% w/v) at 30°C for 18 hours in three biological replicates. Node labels indicate the expected state [corresponding to (A)] and the percentage of cells in that state as determined by Sanger sequencing of colonies from individual cells in each population (at least 66 cells totaled over all three biological replicates).

The register is initially composed of an aligned BxbI *attB-attP* pair and two anti-aligned and orthogonal TP901 *attB-attP* pairs. If ATc is introduced first to the system, then BxbI is expressed and excises the DNA inside of its cognate recognition site pair, which includes a recognition site for TP901. Subsequent introduction of Ara to the system induces the expression of TP901, which recombines its cognate recognition sites on the outer edge of the register, thus inverting everything in between. Conversely, if Ara is introduced first to the system, then the outer TP901 sites invert everything between the edges of the register and the inner TP901 sites invert an inner portion of the register, thus setting the BxbI recognition sites into an anti-aligned configuration. Subsequent application of ATc to the system inverts the sequence of DNA between the BxbI sites. As a result, each permuted substring of the inputs yields a distinct DNA sequence on the register.

To evaluate the performance of the RSM in *Escherichia coli*, we grew five populations of cells that were treated with all five permuted substrings of the inputs ATc and Ara (no input, ATc only, Ara only, ATc → Ara, and Ara → ATc). We Sanger-sequenced the register in colonies of at least 22 cells from each population in each of three biological replicates to determine the percent of cells with the expected DNA sequence (Fig. 3B) (*32*). At least 97% of all cells treated with each permuted substring of inputs adopted the expected state, thus confirming the fidelity of our RSM. Table S1 provides information for the sequenced registers that were not in the expected state.

Because our Sanger sequencing readout of state was low-throughput, we also developed a quantitative polymerase chain reaction (qPCR)–based method to conveniently interrogate state on a population-wide level. The excision and inversion of DNA segments in our register permitted the design of primer pairs that were amplified in some states but not others. We created a computer program, the PCR-based state interrogation tool (PSIT), to identify all possible sets of primer pairs that uniquely identify each state of a given register (fig. S3 and appendix S2). For our two-input, five-state RSM, we chose a set of three primer pairs and performed qPCR on DNA that was isolated from each population of cells treated with all possible permuted substrings of the ATc and Ara inputs. The fractional amount of register DNA amplified was calculated for each primer pair in our set and was compared to what we would expect if all cells in each population adopted just one of the five possible states (*32*). In agreement with our sequencing results, the qPCR measurements of all experimental populations were most similar to what we would expect if all cells in each population adopted their expected state (fig. S4).

Scaling RSMs

We developed a modular register design strategy for building RSMs that enter a distinct state for every permuted substring of inputs (approximately $eN!$ states for N inputs; see table S2 and texts S4 and S5). For N inputs, the design strategy uses $N-1$ recognition sites per recombinase, and hence is limited to register designs for up to seven inputs (13,700 states) because only six orthogonal and directional *attB-attP* pairs can be created per large serine recombinase (*31*).

Because the two-input, five-state RSM shown in Fig. 3A represents only a marginal improvement in information capacity over two-input, four-state systems achievable by combinational computation, we sought to further demonstrate the information capacity enabled by our RSM framework by scaling to a three-input, 16-state RSM (Fig. 4A and fig. S5). The input plasmid for this state machine expresses an additional recombinase, A118, under a 2,4-diacetylphloroglucinol (DAPG)–inducible P_{PhlF} promoter system, and its register uses two orthogonal *attB-attP* pairs for each of the three recombinases (following the design strategy in text S5).

To evaluate the performance of this RSM in *E. coli*, we grew 16 populations of cells that were treated with all 16 permuted substrings of the inputs ATc, Ara, and DAPG. We sequenced the register in colonies of five or six cells from each population in each of three biological replicates to determine the percentage of cells with the expected DNA sequence (Fig. 4B) (*32*). In most populations, 100% of the cells adopted their expected state, and even in the worst-performing population (ATc → Ara → DAPG), 88% of cells adopted their expected state. Table S1 provides information for the sequenced registers that were not in the expected state. We also measured the predominant state of each population by qPCR with a set of six primer pairs elucidated by PSIT (*32*). In agreement with the sequencing results, the qPCR measurements for all experimental populations were most similar to what we would expect if all cells in each population adopted their expected state (fig. S6).

Gene-regulatory RSMs

Our state machine framework enables the creation of state-dependent gene regulation programs that specify which genes should be expressed or not expressed in each state. This could be useful for a wide range of biological applications, such as programming synthetic differentiation cascades,

Box 1. Mathematical discussion of RSMs.

If a RSM with *N* inputs is designed such that each input-driven recombinase only has one *attB-attP* pair on the register, the number of states cannot exceed 2^N. To prove this important claim, we first introduce the concept of irreducibility. An irreducible string of recombinases is one in which, when the recombinases are applied to a register in the given order, each recombinase performs an operation (excision or inversion) on the register. We can make the following two statements about irreducible strings:

Statement 1: Every possible state of a register must be accessible by the application of some irreducible string of recombinases. This follows from considering that (i) each state is the result of a string of recombination operations, and (ii) the string of recombinases corresponding to that string of recombination operations is irreducible by definition.

Statement 2: Assuming a register with one *attB-attP* pair per recombinase, all irreducible strings from the same subset of recombinases generate the same state on the register. This follows from considering that (i) all rearrangeable DNA segments on the register are flanked on both sides by *attB* and/or *attP* sites belonging to the subset of recombinases being applied; (ii) by the definition of irreducibility, each recombinase in the irreducible string will catalyze recombination between its *attB-attP* pair; and (iii) when recombination between *attB* and *attP* sites occurs, they always form the same junctions: The back end of the *attB* will join the front end of the *attP*, and the front end of the *attB* will join the back end of the *attP*. Therefore, all rearrangeable DNA segments will form the same junctions after an irreducible string of recombinases is applied, regardless of the order in which those recombinases are applied.

Now to prove the claim: Given a RSM with N input-driven recombinases and one pair of *attB-attP* per recombinase on its register, all states must be accessible by some irreducible string of recombinases (statement 1), and all irreducible strings from the same subset of the N recombinases must generate the same state (statement 2). Therefore, there cannot be more states than there are subsets of recombinases, which is 2^N (see text S2 for a more detailed version of this proof).

More generally, this proof can be expanded to show that, given k pairs of orthogonal *attB-attP* pairs per recombinase on a register, the number of states it can access will never exceed 2^{kN} (see text S3). For large serine recombinases, there is a limit of $k = 6$ orthogonal and directional *attB-attP* pairs for a given recombinase (*31*). Therefore, the information capacity of RSMs using large serine recombinases is intrinsically bound exponentially.

There are still many unanswered mathematical questions regarding RSM structure. For example, given a DNA sequence, what is the computational difficulty of deciding whether it admits an irreducible ordering of a set of recombinases? Is this problem NP-hard? Also, how can we decide whether an irreducible string of recombinases has minimal length, or whether there might be a shorter irreducible string that produces the same DNA sequence?

encoding the identities and order of biological events into selectable or sortable reporters, or targeting genetic perturbations to cells that experience a particular order of biological events. Gene regulation programs can be implemented by incorporating genetic regulatory elements, such as promoters, terminators, and genes, into the registers of our RSMs. The rearrangement of these elements in each state should then alter gene expression in a predictable manner. Such RSMs are a biological realization of Moore machines from automata theory, where each state is associated with a set of outputs (*1*). We refer to them as gene-regulatory RSMs (GRSMs).

To help researchers design circuits for desired gene regulation programs, we created a large, searchable database of two-input, five-state GRSM registers. To compile this GRSM database (Fig. 5), we first enumerated all possible registers that could result from interleaving functionally distinct parts (made from terminators, constitutive promoters, and genes; see text S6 for more details) before and after each recombinase recognition site in our validated five-state register from Fig. 3A. We evaluated each state of each register for gene transcription, and aggregated registers that implement the same gene regulation program. During this evaluation step, we assumed that all genes had bidirectional terminators on their 3′ ends, thus disallowing the possibility of an RNA polymerase traversing a gene (in either direction) to transcribe another gene. We also assumed that each gene in a register was distinct. These assumptions were made to simplify register designs and keep the database at a manageable size for fast computational search.

To avoid redundancy in the database, we removed any register with superfluous parts (containing terminators, promoters, or genes that do not affect gene regulation in any state) if its "parent" register [the same register except without the superfluous part(s)] was also represented in the database. Moreover, all registers that transcribed either no gene or the same gene in every state were removed from the database, as this gene regulation is trivial to implement.

The resulting database (database S1) contains a total of 5,192,819 GRSM registers that implement 174,264 gene regulation programs. Each register is different in the sense that no two registers have all of the same parts in all of the same positions. Registers in the database regulate the transcription of 1 to 14 genes (fig. S7A). A register for any desired program that regulates up to three genes is likely to be in the database, which comprises 100% of possible single-gene regulation programs, 95% of possible two-gene regulation programs, and 61% of possible three-gene regulation programs (fig. S7B). Moreover, 27% of possible four-gene regulation programs are represented in the database, but the percentage drops off steeply beyond that, as the number of possible gene regulation programs grows exponentially with each additional gene (text S7). One could apply straightforward gene replacement principles to go beyond the scope of regulation programs represented in the database—for example, by replacing multiple distinct genes on a register with copies of the same gene, or replacing a gene with a multicistronic operon (fig. S8). To conveniently use the GRSM database for design or exploration, we created a search function that accepts a user-specified gene regulation program and returns all registers from the database that may be used to implement it (Fig. 5 and appendix S1).

To create functional GRSMs in *E. coli*, we implemented the same input-output plasmid scheme as our two-input, five-state RSM (Fig. 3A), except that we substituted registers from our database on the output plasmid. Fluorescent protein (FP) genes were built on the registers to evaluate gene regulation performance. We grew populations of cells treated with all five permuted substrings of the inputs ATc and Ara, and then used flow cytometry on each population to measure the percentage of cells with distinct FP expression profiles (*32*). We successfully implemented four single-gene regulation programs (Fig. 6, A to D) and one multigene regulation program (in which unique subsets of three distinct FPs were expressed in each state;

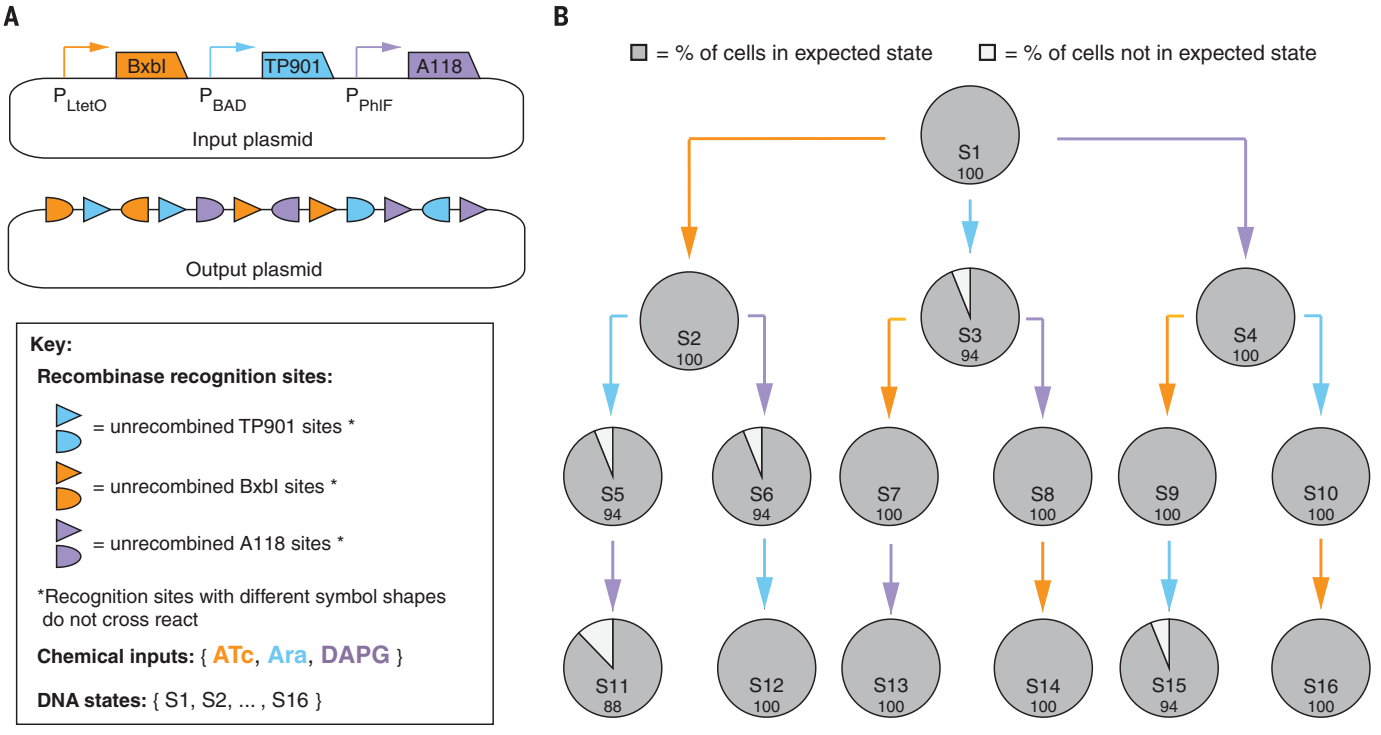

Fig. 4. Scaling to a three-input, 16-state RSM. (**A**) The two plasmids used to implement the RSM. ATc, Ara, and DAPG induce expression of BxbI, TP901, and A118 recombinases, respectively. A detailed state diagram of the register on the output plasmid is shown in fig. S5. (**B**) The performance of the RSM in *E. coli*. Nodes represent populations of cells induced with all permuted substrings of the inputs ATc (orange arrow), Ara (blue arrow), and DAPG (purple arrow). Cultures were treated with saturating concentrations of each input (ATc, 250 ng/ml; Ara, 1% w/v; DAPG, 25 μM) at 30°C for 24 hours in three biological replicates. Node labels indicate the expected state (corresponding to fig. S5) and the percentage of cells in that state as determined by Sanger sequencing of colonies from individual cells in each population (at least 17 cells totaled over all three biological replicates).

Fig. 6E), with at least 94% of cells from each experimental population adopting the expected FP expression profile. These GRSMs enable convenient fluorescent-based reporting on the identity and order of cellular events. For example, the GRSM from Fig. 6E allowed us to evaluate the performance of the underlying RSM with increasing input time durations (by 1-hour steps) by means of flow cytometry (fig. S9). Our findings demonstrated that input durations of 2 hours were sufficient for a majority of cells to adopt their expected state.

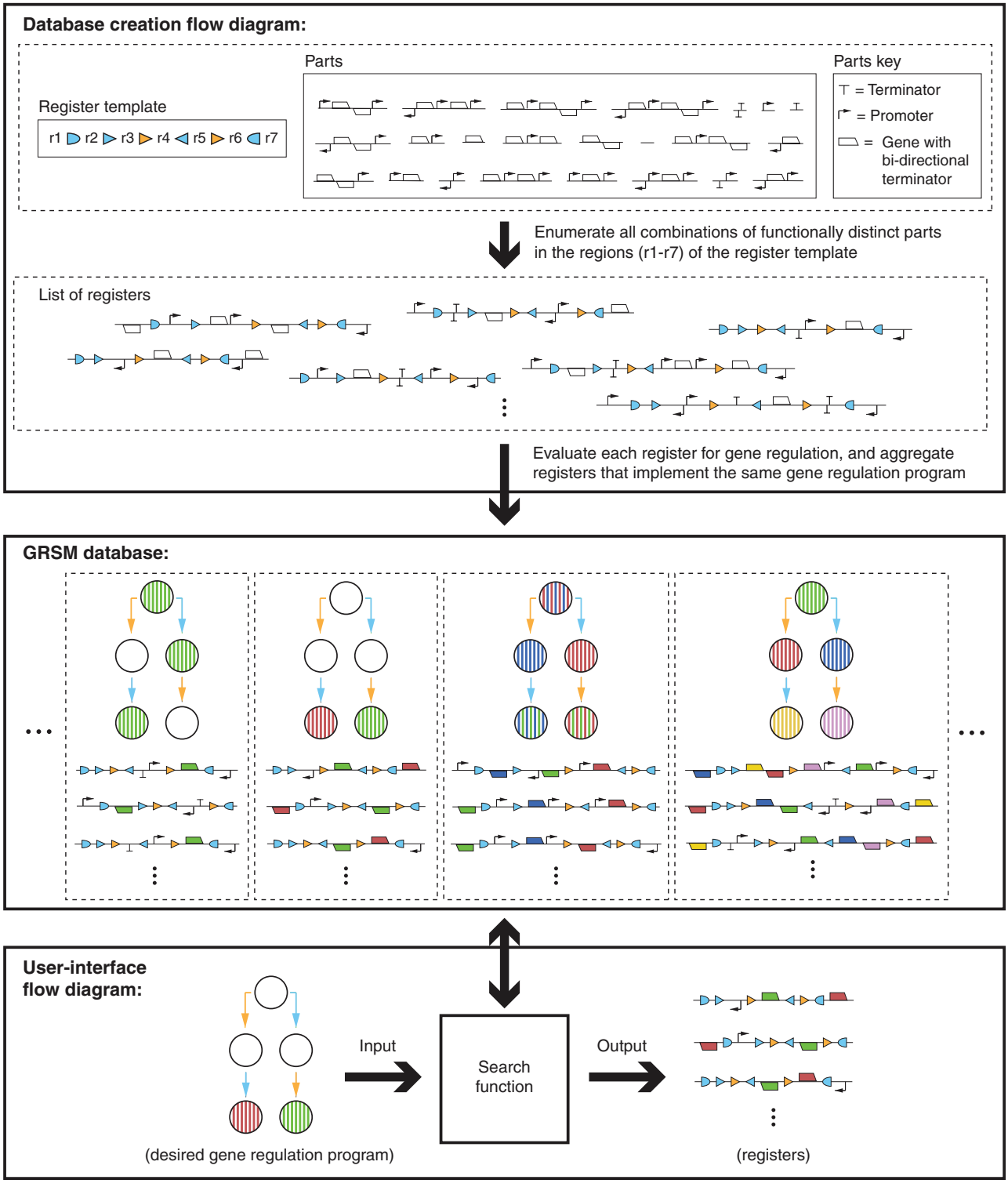

Fig. 5. The GRSM database. (**Top**) Flow diagram depicting how the database was created. (**Middle**) The database has a precompiled list of GRSM registers for distinct gene regulation programs. State diagrams represent gene regulation programs, with each node containing stripes of different colors corresponding to which genes are expressed in that state (no stripes implies no expression of any gene). (**Bottom**) A search function accepts a user-specified gene regulation program and returns registers from the database capable of implementing it.

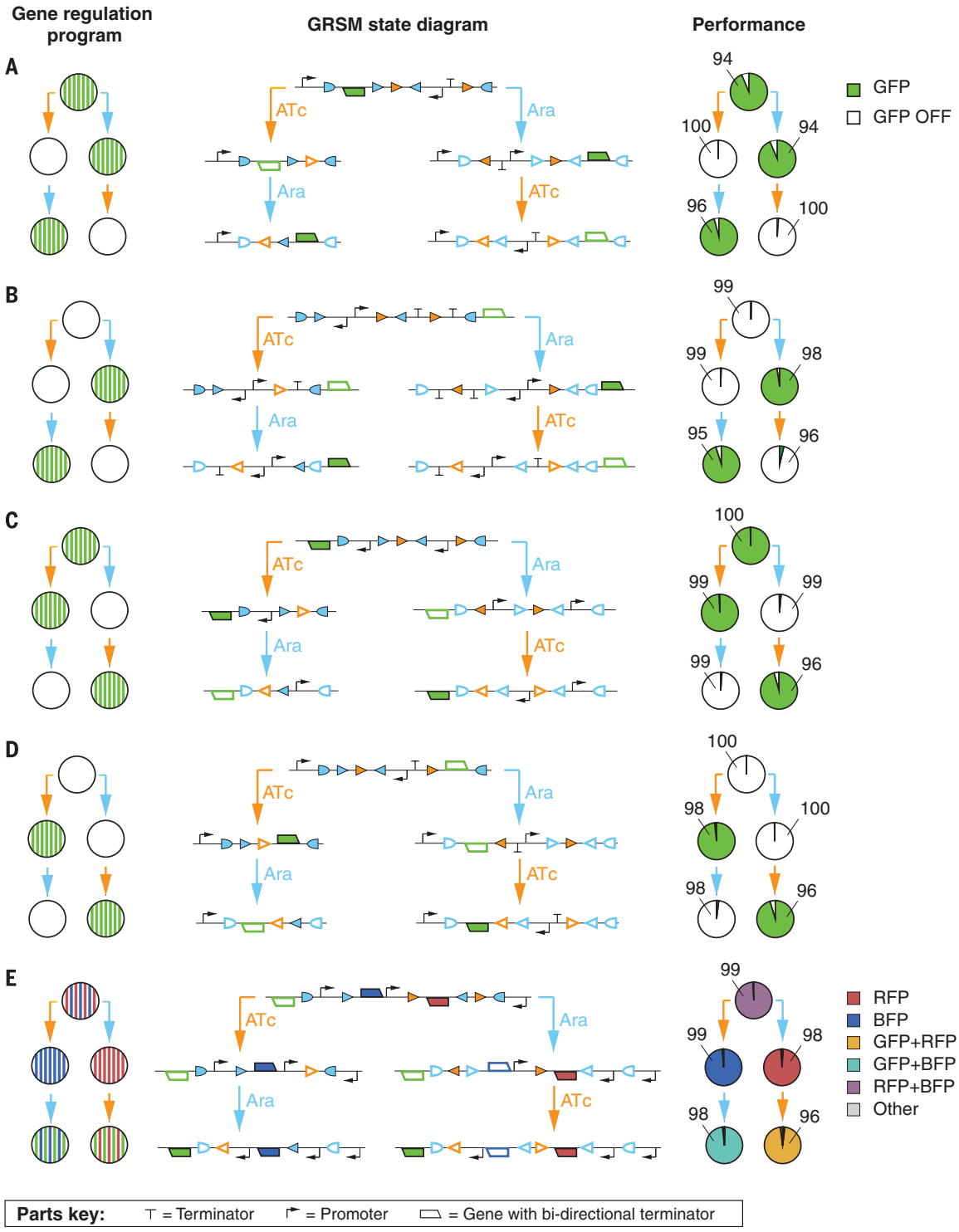

Fig. 6. Implementing two-input, five-state GRSMs. (**A** to **E**) We built GRSMs (one for each panel) in *E. coli* to implement the gene regulation programs depicted at the left, with each node containing stripes of different colors corresponding to which gene products (green, GFP; red, RFP; blue, BFP) are expressed in that state (no stripes implies no expression of any gene). The corresponding GRSM state diagrams are depicted in the middle column, with expressed (ON) fluorescent reporters represented by shaded genes and non-expressed (OFF) fluorescent reporters represented by outlined genes. In the right column, nodes represent populations of cells induced with all permuted substrings of the inputs ATc (orange arrow) and Ara (blue arrow). Cultures were treated with saturating concentrations of each input (ATc, 250 ng/ml; Ara, 1% w/v) at 30°C for 24 hours in three biological replicates. The nodes are shaded according to the percent of cells with different gene expression profiles (ON/OFF combinations of the fluorescent reporters) as measured by flow cytometry. Node labels show the percentage of cells with the expected gene expression profile (averaged over all three biological replicates).

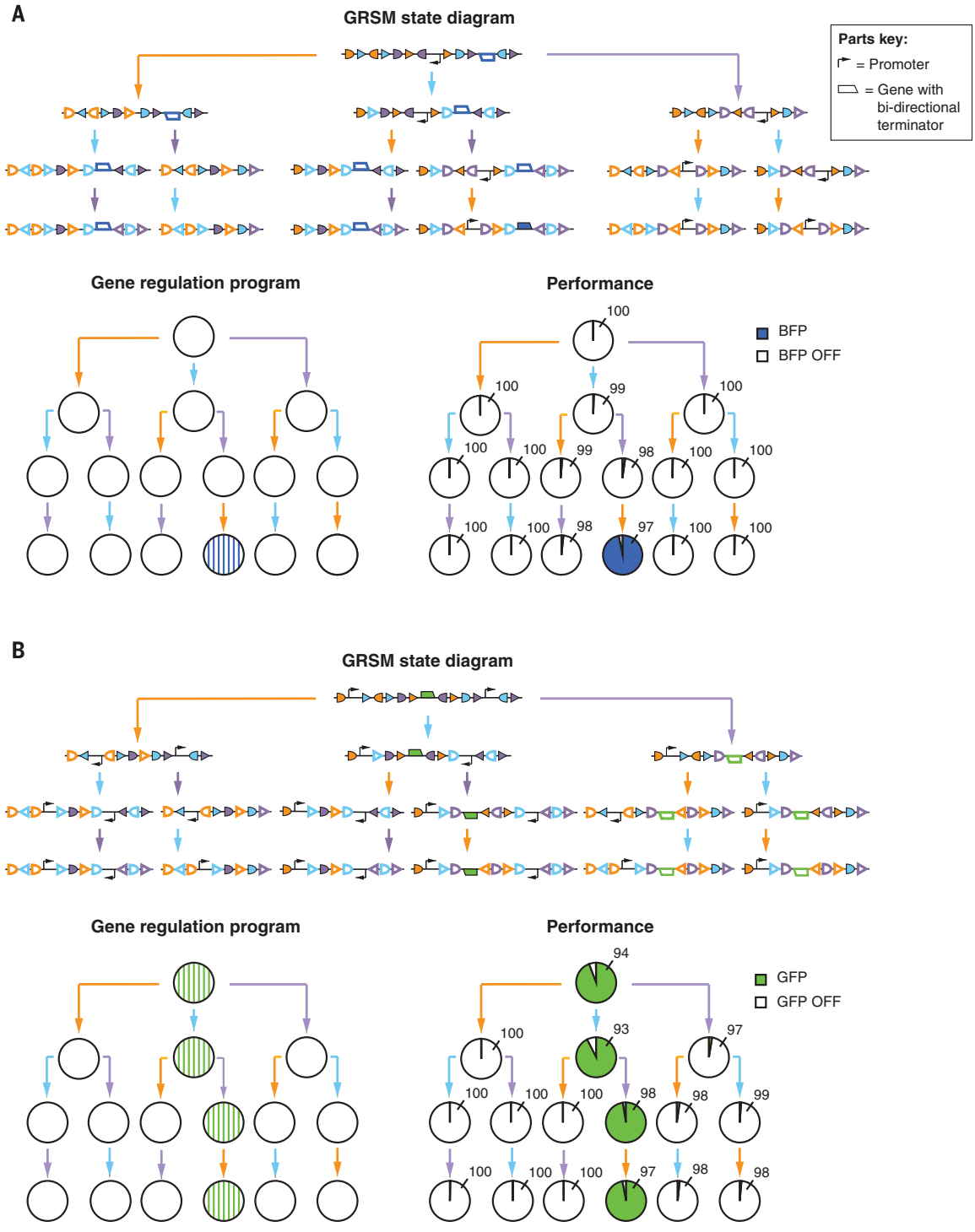

Fig. 7. Implementing three-input, 16-state GRSMs. (**A** and **B**) We built GRSMs in *E. coli* to implement the gene regulation programs depicted at the lower left of each panel, with each node containing stripes of different colors corresponding to which gene products (blue, BFP; green, GFP) are expressed in that state (no stripes implies no expression of any gene). The corresponding GRSM state diagrams are depicted at the top of each panel, with expressed (ON) fluorescent reporters represented by shaded genes and non-expressed (OFF) fluorescent reporters represented by outlined genes. At the lower right of each panel, nodes represent populations of cells induced with all permuted substrings of the inputs ATc (orange arrow), Ara (blue arrow), and DAPG (purple arrow). Cultures were treated with saturating concentrations of each input (ATc, 250 ng/ml; Ara, 1% w/v; DAPG, 25 μM) at 30°C for 24 hours in three biological replicates. The nodes are shaded according to the percentage of cells with or without gene expression as measured by flow cytometry. Node labels show the percentage of cells with the expected gene expression profile (averaged over all three biological replicates).

Because unpredictable behaviors can result when gene regulatory parts are assembled into specific arrangements, certain GRSMs may not implement gene regulation programs as expected. Indeed, this was the case when we initially tested a GRSM that was expected to express green fluorescent protein (GFP) after being exposed to one of two inputs, Ara only or ATc → Ara (fig. S10A) (*32*). Rather than debugging, we constructed two alternative GRSMs using different registers from our database (fig. S10, B and C) that performed better than the initial GRSM, one of which had at least 95% of cells with the expected gene expression profile for each experimental population (fig. S10C). In general, many gene regulation programs represented in our database have multiple possible registers that can implement them (fig. S11). For example, most single-gene regulation programs have at least 373 possible registers, most two-gene regulation programs have at least 55 possible registers, and most three-gene regulation programs have at least 14 possible registers. Even for programs in the database that regulate up to 14 genes, most have at least four possible registers that can implement them. This highly degenerate design space offers a range of GRSM registers that can act as alternatives for one another in the event that a particular register fails to perform to a certain standard. Additional computationally and experimentally derived rules might enable ranking of candidate registers for their likelihood of successful gene regulation function.

To demonstrate the scalability of GRSMs, we built two different three-input, 16-state GRSMs by interleaving genetic parts into the register from Fig. 4A. One GRSM functions as a three-input passcode switch that turns on the expression of a gene (encoding blue fluorescent protein) only when it receives the input Ara → DAPG → ATc (Fig. 7A). The other GRSM expresses a gene (encoding GFP) by default and turns it off if it receives any input that is not along the Ara → DAPG → ATc trajectory (Fig. 7B). Both GRSMs were implemented in *E. coli* and tested with all 16 permuted substrings of the inputs ATc, Ara, and DAPG (*32*). Flow cytometry revealed that at least 93% of cells from each experimental population adopted the expected gene expression profile. Thus, scalable GRSMs that function efficiently can be implemented using our design framework.

Discussion

We created state machines by using recombinases to manipulate DNA registers assembled from overlapping and orthogonal recombinase recognition sites. We used a mathematical framework to analyze the information capacity and scalability of our state machines and understand their limits. For a fixed number of inputs, the information capacity enabled by RSMs is much greater than that of traditional combinational circuits. Furthermore, we created a rich database accessible to the scientific community (database S1 and appendix S1) to enable the automatic design of GRSM registers that implement two-input, five-state gene regulation programs.

We validated our RSM framework by building two-input, five-state and three-input, 16-state RSMs, testing them with Sanger sequencing and qPCR, and applying them to build state-dependent gene regulation programs. Our state machines differ from other strategies for genetic programming, such as combinational Boolean logic gates that are stateless (*33*–*44*), cell counters that do not integrate multiple inputs (*20*), temporal logic circuits that are unable to report on all possible input identities and permutations in a single circuit (*23*), and other multi-input recombinase-based circuits that do not use overlapping recombinase recognition sites and thus cannot perform order-dependent input processing (*21*, *22*).

Although we implemented RSMs in bacteria, we anticipate that our framework will be extensible to other organisms in which recombinases are functional. For example, the large serine recombinases used here (BxbI, TP901, and A118), as well as ϕC31, ϕFC1, ϕRV1, U153, and R4, catalyze recombination in mammalian cells (*45*–*48*). Identification of additional recombinases that function in different organisms should expand the applicability of our framework. The incorporation of reversible recombination events through proteins such as recombination directionality factors could also enable reversible transitions between gene regulatory states (*15*). Depending on desired applications, the prototypical inducible promoters we used here to drive the RSMs could be replaced by sensors that correspond to the desired signals to be recorded. Such sensors need not be based on transcriptional regulation, as long as they can control recombinase activity.

The integration of RSMs into complex systems should enable researchers to investigate temporally distributed events without the need for continual monitoring and/or sampling. For example, by incorporating RSMs into tumor models, scientists may record the identity and order of oncogene activation and tumor suppressor deactivation events in individual cancer cells, and further correlate this information to phenotypic data from transcriptomic analysis or drug assays. In a recent study of myeloproliferative neoplasms containing mutations in both TET2 (a tumor suppressor) and JAK2 (a proto-oncogene), it was discovered that the order in which the mutations occurred played a role in determining disease phenotype, including sensitivity to therapy (*8*). This research underscores the potential impact of order dependencies in other malignancies and the importance of studying them. Cell sorting based on reporter gene expression from GRSMs could be used to separate cells exposed to different identities and orders of gene regulatory perturbations, which could then be further studied to determine functional cellular differences.

Aside from recording and responding to naturally occurring signals, RSMs have potential applications when the signals that control them are applied by a user. For example, RSMs can generate gene expression based not only on simultaneous combinations of inputs, but also on orders of inputs. Thus, they may be useful to bioengineers for programming multiple functions in cell strains for which there are limited numbers of control signals. For example, they could be used to program cell differentiation down many different cell fate paths based on the order and identities of just a few inputs.

Beyond applications in biological research and engineering, our work has also revealed an interesting mathematical structure to recombinase systems. At first glance, the noncommutative behavior of recombinase operations suggests that there might be a superexponential relationship between the number of possible states in a RSM and the number of recombinases it incorporates. Instead, our results show that the number of states is bound exponentially given a finite number of *attB-attP* pairs per recombinase (Box 1 and texts S2 and S3). Many open mathematical problems remain. For example, what is the minimum number of recognition sites on a register needed to implement a particular state machine? Given a gene regulation program of arbitrary scale and complexity, how can we decide whether there exists a corresponding GRSM? We anticipate that solving such problems will be of interest to mathematicians and biologists alike.

Materials and methods

Strains, media, antibiotics, and inducers

All plasmids were implemented and tested in *E. coli* strain DH5αPRO [F-Φ80*lacZ*ΔM15 Δ(*lacZYA-argF*)U169 *deo*R *rec*A1 *end*A1 *hsd*R17(rk$^-$, mk$^+$) *pho*A *sup*E44 *thi*-1 *gyr*A96 *rel*A1 λ$^-$, P_{N25}/tet^R, P_{laciq}/lacI, Sp^r]. All experiments were performed in Azure Hi-Def medium (Teknova, Hollister, CA) supplemented with 0.4% glycerol. For cloning, we used *E. coli* strains DH5αPRO or EPI300 [F-*mcr*A Δ(*mrr-hsd*RMS-*mcr*BC) Φ80lacZM15 Δ*lac*X74 *rec*A1 *end*A1 *ara*D139 Δ(*ara*, *leu*)7697 *gal*U *gal*K λ$^-$ *rps*L (Str^R) *nup*G *trf*A *dhfr*], as indicated below. All cloning was done in Luria-Bertani (LB)–Miller medium (BD Difco) or Azure Hi-Def medium, as indicated below. LB plates were made by mixing LB with agar (1.5% w/v; Apex). For both cloning and experiments, the antibiotics used were chloramphenicol (25 μg/ml) and kanamycin (30 μg/ml). For experiments, the inducers used were ATc (250 ng/ml), Ara (1% w/v), and DAPG (25 μM).

Plasmid construction and cloning

All plasmids were constructed using basic molecular cloning techniques and Gibson assembly (*49*, *50*). Figure S12 shows all plasmids and their relevant parts. Tables S3 and S4 give a list of relevant parts, their sequences, and the sources from which they were derived.

All input plasmids (pNR64 and pNR220) have a kanamycin resistance cassette (*kanR*) and a ColE1 (high copy) origin of replication. The input plasmid pNR64 was adapted from the dual recombinase controller from (*22*) (Addgene #44456). We replaced the chloramphenicol resistance cassette in this dual recombinase controller with *kanR* to make pNR64. To make pNR220, we inserted the PhlF promoter system from (*36*) onto pNR64 to drive the expression of the A118 recombinase, a gift from J. Thomson (USDA-ARS

WRRC, Albany, CA). To control A118 tightly in the absence of any input, we expressed the *phlF* gene (responsible for suppressing transcription from P_{PhlF}) from the strong constitutive proD promoter (*51*). All input plasmids were transformed into chemically competent *E. coli* strain DH5αPRO, and subsequently isolated using the Qiagen QIAprep Spin Miniprep Kit and verified with Sanger sequencing (Quintara Biosciences).

All output plasmids (pNR160, pNR163, pNR164, pNR165, pNR166, pNR186, pNR187, pNR188, pNR291, pNR292, and pNR284) have a chloramphenicol resistance cassette (*camR*) and are built on a bacterial artificial chromosome (BAC) vector backbone to ensure low copy number, as we ideally want ~1 register per cell. The BAC we used is derived from (*52*) and is capable of being induced to a higher copy number with Copy Control (Epicentre) in EPI300 cells. Strings of *attB* and *attP* recognition sites for pNR160 and pNR188 were synthesized from Integrated DNA Technologies and cloned into their respective backbones. For the construction of all GRSM output plasmids (pNR163, pNR164, pNR165, pNR166, pNR186, pNR187, pNR291, pNR292, and pNR284), we interleaved the array of recognition sites on pNR160 (for two-input, five-state) and pNR188 (for three-input, 16-state) with promoters, terminators, and genes using Gibson assembly. In order to prevent unwanted recombination on our plasmids, we avoided reusing identical part sequences on the same plasmid. For promoters, we used proD, BBa_R0051, and BBa_J54200, which have all been previously characterized to have strong expression (*53*). The proD promoter is an insulated promoter, which helps with consistent performance across varying contexts (*51*). We fused the two promoters, BBa_R0051 and BBa_J54200, upstream of 20-nucleotide initial transcribed sequences (ATATAGTGAACAAGGATTAA and ATAGGTTAAAAGCCAGACAT, respectively) characterized in (*54*), and named the concatenated parts proNR3 and proNR4, respectively. We chose terminators for our GRSMs from among the set of validated strong and sequence diverse terminators characterized in (*55*). We often constructed terminators in tandem to increase termination efficiency. Lastly, we used the fluorescent reporter genes *gfpmut3b* (*56*), *mrfp* (*57*), and *mtagbfp* (*58*) to produce outputs. The ribosome binding site (RBS) of each gene was optimized using the Salis Lab RBS calculator (*59*). Upstream of each RBS, we fused a self-cleaving hammerhead ribozyme to prevent the upstream 5′ untranslated transcript region from interfering with translation of the downstream gene (*60*). All output plasmids were transformed into chemically competent *E. coli* strain EPI300 or DH5αPRO, and subsequently isolated using the Qiagen QIAprep Spin Miniprep Kit and verified with Sanger sequencing (Quintara Biosciences).

Like the output plasmids, all plasmids to test the forward (*attB-attP* → *attL-attR*) and reverse (*attL-attR* → *attB-attP*) recombination efficiencies for each recombinase used in this study (see fig. S1) have *camR* and are built on a BAC. The forward reaction test plasmids (pNR230 for BxbI, pNR239 for A118, and pNR276 for TP901) were each constructed with a reverse-oriented *gfpmut3b* (attached to the same RBS and ribozyme as on the output plasmids described above) downstream of a forward-oriented proD promoter, and with anti-aligned *attB* and *attP* sites for the cognate recombinase flanking the gene. Each forward reaction test plasmid was transformed into chemically competent *E. coli* strain DH5αPRO, and subsequently isolated using the Qiagen QIAprep Spin Miniprep Kit and verified with Sanger sequencing (Quintara Biosciences). To generate the reverse reaction test plasmids (pNR279 for BxbI, pNR280 for A118, and pNR287 for TP901), we transformed each forward reaction test plasmid into chemically competent *E. coli* strain DH5αPRO containing the pNR220 input plasmid, induced the cognate recombinase for each test plasmid, and isolated the recombined plasmid from cells using the Qiagen QIAprep Spin Miniprep Kit. Each reverse reaction test plasmid was then transformed into chemically competent *E. coli* strain DH5αPRO, and subsequently isolated again using the Qiagen QIAprep Spin Miniprep Kit and verified with Sanger sequencing (Quintara Biosciences). The second transformation and isolation step for these test plasmids was done to separate them from the pNR220 plasmid, which inevitably was present in the purified DNA solution after the first isolation step.

RSM implementation

All RSMs were implemented with a two-plasmid system (an input plasmid and an output plasmid). Table S5 shows each RSM and the names of the input and output plasmids used to implement them. All two-input RSMs used the pNR64 input plasmid with various output plasmids depending on the desired gene regulation program. All three-input RSMs used the pNR220 input plasmid with various output plasmids depending on the desired gene regulation program.

For the two-input, five-state RSMs, the input plasmid (pNR64) and the output plasmid were simultaneously transformed into chemically competent *E. coli* DH5αPRO cells. Post-transformation, the cells were plated on LB plates with chloramphenicol and kanamycin. Colonies from these plates were used to initiate RSM testing experiments (see below).

For the three-input, 16-state RSMs, we first transformed the input plasmid (pNR220) into chemically competent *E. coli* DH5αPRO cells and plated the transformants onto LB plates with kanamycin. Subsequently, we inoculated a colony in Azure Hi-Def medium (with kanamycin) and grew it overnight at 37°C, then diluted it 1:2000 into fresh medium (same as the overnight) and let it regrow at 37°C to an OD_{600} of 0.2 to 0.5. The cells from this culture were then made chemically competent and transformed with the output plasmid. The purpose for the sequential transformation in this case was to allow time for the *phlF* gene (on the input plasmid) to be expressed at a high enough level to suppress expression of the A118 recombinase from the P_{PhlF} promoter (also on the input plasmid). This was to ensure minimal recombinase levels when the output plasmid was introduced into the system; otherwise the register on the output plasmid could have falsely recorded a chemical induction event prior to its actual occurrence. After transformation of the output plasmid, the cells were plated on an LB plate with chloramphenicol and kanamycin. Colonies from these plates were used to initiate RSM testing experiments (see below).

Experiment for testing the two-input, five-state RSM from Fig. 3A

To test the two-input, five-state RSM for one biological replicate, a colony of *E. coli* cells containing input plasmid pNR64 and output plasmid pNR160 was inoculated into medium with kanamycin and chloramphenicol, grown overnight (~18 hours) at 37°C, and subjected to two rounds of induction followed by a round of outgrowth. For the first round of induction, the overnight culture was diluted 1:250 into medium with no inducer, medium with ATc, and medium with Ara, and grown at 30°C for 18 hours. For the second round of induction, these three cultures were then diluted again 1:250 into fresh medium; the non-induced culture was diluted into medium with no inducer again, the ATc-induced culture was diluted into medium with no inducer and medium with Ara, and the Ara-induced culture was diluted into medium with no inducer and medium with ATc. These cultures were again grown at 30°C for 18 hours. The resulting cultures represented five populations of cells treated with all five permuted substrings of the inputs ATc and Ara. Lastly, for the outgrowth, these cultures were diluted 1:250 into medium with no inducer and grown at 37°C for ~18 hours. The purpose of this final outgrowth was to allow all cell populations to normalize to conditions without inducer, such that detected differences between populations could be attributed to their history of inputs rather than their current environment. This experiment was repeated with a different starting colony for each biological replicate. All cultures were grown in 250 μl of medium (in 96-well plates) shaken at 900 rpm. All media contained chloramphenicol and kanamycin. Final populations from the experiment were analyzed with sequencing assays and qPCR assays (see below).

Sequencing assay for testing the two-input, five-state RSM from Fig. 3A

For the sequencing assay, each of the five experimental populations described above (from each of three biological replicates) were diluted $1:10^6$, plated (100 μl) onto LB plates with chloramphenicol and kanamycin, and grown overnight at 37°C such that each resulting colony represented the clonal population of a single cell from each experimental population. The register region on the output plasmid for around 24 (at least 22) colonies from each plate (experimental population) was amplified with colony PCR and sent for Sanger sequencing (Quintara Biosciences). Chromatograms from the sequencing reactions were aligned to the expected register sequence to determine whether they matched. Results from all three replicates were totaled, and the percent

of cells matching their expected sequence is displayed in Fig. 3B.

qPCR assay for testing the two-input, five-state RSM from Fig. 3A

For the qPCR assay, plasmids from each of the five experimental populations described above (from each of three biological replicates) were isolated with the QIAprep Spin Miniprep Kit and used as template in qPCR reactions. All qPCR reactions were performed on the Roche LightCycler 96 Real-Time System using KAPA SYBR FAST Master Mix and according to Kapa Biosystems' recommended protocol (200 nM each primer, 10 μl of 2× master mix, and no more than 20 ng of template in a 20-μl reaction). Each template was qPCR-amplified with each of three primer pairs (pp1, pp2, and pp3) elucidated by PSIT (described below; see appendix S2 for the program), as well as a normalizing primer pair (ppN) that amplified the backbone of the output plasmid. Figure S13 shows the regions on the register to which the three PSIT primer pairs bind and the register states that they are supposed to amplify. Table S6 gives the primer sequences. Along with the experimental templates, we also ran qPCR reactions of each primer pair with control template made up entirely of output plasmid containing register state S3 (fig. S13) that would get amplified by each primer pair. We isolated this output plasmid from our Ara-treated *E. coli* population and sequence-verified it to make sure that the register state matched S3. We calculated the "fractional amount" of output plasmid amplified by each primer pair (pp1, pp2, or pp3) for each experimental template (t1, t2, t3, t4, or t5) as

$$f_{tx,\,ppy} = 2^{(Cq_{tx,\,ppn} - Cq_{tc,\,ppn}) - (Cq_{tx,\,ppy} - Cq_{tc,\,ppy})}$$

where *tx* is the experimental template of interest (t1, t2, t3, t4, or t5), *ppy* is the primer pair of interest (pp1, pp2, or pp3), *tc* is the control template (output plasmid in S3), *ppn* is the normalizing primer pair (ppN), and *Cq* is the Cq value from the qPCR reaction of the template and primer pair indicated in its subscript.

From these $f_{tx,\,ppy}$ values, we created a qPCR result vector for each experimental template, $\mathbf{f}_{tx}$:

$$\mathbf{f}_{tx} = [f_{tx,\,pp1},\, f_{tx,\,pp2},\, f_{tx,\,pp3}]$$

This result vector was compared to the theoretical result vector that we would get if the template were made up entirely of a register from one particular state in our RSM, $\mathbf{f}_{ts}$:

$$\mathbf{f}_{ts} = [f_{ts,\,pp1},\, f_{ts,\,pp2},\, f_{ts,\,pp3}]$$

where *ts* is the template made entirely of register from one state (S1, S2, S3, S4, or S5). The $f_{ts,\,ppy}$ values are 0 or 1 depending on whether the particular primer pair *ppy* amplifies that state (fig. S13). The similarity of $\mathbf{f}_{tx}$ to $\mathbf{f}_{ts}$ was quantified by Euclidean distance, $D_{tx,\,ts}$:

$$D_{tx,\,ts} = |\mathbf{f}_{tx} - \mathbf{f}_{ts}|$$

$$= \sqrt{(f_{tx,\,pp1} - f_{ts,\,pp1})^2 + (f_{tx,\,pp2} - f_{ts,\,pp2})^2 + (f_{tx,\,pp3} - f_{ts,\,pp3})^2}$$

The Euclidean distances between the qPCR result vectors of each experimentally derived template and the theoretical qPCR result vectors of each state are displayed in a heat map in fig. S4 for each of three biological replicates.

Experiment for testing the three-input, 16-state RSM from Fig. 4A

To test the three-input, 16-state RSM for one biological replicate, a colony of *E. coli* cells containing input plasmid pNR220 and output plasmid pNR188 was inoculated into medium with kanamycin and chloramphenicol, grown overnight (~18 hours) at 37°C, and subjected to three rounds of induction followed by a round of outgrowth. For the first round of induction, the overnight culture was diluted 1:250 into medium with no inducer, medium with ATc, medium with Ara, and medium with DAPG, and grown at 30°C for 24 hours. For the second round of induction, these four cultures were then diluted again 1:250 into fresh media: The noninduced culture was diluted into medium with no inducer; the ATc-induced culture was diluted into medium with no inducer, medium with Ara, and medium with DAPG; the Ara-induced culture was diluted into medium with no inducer, medium with ATc, and medium with DAPG; and the DAPG-induced culture was diluted into medium with no inducer, medium with ATc, and medium with Ara. These cultures were again grown at 30°C for 24 hours. For the third round of induction, each of these 10 cultures were diluted again 1:250 into fresh media: The noninduced → noninduced, ATc → noninduced, Ara → noninduced, and DAPG → noninduced cultures were diluted into medium with no inducer; the ATc → Ara and Ara → ATc cultures were diluted into medium with no inducer and medium with DAPG; the ATc → DAPG and DAPG → ATc cultures were diluted into medium with no inducer and medium with Ara; and the Ara → DAPG and DAPG → Ara cultures were diluted into medium with no inducer and medium with ATc. These cultures were again grown at 30°C for 24 hours. The resulting cultures represented 16 populations of cells treated with all 16 permuted substrings of the inputs ATc, Ara, and DAPG. Lastly, for the outgrowth, these cultures were diluted 1:250 into medium with no inducer and grown at 37°C for 18 hours. This experiment was repeated with a different starting colony for each biological replicate. All cultures were grown in 250 μl of medium (in 96-well plates) shaken at 900 rpm. All media contained chloramphenicol and kanamycin. Final populations from the experiment were analyzed with sequencing assays and qPCR assays (see below).

Sequencing assay for testing the three-input, 16-state RSM from Fig. 4A

For the sequencing assay, each of the 16 experimental populations described above (from each of three biological replicates) were diluted 1:10^6, plated (100 μl) onto LB plates with chloramphenicol and kanamycin, and grown overnight at 37°C such that each resulting colony represented the clonal population of a single cell from each experimental population. The register region on the output plasmid for five or six colonies from each plate (experimental population) was amplified with colony PCR and sent for Sanger sequencing (Quintara Biosciences). Chromatograms from the sequencing reactions were aligned to the expected register sequence to determine whether they matched. Results from all three biological replicates were totaled, and the percent of cells matching their expected sequence is displayed in Fig. 4B.

qPCR assay for testing the three-input, 16-state RSM from Fig. 4A

For the qPCR assay, plasmids from each of the 16 experimental populations described above (from each of three biological replicates) were isolated with the Qiagen QIAprep Spin Miniprep Kit and used as template in qPCR reactions. As with the two-input, five-state RSM testing, all qPCR reactions were performed on the Roche LightCycler 96 Real-Time System using KAPA SYBR FAST Master Mix and according to the Kapa Biosystems recommended protocol (200 nM each primer, 10 μl of 2× master mix, and no more than 20 ng of template in a 20-μl reaction). Each template was qPCR-amplified with each of six primer pairs (pp1, pp2, pp3, pp4, pp5, and pp6) elucidated by PSIT as well as a normalizing primer pair (ppN) that amplified the backbone of the output plasmid. Figure S14 shows the regions on the register to which the six PSIT primer pairs bind and the register states that they are supposed to amplify. Table S7 gives the actual primer sequences. Similar to the two-input, five-state system, we also ran qPCR reactions of each primer pair with control template made up entirely of output plasmid containing a register that would get amplified by each primer pair. Unlike with the two-input, five-state RSM, however, there was no single register state that would get amplified by each primer pair. So we ended up using an output plasmid in state S2 as a control template for pp1, pp4, and pp5 and an output plasmid in state S8 as a control template for pp2, pp3, and pp6 (fig. S14). The plasmid with register state S2 was isolated from our ATc-treated *E. coli* population (and sequence-verified), and the plasmid with register state S8 was isolated from our Ara → DAPG–treated *E. coli* population (and sequence-verified). We proceeded with calculating the fractional amount of plasmid amplified by each primer pair for each experimental template, and then comparing the data for each template to each theoretical state (with Euclidean distance) the same way as we did for the two-input, five-state RSM, except generalized to six primer pairs and 16 states. That is,

$$\mathbf{f}_{tx} = [f_{tx,\,pp1},\, f_{tx,\,pp2},\, \ldots,\, f_{tx,\,pp6}]$$

$$\mathbf{f}_{ts} = [f_{ts,\,pp1},\, f_{ts,\,pp2},\, \ldots,\, f_{ts,\,pp6}]$$

$$D_{tx,\,ts} = |\mathbf{f}_{tx} - \mathbf{f}_{ts}|$$

$$= \sqrt{(f_{tx,\,pp1} - f_{ts,\,pp1})^2 + \ldots + (f_{tx,\,pp6} - f_{ts,\,pp6})^2}$$

The Euclidean distances between the qPCR result vectors of each experimentally derived template

and the theoretical qPCR result vectors of each state are displayed in a heat map in fig. S6 for each of three biological replicates.

Designing the GRSM registers from Fig. 6 and fig. S10

We inputted our desired gene regulation programs into the database search function [coded in MATLAB R2013b (Mathworks, Natick, MA); appendix S1], and received an output list of registers, from which we chose our candidates for implementation. Table S8 shows the MATLAB search function input matrix we used to specify our desired gene regulation programs, as well as the search function output vectors that we chose as our registers to implement the gene regulation programs, as per the instructions on how to use the search function (appendix S1).

Testing the GRSMs from Fig. 6 and fig. S10

The experiments to test the two-input, five-state GRSMs followed the same format as the experiment to test the two-input, five-state RSM from Fig. 3A, except that we used 24-hour inductions instead of 18-hour inductions for the induction rounds, and instead of analyzing the experimental populations with sequencing and qPCR assays, we used a fluorescence assay (see below).

Testing the GRSMs from Fig. 7

The experiments to test the three-input, 16-state GRSMs followed the same format as the experiment to test the three-input, 16-state RSM from Fig. 4A, except that instead of analyzing the experimental populations with sequencing and qPCR assays, we used a fluorescence assay (see below).

Testing the reversibility of BxbI, TP901, and A118 in fig. S1

For each recombinase in our study (BxbI, TP901, and A118), we isolated two plasmids that were recombined versions of each other: one with *attB-attP* and no GFP expression (pNR230 for BxbI, pNR239 for A118, and pNR276 for TP901), and the other with *attL-attR* and GFP expression (pNR279 for BxbI, pNR280 for A118, and pNR287 for TP901). We transformed each of these plasmids into chemically competent *E. coli* DH5αPRO containing the input plasmid pNR220 (prepared as described above). To measure recombination for each transformant, a colony was inoculated into media with kanamycin and chloramphenicol, grown overnight (~18 hours) at 37°C, and subjected to a round of induction followed by a round of outgrowth. For the induction, the overnight culture was diluted 1:250 into medium with no inducer and medium with inducer (ATc for BxbI, Ara for TP901, or DAPG for A118) and grown at 30°C for 16 hours. For the outgrowth, these cultures were diluted 1:250 into medium with no inducer and grown at 37°C for 18 hours. This experiment was repeated with a different starting colony for each of three biological replicates. All cultures were grown in 250 μl of medium (in 96-well plates) shaken at 900 rpm. We measured the percentage of cells from each population expressing GFP, as described below.

RSM time course experiment in fig. S9

For one biological replicate, a colony of *E. coli* DH5αPRO cells containing input plasmid pNR64 and output plasmid pNR291 was inoculated into medium with kanamycin and chloramphenicol, grown overnight (~18 hours) at 37°C, rediluted 1:75 into fresh medium, split into 11 cultures, and grown at 30°C. When cells reached an OD_{600} of 0.1, we rediluted cells from one culture 1:125 into fresh medium and let them outgrow at 37°C. This (uninduced) population would become the 0-hour time point in fig. S9, C to E. All other cultures were subjected to induction prior to outgrowth. Ara was directly added to five of the cultures, and ATc was directly added to the other five and they were allowed to continue growing at 30°C. Each of the five cultures for each input would become induction time points separated by 1-hour steps (for each input); we refer to them as input seed cultures. After 1 hour, we diluted cells from one ATc seed culture 1:125 into fresh medium and let them outgrow at 37°C. This would become the 1-hour time point for ATc in fig. S9C. From the same seed culture, we also diluted cells 1:25 into medium with Ara and let them grow for the equivalent amount of input exposure time (1 hour) at 30°C before diluting 1:125 into fresh medium and letting them outgrow at 37°C. This would become the 1-hour time point for ATc → Ara in fig. S9E. Then, for the same seed culture, we directly added Ara and let the cells grow for the equivalent amount of input exposure time (1 hour) at 30°C before diluting 1:125 into fresh medium and letting them outgrow at 37°C. This would become the 1-hour time point for ATc → Ara in fig. S9D. The same procedure was done for an Ara seed culture after 1 hour, except with ATc as the sequentially added input. This process was subsequently repeated at 2 hours with different ATc and Ara seed cultures, and so on for 3, 4, and 5 hours. The outgrowth for all cell populations continued for 16 hours after the final cells were diluted for outgrowth (10 hours after the initial induction began). This experiment was repeated for three biological replicates. All cultures were grown in 250 μl of medium (in 96-well plates) shaken at 900 rpm. All media contained chloramphenicol and kanamycin. Final populations from the experiment were analyzed with flow cytometry (see below).

Fluorescence assay

For all experiments with a fluorescence assay, we diluted cells 1:125 into phosphate-buffered solution (PBS, Research Products International) and ran them on a BD-FACS LSRFortessa-HTS cell analyzer (BD Biosciences). We measured 30,000 cells for each sample and consistently gated by forward scatter and side scatter for all cells in an experiment. GFP (product of *gfpmut3b*) intensity was measured on the FITC channel (488-nm excitation laser, 530/30 detection filter), RFP (product of *mrfp*) intensity was measured on the PE–Texas Red channel (561-nm excitation laser, 610/20 detection filter), and BFP (product of *mtagbfp*) intensity was measured on the PacBlue channel (405-nm excitation laser, 450/50 detection filter). A fluorescence threshold was applied in each channel to determine the percent of cells with expressed (ON) versus not expressed (OFF) fluorescent proteins. The threshold was based on a negative control (*E. coli* DH5αPRO containing pNR64 and a BAC with no fluorescent reporter genes) population, such that 0.1% of these negative control cells were considered to have ON fluorescent protein expression in each channel (corresponding to a 0.1% false positive rate).

All fluorescence-based experiments had three biological replicates. For the recombinase reversibility experiment (fig. S1) and the RSM time course experiment (fig. S9), the data for all three replicates is shown. For the GRSM experiments (Figs. 6 and 7 and fig. S10), the data from all three replicates are averaged. For these experiments, the largest standard error for the percent of any fluorescent subpopulation was 1.22%.

GRSM database and search function

The GRSM database was constructed (as discussed in the main text) using MATLAB R2013b (Mathworks), partly run on the Odyssey cluster supported by the FAS Division of Science, Research Computing Group at Harvard University.

The database contains three arrays: *registerArray* (an array of GRSM registers), *grpArray* (an array of gene regulation programs), and *register2grp* (an array that maps each register in *registerArray* to its corresponding gene regulation program in *grpArray*, by index).

Each gene regulation program in *grpArray* is represented by a 70-element vector of 0s and 1s. Each contiguous stretch of 14 elements belongs to a state—S1, S2, S3, S4, and S5, respectively—corresponding to the states in Fig. 3A. And within each state, each element (1 to 14) represents a gene (G1 to G14, respectively). For example, given a vector in *grpArray*, element 1 represents G1 in S1, element 15 represents G1 in S2, element 29 represent G1 in S3, element 43 represent G1 in S4, element 57 represents G1 in S5, element 2 represents G2 in S1, element 16 represents G2 in S2, and so on. The binary value of each element indicates whether that gene in that particular state is OFF (0) or ON (1). If the value of any given gene in every state in a gene regulation program is 0, then that gene does not exist in the regulation program.

Each register in *registerArray* is represented by a seven-element vector of numbers 1 through 25. Each element of the vector corresponds to a DNA region (a to g) interleaving the recognition sites of the register shown in Fig. 3A. The value of each element (1 to 25) represents a part, as defined in table S9. Each part is made up of genes, terminators, and constitutive promoters, arranged such that each part is functionally distinct (see text S6). Nonpalindromic parts (as indicated in table S9) can appear inverted on the register, in which case they take on a negative value. For example, part 1 is a gene, which is a nonpalindromic part. If it appears as a "1" on an element of a register vector, then it is facing left to right (5′ to 3′), and if it appears as a "–1" on an element of a register vector, then it is facing right to left (5′ to 3′).

Note that all explicitly depicted terminators in the parts (table S9) are unidirectional; thus, transcription can move through them in the reverse direction. However, the unidirectional terminator in part 3 can be replaced by a bidirectional terminator without changing the function of the part. This is because placing an additional terminator upstream of the promoter in part 3 would only terminate transcription that would subsequently be reinitiated in the same direction. Also, the unidirectional nature of part 7 is not always necessary to the gene regulation program of the underlying register. That is, sometimes part 7 (a unidirectional terminator by itself) can be replaced by part 4 (a bidirectional terminator by itself) without affecting the gene regulation implemented by the underlying register. To make this distinction clear to database users, we parsed all occurrences of part 7 in the *registerArray* and replaced it with a special identifier, part 15, if its unidirectional nature is not important to the gene regulation program of the underlying register. Therefore, all occurrences of part 7 in *registerArray* now represent parts that necessitate "terminator read-through" (transcription through their unidirectional terminators in the reverse direction) for the gene regulation program of the underlying register. Likewise, because convergent (face-to-face) promoters can destructively interfere with each other (*61*), we made a special distinction for parts with promoters that necessitate "promoter read-through" (transcription through their promoters in the reverse direction; table S9). Because part 10 (a promoter by itself), depending on its register context, can sometimes necessitate read-through and sometimes not, we parsed all occurrences of part 10 in *registerArray* and replaced it with a special identifier, part 14, if it does not necessitate read-through for the gene regulation program of the underlying register. Therefore, all occurrences of part 10 in *registerArray* now represent parts that necessitate promoter read-through for the proper gene regulation program of the underlying register.

All parts with genes in *registerArray* also have bidirectional terminators on the 3′ ends of those genes. These terminators are not explicitly depicted in table S9. Although the database has otherwise been reduced to avoid superfluous terminators, promoters, and genes, the implicit terminators on the 3′ ends of genes may sometimes be superfluous. That is, they may not be necessary for the proper gene regulation program of the underlying register.

Lastly, the array *register2grp* has the same number of elements as *registerArray*. It maps each register in *registerArray* to a value that is the index of its corresponding gene regulation program in *grpArray*.

We present the database as a MATLAB MAT-file (database S1), where each array is stored in a MATLAB variable. The search function for this MAT-file database was also created in MATLAB R2013b and requires MATLAB software to run. Code for the MATLAB search function and more information on how it works are included in appendix S1.

PCR-based state interrogation tool (PSIT)

The PSIT algorithm uses an abstract data type—the class *DNARegister*—to represent registers. To determine what sets of primer pairs may be used to uniquely detect an inputted *DNARegister* and all of its recombined states, the algorithm (i) "recombines" the input register, generating *DNARegister* instances for all states that result from any permuted substring of inputs; (ii) generates a list of primer pairs made up of all possible primers that bind to each region between recognition sites and on the terminal ends of the recognition site arrays; (iii) narrows the list to primer pairs that only amplify in any given state when they are on adjacent regions; and (iv) determines all subsets of this final list of primer pairs that can be used to uniquely identify each possible state of the DNA register. This final list of primer pair subsets is then returned as output along with details regarding which primer pairs amplify in which states. For qPCR compatibility purposes, step iii ensures that every amplicon is short and that every primer pair always yields the same amplicon when it amplifies (regardless of state). The PSIT program was implemented in Python 2.7. Code for the PSIT program and more information on how it works are included in appendix S2.

REFERENCES AND NOTES

1. J. E. Hopcroft, J. D. Ullman, *Introduction to Automata Theory, Languages, and Computation* (Addison-Wesley, ed. 1, 1979).
2. S. M. Kaech, W. Cui, Transcriptional control of effector and memory $CD8^+$ T cell differentiation. *Nat. Rev. Immunol.* **12**, 749–761 (2012). doi: 10.1038/nri3307; pmid: 23080391
3. N. Yosef *et al*., Dynamic regulatory network controlling TH17 cell differentiation. *Nature* **496**, 461–468 (2013). doi: 10.1038/nature11981; pmid: 23467089
4. S. Agarwal, K. L. Holton, R. Lanza, Efficient differentiation of functional hepatocytes from human embryonic stem cells. *Stem Cells* **26**, 1117–1127 (2008). doi: 10.1634/stemcells.2007-1102; pmid: 18292207
5. C. E. Murry, G. Keller, Differentiation of embryonic stem cells to clinically relevant populations: Lessons from embryonic development. *Cell* **132**, 661–680 (2008). doi: 10.1016/j.cell.2008.02.008; pmid: 18295582
6. T. Brambrink *et al*., Sequential expression of pluripotency markers during direct reprogramming of mouse somatic cells. *Cell Stem Cell* **2**, 151–159 (2008). doi: 10.1016/j.stem.2008.01.004; pmid: 18371436
7. R. Jaenisch, R. Young, Stem cells, the molecular circuitry of pluripotency and nuclear reprogramming. *Cell* **132**, 567–582 (2008). doi: 10.1016/j.cell.2008.01.015; pmid: 18295576
8. C. A. Ortmann *et al*., Effect of mutation order on myeloproliferative neoplasms. *N. Engl. J. Med.* **372**, 601–612 (2015). doi: 10.1056/NEJMoa1412098; pmid: 25671252
9. E. Fokas, W. G. McKenna, R. J. Muschel, The impact of tumor microenvironment on cancer treatment and its modulation by direct and indirect antivascular strategies. *Cancer Metastasis Rev.* **31**, 823–842 (2012). doi: 10.1007/s10555-012-9394-4; pmid: 22825313
10. A. N. Hata *et al*., Tumor cells can follow distinct evolutionary paths to become resistant to epidermal growth factor receptor inhibition. *Nat. Med.* **22**, 262–269 (2016). doi: 10.1038/nm.4040; pmid: 26828195
11. J. Shah, P. T. Desai, D. Chen, J. R. Stevens, B. C. Weimer, Preadaptation to cold stress in *Salmonella enterica* serovar Typhimurium increases survival during subsequent acid stress exposure. *Appl. Environ. Microbiol.* **79**, 7281–7289 (2013). doi: 10.1128/AEM.02621-13; pmid: 24056458
12. R. Roemhild, C. Barbosa, R. E. Beardmore, G. Jansen, H. Schulenburg, Temporal variation in antibiotic environments slows down resistance evolution in pathogenic *Pseudomonas aeruginosa*. *Evol. Appl.* **8**, 945–955 (2015). doi: 10.1111/eva.12330; pmid: 26640520
13. Y. Benenson, Biomolecular computing systems: Principles, progress and potential. *Nat. Rev. Genet.* **13**, 455–468 (2012). doi: 10.1038/nrg3197; pmid: 22688678
14. K. Oishi, E. Klavins, Framework for engineering finite state machines in gene regulatory networks. *ACS Synth. Biol.* **3**, 652–665 (2014). doi: 10.1021/sb4001799; pmid: 24932713
15. J. Bonnet, P. Subsoontorn, D. Endy, Rewritable digital data storage in live cells via engineered control of recombination directionality. *Proc. Natl. Acad. Sci. U.S.A.* **109**, 8884–8889 (2012). doi: 10.1073/pnas.1202344109; pmid: 22615351
16. T. S. Ham, S. K. Lee, J. D. Keasling, A. P. Arkin, Design and construction of a double inversion recombination switch for heritable sequential genetic memory. *PLOS ONE* **3**, e2815 (2008). doi: 10.1371/journal.pone.0002815; pmid: 18665232
17. T. S. Ham, S. K. Lee, J. D. Keasling, A. P. Arkin, A tightly regulated inducible expression system utilizing the fim inversion recombination switch. *Biotechnol. Bioeng.* **94**, 1–4 (2006). doi: 10.1002/bit.20916; pmid: 16534780
18. L. Yang *et al*., Permanent genetic memory with >1-byte capacity. *Nat. Methods* **11**, 1261–1266 (2014). doi: 10.1038/nmeth.3147; pmid: 25344638
19. L. Prochazka, B. Angelici, B. Haefliger, Y. Benenson, Highly modular bow-tie gene circuits with programmable dynamic behaviour. *Nat. Commun.* **5**, 4729 (2014). doi: 10.1038/ncomms5729; pmid: 25311543
20. A. E. Friedland *et al*., Synthetic gene networks that count. *Science* **324**, 1199–1202 (2009). doi: 10.1126/science.1172005; pmid: 19478183
21. P. Siuti, J. Yazbek, T. K. Lu, Synthetic circuits integrating logic and memory in living cells. *Nat. Biotechnol.* **31**, 448–452 (2013). doi: 10.1038/nbt.2510; pmid: 23396014
22. J. Bonnet, P. Yin, M. E. Ortiz, P. Subsoontorn, D. Endy, Amplifying genetic logic gates. *Science* **340**, 599–603 (2013). pmid: 23539178
23. V. Hsiao, Y. Hori, P. W. K. Rothemund, R. M. Murray, A population-based temporal logic gate for timing and recording chemical events. *Mol. Syst. Biol.* **12**, 869 (2016). doi: 10.15252/msb.20156663; pmid: 23539178
24. N. D. F. Grindley, K. L. Whiteson, P. A. Rice, Mechanisms of site-specific recombination. *Annu. Rev. Biochem.* **75**, 567–605 (2006). doi: 10.1146/annurev.biochem.73.011303.073908; pmid: 16756503
25. W. R. A. Brown, N. C. O. Lee, Z. Xu, M. C. M. Smith, Serine recombinases as tools for genome engineering. *Methods* **53**, 372–379 (2011). doi: 10.1016/j.ymeth.2010.12.031; pmid: 21195181
26. H. M. Thorpe, M. C. Smith, *In vitro* site-specific integration of bacteriophage DNA catalyzed by a recombinase of the resolvase/invertase family. *Proc. Natl. Acad. Sci. U.S.A.* **95**, 5505–5510 (1998). doi: 10.1073/pnas.95.10.5505; pmid: 9576912
27. P. Ghosh, N. R. Pannunzio, G. F. Hatfull, Synapsis in phage Bxb1 integration: Selection mechanism for the correct pair of recombination sites. *J. Mol. Biol.* **349**, 331–348 (2005). doi: 10.1016/j.jmb.2005.03.043; pmid: 15890199
28. P. A. Rowley, M. C. A. Smith, E. Younger, M. C. M. Smith, A motif in the C-terminal domain of ϕC31 integrase controls the directionality of recombination. *Nucleic Acids Res.* **36**, 3879–3891 (2008). doi: 10.1093/nar/gkn269; pmid: 18502775
29. M. C. A. Smith, R. Till, M. C. M. Smith, Switching the polarity of a bacteriophage integration system. *Mol. Microbiol.* **51**, 1719–1728 (2004). doi: 10.1111/j.1365-2958.2003.03942.x; pmid: 15009897
30. P. Ghosh, L. A. Bibb, G. F. Hatfull, Two-step site selection for serine-integrase-mediated excision: DNA-directed integrase conformation and central dinucleotide proofreading. *Proc. Natl. Acad. Sci. U.S.A.* **105**, 3238–3243 (2008). doi: 10.1073/pnas.0711649105; pmid: 18299577
31. S. D. Colloms *et al*., Rapid metabolic pathway assembly and modification using serine integrase site-specific recombination. *Nucleic Acids Res.* **42**, e23 (2014). doi: 10.1093/nar/gkt1101; pmid: 24225316
32. See the Materials and Methods section.
33. B. Wang, R. I. Kitney, N. Joly, M. Buck, Engineering modular and orthogonal genetic logic gates for robust digital-like synthetic biology. *Nat. Commun.* **2**, 508 (2011). doi: 10.1038/ncomms1516; pmid: 22009040
34. R. Gaber *et al*., Designable DNA-binding domains enable construction of logic circuits in mammalian cells. *Nat. Chem. Biol.* **10**, 203–208 (2014). doi: 10.1038/nchembio.1433; pmid: 24413461

35. J. J. Lohmueller, T. Z. Armel, P. A. Silver, A tunable zinc finger-based framework for Boolean logic computation in mammalian cells. *Nucleic Acids Res.* **40**, 5180–5187 (2012). doi: 10.1093/nar/gks142; pmid: 22323524
36. A. A. Nielsen, C. A. Voigt, Multi-input CRISPR/Cas genetic circuits that interface host regulatory networks. *Mol. Syst. Biol.* **10**, 763 (2014). doi: 10.15252/msb.20145735; pmid: 25422271
37. S. Regot *et al*., Distributed biological computation with multicellular engineered networks. *Nature* **469**, 207–211 (2011). doi: 10.1038/nature09679; pmid: 21150900
38. T. S. Moon, C. Lou, A. Tamsir, B. C. Stanton, C. A. Voigt, Genetic programs constructed from layered logic gates in single cells. *Nature* **491**, 249–253 (2012). doi: 10.1038/nature11516; pmid: 23041931
39. A. Tamsir, J. J. Tabor, C. A. Voigt, Robust multicellular computing using genetically encoded NOR gates and chemical 'wires'. *Nature* **469**, 212–215 (2011). doi: 10.1038/nature09565; pmid: 21150903
40. M. N. Win, C. D. Smolke, Higher-order cellular information processing with synthetic RNA devices. *Science* **322**, 456–460 (2008). doi: 10.1126/science.1160311; pmid: 18927397
41. W. S. Teo, M. W. Chang, Development and characterization of AND-gate dynamic controllers with a modular synthetic GAL1 core promoter in *Saccharomyces cerevisiae*. *Biotechnol. Bioeng.* **111**, 144–151 (2014). doi: 10.1002/bit.25001; pmid: 23860786
42. S. Ausländer, D. Ausländer, M. Müller, M. Wieland, M. Fussenegger, Programmable single-cell mammalian biocomputers. *Nature* **487**, 123–127 (2012).pmid: 22722847
43. J. M. Callura, D. J. Dwyer, F. J. Isaacs, C. R. Cantor, J. J. Collins, Tracking, tuning, and terminating microbial physiology using synthetic riboregulators. *Proc. Natl. Acad. Sci. U.S.A.* **107**, 15898–15903 (2010). doi: 10.1073/pnas.1009747107; pmid: 20713708
44. J. Hasty, D. McMillen, J. J. Collins, Engineered gene circuits. *Nature* **420**, 224–230 (2002). doi: 10.1038/nature01257; pmid: 12432407
45. A. C. Groth, E. C. Olivares, B. Thyagarajan, M. P. Calos, A phage integrase directs efficient site-specific integration in human cells. *Proc. Natl. Acad. Sci. U.S.A.* **97**, 5995–6000 (2000). doi: 10.1073/pnas.090527097; pmid: 10801973
46. E. C. Olivares, R. P. Hollis, M. P. Calos, Phage R4 integrase mediates site-specific integration in human cells. *Gene* **278**, 167–176 (2001). doi: 10.1016/S0378-1119(01)00711-9; pmid: 11707334
47. S. M. Stoll, D. S. Ginsburg, M. P. Calos, Phage TP901-1 site-specific integrase functions in human cells. *J. Bacteriol.* **184**, 3657–3663 (2002). doi: 10.1128/JB.184.13.3657-3663.2002; pmid: 12057961
48. A. Keravala *et al*., A diversity of serine phage integrases mediate site-specific recombination in mammalian cells. *Mol. Genet. Genomics* **276**, 135–146 (2006). doi: 10.1007/s00438-006-0129-5; pmid: 16699779
49. J. Sambrook, E. Fritsch, T. Maniatis, *Molecular Cloning: A Labratory Manual* (Cold Spring Harbor Laboratory Press, ed. 2, 1989).
50. D. G. Gibson *et al*., Enzymatic assembly of DNA molecules up to several hundred kilobases. *Nat. Methods* **6**, 343–345 (2009). doi: 10.1038/nmeth.1318; pmid: 19363495
51. J. H. Davis, A. J. Rubin, R. T. Sauer, Design, construction and characterization of a set of insulated bacterial promoters. *Nucleic Acids Res.* **39**, 1131–1141 (2011). doi: 10.1093/nar/gkq810; pmid: 20843779
52. J. Wild, Z. Hradecna, W. Szybalski, Conditionally amplifiable BACs: Switching from single-copy to high-copy vectors and genomic clones. *Genome Res.* **12**, 1434–1444 (2002). doi: 10.1101/gr.130502; pmid: 12213781
53. iGem Registry of Standard Biological Parts (parts.igem.org).
54. L. M. Hsu *et al*., Initial transcribed sequence mutations specifically affect promoter escape properties. *Biochemistry* **45**, 8841–8854 (2006). doi: 10.1021/bi060247u; pmid: 16846227
55. Y. J. Chen *et al*., Characterization of 582 natural and synthetic terminators and quantification of their design constraints. *Nat. Methods* **10**, 659–664 (2013). doi: 10.1038/nmeth.2515; pmid: 23727987
56. B. P. Cormack, R. H. Valdivia, S. Falkow, FACS-optimized mutants of the green fluorescent protein (GFP). *Gene* **173**, 33–38 (1996). doi: 10.1016/0378-1119(95)00685-0; pmid: 8707053
57. R. E. Campbell *et al*., A monomeric red fluorescent protein. *Proc. Natl. Acad. Sci. U.S.A.* **99**, 7877–7882 (2002). doi: 10.1073/pnas.082243699; pmid: 12060735
58. O. M. Subach *et al*., Conversion of red fluorescent protein into a bright blue probe. *Chem. Biol.* **15**, 1116–1124 (2008). doi: 10.1016/j.chembiol.2008.08.006; pmid: 18940671
59. H. M. Salis, E. A. Mirsky, C. A. Voigt, Automated design of synthetic ribosome binding sites to control protein expression. *Nat. Biotechnol.* **27**, 946–950 (2009). doi: 10.1038/nbt.1568; pmid: 19801975
60. C. Lou, B. Stanton, Y. J. Chen, B. Munsky, C. A. Voigt, Ribozyme-based insulator parts buffer synthetic circuits from genetic context. *Nat. Biotechnol.* **30**, 1137–1142 (2012). doi: 10.1038/nbt.2401; pmid: 23034349
61. B. P. Callen, K. E. Shearwin, J. B. Egan, Transcriptional interference between convergent promoters caused by elongation over the promoter. *Mol. Cell* **14**, 647–656 (2004). doi: 10.1016/j.molcel.2004.05.010; pmid: 15175159

ACKNOWLEDGMENTS

The dual recombinase controller was a gift from D. Endy (Addgene plasmid #44456) and is available at Addgene under a material transfer agreement. All plasmids created in this project are also available on Addgene. We thank J. Thomson (USDA-ARS WRRC, Albany, CA) for the *a118* gene, A. A. K. Nielsen and C. A. Voigt for the *phlF* gene, J. Shin and C. A. Voigt for hammerhead ribozyme parts, C. J. McClune and C. A. Voigt for helpful discussions on recombinase systems, and the FAS Division of Science, Research Computing Group, at Harvard University for supporting computations involved in the creation of the GRSM database on the Odyssey cluster. A MAT file containing the GRSM database is provided in database S1. Supported by the Ford Foundation Predoctoral Fellowships Program and Molecular Biophysics Training Grant NIH/NIGMS T32 GM008313 (N.R.); the NSF Alan T. Waterman Award, grant 1249349 (S.A.); the Center for Microbiome Informatics and Therapeutics; and NIH grants DP2 OD008435 and P50 GM098792, Office of Naval Research grants N00014-13-1-0424 and N0001411110725, NSF grant MCB-1350625, and an NSF Expeditions in Computing Program Award (1522074) as part of the Living Computing Project. The project or effort depicted was or is also sponsored by the Defense Advanced Research Projects Agency (HR0011-15-C-0091). The content of the information does not necessarily reflect the position or the policy of the U.S. government. T.K.L. and N.R. have filed a patent application based on this work with the US Patent and Trademark Office. Author contributions: N.R. and T.K.L. conceived the work; N.R., A.P.S., and A.C.F. performed the cloning and experiments; N.R. performed data analysis and developed the GRSM database and search function; A.P.S. developed the PSIT program; S.A. provided the mathematical analysis; and all authors reviewed the paper.

SUPPLEMENTARY MATERIALS

www.sciencemag.org/content/353/6297/aad8559/suppl/DC1
Texts S1 to S8
Figs. S1 to S14
Tables S1 to S10
Database S1
Appendices S1 and S2
Reference (*62*)

13 November 2015; accepted 2 June 2016
10.1126/science.aad8559

REPORTS

COMPOSITES

Layered and scrolled nanocomposites with aligned semi-infinite graphene inclusions at the platelet limit

Pingwei Liu,[1] Zhong Jin,[1,2] Georgios Katsukis,[1] Lee William Drahushuk,[1] Steven Shimizu,[1] Chih-Jen Shih,[1] Eric D. Wetzel,[3] Joshua K. Taggart-Scarff,[3] Bo Qing,[4] Krystyn J. Van Vliet,[4,5] Richard Li,[6] Brian L. Wardle,[6] Michael S. Strano[1]*

Two-dimensional (2D) materials can uniquely span the physical dimensions of a surrounding composite matrix in the limit of maximum reinforcement. However, the alignment and assembly of continuous 2D components at high volume fraction remain challenging. We use a stacking and folding method to generate aligned graphene/polycarbonate composites with as many as 320 parallel layers spanning 0.032 to 0.11 millimeters in thickness that significantly increases the effective elastic modulus and strength at exceptionally low volume fractions of only 0.082%. An analogous transverse shear scrolling method generates Archimedean spiral fibers that demonstrate exotic, telescoping elongation at break of 110%, or 30 times greater than Kevlar. Both composites retain anisotropic electrical conduction along the graphene planar axis and transparency. These composites promise substantial mechanical reinforcement, electrical, and optical properties at highly reduced volume fraction.

The concept of nanocomposites is motivated by the observation that filler particles can stiffen and strengthen otherwise softer materials such as polymers to form lightweight, sturdy composites. Eshelby (*1*) first demonstrated this possibility mathematically for ellipsoidal "inclusions" in a solid. In practice, however, it has proven exceedingly difficult to insert closely spaced but distinctly separated nanoparticles within a material, a fundamental requirement for strengthening it. For anisotropic nanoparticles, such as platelets, nanofibers, or nanotubes (*2*, *3*), mechanical reinforcement can occur at very low volume fractions of the added filler, because the particles can align along preferential axes of strain (*4*–*6*). For a platelet filler such as graphene or other two-dimensional (2D) materials, however, a unique limit can be realized as the aspect ratio, a, of the aligned plates approaches infinity. A closely spaced stack of aligned, semi-infinite plates of nanometer or atomic thickness approaches a limit of maximal mechanical reinforcement at minimal platelet addition per mass of material. It has only recently become possible to test this $a \rightarrow \infty$ limit with the development of chemical vapor deposition (CVD) methods of creating single-unit cell- or atom-thickness films, such as graphene (*7*, *8*) and other 2D materials (*9*) that can span the physical dimensions of a composite large enough for testing. In this work, we introduce two fabrication methods that can take a thin layer of molecular thickness and construct large composite stacks that scale exponentially with the number of processing steps. An analogous shear scrolling method creates Archimedean scroll fibers from single layers with similar scaling. The methods produce materials that demonstrate the $a \rightarrow \infty$ limit while combining electrical and optical properties at minimal volume fraction of the filler.

The planar stacking method generates a thickness that exponentially scales with each successive quadrant fold or segmentation, j, as 4^j. Further hot-pressing promotes the interlayer integration (Fig. 1A). Replicating the process j times generates a nanocomposite of $i \times 4^j$ layers and a lateral dimension of $W/4^j$, where i is the initial stacking or number of layers and W is the initial width of the i-layer composite (Figs. 1, B to D). We use polycarbonate (PC) as the polymer matrix due to its transparency and mechanical strength, creating bulk composites from CVD monolayer, polycrystalline graphene (*10*) (Fig. 2A) with layer numbers of 8 to 320 and volume fractions (V_Gs) of 0.003 to 0.185% (figs. S1 and S2 and table S1). The graphene layers appear intact upon this processing because the size of the translucent area containing graphene exhibits little change after each pressing step. Raman spectroscopy (Fig. 2, B and C, and fig. S3) confirms that the absolute intensity of the graphene 2D peak (I_{2D}) decreases with increasing layer number, approximately following the Lambert-Beer law (fig. S3C and supplementary text 1).

$$-\lg\left(I_{2D}/n\right) = kn + c \quad (1)$$

The equation is verified by well-fit least-squares regression of these data for graphene/polycarbonate (G/PC) composites of $V_G \approx 0.030\%$ and of $V_G \approx 0.009\%$, each ranging from 1 to 144 layers (Fig. 2C). The differences between the two fitted curves are very small due to the very low extinction coefficient (≈ 0) of the highly transparent PC layer. The composites have high optical transmittance of 90% at 9 layers and 58% at 36 layers, following the Lambert-Beer law (fig. S4), corresponding to a transmittance of 98% per layer, in agreement with the known visible light transmittance of monolayer graphene (*11*). We also found an alternate route to stacked, planar composites by monomer impregnation and in situ polymerization within expanded graphite derived from the thermal treatment of iodine chloride–intercalated highly ordered pyrolytic graphite (*12*), achieving up to $V_G \approx 0.60\%$ (fig. S5). However, the quality and control of layer spacing for the resulting composite was found to be lower than the 4^j method (fig. S5E).

We also use an analogous stacking procedure to create Archimedean spiral fibers (Fig. 1, E to I, and figs. S6 to S8). A transverse shear force scrolls a single G/PC film (2.0 × 2.2 cm) into a fiber (Fig. 1E) of diameter 105 ± 2 μm (fiber 1) measured optically (figs. S6 and S7) and 160 ± 4 μm (fiber 2) (Fig. 1F and figs. S6 and S8). The layer spacing of 180 and 410 nm, respectively, induces an observable multilayer thin-film interference in Fig. 1F (and fig. S6, B and C), respectively. The fiber axial cross section has a deformed spiral structure (Fig. 1, G to I, and fig. S9). Both methods can control the resulting V_G over three orders of magnitude from 0.003 to 2.55% (table S1).

Despite having vanishingly small V_Gs, such aligned composites demonstrate substantial increases in both the uniaxial tensile storage moduli (E') and loss moduli (E'') from dynamic mechanical analysis (DMA) (Fig. 3, A and B). Two 4^j planar samples with $V_G \approx 0.082$ and 0.185%, respectively, both at 40 layers, have significantly higher E' than pure PC controls (Fig. 3A), with E'/E'_{PC} = 2.36/2.04 (GPa/GPa) and 2.70/2.04 at 30°C, for example, or an increased stiffness ΔE up to 0.66 GPa or 30%. We estimate the effective elastic modulus of the component graphene layers as 360 GPa with the rule of mixtures, agreeing with reported values of 210 to 510 GPa for CVDGs with ripples (*13*, *14*). Uniaxial tension (fig. S10) and microindentation results (fig. S11) demonstrate similar elastic modulus increase with a linear dependence on V_G. For comparison, a minimum of $2\% < V_G < 5\%$, 10 times more than 4^j composites, is required to achieve comparable stiffness of PC nanocomposites in the limit of 3D random orientation for graphene oxide (GO) or derivatives with typical aspect ratios a = 20 to 50 (*15*–*18*) (Fig. 3C). Nanoplatelets with smaller a values contribute less to reinforcement (fig. S12); GOx (or derivatives)

[1]Department of Chemical Engineering, Massachusetts Institute of Technology, Cambridge, MA 02139, USA. [2]Key Laboratory of Mesoscopic Chemistry of MOE and Collaborative Innovation Center of Chemistry for Life Sciences, School of Chemistry and Chemical Engineering, Nanjing University, Nanjing, Jiangsu 210093, China. [3]U.S. Army Research Laboratory, Aberdeen Proving Ground, MD 21005-5069, USA. [4]Department of Biological Engineering, Massachusetts Institute of Technology, Cambridge, MA 02139, USA. [5]Department of Materials Science and Engineering, Massachusetts Institute of Technology, Cambridge, MA 02139, USA. [6]Department of Aeronautics and Astronautics, Massachusetts Institute of Technology, Cambridge, MA 02139, USA.
*Corresponding author. Email: strano@mit.edu

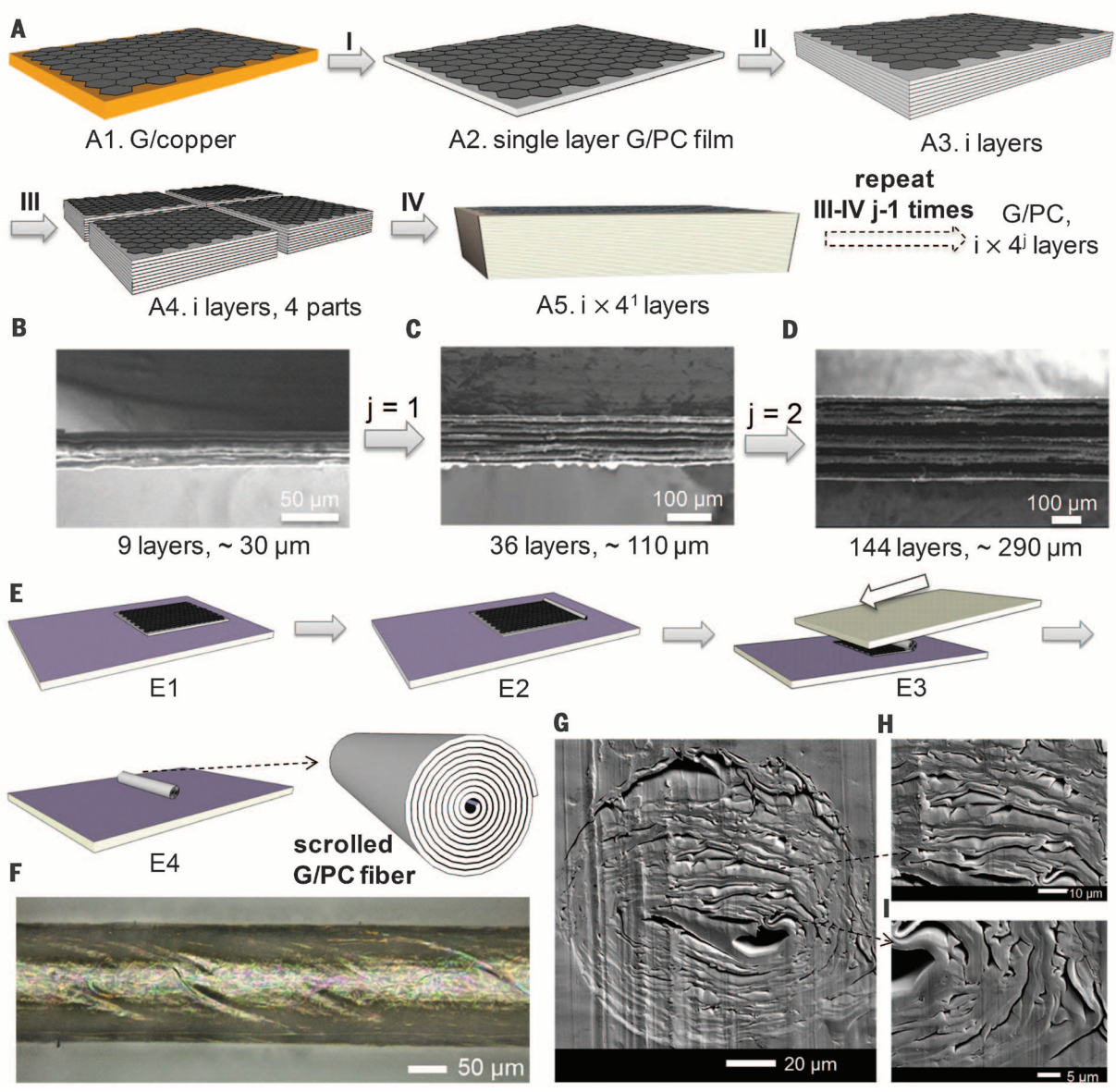

Fig. 1. Fabrication of G/PC composites with aligned, semi-infinite CVD graphene. (**A**) A 4^j stacking method for planar 4^j composites: (I) spin-coating of PC solution and etching out copper, (II) stacking *i* layers of G/PC films, (III) cutting/folding, and (IV) stacking and hot-pressing at 37 MPa and 155°C. (**B** to **D**) SEM images of the planar composites with i = 9 (3570 nm/layer, $V_G \approx 0.009\%$), j = 1, and j = 2, respectively. (**E**) The transverse shear method for scrolled nanocomposite fiber. (E1) A single layer of G/PC film supported on Si/SiO_2 substrate. (E2) The supported film with folds at one end created by a glass capillary. (E3) The scrolling of the film by the transverse shear force exerted by the two Si/SiO_2 wafers. (E4) A scrolled fiber with Archimedean spiral pattern in the cross-section plane. (**F**) Optical microscope image of fiber 2 with diameter (d) = 160 ± 4 μm. (**G** to **I**) SEM images of fiber 2 with d = 131 ± 3 μm in the cross-section plane. Scale bars are 20, 10, and 5 μm, respectively.

with multilayer structures generally have poor interlayer bonding (*19*, *20*), which further minimizes the reinforcement. The atomic thinness of monolayer CVDG and its near-infinite a maximize this reinforcement (Fig. 3C).

We also verified that the PC matrix of our composite is not itself stiffening, evidenced by the reduction of the glass transition temperature (T_g) from 151.3° to 141.8°C at higher V_Gs (fig. S13) and no detectable increase in crystallinity of the PC (Fig. 3A). The reinforcement then comes from the direct load transfer to graphene filler itself (*21*), distinguishing it from cases where the inclusion (e.g., GO) stiffens the polymer matrix and increases T_g by restricting polymer-chain mobility near the polymer-inclusion interface (*19*, *22*) (fig. S14 and supplementary text 5). To date, we have demonstrated composites with V_G as high as 0.185%, but the 4^j and shear scrolling methods allow one to reach as high as 2.5% (table S1), translating to ΔE (or $\Delta E'$) = 9.0 to 20.6 GPa (Fig. 3C). Planar 4^j samples at $V_G \approx 0.185\%$ also show higher E'' peak values (0.50 GPa) compared with those at $V_G \approx$ 0.082% (0.40 GPa) and the PC control (0.26 GPa) (Fig. 3A). These samples possess an enhanced energy dissipation mechanism from in-plane translation and frictional sliding at the layer interfaces (fig. S10A) (*23*). Both E' and E'' increase with V_G, promising materials of stiffness and damping exceeding that of the matrix polymer at negligible increases in weight (*24*).

The spiral fibers also demonstrate interesting mechanical properties. Two Archimedean scroll fibers—fiber 1 ($V_G \approx 0.185\%$) and fiber 2 (0.082%)—exhibit higher E' of 2.07 and 1.62 GPa, respectively, compared with PC controls at 1.14 GPa over 30° to 150°C (Fig. 3B). However, the stiffness of these scroll fiber composites was generally lower than that of the planar 4^j composites. The scrolled structures of the fibers demonstrate a telescoping compliance mechanism (Fig. 3D, I) that involves internal axial rotation in addition

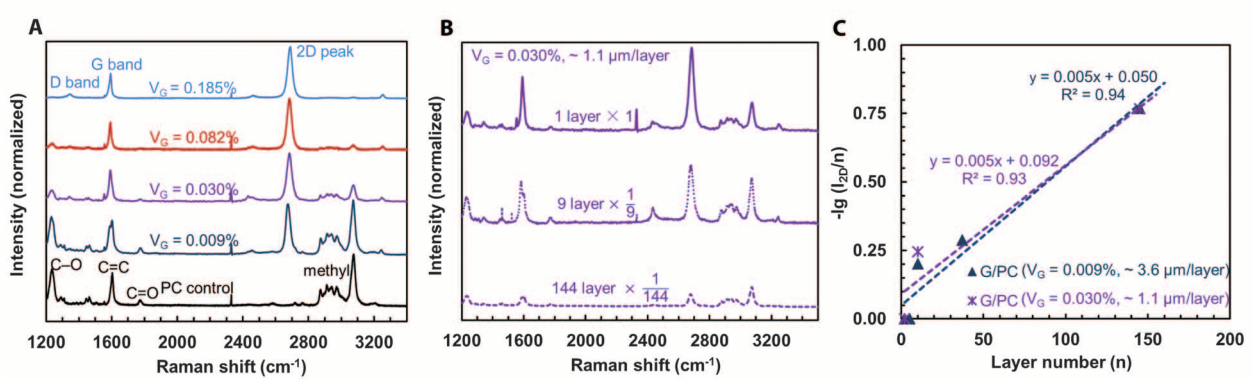

Fig. 2. Raman spectroscopy study of G/PC composites. (**A**) Raman spectra of G/PC composites (1 layer) and PC matrix control. The intensity ratio of 2D peak to G peak (I_{2D}/I_G) = 2.1 indicates the monolayer nature of graphene (*8*, *10*). A small D band at 1350 cm^{-1} illustrates the polycrystalline nature of CVDG (*10*). The resonance-enhanced graphene Raman cross section is 18,000 times as large as PC (fig. S4A). (**B**) Raman spectra of G/PC composites ($V_G \approx 0.030\%$) with layer number (n) of 1, 9, and 144; the spectroscopy intensity was normalized by n. (**C**) Plots of $-\lg(I_{2D}/n)$ against n for G/PC composites with $V_G \approx 0.009$ and 0.030%.

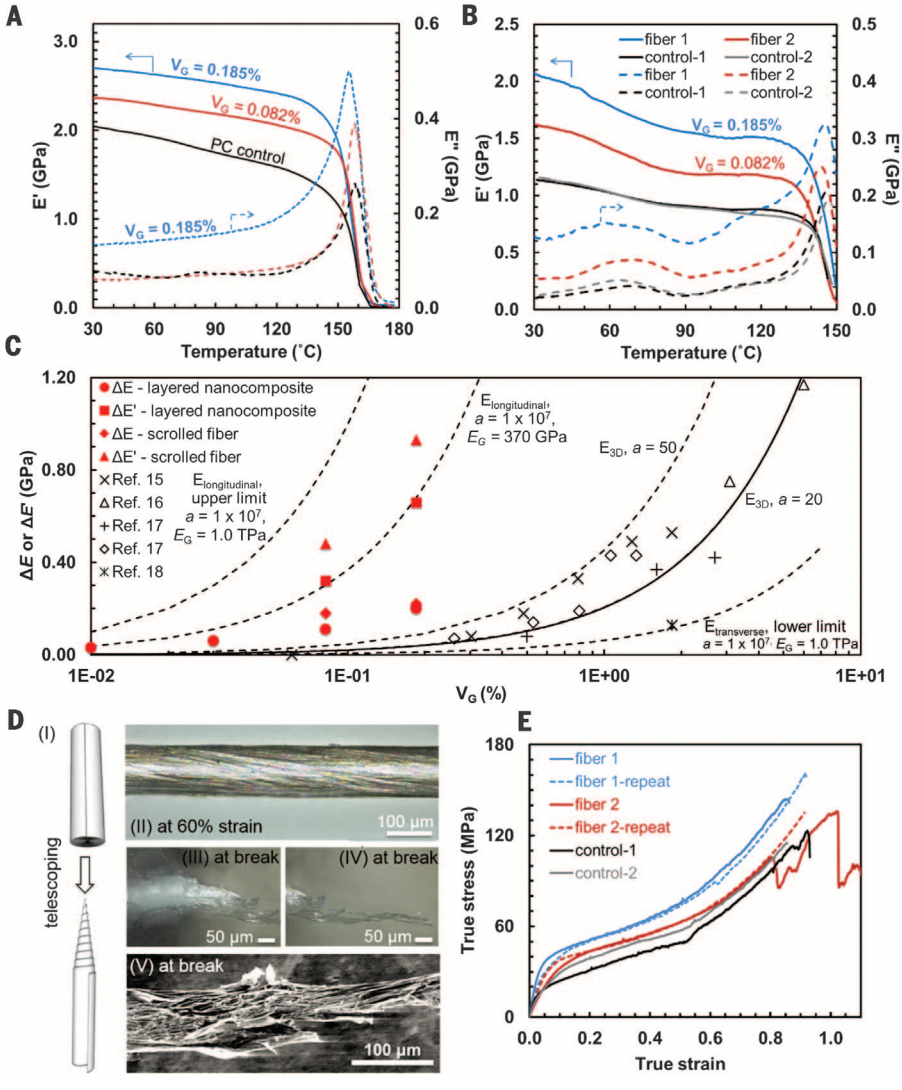

Fig. 3. Mechanical characterization of G/PC planar and scrolled fiber nanocomposites. (**A**) The storage modulus (E') and loss modulus (E'') versus temperature curves of two 40-layer planar composites with $V_G \approx 0.185$ and 0.082%, and PC matrix control (strain amplitude = 0.34%; frequency = 1 Hz). (**B**) E' and E'' versus temperature curves of fiber 1 ($V_G \approx 0.185\%$), fiber 2 (0.082%), control-1 and control-2 (with similar scroll structure). (**C**) A comparison of the elastic modulus increase (ΔE and $\Delta E'$) with respect to the PC matrix, against V_G of planar composites and scrolled fibers with reported data of various G/PC composites (*15*–*18*). The dashed lines are predicted by Mori-Tanaka theory (supplementary text 2). (**D**) The ideal telescoping mechanism (I). In practice, deformation occurs internally in the bulk of the fiber and not near the gripped fiber ends; the optical image of the scrolled fiber 2 in tensile with $d = 120 \pm 2$ μm at 60% strain (II) and at break (III and IV); SEM image of scrolled fiber (control-1) at break (V), demonstrating layer separations during failure. (**E**) True stress-strain responses of two composite fibers and their PC control fibers with similar scroll structures.

to the interlayer translation shown in the planar 4^j systems (fig. S10A). These fibers still exhibited measurable increases in stiffness $\Delta E'$ of 0.38 and 0.93 GPa, however, and larger effective E_G of the CVDG at 500 GPa. This telescoping compliance may necessarily reduce in-plane ripples to realize this increase. The scroll fibers also helically telescope in tension, necessarily reducing the diameter and densifying the structure uniformly (Fig. 3D, II, and fig. S15A). Axial rotation, in addition to translation, increases the path length per unit axial strain, hence increasing the E'' and energy dissipation through interfacial friction, increasing at higher V_G (Fig. 3B).

These fibers also show an extraordinary elongation at break ($\varepsilon_{max,\ fiber}$) up to 1.10 (Fig. 3E and fig. S15, B to E), compared with $\varepsilon_{max} = 0.75$ for a monolithic PC film (fig. S15F) (*25*) and higher ultimate strengths of 160 MPa (fiber 1) and 135 MPa (fiber 2), compared with 120 MPa for the PC films (fig. S15F) and fiber (Figs. 3E). A helical telescoping/twisting of the scrolled layers can explain these, which are generally found in natural structural materials to provide higher strength and toughness (*26*). For an Archimedean spiral described by radius r, the cross section follows $r = t\theta$, with t the interlayer distance between successive turnings through the angle θ. The scroll fiber is unique,

requiring that failure traverses the entire path length S_θ of the spiral inclusion (graphene), given by

$$S_\theta = \frac{1}{2}t\left[\theta\sqrt{1+\theta^2} + \ln\left(\theta + \sqrt{1+\theta^2}\right)\right] \quad (2)$$

where S_θ is identically the starting width of the graphene sheet (2.2 cm). For a fiber of diameter 131 ± 3 μm, as in Fig. 1G, Eq. 3 predicts a t of 390 ± 20 nm, in agreement with ellipsometer measurement values of 390 ± 4 nm (table S1). The scroll architecture mandates that all of $m = S_\theta / b_{c\text{-}c}$ (where $b_{c\text{-}c}$ is the carbon-carbon bond length, 0.142 nm) carbon-carbon bonds in the graphene rupture for complete failure or collapse, a process that takes place over a large strain range due to the semi-infinite nature of the graphene herein. This can be seen in the images of the break sites with visible spiral ripping in III to V of Fig. 3D. The spiral geometry predicts that for an initial l (length) × S_θ graphene sheet, the failure strain $\varepsilon_{max,\ fiber}$ is

$$\varepsilon_{max,fiber} = \frac{\sqrt{l^2 + S_\theta^2} - l}{l} + \varepsilon_{max,film} \quad (3)$$

where $\varepsilon_{max,\ film}$ is the failure strain of the planar composite film. For a typical scroll fiber in this work, with l = 2 cm, S_θ = 2.2 cm, and $\varepsilon_{max,\ film}$ = 0.75, we calculate $\varepsilon_{max,\ fiber}$ = 1.24 theoretically, higher than the maximum experimental value of 1.10 (Fig. 3E and fig. S15, B to E).

Last, this approach at the platelet limit offers interesting opportunities to modify the properties of matrices with exceedingly small amounts of an inclusion. PC is transparent but electrically insulating. Graphene electrical continuity was maintained during stacking and folding, as demonstrated by the highly anisotropic electrical conduction in planar 4^j samples at a mere $V_G \approx 0.003\%$ while retaining transparency. Percolation values of 0.14 to 1.3% were reported for various random composites of GO/PC (*15*, *16*, *17*, *27*), for example. A tungsten microprobe (Fig. 4A and fig. S12) inserted perpendicularly to the graphene layer direction at 1.00 μm/s into the grounded composite while maintaining circuit continuity (Fig. 4B) shows discrete current steps as each successive layer is contacted (Fig. 4C), reaching a maximum of about 0.2 μA after the contact of the fourth layer of graphene. Discretized conduction is seen in the all-points histogram in Fig. 4D and fig. S16, with Fig. 4, E and F, showing the scanning electron microscope (SEM) images of the deformation and penetration site with a tapered hole and peripheral diameter = 19.5 ± 0.5 μm. Overall, 4^j composites have anisotropic conduction with σ = 4.17 S/cm in plane at $V_G \approx 0.185\%$, and no continuity orthogonal to alignment, with similar results for scroll fiber composites. This ability to individually address each layer electrically within the composite can allow for complex circuits to be formed therein.

In conclusion, these results highlight new material properties available at this extreme platelet limit for nanocomposites. The 4^j stacking and shear scrolling methods offer straightforward, simple processing steps compared with more complex methods designed to achieve good dispersion at scale (supplementary text 6). The synthesis and transfer of CVD graphene is also advancing rapidly (*28*) with recent increases in scale (*29*). Scrolled fiber architecture promises high elongation at break, strength, and anisotropic conductivity while allowing many different host polymer matrices throughout the interior, distinct from a pure carbon fiber architecture. There exists a substantial opportunity to generate composite materials with new combinations of mechanical reinforcement, electrical, and optical properties at miniscule additions of a semi-infinite nanoplatelet filler.

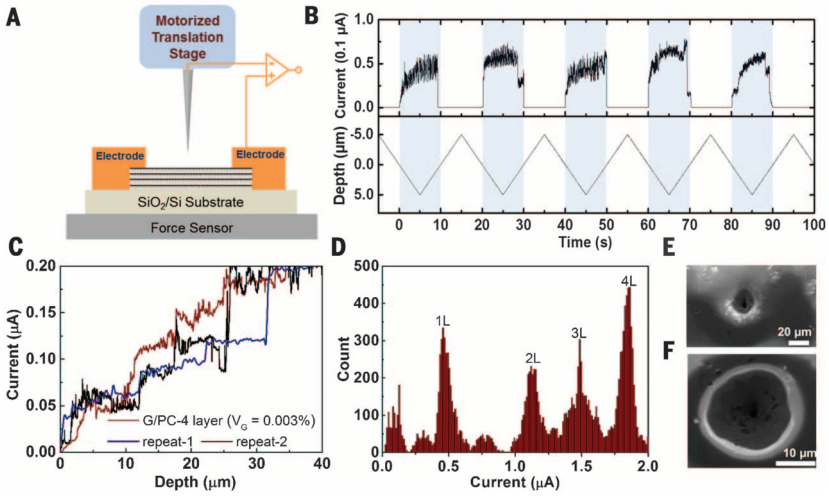

Fig. 4. Electric properties study of the planar composites. (**A**) A microprobe system for simultaneously testing the electrical properties of the G/PC composite; a tungsten microprobe mounted on the motorized translation stage system has a shaft diameter of 80 μm tapering to a 100-nm tip. As the conducting probe contacts each successive layer of graphene, conducting through the probe discretely increases. (**B**) Periodic current cycles formed by the contact and disengagement of the microprobe with G/PC composite surface. The velocity of the microprobe was kept at 1.00 μm/s (down) and –1.00 μm/s (up) alternately with a time span of 10 s and voltage = 1.0 mV. Light blue color areas indicate the contacting durations between the microprobe and the composite surface. (**C**) The electric current curves versus depth trace during the microprobe movement (1.00 μm/s, 1.0 mV) and penetration process for three similar G/PC composite samples ($V_G \approx 0.003\%$, four layers). (**D**) The histogram profiles of the value distribution (count) of electric current signals measured in (C) (red). (**E** and **F**) SEM images of a typical fracture site on the composite film punched by the microprobe; scale bars are 20 and 10 μm, respectively.

REFERENCES AND NOTES

1. J. D. Eshelby, *Proc. R. Soc. London Ser. A* **241**, 376–396 (1957).
2. X. Wang *et al.*, *Mater. Res. Lett.* **1**, 19–25 (2013).
3. Z. Zhou *et al.*, *Carbon* **75**, 307–313 (2014).
4. H. Liu, L. C. Brinson, *Compos. Sci. Technol.* **68**, 1502–1512 (2008).
5. P. M. Ajayan, J. M. Tour, *Nature* **447**, 1066–1068 (2007).
6. C.-W. Nan, Q. Jia, *MRS Bull.* **40**, 719–724 (2015).
7. A. Reina *et al.*, *Nano Lett.* **9**, 30–35 (2009).
8. X. Li *et al.*, *Science* **324**, 1312–1314 (2009).
9. Y.-H. Lee *et al.*, *Adv. Mater.* **24**, 2320–2325 (2012).
10. A. C. Ferrari *et al.*, *Phys. Rev. Lett.* **97**, 187401 (2006).
11. R. R. Nair *et al.*, *Science* **320**, 1308 (2008).
12. C.-J. Shih *et al.*, *Nat. Nanotechnol.* **6**, 439–445 (2011).
13. C. S. Ruiz-Vargas *et al.*, *Nano Lett.* **11**, 2259–2263 (2011).
14. Q.-Y. Lin *et al.*, *ACS Nano* **7**, 1171–1177 (2013).
15. J. R. Potts, S. Murali, Y. Zhu, X. Zhao, R. S. Ruoff, *Macromolecules* **44**, 6488–6495 (2011).
16. P. Steurer, R. Wissert, R. Thomann, R. Mülhaupt, *Macromol. Rapid Commun.* **30**, 316–327 (2009).
17. H. Kim, C. W. Macosko, *Polymer (Guildf.)* **50**, 3797–3809 (2009).
18. B. Shen, W. Zhai, M. Tao, D. Lu, W. Zheng, *Compos. Sci. Technol.* **86**, 109–116 (2013).
19. H. Kim, A. A. Abdala, C. W. Macosko, *Macromolecules* **43**, 6515–6530 (2010).
20. J. R. Potts, D. R. Dreyer, C. W. Bielawski, R. S. Ruoff, *Polymer (Guildf.)* **52**, 5–25 (2011).
21. X. Li, G. B. McKenna, *ACS Macro Lett.* **1**, 388–391 (2012).
22. T. Ramanathan *et al.*, *Nat. Nanotechnol.* **3**, 327–331 (2008).
23. N. A. Koratkar *et al.*, *Appl. Phys. Lett.* **87**, 063102 (2005).
24. J. Meaud *et al.*, *ACS Nano* **8**, 3468–3475 (2014).
25. M. J. Kendall, C. R. Siviour, *Philos. Trans. R. Soc.* **372**, 20130202 (2014).
26. S. E. Naleway, M. M. Porter, J. McKittrick, M. A. Meyers, *Adv. Mater.* **27**, 5455–5476 (2015).
27. M. Yoonessi, J. R. Gaier, *ACS Nano* **4**, 7211–7220 (2010).
28. E. O. Polat *et al.*, *Sci. Rep.* **5**, 16744 (2015).
29. W. Ren, H.-M. Cheng, *Nat. Nanotechnol.* **9**, 726–730 (2014).

ACKNOWLEDGMENTS

This work was primarily funded by 2009 U.S. Office of Naval Research Multidisciplinary University Research Initiatives (MURI) grant on Graphene Approaches to Terahertz Electronics (GATE) at Massachusetts Institute of Technology (MIT), Harvard University, and Boston University. This work was also supported in part by the U.S. Army Research Laboratory (ARL) and the U.S. Army Research Office (ARO) through the Institute for Soldier Nanotechnologies (ISN), under contract number W911NF-13-D-0001. R.L. is supported by a NASA Space Technology Research Fellowship (NSTRF), and B.Q. is supported by a National Defense Science and Engineering Graduate (NDSEG) Fellowship. We appreciate characterization support from the ISN at MIT funded by U.S. ARO and MIT Department of Materials Science and Engineering NanoLab. We also thank A. Schwartzman (MIT NanoLab) for the microindentation and uniaxial tensile test of 4^j samples; P. Moy and V. Wu of ARL for the imaging of the scrolled fibers in the tensile test; and E. Cohen for careful review of the manuscript and differential scanning calorimetry/dynamic mechanical analysis data.

SUPPLEMENTARY MATERIALS

www.sciencemag.org/content/353/6297/364/suppl/DC1
Materials and Methods
Supplementary Text
Figs. S1 to S18
Table S1
References (*30*–*59*)

7 February 2016; accepted 21 June 2016
10.1126/science.aaf4362

METALLURGY

A lightweight shape-memory magnesium alloy

Yukiko Ogawa, Daisuke Ando,* Yuji Sutou,* Junichi Koike

Shape-memory alloys (SMAs), which display shape recovery upon heating, as well as superelasticity, offer many technological advantages in various applications. Those distinctive behaviors have been observed in many polycrystalline alloy systems such as nickel titantium (TiNi)–, copper-, iron-, nickel-, cobalt-, and Ti-based alloys but not in lightweight alloys such as magnesium (Mg) and aluminum alloys. Here we present a Mg SMA showing superelasticity of 4.4% at –150°C and shape recovery upon heating. The shape-memory properties are caused by reversible martensitic transformation. This Mg alloy includes lightweight scandium, and its density is about 2 grams per cubic centimeter, which is one-third less than that of practical TiNi SMAs. This finding raises the potential for development and application of lightweight SMAs across a number of industries.

Shape-memory alloys (SMAs) are materials that exhibit shape recovery upon heating, as well as superelasticity. SMAs have a recoverable strain of more than 2% and are therefore used for various industrial applications such as antennas for cellular phones, eyeglass frames, coupling devices, fasteners, medical devices, seismic dampers, etc. (*1*–*3*). Moreover, SMAs have been attracting attention recently for aerospace applications because of their self-deployable and vibration mitigation characteristics (*4*, *5*). Shape-memory behavior was first discovered in a Au-Cd alloy in 1932 (*6*). Since then, the distinctive behavior accompanying martensitic transformation has been observed in many kinds of polycrystalline alloy systems—such as TiNi-, Cu-, Fe-, Ni-, Co-, and Ti-based alloys—but not in lightweight alloys such as Mg and Al alloys. Lightweight SMAs would be valuable for aerospace applications because the reduction in weight could lead to a large increase in fuel efficiency of rockets and spacecraft.

Magnesium alloys with a density below 2 g/cm^3 [such as Mg-Al-Zn, Mg-Zn-Zr, Mg-Zn-Y, and Mg-Y-RE (RE, rare earth element) (*7*–*9*)] are the lightest-weight practical alloys. These alloys have been used for various industrial products such as portable electronic devices, automobile components, and aerospace components (*7*, *8*, *10*). However, conventional Mg alloys show poor plastic deformability at room temperature (RT) because of their hexagonal close-packed (hcp) structure, which exhibits high plastic anisotropy. The poor plastic deformability of most Mg alloys limits their practical application. Mg-Li alloys have excellent plastic deformability because they have a body-centered cubic (bcc) structure, which shows isotropic plastic behavior (*9*, *11*, *12*). Therefore, wrought Mg-Li alloys are used for objects such as portable electronic devices. In addition, Mg-Li–based alloys with higher specific strength and superior corrosion resistance compared with conventional Mg alloys have been developed (*13*). Such bcc-type Mg alloys have properties that allow superior functionality as opposed to conventional hcp-type Mg alloys.

Magnesium-scandium alloys are the only other alloys with a bcc structure designated as β phase in a Mg-rich composition [Mg ~ 80 atomic % (at %)] in a higher temperature range (fig. S1) (*14*). A Mg-Sc alloy with both β and α phases has both a high ultimate tensile strength of 280 MPa and a large tensile elongation of ~30% at RT (*15*). Moreover, a β-type Mg-Sc alloy shows an age hardening at ~200°C due to the formation of fine hcp (α) needles and/or plates in a β matrix and exhibits an extremely high hardness of ~230 Vickers pyramid number (HV) (*16*). Such age hardening due to the formation of α precipitates in a β matrix occurs in various Ti-based alloys with a bcc structure, called β-type Ti alloys (*17*). Metastable β-type Ti alloys that show age hardening commonly have thermal-induced, stress-induced, or both types of martensitic transformation (*18*–*22*). Some β-type Ti alloys exhibit shape-memory effect and superelasticity, which are due to thermoelastic thermal- and stress-induced martensitic transformations, respectively, from a bcc to an orthorhombic structure (*22*–*27*). We herein report a metastable β-type Mg alloy including Sc that shows thermoelastic martensitic transformation and exhibits superelasticity with recoverable strain of 4.4% at –150°C and shape recovery upon heating.

Using x-ray diffraction (XRD), we find that the heat-treated β-type Mg–20.5 at % Sc alloy (Fig. 1) undergoes a stress-induced transformation by cold-rolling at RT. The heat-treated sample is mainly composed of the bcc (β) phase, with some small peaks from the hcp (α) phase. Our optical microscopy results confirm that a small amount of the α phase was preferentially formed at grain boundaries, which indicates that the α phase is formed during quenching. The lattice parameters of the β and α phases are estimated to be a_0 = 0.3597 nm (β phase) and a = 0.3242 nm and c = 0.5204 nm (α phase). The intensity of the peaks for the β phase (Fig. 1, black) decreases, and new peaks (indicated by "M") appear after heavy cold-rolling at RT (Fig. 1, red). This suggests the possibility of martensitic transformation in the β-type Mg-Sc alloy, as well as in the β-type Ti-based alloy. Using transmission electron microscopy (TEM), we also observed platelike martensites in the cold-rolled specimen (fig. S2).

This finding motivated us to investigate the stress-strain behaviors of the β-type Mg–20.5 at % Sc alloy specimens at various temperatures. The cyclic stress-strain curves show a strain of up to 4% for specimens at 20°, –50°, –100°, and –150°C (Fig. 2, A to D). We loaded specimens first in tension up to a strain of 1% before unloading, followed by reloading up to a strain of 2% in the second cycle, and so forth. The grain size (d) relative to sheet thickness (t) of these four samples was $0.42 \le d/t \le 0.67$. We used the electron backscatter diffraction technique to confirm that the specimen heat-treated at 690°C and then quenched had a random texture (fig. S3). The specimen shows negligible work hardening at 20°C after yielding. Plastic deformation is retained at this testing temperature when the applied stress is removed, indicating no superelasticity. The yield stress at –50° and –100°C becomes higher than at 20°C. We do not observe superelasticity at these testing temperatures, as plastic strain remains after unloading. The specimen exhibits "flag-shaped" stress-strain behavior characteristically observed in superelastic alloys with recovery of the original shape after unloading at –150°C. We applied stress-strain curves up to an 8% strain (Fig. 2E) for the specimen with d/t = 0.66 at –150°C, where the specimen fractured at a tensile strain of 8.8%. The stress-strain curves reveal typical behavior observed for other SMAs (*24*–*26*), with a plateau region after yielding, followed by an apparent work-hardening region. After removal of the applied strain of 8%, the specimen shows 6% recoverable strain that includes both ordinary elastic strain and superelastic strain. The superelastic strain ε_{SE}^{i} in a specimen with applied strain $\varepsilon_t^i - \varepsilon_e^i$ (where ε_t^i is the strain applied to the specimen, ε_e^i is the ordinary elastic strain, and i is the number of cycles) increases with increasing applied strain and then eventually saturates at a maximum superelastic strain $\varepsilon_{SE}^{MAX} = 4.4\%$ (Fig. 2F). We defined ε_{SE}^{i} by $\varepsilon_{SE}^{i} = \varepsilon_t^i - \varepsilon_e^i - \varepsilon_r^i$, where ε_r^i is the residual strain after removal of the stress (fig. S4). The maximum superelastic strain is about the same as that of a β-type Ti-based superelastic alloy (*22*, *24*–*27*). The XRD pattern of the tensile-fractured specimen tested at –150°C (Fig. 1A, blue) also shows the occurrence of the stress-induced phase, which is partially stabilized up to RT. By TEM observation at RT, we found that there are stabilized martensite plates in the tensile-fractured specimen (fig. S5), which indicates that the superelasticity is due to a stress-induced martensitic transformation. Superelastic strain by stress-induced martensitic transformation improves by the increment of d/t, which is equivalent to the relaxation of grain constraints (*28*). The present β-type Mg-Sc alloy showed the same tendency (fig. S6).

The temperature dependence of yield stress (σ_y) and superelastic strain ($\varepsilon_{SE}^{i=3}$) in the β-type Mg–20.5 at % Sc alloy specimens are shown in Fig. 3, A and B, respectively. The d/t value of all specimens was in the range of $0.30 \le d/t \le 0.72$.

Department of Materials Science, Graduate School of Engineering, Tohoku University, 6-6-11, Aoba-yama, Aoba-ku, Sendai 980-8579, Japan.
*Corresponding author. Email: dando@material.tohoku.ac.jp (D.A.); ysutou@material.tohoku.ac.jp (Y.S.)

We carried out cyclic tensile testing several times (as needed) at a certain temperature to eliminate the d/t dependence on stress-strain behavior. There should be little dependence of σ_y and $\varepsilon_{SE}^{i=3}$ on loading direction because the specimens have a random crystal orientation (fig. S3). We found that yield stress (σ_y) decreases linearly with increasing temperature above –100°C, and we observed no superelasticity (Fig. 3, A and B). This behavior indicates that σ_y corresponds to the critical stress for slip. Meanwhile, σ_y tends to linearly decrease with decreasing temperature (T) below around –120°C. This result suggests that the Clausius-Clapeyron relationship is valid between σ_y and T.

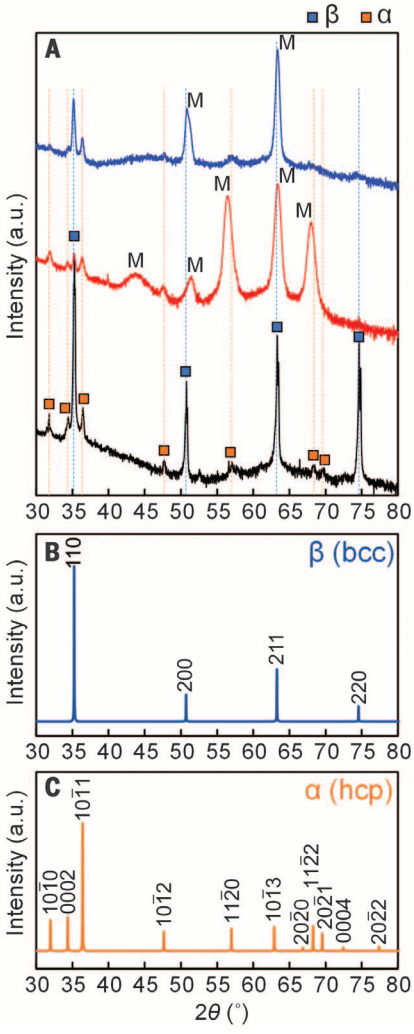

Fig. 1. XRD patterns of Mg–20.5 at % Sc specimens at RT. (**A**) XRD patterns at RT of a heat-treated specimen at 690°C for 0.5 hours (black), a cold-rolled specimen after the heat treatment (red), and a tensile-fractured specimen at –150°C (blue). X-ray intensity is shown on a logarithmic scale. The α and β phases are hcp and bcc structures, respectively. The peaks indicated by "M" are derived from a stress-induced phase. a.u., arbitrary units. (**B**) Reference powder XRD pattern of the β phase. (**C**) Reference powder XRD pattern of the α phase. Those reference patterns were generated on the basis of the lattice parameters of each phase.

Therefore, σ_y corresponds to the critical transition stress required to induce martensite, and the critical maximum temperature for superelasticity lies between –100° and –125°C. Such stress-temperature characteristics are very similar to those observed in conventional SMAs (*29*). Generally, the temperature at which the straight line of σ_y versus T (Fig. 3A, blue dashed line) intersects with the x axis (σ = 0) is defined as the thermal-induced martensitic transformation–starting temperature, M_s. The M_s of the β-type Mg–20.5 at % Sc alloy does not seem to exist at temperatures exceeding –273°C (0 K). We used XRD measurement to confirm that there is no thermal-induced martensite phase at –190°C (fig. S8A). Moreover, we measured electrical resistance as a function of temperature and deduced no substantial change upon martensitic transformation in the electrical resistivity of the β-type Mg–20.5 at % Sc alloy during cooling from 25° to –272.6°C and heating from –272.6° to 25°C. These results suggest that the β-type Mg–20.5 at % Sc alloy does not thermally transform into the martensite phase. This behavior is consistent with Ni-rich Ti-Ni alloys where superelasticity due to a stress-induced martensitic transformation was observed, even in an alloy composition that does not show a thermal-induced martensitic transformation (*30*).

The β-type Mg–20.5 at % Sc alloy is a low-temperature SMA and displays superelasticity only at temperatures below around –120°C. Meanwhile, the martensitic transformation temperature was found to strongly depend on Sc content and to increase with decreasing Sc content (*31*). We confirmed that a small β-type Mg–18.3 at % Sc sheet piece, taken from the topmost part of the melted ingot, exhibited shape recovery upon heating from –30°C to RT (fig. S7). We used in situ XRD to verify that the thermal-induced martensite phase was an orthorhombic structure in a β-type Mg-Sc piece—also taken from the topmost part of the melted ingot—with an average Sc content of 19.2 at % (fig. S8B). These results indicate that the superelasticity obtained in the β-type Mg–20.5 at % alloy is due to a reversible martensitic transformation between the β parent phase and the orthorhombic martensite phase. These findings also suggest that a possible way to increase the operating temperature of a β-type Mg-Sc superelastic alloy is to reduce Sc content.

The temperature dependence of transition stress (σ_y) for stress-induced martensitic transformation obeys the Clausius-Clapeyron relationship, which is expressed as $d\sigma_y/dT = -\Delta S/\varepsilon$, where ΔS is the entropy change of the transformation per unit volume and ε is transformation strain (*22*). We estimated the slope of the σ_y-versus-T line to be ~1.8 MPa/°C at temperatures below –100°C (Fig. 3A). Moreover, the transformation strain is equal to the obtained maximum superelastic strain of 0.44 (Fig. 2F). Therefore, we estimate ΔS = –1.1 J/mol K for the stress-induced martensitic transformation in the β-type Mg–20.5 at % Sc alloy with a calculated molar volume of 1.4×10^{-5} m^3/mol, estimated from the lattice parameter of the bcc structure. The change in entropy is similar to β-type Ti

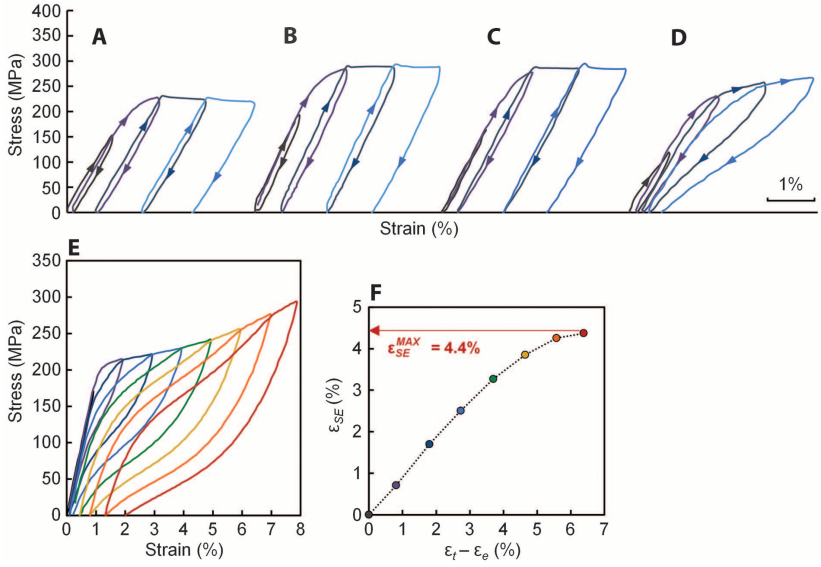

Fig. 2. Cyclic tensile stress-strain curves of Mg–20.5 at % Sc specimens heat-treated at 690°C for 0.5 hours. (**A** to **D**) Stress-strain curves of the specimen with (A) d/t = 0.67 at 20°C, (B) d/t = 0.50 at –50°C, (C) d/t = 0.42 at –100°C, and (D) d/t = 0.46 at –150°C. The specimens were initially loaded in tension up to a strain of 1% before unloading (gray), followed by reloading up to a strain of 2% in the second cycle (purple), then followed by reloading up to a strain of 3% in the third cycle (blue), and so forth up to a strain of 4% (light blue). The tensile direction was parallel to the rolling direction. (**E**) Stress-strain curves of the specimen with d/t = 0.66 at –150°C. The tensile direction was parallel to the rolling direction, and tensile strain was applied up to a strain of 8%, where first-, second-, third-, fourth-, fifth-, sixth-, seventh-, and eighth-cycle curves are colored gray, purple, blue, light blue, green, yellow, orange, and red, respectively. (**F**) Plots of the superelastic strain ε_{SE} as a function of the applied strain $\varepsilon_t - \varepsilon_e$. The maximum superelastic strain of 4.4% is obtained.

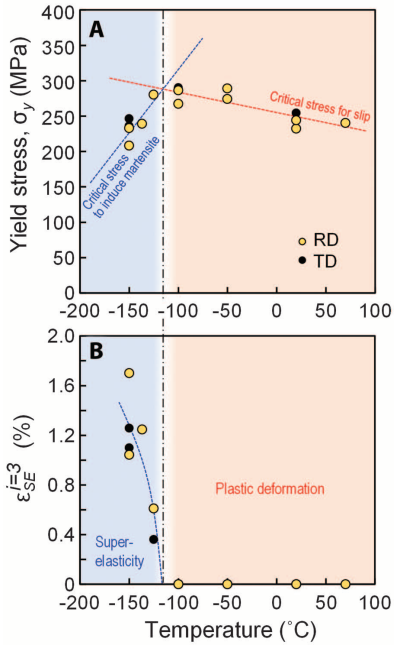

Fig. 3. Temperature dependence of yield stress and superelastic strain in Mg–20.5 at % Sc specimens heat-treated at 690°C for 0.5 hours. (**A**) Yield stress (σ_y) as a function of temperature. (**B**) Superelastic strain ($\varepsilon_{SE}^{i=3}$) as a function of temperature. σ_y and $\varepsilon_{SE}^{i=3}$ are defined as shown in fig. S4. The yellow and black circles indicate data points for specimens tensile loaded along the rolling direction (RD) and transverse direction (TD), respectively. The red and blue dashed lines in (A) indicate the critical stress for slip and the critical stress to induce the martensite phase, respectively, where the slope in each region was determined by the least-squares method with all data points in each region. The red-shaded area indicates the plastic deformation region, and the blue-shaded area denotes the superelasticity region. The black dot-dashed line indicates critical temperature for superelasticity.

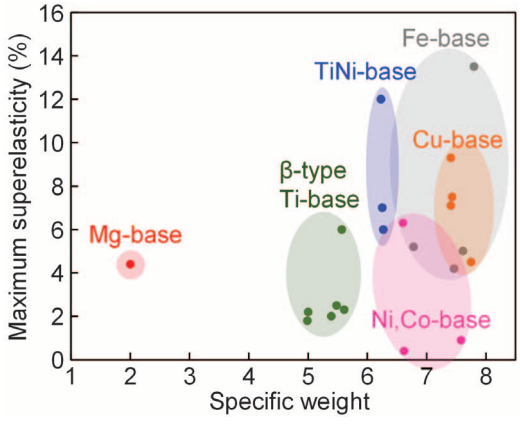

Fig. 4. Relationship between maximum superelastic strain and specific weight of polycrystalline SMAs. For comparison with the present Mg-based SMA (red), we chose practicable TiNi-based (blue), β-type Ti-based (green), Cu-based (orange), Fe-based (gray), and Ni- and Co-based (pink) polycrystalline SMAs. The specific weight of a material is defined as the ratio of the density of the material (grams per cubic centimeter) to the density of water (1 g/cm^3). The alloy composition, maximum superelastic strain, and specific weight of those alloys are listed in table S1.

alloy (–1.3 J/mol K), further supporting a martensitic transformation from a bcc to an orthorhombic structure (*22*).

Polycrystalline Mg alloys with an hcp structure show a small pseudoelasticity with a recoverable strain of about 0.2 to 0.4%, which generates nonlinearity of the unloading curve (*32*, *33*). The reversal of deformation twins during unloading causes the observed nonlinearity in polycrystalline Mg alloys with the hcp structure. Our β-type Mg-Sc alloy shows a large superelasticity of 4.4% recoverable strain, accompanying stress-induced martensitic transformation (Fig. 2E). We can compare superelastic strain and specific weight in various polycrystalline SMAs (Fig. 4 and table S1), and the plots of superelastic strain versus critical temperature in various polycrystalline SMAs are also shown in fig. S9. TiNi-based SMAs, which are widely used, have a specific weight of ~6. Fe-, Cu-, Ni-, and Co-based SMAs are heavier, whereas β-type Ti-based SMAs are lighter than TiNi-based SMAs. The present β-type Mg-Sc superelastic alloy possesses a specific weight of just 2, and its superelastic strain is comparable to that of β-type Ti SMAs. This lightweight Mg-Sc SMA has potential impact for aerospace applications, among others. SMAs have been attracting attention for use as self-deployable space habitat frames and damping devices for spacecraft systems (*4*, *5*). A weight reduction of aerospace components can lead to an increase in fuel efficiency of rockets and spacecraft. The β-type Mg–20.5 at % Sc SMA is a low-temperature superelastic alloy and is much more expensive than conventional SMAs (*31*), which limits immediate applications but serves as the basis for development of lightweight SMAs. The present findings offer new insights into the study of lightweight functional materials.

REFERENCES AND NOTES

1. J. Van Humbeeck, *Mater. Sci. Eng. A* **273-275**, 134–148 (1999).
2. T. Duerig, A. Pelton, D. Stöckel, *Mater. Sci. Eng. A* **273-275**, 149–160 (1999).
3. M. C. Piedboeuf, R. Gauvin, M. Thomas, *J. Sound Vibrat.* **214**, 885–901 (1998).
4. L. Santo, F. Quadrini, A. Accettura, W. Villadei, *Proc. Eng.* **88**, 42–47 (2014).
5. D. J. Hartl, D. C. Lagoudas, *Proc. IMechE.* **221**, 535–552 (2007).
6. A. Ölander, *J. Am. Chem. Soc.* **54**, 3819–3833 (1932).
7. I. J. Polmear, *Mater. Sci. Technol.* **10**, 1–16 (1994).
8. B. L. Mordike, T. Ebert, *Mater. Sci. Eng. A* **302**, 37–45 (2001).
9. Z. Yang, J. P. Li, J. X. Zhang, G. W. Lorimer, J. Robson, *Acta. Metall. Sin.* **21**, 313–328 (2008).
10. M. K. Kulekci, *Int. J. Adv. Manuf. Technol.* **39**, 851–865 (2008).
11. T. G. Byrer, E. L. White, P. D. Frost, "The development of magnesium lithium alloys for structural applications" (NASA contractor report, Battelle Memorial Institute, 1963).
12. M. M. Avedesian, H. Baker, Eds., *Magnesium and Magnesium Alloys* (ASM International, 1999).
13. W. Xu *et al.*, *Nat. Mater.* **14**, 1229–1235 (2015).
14. B. J. Beaudry, A. H. Daane, *J. Less Common Met.* **18**, 305–308 (1969).
15. Y. Ogawa, D. Ando, Y. Sutou, J. Koike, *J. Jpn. Inst. Met. Mater.* **80**, 171–175 (2016).
16. D. Ando, Y. Ogawa, T. Suzuki, Y. Sutou, J. Koike, *Mater. Lett.* **161**, 5–8 (2015).
17. G. Lütjering, J. C. Williams, *Titanium* (Springer, 2003).
18. T. W. Duerig, G. T. Terlinde, J. C. Williams, *Metall. Trans. A* **11**, 1987–1998 (1980).
19. E. S. N. Lopes, A. Cremasco, C. R. M. Afonso, R. Caram, *Mater. Charact.* **62**, 673–680 (2011).
20. K. Endoh *et al.*, *Mater. Today Proc.* **2** (suppl. 3), S817–S820 (2015).
21. H. Ohyama, H. Nakamori, Y. Ashida, T. Maki, *ISIJ Int.* **32**, 222–231 (1992).
22. H. Y. Kim, S. Hashimoto, J. I. Kim, H. Hosoda, S. Miyazaki, *Mater. Trans.* **45**, 2443–2448 (2004).
23. C. Baker, *Met. Sci. J.* **5**, 92–100 (1971).
24. E. Takahashi, T. Sakurai, S. Watanabe, N. Masahashi, S. Hanada, *Mater. Trans.* **43**, 2978–2983 (2002).
25. Y. Fukui, T. Inamura, H. Hosoda, K. Wakashima, S. Miyazaki, *Mater. Trans.* **45**, 1077–1082 (2004).
26. T. Maeshima, S. Ushimaru, K. Yamauchi, M. Nishida, *Mater. Trans.* **47**, 513–517 (2006).
27. Y. Tomio, T. Furuhara, T. Maki, *Mater. Trans.* **50**, 2731–2736 (2009).
28. Y. Sutou, T. Omori, R. Kainuma, K. Ishida, *Acta Mater.* **61**, 3842–3850 (2013).
29. S. Miyazaki, K. Otsuka, *ISIJ Int.* **29**, 353–377 (1989).
30. Y. Wang, X. Ren, K. Otsuka, *Phys. Rev. Lett.* **97**, 225703 (2006).
31. Materials and methods and supplementary text are available as supplementary materials on *Science* Online.
32. M. A. Gharghouri, G. C. Weatherly, J. D. Embury, J. Root, *Philos. Mag.* **79**, 1671–1695 (1999).
33. C. H. Cáceres, T. Sumitomo, M. Veidt, *Acta Mater.* **51**, 6211–6218 (2003).

ACKNOWLEDGMENTS

We thank N. Ueshima and K. Oikawa (Tohoku University, Japan) for help with the tensile testing experiment; X. Xu, T. Omori, and R. Kainuma (Tohoku University, Japan) for help with the XRD and Physical Property Measurement System experiments; K. Kobayashi and T. Miyazaki (Tohoku University, Japan) for help with TEM measurements; and K. Yoshimi and K. Ishida (Tohoku University, Japan) for fruitful discussions. This work was supported by the Japan Society for the Promotion of Science KAKENHI, Grant-in-Aid for Young Scientists (A), grant no. 15H05549, and Tohoku University Division for International Advanced Research and Education. The present authors are inventors on Japanese patent application no. 2015-201830, applied for by Tohoku University. The data are available from the corresponding authors upon request.

SUPPLEMENTARY MATERIALS

www.sciencemag.org/content/353/6297/368/suppl/DC1
Materials and Methods
Supplementary Text
Figs. S1 to S9
Tables S1 and S2
References (*34*, *35*)

9 March 2016; accepted 28 June 2016
10.1126/science.aaf6524

QUANTUM GASES

Observation of the Efimovian expansion in scale-invariant Fermi gases

Shujin Deng,[1]* Zhe-Yu Shi,[2]* Pengpeng Diao,[1] Qianli Yu,[1] Hui Zhai,[2] Ran Qi,[3]† Haibin Wu[1,4]†

Scale invariance plays an important role in unitary Fermi gases. Discrete scaling symmetry manifests itself in quantum few-body systems such as the Efimov effect. Here, we report on the theoretical prediction and experimental observation of a distinct type of expansion dynamics for scale-invariant quantum gases. When the frequency of the harmonic trap holding the gas decreases continuously as the inverse of time *t*, the expansion of the cloud size exhibits a sequence of plateaus. The locations of these plateaus obey a discrete geometric scaling law with a controllable scale factor, and the expansion dynamics is governed by a log-periodic function. This marked expansion shares the same scaling law and mathematical description as the Efimov effect.

Interaction between dilute ultracold atoms is described by the s-wave scattering length. For a spin-1/2 Fermi gas, when the scattering length diverges at a Feshbach resonance, there is no length scale other than the interparticle spacing in this many-body system, and therefore the system, known as the unitary Fermi gas, becomes scale invariant. The spatial scale invariance leads to universal thermodynamics and transport properties, as revealed by many experiments (*1*–*13*). On the other hand, in a boson system with an infinite scattering length, three-body bound states can form, where the extra length scale of the three-body parameter turns the continuous scaling symmetry into a discrete scaling symmetry and gives rise to an infinite number of three-body bound states whose energies obey a geometric scaling symmetry. This so-called Efimov effect (*14*, *15*) has been observed in cold atom experiments (*16*–*23*), with recent work confirming the geometric scaling of the energy spectrum (*24*–*27*).

For a harmonic trapped gas, the expansion dynamics offers great insight to the property of the gas (*28*–*33*). Here, we consider what happens to a scale-invariant quantum gas held in a harmonic trap when the trap is gradually opened up by decreasing the trap frequency ω as $1/(\sqrt{\lambda}t)$, where λ is a constant and t is time (Fig. 1, A and B). Naïvely, by dimensional analysis, one would expect that the cloud size $\mathcal{R}$ just increases as $\sqrt{t}$. Here we show, both theoretically and experimentally, that when λ is smaller than a critical value, the expansion dynamics displays a discrete scaling symmetry in the time domain. As a function of t, $\mathcal{R}$ displays a sequence of plateaus, which means that at a set of discrete times t_n the cloud expansion stops, despite the continuous decreasing of the trap frequency. The locations of the plateaus t_n obey a geometric scaling behavior.

To explain these dynamics, we first point out why $\omega = 1/(\sqrt{\lambda}t)$ is special. For simplicity, we first consider a three-dimensional (3D) isotropic trap $V(r) = m\omega^2 r^2/2$. In the absence of a trapping potential, the system is invariant under a scale transformation $r \to \Lambda r$, whereas in the presence of a static harmonic trap, the fixed harmonic length introduces an additional length scale that breaks this spatial scale invariance. Nevertheless, if ω changes as $1/(\sqrt{\lambda}t)$, the time-dependent Schrödinger equation exhibits a space-time scaling symmetry under the transformation $r \to \Lambda r$ and $t \to \Lambda^2 t$.

Defining the cloud size as $\hat{R}^2 = \sum_i \mathbf{r}_i^2/N$, the equation-of-motion for $\hat{R}^2$ can be derived as $i\frac{d}{dt}\langle\hat{R}^2\rangle = \langle[\hat{R}^2, \hat{H}(t)]\rangle = \frac{2i}{N}\langle\hat{D}\rangle$, where $\hat{D} = \sum_i \frac{1}{2}(\mathbf{r_i}\cdot\mathbf{p_i} + \mathbf{p_i}\cdot\mathbf{r_i})$ is the generator of a spatial scaling transformation. Using the fact that the system is scale invariant, and by taking higher-order time derivatives of $\langle\hat{R}^2\rangle$, we conclude that the cloud size $\langle\hat{R}^2\rangle$ obeys the differential equation (see supplementary text S1):

$$\frac{d^3}{dt^3}\langle\hat{R}^2\rangle + \frac{4}{\lambda t^2}\frac{d}{dt}\langle\hat{R}^2\rangle - \frac{4}{\lambda t^3}\langle\hat{R}^2\rangle = 0 \qquad (1)$$

In the experiment, we start with a finite initial trap frequency ω_0 before turning it down (Fig. 1B). The system is at equilibrium for $t < t_0$, and at $t = t_0^+$, $\langle\hat{R}^2\rangle(t_0) = R_0^2$ and $\frac{d^m}{dt^m}\langle\hat{R}^2\rangle|_{t=t_0} = 0$ for $m = 1, 2$. This sets a boundary condition for Eq. 1 that can turn its continuous scaling symmetry in the time domain into a discrete one.

The solution of Eq. 1 can be generally written in a form as $\langle R^2(t)\rangle = C_1 f_1^2 + C_2 f_1 f_2 + C_3 f_2^2$ (The constants C_1, C_2, and C_3 are determined by the boundary conditions), where f_1 and f_2 are two linear independent solutions (see supplementary text S1) of

$$\frac{d^2 f}{dt^2} + \frac{1}{\lambda t^2} f = 0 \qquad (2)$$

By replacing $f(t)$ with $\psi(r)$ and t with r and regarding ψ as a real wave function and r as the hyper-radius, Eq. 2 becomes the zero-energy

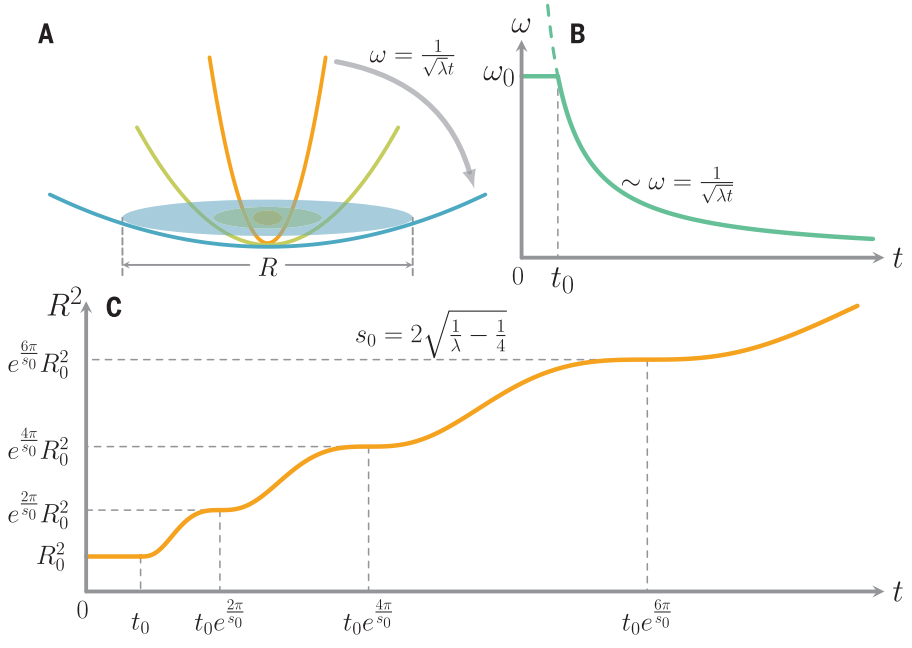

Fig. 1. The schematic of the Efimovian expansion. (**A** and **B**) A scale-invariant ultracold gas is first held in a harmonic trap with frequency ω_0. Then, starting from $t_0 = 1/(\sqrt{\lambda}\omega_0)$, the trap frequency starts to decrease as $1/(\sqrt{\lambda}t)$, and the cloud expands. (**C**) The theoretical predication of the Efimovian expansion: The cloud size $\mathcal{R}$ as a function of time t follows a log-periodic function and exhibits a series of plateaus. The locations of the plateaus obey a geometric scaling law.

[1]State Key Laboratory of Precision Spectroscopy, East China Normal University, Shanghai 200062, P. R. China. [2]Institute for Advanced Study, Tsinghua University, Beijing 100084, P. R. China. [3]Department of Physics, Renmin University of China, Beijing 100872, P. R. China. [4]Collaborative Innovation Center of Extreme Optics, Shanxi University, Taiyuan 030006, China.
*These authors contributed equally to this work. †Corresponding author. Email: qiran@ruc.edu.cn (R.Q.); hbwu@phy.ecnu.edu.cn (H.W.)

Schrödinger equation for the Efimov effect in the hyperspherical coordinate (*14*, *15*). This reveals a connection between this dynamical expansion and the Efimov problem. $\lambda = 4$ is a special point for Eq. 2. For $\lambda < 4$, there are two independent solutions of Eq. 2, $f_1 = \sqrt{t}\cos((s_0/2)\ln t)$ and $f_2 = \sqrt{t}\sin((s_0/2)\ln t)$, where $s_0 = 2\sqrt{1/\lambda - 1/4}$; $\langle R^2 \rangle$ then takes a log-periodic form

$$\frac{\langle \hat{R}^2 \rangle(t)}{R_0^2} = \frac{t}{t_0}\frac{1}{\sin^2\varphi}[1 - \cos\varphi \cdot \cos(s_0 \ln\frac{t}{t_0} + \varphi)] \quad (3)$$

where $\varphi = -\arctan s_0$ is determined by the boundary condition at $t = t_0$. Equation 3 clearly reveals the discrete scaling symmetry—i.e., when $t_2 = e^{2\pi/s_0} t_1$, $\langle \hat{R}^2 \rangle(t_2) = e^{2\pi/s_0} \langle \hat{R}^2 \rangle(t_1)$, and $\frac{d^m}{dt^m}\langle \hat{R}^2 \rangle|_{t=t_2} = e^{-2\pi(m-1)/s_0} \frac{d^m}{dt^m}\langle \hat{R}^2 \rangle|_{t=t_1}$ for all the m-th order derivatives. Therefore, at time $t_n = e^{2\pi n/s_0} t_0$, the first- and second-order time derivatives for $\langle \hat{R}^2 \rangle$ become zero and the cloud expansion is strongly suppressed, that is to say, the expansion dynamics shows a series of plateaus around each t_n. A similar conclusion can also be obtained from the hydrodynamics expansion equations (*34*, *35*). Note that s_0 is tunable by the speed of the decrease of the trap frequency $\omega(t)$. When $\lambda > 4$, $\langle \hat{R}^2 \rangle$ simply follows a power law as $\langle \hat{R}^2 \rangle(t) \sim t^{1+\eta}$ for $t \gg t_0$, where $\eta = \sqrt{1 - 4/\lambda}$. A detailed comparison between this expansion and the Efimov effect is summarized in table S1. We will refer to this effect as the Efimovian expansion.

In our experiment, we use a balanced mixture of ^{6}Li fermions in the lowest two hyperfine states $|\uparrow\rangle \equiv |F = 1/2, M_F = -1/2\rangle$ and $|\downarrow\rangle \equiv |F = 1/2, M_F = 1/2\rangle$. Fermionic atoms are loaded into a cross-dipole trap to perform evaporative cooling. The resulting potential has a cylindrical symmetry around the z axis, and the trap anisotropic frequency ratio ω_r/ω_z is about 9. The above theoretical considerations hold for the isotropic case, but similar results can be obtained for an anisotropic trap (see supplementary text S2). Starting at the initial time t_0, the trap potential is lowered as

$$V(r) = \frac{m}{2\lambda_r t^2} r^2 + \frac{m}{2\lambda_z t^2} z^2 \quad (4)$$

Because $\lambda_r/\lambda_z = (\omega_z/\omega_r)^2 \ll 1$ the effect is more pronounced along the axial direction than in the transverse direction. Therefore, hereafter we focus on the cloud expansion along the axial direction. Theory shows (see supplementary text S2) that the axial cloud square size $\mathcal{R}_z^2$ obeys the same form as Eq. 3, except

$$s_0 = \omega_b \sqrt{1/\lambda_z - 1/4} \quad (5)$$

where ω_b is a factor related to the breathing mode frequency, $\omega_b = 2$ for the noninteracting gas, and $\omega_b = \sqrt{12/5}$ for the unitary Fermi gas along the axial direction. A Feshbach resonance is used to tune the interaction of the atoms either to the noninteracting regime with the magnetic field B = 528 G or to the unitary regime with B = 832 G. The trap frequency is lowered by decreasing the laser intensity, and λ_z is controlled by the decrease rate of the laser intensity, with the initial axial trap depth always fixed at 5% U_0, where U_0 is the full trap potential. Thus, different λ_z corresponds to different $t_0 = 1/(\sqrt{\lambda_z}\omega_z^0)$, where ω_z^0 is the initial axial trap frequency. Finally, after certain expansion time t_{exp} with the trap, the trap is completely turned off and the cloud is probed by standard resonant absorption imaging techniques after a time-of-flight expansion time t_{tof} = 200 μs. Each data point is an average of five shots of the measurements at identical parameters.

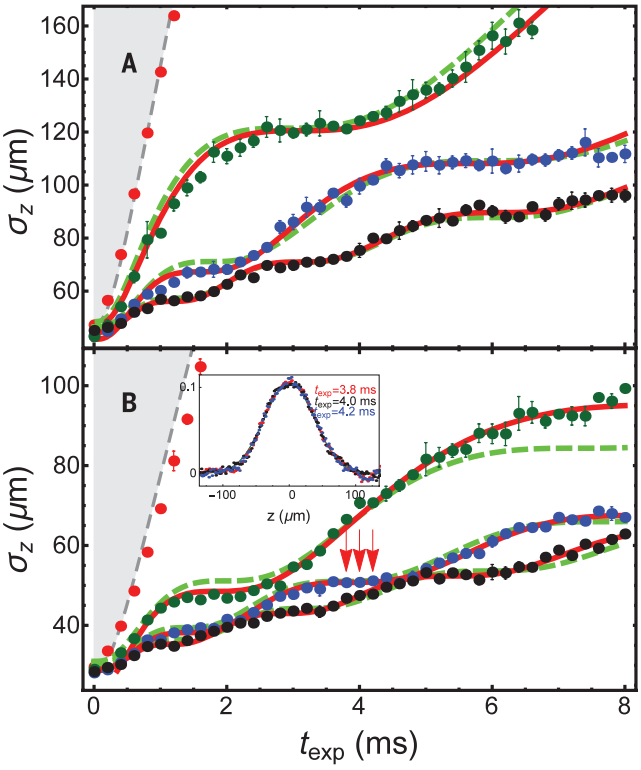

Fig. 2. Experimental observation of the Efimovian expansion. The mean axial cloud size σ_z (with $\sigma_z^2 = 2\langle \hat{R}_z^2 \rangle$) versus the expansion time $t_{exp} = t - t_0$ for (**A**) a noninteracting Fermi gas of ^{6}Li measured at B = 528 G and (**B**) a unitary Fermi gas measured at B = 832 G. Dots are measured data. Black, blue, and green dots denote λ_z = 0.02, 0.07, and 0.36 for (A), and λ_z = 0.01, 0.02, and 0.06 for (B). The dashed lines are the theory curves based on Eq. 3 (with s_0 given by Eq. 5) without any free parameters, and the solid lines are the best fit using the function form of Eq. 3, with s_0 as a fitting parameter. Red dots in both figures denote the case with $\lambda_z = 4$, and the shaded area is the regime where expansion does not show discrete scaling symmetry. The inset in (B) shows three successive density profiles (after the time-of-flight) when the time t_{exp} is located inside a plateau, as indicated by the arrows. Error bars, mean ± SD.

The time-of-flight density profile along the axial direction is fitted by a Gaussian function as $A_0 + A_1 e^{-z^2/\sigma_z^2}$, from which we obtain $\sigma_{z,obs}$. $\sigma_{z,obs}$ is related to the in situ cloud size by a scale factor b_z via $\sigma_{z,obs} = b_z(t_{tof})\sigma_z$; $b_z(t_{tof})$ can be obtained from either hydrodynamic or ballistic expansion equation with the time-of-flight time t_{tof} (see supplementary text S5). Because the trap is quite anisotropic, the cloud expands slowly along the axial direction during a short time-of-flight, and the expansion factor b_z only gives a quantitative correction to the results. Figure 2 shows the typical measurements of σ_z with different λ_z for both the noninteracting and the unitary Fermi gases. For instance, for $\lambda_z = 0.06$, we decrease the trap frequency from $2\pi \times 567.3$ Hz to $2\pi \times 71.0$ Hz within 8 ms. Dots are the measured data, and the solid and the dashed lines are both theoretical curves based on Eq. 3, taking s_0 as a fitting parameter or using s_0 given by Eq. 5, respectively. Because σ_z is obtained by a Gaussian fit to the density profile, $\sigma_z^2 = 2\langle \hat{R}_z^2 \rangle$, and thus the theoretical expression for $\sigma_z/\sigma_{z,0}$ is simply a square root of Eq. 3. Figure 2 clearly shows the plateaus for the expansion dynamics and an excellent agreement between theory and experiment. Density profiles for three successive measurement times inside a plateau almost perfectly overlap with each other (Fig. 2B, inset), which confirms that the expansion stops at the plateau.

For smaller λ_z, the trap frequency decreases slower, the plateaus become denser, and the difference in height between two adjacent plateaus becomes smaller. The adiabatic limit is reached for $\lambda_z \to 0$, where the mean square of the cloud size follows a linear expansion as expected.

For the critical value $\lambda_z = 4$ (red dots in Fig. 2), no plateaus are observed within finite expansion time. How the plateaus disappears as $\lambda_z \to 4$ could not be measured here. This is because as $\lambda_z \to 4$, s_0 decreases toward zero, the period increases exponentially, and therefore even the first plateau would appear after a very long expansion time. On the other hand, there is a lower limit for the trap frequency below which atoms cannot be trapped. Together with the fact that the larger the λ_z, the faster the trapping frequency drops and the shorter the expansion time, the plateaus could not be observed even before reaching the critical value $\lambda_z = 4$ within the finite expansion time. Nevertheless, for comparison, we have performed measurements where the trapping frequency decreases with similar average speeds in Fig. 2, but the time dependence of $\omega(t)$ is different from $1/t$, which breaks the aforementioned

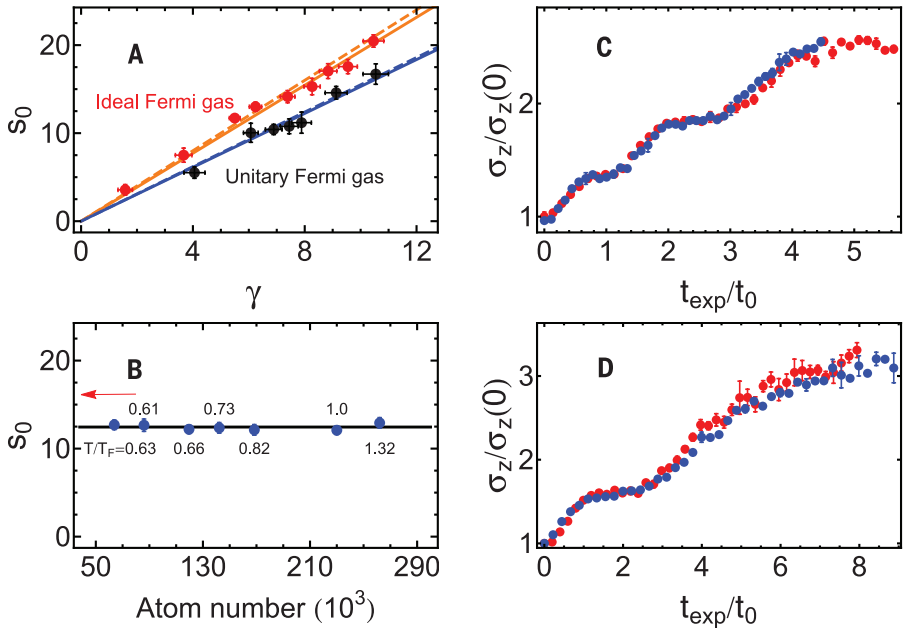

Fig. 3. Universality of the Efimovian expansion. (**A**) s_0 obtained from fitting the expansion curves v.s. $\gamma \equiv \sqrt{1/\lambda_z - 1/4}$. The solid lines are the linear fitting curves, and the dashed lines are $s_0 = \omega_b\gamma$, with $\omega_b = 2$ for the noninteracting fermions and $\omega_b = \sqrt{12/5}$ for the unitary Fermi gas. (**B**) For a given $\lambda_z = 0.017$ and for the unitary Fermi gas, s_0 is obtained from fitting the expansion curves for different fermion numbers and temperatures as indicated (T_F is the Fermi temperature). The solid line is the theory value for the unitary Fermi gas, and the arrow indicates the theory value for the noninteracting Fermi gas with the same λ_z. $\sigma_z/\sigma_{z,0}$ as a function of t_{exp}/t_0 for the noninteracting (red dots) and the unitary Fermi gas (blue dots) with $s_0 = 10.53$ in (**C**) and $s_0 = 5.88$ in (**D**). Error bars, mean ± SD.

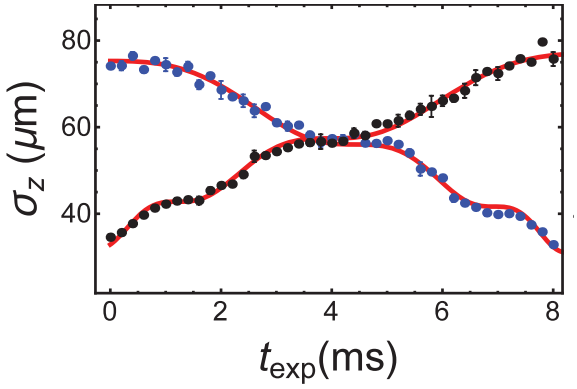

Fig. 4. Time-reversal symmetry of the Efimovian expansion. σ_z for the expansion and its inverted compression process from t_0 to t_f. $t_{exp} = t - t_0$. Black dots are the expansion process, with $\omega = 1/(\sqrt{\lambda}t)$ and the frequency changing from $\omega_0 = 1/(\sqrt{\lambda}t_0)$ (at t_0) to $\omega_f = 1/(\sqrt{\lambda}t_f)$ (at t_f). Blue dots are the inverted compression process, with $\omega = 1/(\sqrt{\lambda}(t_f + t_0 - t))$ and the frequency changing from ω_f (at t_0) to ω_0 (at t_f). Here, $\lambda_z = 0.01$ and the data are taken in the unitary regime. Error bars, mean ± SD.

spatial-time scaling symmetry. The plateaus are indeed not observed in the expansion (fig. S2).

We now demonstrate that these dynamics are universal. First, we should verify that s_0 relates to λ_z via Eq. 5. In the experiment, λ_z is determined by the trap frequencies measured by the parametric resonance, and s_0 is extracted from the best fit of the expansion data in Fig. 2. The universal relation between s_0 and $\gamma \equiv \sqrt{1/\lambda_z - 1/4}$ is plotted in Fig. 3A. $s_0(\gamma)$ can fit very well with a linear function $s_0 = \kappa\gamma$, which gives the slope $\kappa = 1.94 \pm 0.03$ for the noninteracting case and $\kappa = 1.53 \pm 0.03$ for the unitary Fermi gas. These are in good agreement with $\omega_b = 2$ for the noninteracting case and $\omega_b = \sqrt{12/5} = 1.55$ for the unitary case. The Efimovian expansion is also robust and insensitive to the temperature and atom number of the Fermi gas (Fig. 3B).

Second, we notice that the noninteracting and the unitary cases only differ in the relation between s_0 and λ, and once s_0 is given to be the same, the dynamics are exactly identical for these two different systems (Fig. 3, C and D). In other words, $\mathcal{R}_z/\mathcal{R}_z(0)$ is a function of s_0 (or φ) and t/t_0 is a universal function for all scale-invariant systems.

Finally, we study a time-reversed compression process. Consider an expansion process from t_0 to t_f, where the trap frequency decreases from $\omega_0 = 1/(\sqrt{\lambda}t_0)$ to $\omega_f = 1/(\sqrt{\lambda}t_f)$. Now we consider an inverted process of increasing the trap frequency as $\omega = 1/(\sqrt{\lambda}(t_f + t_0 - t))$, where the trap frequency increases from ω_f to ω_0 when t changes from t_0 to t_f. For the compression dynamics to really invert the expansion dynamics, t_f has to be carefully chosen to satisfy $t_f = e^{2\pi n/s_0}t_0$. We perform such an experiment (Fig. 4) showing that the dynamical process with a carefully chosen boundary is time-reversal symmetric. The small asymmetry arises because the lowering of the trap during expansion (black dots) causes evaporative cooling, which decreases cloud sizes correspondingly.

Our results are universal for all scale-invariant quantum gases. Future experiments can test them with a Tonks gas in 1D and in a 2D quantum gas, where the deviation from the log-periodic behavior can be used to calibrate the scaling symmetry anomaly in 2D (*36*–*39*). In the 3D case, it will be interesting to investigate the scaling symmetry breaking when the system is tuned away from the scale-invariant points of zero and infinite s-wave scattering length. The study could also be generalized to observe a dynamic analogy of a recently proposed super-Efimov effect (*40*–*42*).

REFERENCES AND NOTES

1. J. Kinast *et al.*, *Science* **307**, 1296–1299 (2005).
2. S. Nascimbène, N. Navon, K. J. Jiang, F. Chevy, C. Salomon, *Nature* **463**, 1057–1060 (2010).
3. M. Horikoshi, S. Nakajima, M. Ueda, T. Mukaiyama, *Science* **327**, 442–445 (2010).
4. N. Navon, S. Nascimbène, F. Chevy, C. Salomon, *Science* **328**, 729–732 (2010).
5. M. J. H. Ku, A. T. Sommer, L. W. Cheuk, M. W. Zwierlein, *Science* **335**, 563–567 (2012).
6. L. A. Sidorenkov *et al.*, *Nature* **498**, 78–81 (2013).
7. C. Cao *et al.*, *Science* **331**, 58–61 (2011).
8. A. Sommer, M. Ku, G. Roati, M. W. Zwierlein, *Nature* **472**, 201–204 (2011).
9. D. Stadler, S. Krinner, J. Meineke, J.-P. Brantut, T. Esslinger, *Nature* **491**, 736–739 (2012).
10. J.-P. Brantut *et al.*, *Science* **342**, 713–715 (2013).
11. M. Koschorreck, D. Pertot, E. Vogt, M. Köhl, *Nat. Phys.* **9**, 405–409 (2013).
12. A. B. Bardon *et al.*, *Science* **344**, 722–724 (2014).
13. E. Elliott, J. A. Joseph, J. E. Thomas, *Phys. Rev. Lett.* **112**, 040405 (2014).
14. V. Efimov, *Phys. Lett. B* **33**, 563–564 (1970).
15. E. Braaten, H.-W. Hammer, *Phys. Rep.* **428**, 259–390 (2006).
16. T. Kraemer *et al.*, *Nature* **440**, 315–318 (2006).
17. S. Knoop *et al.*, *Nat. Phys.* **5**, 227–230 (2009).
18. J. R. Williams *et al.*, *Phys. Rev. Lett.* **103**, 130404 (2009).
19. S. E. Pollack, D. Dries, R. G. Hulet, *Science* **326**, 1683–1685 (2009).
20. M. Berninger *et al.*, *Phys. Rev. Lett.* **107**, 120401 (2011).
21. S. Roy *et al.*, *Phys. Rev. Lett.* **111**, 053202 (2013).
22. R. S. Bloom, M.-G. Hu, T. D. Cumby, D. S. Jin, *Phys. Rev. Lett.* **111**, 105301 (2013).
23. M. Kunitski *et al.*, *Science* **348**, 551–555 (2015).
24. M. Zaccanti *et al.*, *Nat. Phys.* **5**, 586–591 (2009).
25. B. Huang, L. A. Sidorenkov, R. Grimm, J. M. Hutson, *Phys. Rev. Lett.* **112**, 190401 (2014).
26. S. K. Tung, K. Jiménez-García, J. Johansen, C. V. Parker, C. Chin, *Phys. Rev. Lett.* **113**, 240402 (2014).
27. R. Pires *et al.*, *Phys. Rev. Lett.* **112**, 250404 (2014).
28. M. H. Anderson, J. R. Ensher, M. R. Matthews, C. E. Wieman, E. A. Cornell, *Science* **269**, 198–201 (1995).
29. K. B. Davis *et al.*, *Phys. Rev. Lett.* **75**, 3969–3973 (1995).

30. K. M. O'Hara, S. L. Hemmer, M. E. Gehm, S. R. Granade, J. E. Thomas, *Science* **298**, 2179–2182 (2002).
31. C. Fort *et al.*, *Phys. Rev. Lett.* **95**, 170410 (2005).
32. L. Sanchez-Palencia *et al.*, *Phys. Rev. Lett.* **98**, 210401 (2007).
33. M. Greiner, O. Mandel, T. Esslinger, T. W. Hänsch, I. Bloch, *Nature* **415**, 39–44 (2002).
34. Y. Castin, *C. R. Phys.* **5**, 407–410 (2004).
35. L. P. Pitaevskii, A. Rosch, *Phys. Rev. A* **55**, R853–R856 (1997).
36. E. Vogt *et al.*, *Phys. Rev. Lett.* **108**, 070404 (2012).
37. J. Hofmann, *Phys. Rev. Lett.* **108**, 185303 (2012).
38. E. Taylor, M. Randeria, *Phys. Rev. Lett.* **109**, 135301 (2012).
39. C. Gao, Z. Yu, *Phys. Rev. A* **86**, 043609 (2012).
40. Y. Nishida, S. Moroz, D. T. Son, *Phys. Rev. Lett.* **110**, 235301 (2013).
41. A. G. Volosniev, D. V. Fedorov, A. S. Jensen, N. T. Zinner, *J. Phys. At. Mol. Opt. Phys.* **47**, 185302 (2014).
42. C. Gao, J. Wang, Z. Yu, *Phys. Rev. A* **92**, 020504 (2015).

ACKNOWLEDGMENTS

We thank P. Zhang for helpful discussions. This research is supported by the National Natural Science Foundation of China (NSFC) (grant nos. 11374101 and 91536112) and the Shu Guang project (14SG22) of Shanghai Municipal Education Commission and Shanghai Education Development Foundation. Z.S. and H.Z. are supported by MOST (grant no. 2016YFA0301604), Tsinghua University Initiative Scientific Research Program and NSFC grant no. 11325418. R.Q. is supported by the Fundamental Research Funds for the Central Universities and the Research Funds of Renmin University of China under grant no. 15XNLF18 and no. 16XNLQ03.

SUPPLEMENTARY MATERIALS

www.sciencemag.org/content/353/6297/371/suppl/DC1
Materials and Methods
Supplementary Text
Figs. S1 to S3
Table S1
References (*43*, *44*)

13 December 2015; accepted 21 June 2016
10.1126/science.aaf0666

PHYSICS

Electron microscopy of electromagnetic waveforms

A. Ryabov[1,2] and P. Baum[1,2]*

Rapidly changing electromagnetic fields are the basis of almost any photonic or electronic device operation. We report how electron microscopy can measure collective carrier motion and fields with subcycle and subwavelength resolution. A collimated beam of femtosecond electron pulses passes through a metamaterial resonator that is previously excited with a single-cycle electromagnetic pulse. If the probing electrons are shorter in duration than half a field cycle, then time-frozen Lorentz forces distort the images quasi-classically and with subcycle time resolution. A pump-probe sequence reveals in a movie the sample's oscillating electromagnetic field vectors with time, phase, amplitude, and polarization information. This waveform electron microscopy can be used to visualize electrodynamic phenomena in devices as small and fast as available.

Electron microscopy works at wavelengths 100,000× smaller than that of light and therefore allows studying matter and materials with subatomic resolution (*1*, *2*). With added temporal resolution, ultrafast reaction paths in physical and chemical transitions can also be recorded (*3*, *4*).

Rather elusive for electron microscopy, however, have been electrodynamic phenomena, although oscillating currents and fields are fundamental to the operation of almost any information processing device or metamaterial. Based on differential phase contrast (*5*, *6*), ptychography (*7*), or laser-electron energy exchange techniques (*8*), electron microscopy studies on electromagnetism could reveal electrostatic field distributions (*9*–*11*), ultrafast carrier diffusions (*12*, *13*), or cycle-averaged nanophotonic dynamics (*14*–*16*), but so far not the fundamental electromagnetic waveforms with their rapidly oscillating field vectors.

We merged the electron microscope's supremacy in matter characterizations with a subcycle and subwavelength access to electromagnetic phenomena (Fig. 1). Femtosecond electron pulses (Fig. 1, blue) at 70 keV central energy are generated by pulsed-laser photoemission (*17*). The electron wavepackets (*18*) are further compressed in time by a terahertz field (Fig. 1, red) in grazing incidence to a foil (*19*). Alternatives here could be beam blanking (*20*), microwave compression (*18*), photon-gating (*21*), or ponderomotive bunching (*22*). A magnetic lens (Fig. 1, gray) widens the beam for passage through the sample with close-to-zero divergence. The proof-of-principle sample is a metal split-ring resonator (Fig. 1, yellow), which is a typical building block for metamaterials (*23*) or surfaces (*24*) with optical effects otherwise not available (*25*, *26*). The resonator with ~250 μm radius is excited with a single-cycle, phase-locked electromagnetic pulse of 0.1 to 0.8 THz bandwidth (*17*). It propagates along the z axis with a linear polarization oriented ~5° off the y axis. The electron pulse duration at the sample is ~15 times shorter than the excitation half-cycle. An objective magnetic lens (Fig. 1, gray) magnifies the shadowed electron beam onto a screen (Fig. 1, green). Some intentional defocus makes the scheme sensitive to local beam deflections (Fig. 1, dotted lines) and allows concluding from the distorted screen images, taken at a sequence of electron/field delay times, to the time-frozen electrodynamics in the sample.

First results are shown in Fig. 2, obtained with the excitation field depicted in Fig. 2A and at a magnification of about 5×. The electron pulses are characterized by streaking (*19*) and have 80-fs duration (Fig. 2B). The resonator, which was laser-machined into 30-μm-thick aluminum foil (Fig. 2C), shows some imperfections, in particular fringy edges and off-center circles. An isosurface of the time-dependent shadow pattern deformations reveals pronounced temporal oscillations (Fig. 2D). The raw images (shown

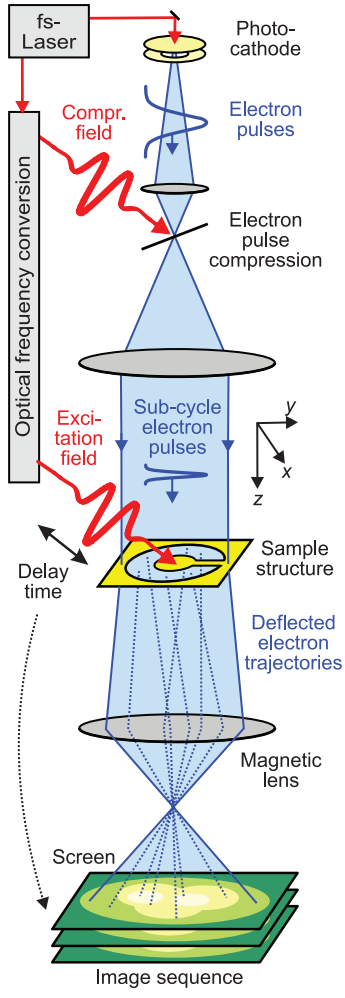

Fig. 1. Concept and experimental setup. A femtosecond laser produces single-cycle terahertz pulses (red) and a beam of femtosecond electron pulses (blue). The terahertz radiation compresses the electrons in time and also triggers electromagnetic resonance in the sample (yellow). The electron pulses are locally and instantaneously distorted (dotted lines) and therefore reveal the electrodynamics of the sample.

[1]Ludwig-Maximilians-Universität München, Am Coulombwall 1, 85748 Garching, Germany. [2]Max Planck Institute of Quantum Optics, Hans-Kopfermann-Straße 1, 85748 Garching, Germany.
*Corresponding author. Email: peter.baum@lmu.de

for a subset of pump-probe delays (in Fig. 2E) become distorted in a self-overlapping way before returning to the original at later times (movie S1). Another example of raw data is shown in movie S2.

For analyzing our experiment, we denote the spatiotemporal electric and magnetic fields around the resonator with $E(x, y, z, t)$ and $B(x, y, z, t)$. $v_{el} \approx 0.53c$ is the electron velocity (c, speed of light), $\tau_{el} \approx 80$ fs (full width at half maximum) is the electron pulse duration, $f_{max} \approx 0.8$ THz is the highest frequency excited, $D_z \approx 30$ μm is the mode thickness along the z axis, and $\alpha_{em} \approx 60$ μrad (root mean square) is the beam divergence at the sample (~20 nm source emittance and ~340 μm beam radius). We make these approximations: (i) $\tau_{el} \ll 1/f_{max}$, the electron pulses are much shorter than a wave cycle; (ii) $D_z/v_e \ll 1/f_{max}$, subcycle transition time; (iii) $\alpha_{em} \approx 0$, the probe beam is collimated; (iv) two-dimensional fields $E_{x,y}(x, y, t)$ and $B_{x,y}(x, y, t)$ suitably describe the resonator response; and (v) magnetic fields are negligible (*17*). Conditions (i) and (ii) are essential to the concept, and (iii) to (v) are specific to the particular geometry. With m_e and e the electron mass and charge, respectively, we obtain for the change in angles $\alpha_{x,y}$ at each position in the beam, at each pump-probe delay τ

$$\alpha_{x,y}(x, y, \tau) \approx \frac{eE_{x,y}(x, y, \tau)D_z}{m_e v_e^2} \quad (1)$$

Each ray in the electron beam profile acquires a local-field–dependent momentum kick that is directly proportional to the local waveform, frozen in time at the chosen probe delay.

On the screen, electrons from faraway locations can end up at the same positions, and inversion is nonbijective. We therefore measured for each pump-probe delay a batch of screen images, in which the excitation peak field strength E_{exc} is gradually increased from zero to the available maximum. Because of the collimated illumination, this method is related to measuring the evolution of the distorted beam profile along the z axis. The data set is four-dimensional and comprises 250 by 250 image pixels, 150 pump-probe delays, and 16 different excitation field strengths. At a 50-kHz pump-probe repetition rate, the total accumulation time is ~1 hour. We calculated $\alpha_{x,y}(x, y, \tau)$ for each delay step with a least-square fitting algorithm (*17*) and $E_{x,y}(x, y, \tau)$ via Eq. 1.

Shown in Fig. 3A are three vector-field snapshots at 2.8, 3.2, and 3.8 ps delay, respectively, as a subset of the full results (movie S3). The triangle tips denote the vectorial direction, and field strength is encoded in color and size. Some high-frequency temporal noise was diminished with a low-pass Gaussian filter at 1 THz. The vector field at 2.8 ps shows three local maxima (Fig. 3A, top, right, and left). We see an asymmetry in x, a predominantly radial polarization everywhere, and at each angle, a radially decreasing field strength. The peak field is 7 V/μm, which is ~3.5 times higher than the driving field. Shown in Fig. 3B are the time-dependent electric fields at two selected positions (Fig. 3A, white circles), and the time-dependent polarization is plotted in Fig. 3B, right. The fields initially follow the single-cycle excitation pulse, but after ~4 ps, when the excitation has diminished, they evolve into slower oscillation cycles with decaying amplitude. Fitting each such time trace with a damped-harmonic oscillator model reveals a map of central frequencies (0.27 to 0.30 THz), dampings (3 to 6 ps), and group delays (±0.1 ps). These ranges indicate that a single delocalized mode is predominant after the excitation.

An analysis of the collective carrier motion causing the observed near-field dynamics is shown in Fig. 3C. The surface charge density $\sigma = \varepsilon_0 E_\perp$ is plotted along a path around the inner edge of the resonator. The peak charge is ~400 $e/\mu m^2$, and ~20 $e/\mu m^2$ are detectable above the noise. Three spatial regions are evident, one at the top (±180°) and two others left and right of the gap (~±45°). The dynamics around the gap extend by more than ±90° and the phase is shifted with respect to the top region. Some features in Fig. 3C have a tilt, indicating in part an azimuthally traveling excitation, which is also observable in the raw data and result movies (movies S1 and S3, respectively). Circular motion ceases after ~4 ps, and the remaining dynamics are mostly symmetric with the x axis. It appears that the excitation first localizes at the gap and top half, while subsequently creating a spread out, rather symmetric, and longer lived mode with mostly radial polarization.

Next, we used our waveform electron microscopy to characterize a rectangular aperture and butterfly resonator, which are typical elements for field enhancement in optics. A snapshot at 2.2 ps delay of the field in the slit (730 by 100 μm^2) is shown in

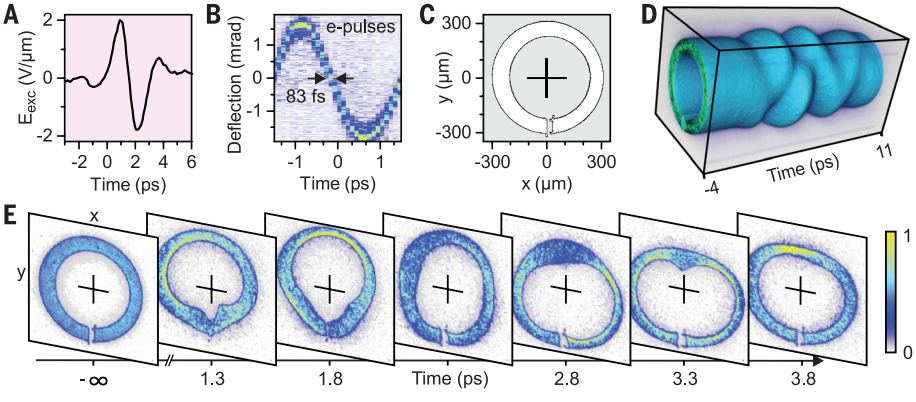

Fig. 2. Waveform microscopy results. (**A**) Electric field for sample excitation. (**B**) Electron pulse characterization (*19*). (**C**) Shape of the split-ring resonator. (**D**) Isosurface of the time-dependent shadow images. (**E**) Subset of raw images on the screen (full results in movies S1 and S2).

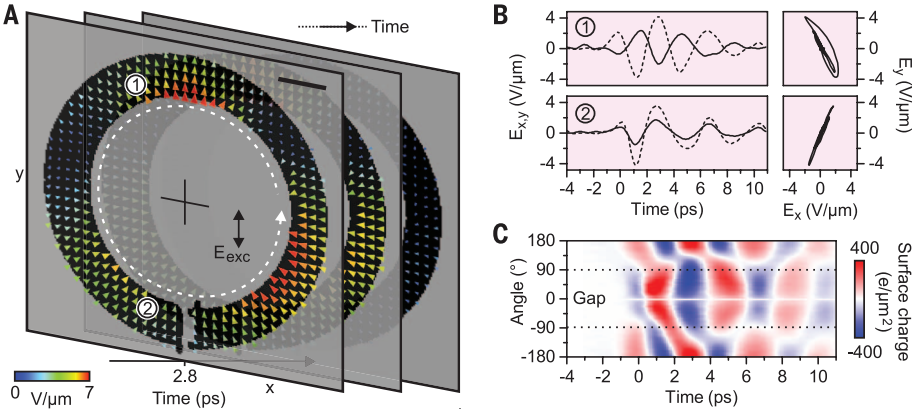

Fig. 3. Space-time-field results in a split-ring resonator. (**A**) Time-frozen electric field vectors at three delay times (full results in movie S3). Scale bar, 100 μm. (**B**) Time-dependent fields (left) and polarizations (right) at locations (1) and (2) in (A). (**C**) Space-time map of the surface carrier density at the inner edge [(A), white dashed line].

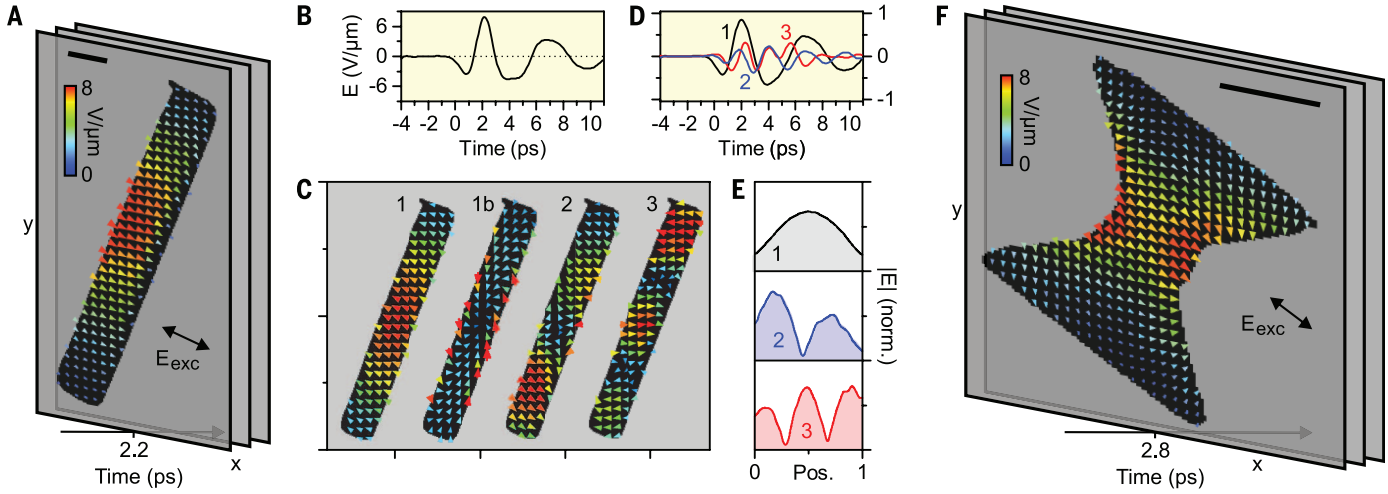

Fig. 4. Rectangle and butterfly resonators. (**A**) Time-frozen electric field vectors at 2.2 ps delay (full results in movie S4). (**B**) Time-dependent field at the center. (**C**) First four modes revealed through singular value decomposition. (**D**) Time traces (amplitudes, scaled) of modes 1, 2, and 3. (**E**) Electric field strengths along a line through the center. (**F**) Butterfly resonator, electric field vectors at 2.8 ps delay (full results in movie S5). Scale bars, 100 μm.

Fig. 4A (full results in movie S4). The waveform in the center is shown in Fig. 4B. The frequency at early times is higher than at later times, when the oscillations show a nonharmonic shape with damped peak regions. This indicates the presence of multiple modes at different frequencies, but phase-locked. In order to find those, we invoked a principle component analysis via singular value decomposition. The first four modes are depicted in Fig. 4C; further ones have no clear shape or time structure anymore. Three of the modes have a series of maxima that are almost equidistantly distributed over the slit length. Mode 1b is different and has a shape with vortex polarization; we attribute this to residual magnetic field effects (*17*) and a slight tilt of the structure with respect to the electron beam. The time traces from the decomposition matrix are shown in Fig. 4D. Mode 1 is centered at 0.20 THz, mode 2 at 0.39 THz, and mode 3 at 0.54 THz. Cuts through the modes along the slit's long axis at center are shown in Fig. 4E. Evident are one, two, and three spatial maxima, respectively, but with some asymmetries and slightly elliptical polarization in modes 2 and 3. Singular value decomposition neither assumes any electromagnetic boundary conditions nor enforces harmonic-oscillator solutions. That nevertheless a series of oscillation orders with dispersion and nontrivial phase relations can be identified is a virtue of the complete spatial, temporal, and vectorial data set obtained with waveform electron microscopy. In the butterfly-shaped resonator (Fig. 4F and movie S5), there is only one mode excited (frequency, 0.3 THz; damping, ~5 ps). The field enhancement at 2.8 ps is ~9 close to the metal and ~6 in the middle, which is lower than desirable, because the rounded crests of our structure apparently disperse the field lines at the center.

The ability to record field vectors in space and time is essentially a consequence of the electron's charge, which is usually detrimental in ultrafast microscopy via space charge effects, but here the charge is exploited as a local, sensitive, directional, and noninvasive probe of electromagnetic field cycles. We estimate the angular and spatial resolutions achievable in a state-of-the-art instrument at few-nanometer resolution by invoking a ray-optical analysis (*17*). The result is plotted in fig. S4 in dependence on defocus. Letting the spatial resolution degrade by only a factor of two from the optimum value is already sufficient for an angular resolution below 20 μrad. Via Eq. 1 and assuming a 100-nm-deep structure along the z axis, we obtained a measurable field strength of ~0.0026 V/nm or ~1 V per 40 nm, which overlaps with the conditions in working electronic or plasmonic circuitry. In the experiment, the angular resolution was 60 to 80 μrad (*17*), which is close to $\alpha_{em} \approx 60$ μrad of the beam. At reasonable signal-to-noise levels, the illumination's uncorrelated divergence determines the angular resolution. The ultimate limit with coherent femtosecond emitters (*27*) and a wave-based analysis (*6*, *7*) is defined by the de Broglie wavelength of the electrons.

Magnetic fields, which are important in negative-index metamaterials or memory devices, can be revealed and separated from the electric-field deflections by making two experiments at different electron velocities; the electric parts of the Lorentz force scales proportionally to $1/v_e^2$, whereas the magnetic deflection follows a $1/v_e$ law. Energy-filtered imaging can measure forward momentum changes and, in combination with tomography, reveal the complete electric and magnetic vector fields in space and time. Surface studies with a scanning electron microscope are also feasible, given its sensitivity to (transient) surface voltages, energy losses, or secondary electron trajectory asymmetries.

Microwave-compressed (*18*), photon-gated (*21*), or deflection-selected (*20*) electron pulses are approaching the few-femtosecond regime of pulse duration. This allows waveform imaging at multiterahertz frequencies, faster than any electronic devices available. Metamaterials operate at lightwave frequencies, at which ~1-fs resolution is required for subcycle sampling. Recently, attosecond electron pulse trains (*28*) have been realized in an electron microscope (*29*). With cycle-synchronous excitation and probing (*28*), waveform electron microscopy will enable a direct visualization of nanophotonic phenomena at lightwave frequencies. Isolated attosecond electron pulses may potentially be generated via single-electron wavepacket compression (*18*) or ponderomotive effects (*22*) and will be useful for studying nonlinear or strong-field phenomena that are not reversible between adjacent excitation cycles.

In principle, any light-matter interaction starts with atomic-scale charge displacements, and waveform electron microscopy at subatomic resolution (*5*, *6*) could potentially reveal those motions. More straightforward, however, will be studies of collective carrier dynamics and field effects in nanoscale devices—for example, in electronics, metamaterials, nanophotonic circuitry, near-field sensors, or light-harvesting nanostructures. That waveform imaging and shape characterization now require only one instrument—the electron microscope—will likely be advantageous for such investigations.

REFERENCES AND NOTES

1. P. E. Batson, N. Dellby, O. L. Krivanek, *Nature* **418**, 617–620 (2002).
2. R. Erni, M. D. Rossell, C. Kisielowski, U. Dahmen, *Phys. Rev. Lett.* **102**, 096101 (2009).
3. A. H. Zewail, *Science* **328**, 187–193 (2010).
4. R. J. D. Miller, *Science* **343**, 1108–1116 (2014).
5. N. Shibata *et al.*, *Nat. Phys.* **8**, 611–615 (2012).
6. K. Müller *et al.*, *Nat. Commun.* **5**, 5653 (2014).
7. M. J. Humphry, B. Kraus, A. C. Hurst, A. M. Maiden, J. M. Rodenburg, *Nat. Commun.* **3**, 730 (2012).
8. B. Barwick, D. J. Flannigan, A. H. Zewail, *Nature* **462**, 902–906 (2009).
9. J. Cumings, A. Zettl, M. R. McCartney, J. C. H. Spence, *Phys. Rev. Lett.* **88**, 056804 (2002).
10. M. Lohr *et al.*, *Ultramicroscopy* **117**, 7–14 (2012).
11. N. Shibata *et al.*, *Sci. Rep.* **5**, 10040 (2015).

12. M. Müller, A. Paarmann, R. Ernstorfer, *Nat. Commun.* **5**, 5292 (2014).
13. E. Najafi, T. D. Scarborough, J. Tang, A. Zewail, *Science* **347**, 164–167 (2015).
14. A. Yurtsever, R. M. van der Veen, A. H. Zewail, *Science* **335**, 59–64 (2012).
15. E. Quinonez, J. Handali, B. Barwick, *Rev. Sci. Instrum.* **84**, 103710 (2013).
16. L. Piazza *et al*., *Nat. Commun.* **6**, 6407 (2015).
17. Materials and methods are available as supplementary materials on *Science* Online.
18. A. Gliserin, M. Walbran, F. Krausz, P. Baum, *Nat. Commun.* **6**, 8723 (2015).
19. C. Kealhofer *et al*., *Science* **352**, 429–433 (2016).
20. A. Lassise, P. H. A. Mutsaers, O. J. Luiten, *Rev. Sci. Instrum.* **83**, 043705 (2012).
21. M. T. Hassan, H. Liu, J. S. Baskin, A. H. Zewail, *Proc. Natl. Acad. Sci. U.S.A.* **112**, 12944–12949 (2015).
22. L. J. Wong, B. Freelon, T. Rohwer, N. Gedik, S. G. Johnson, *New J. Phys.* **17**, 013051 (2015).
23. N. I. Zheludev, *Science* **328**, 582–583 (2010).
24. A. V. Kildishev, A. Boltasseva, V. M. Shalaev, *Science* **339**, 1232009 (2013).
25. R. A. Shelby, D. R. Smith, S. Schultz, *Science* **292**, 77–79 (2001).
26. X. Ni, Z. J. Wong, M. Mrejen, Y. Wang, X. Zhang, *Science* **349**, 1310–1314 (2015).
27. D. Ehberger *et al*., *Phys. Rev. Lett.* **114**, 227601 (2015).
28. P. Baum, A. H. Zewail, *Proc. Natl. Acad. Sci. U.S.A.* **104**, 18409–18414 (2007).
29. A. Feist *et al*., *Nature* **521**, 200–203 (2015).

ACKNOWLEDGMENTS

This work was supported by ERC and Munich-Centre for Advanced Photonics. We thank F. Krausz for awesome support and discussions and acknowledge I. Zhuravlev (Vocord SoftLab) for help with GPU programming.

SUPPLEMENTARY MATERIALS

www.sciencemag.org/content/353/6297/374/suppl/DC1
Materials and Methods
Figs. S1 to S4
References (*30*–*36*)
Movies S1 to S5

13 April 2016; accepted 23 June 2016
10.1126/science.aaf8589

WATER RESOURCES

Connections between groundwater flow and transpiration partitioning

Reed M. Maxwell[1]* and Laura E. Condon[2]

Understanding freshwater fluxes at continental scales will help us better predict hydrologic response and manage our terrestrial water resources. The partitioning of evapotranspiration into bare soil evaporation and plant transpiration remains a key uncertainty in the terrestrial water balance. We used integrated hydrologic simulations that couple vegetation and land-energy processes with surface and subsurface hydrology to study transpiration partitioning at the continental scale. Both latent heat flux and partitioning are connected to water table depth, and including lateral groundwater flow in the model increases transpiration partitioning from 47 ± 13 to 62 ± 12%. This suggests that lateral groundwater flow, which is generally simplified or excluded in Earth system models, may provide a missing link for reconciling observations and global models of terrestrial water fluxes.

Evapotranspiration (*ET*) is the largest terrestrial water flux, typically accounting for more water than runoff and for about 60% of precipitation (*1*). It contributes a substantial portion of the global land-energy budget (*2*) as latent heat (*LH*) flux, which affects regional climate (*3*). Evapotranspiration commonly refers to the combination of all evaporation (*E*) from bare soil, water bodies, plant canopy, and sublimation from snow, and transpiration (*T*) through plant stoma during photosynthesis. Here we focus on the partitioning of *ET* into bare soil *E* and plant *T*. Because *T* depends on plant processes, whereas *E* depends on shallow soil moisture and energy availability, these two factors respond differently to physical drivers and stress. Disentangling these fluxes over large scales is a key step toward improved understanding and prediction of watershed dynamics, especially when considering future stresses.

Connectivity between the surface and the subsurface provides a fundamental control on water-energy fluxes and partitioning (*4*). Connections between the water table and evapotranspiration have been shown in model simulations (*5*–*9*) and observations of regional systems (*10*). Although theory to estimate and simulate evapotranspiration has evolved much over past decades (*11*), lateral groundwater flow has yet to be incorporated in continental-scale partitioning estimates (*12*). Quantifying the role of groundwater is important, because if partitioning is tied to water table depth and lateral flow, accurate predictions of future water availability will require a more detailed understanding of the underlying processes controlling groundwater surface water interactions than are currently included in most Earth system simulators. Current research on partitioning relies on either isotope approaches or land surface models (*13*). These are fundamentally different methods, but both make critical assumptions about groundwater contributions to *T* and simplify groundwater surface water interactions. Discrepancies in partitioning estimates remain, and some have suggested that it may be systematically underestimated by current Earth system models (*13*, *14*).

We used a continental-scale integrated hydrology model simulation to study the role that lateral groundwater flow plays in evapotranspiration partitioning (*15*). We used the ParFlow model (*16*, *17*), which couples groundwater and surface water flow with vegetation processes and snow dynamics (*7*, *18*) to solve a complete water and energy balance [figs. S1, S2, and S4 (*15*)]. The domain covers 6.3 million km^2 and encompasses major river basins in North America [including the Mississippi, Colorado, and Ohio basins; see Fig. 1 and fig. S3 (*15*)]. Simulations were run for one water year at hourly resolution driven by reconstructed meteorology. Transient simulations were initialized using the results of a prior steady-state model over the same domain (*19*) and additional transient model initialization [tables S1 and S2 (*15*)]. The model was compared to 1.2 million transient observations of stream flow, groundwater, and snow, and was shown to match observed behavior [figs. S5 to S20 (*15*)].

This simulation generated roughly 1.3 trillion outputs over the 1-year period, covering all key components of the water energy budget. Two variables that exemplify hydrologic stores and land-energy fluxes—water table depth and *LH* flux (the energy counterpart to *ET*)—show many scales of detail within these output fields (Fig. 1). For example, although groundwater is generally shallower in the more humid eastern region of the domain and deeper in arid western regions, laterally convergent flow drives local variability, creating shallow water tables in river valleys that can supply surface water export. We see similar patterns in *LH* flux, large-scale trends also driven by climate gradients, yet nested hillsllope-scale fluctuations persist.

The integrated model we used provides the ability to explicitly evaluate interactions between variables that are excluded from other global approaches (i.e., water table depth and individual land-energy flux components such as *T* and *E*). For example, the ratios of plant transpiration to total evapotranspiration (*T*/*ET*) are calculated directly from model outputs and compared to compiled stand-scale (*14*) and global (*4*, *20*, *21*) isotopically based partitioning estimates [Fig. 2, A and B (*15*)]. We see broad agreement between model simulations and estimates across scale; the domain-averaged *T*/*ET* of 62 ± 12% agrees with recent global isotopically derived estimates (*4*, *14*, *20*, *21*).

To determine the role of lateral groundwater flow in these partitioning estimates, we performed a second simulation that is identical to the base case but allowed only vertical water movement, with no topographic influences or lateral flow. This approach is similar to current practice in land surface models (*15*). This "no lateral flow" simulation resulted in a domain-averaged *T*/*ET*

[1]Integrated GroundWater Modeling Center, Department of Geology and Geological Engineering, Colorado School of Mines, Golden, CO, USA. [2]Department of Civil and Environmental Engineering, Syracuse University, Syracuse, NY, USA.
*Corresponding author. Email: rmaxwell@mines.edu

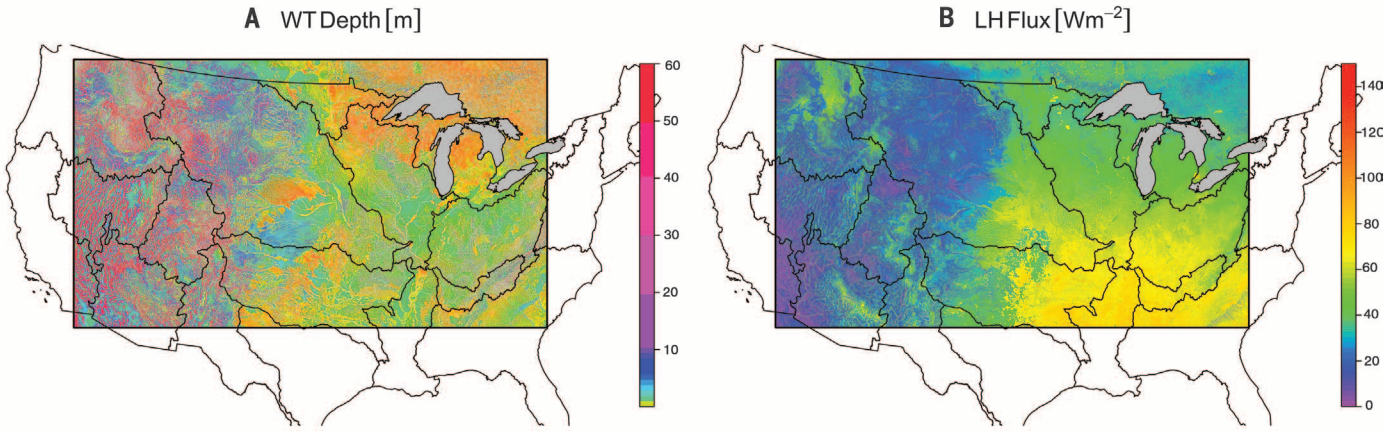

Fig. 1. Simulation results display great spatial complexity. Plots of transient (water year 1985) annually averaged water table (WT) depth (**A**) and *LH* flux (**B**) demonstrate the great detail we see in this simulation. Water table varies with climatic region; it is generally deeper west of the aridity divide and shallower in the east. Likewise, *LH* flux is also greater in less water-limited regions but exhibits larger values in river valleys, where the water table depths are locally shallow under what might otherwise be water-limited conditions.

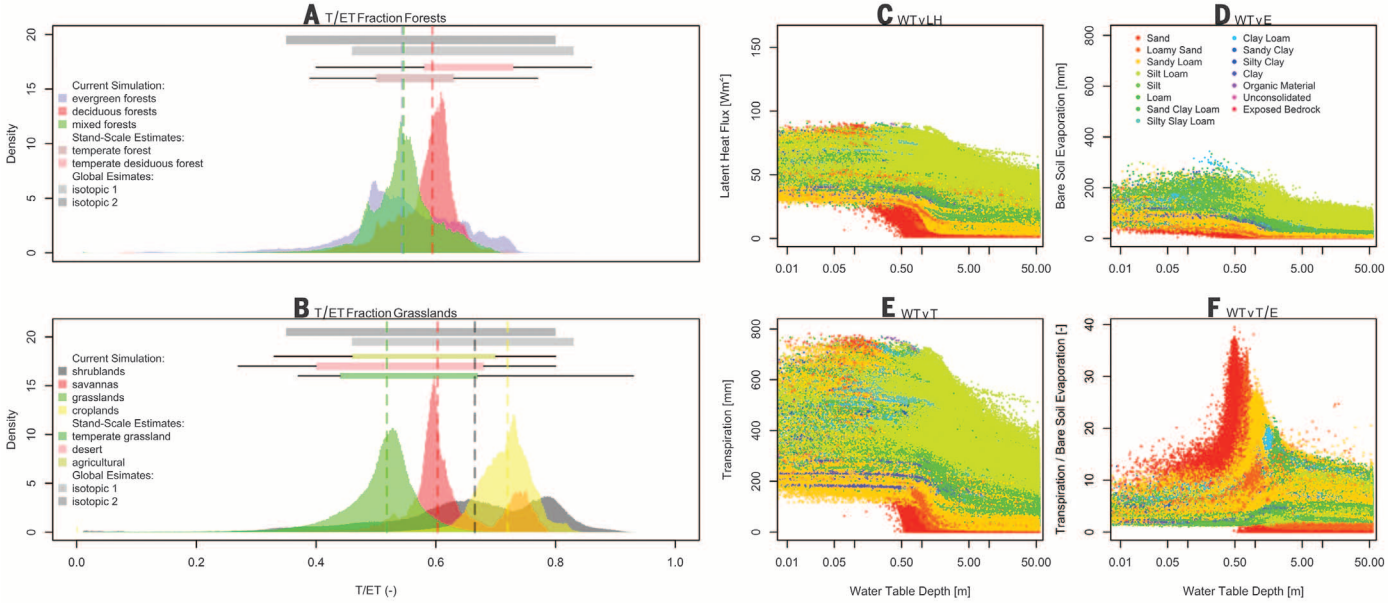

Fig. 2. Simulated annually averaged histograms of evapotranspiration partitioning compare favorably to observations and are related to water table depth. Simulated *T/ET* ratios (**A** and **B**) plotted by land cover type agree with stand-scale estimates and observations (*14*) and are bracketed by global isotopic estimates, isotopic 1 (*4*) and isotopic 2 (*20*, *21*), shown here as box plots spanning the ± mean 1 SD. Scatterplots of water table versus *LH* flux (**C**), bare soil evaporation (**D**), and *T* (**E**) suggest that groundwater's role in moderating these fluxes (*7*–*9*, *27*) extends across our continental-scale domain. When plotted as a function of water table depth, the *T/E* ratio (**F**) peaks at the middle of the groundwater critical depth range, suggesting that *T* may be as much as 35 times greater than *E* because of lateral groundwater flow.

of 47 ± 13%, suggesting that lateral groundwater flow plays a substantial role in the partitioning of evapotranspiration. This shift was seen systematically across all vegetation types, resulting in a lower prediction of stand and global scale estimates [fig. S20 (*15*)]. This indicates that topographically driven lateral flow provides an additional water source for transpiration in groundwater convergence zones.

To evaluate the relationships between partitioning and groundwater directly, we plotted the annual average *LH* flux, accumulated *T* and *E*, and *T/E* ratio against water table depth for nine tree and shrub land cover types, colored by soil type: more than 3.2 million points in total (Fig. 2, B to E). The distinct patterns shown in all four plots indicate a connection between water table depth and land-energy fluxes. Plots of *LH*, *T*, and *E* each follow logistic curves with three distinct regions: (i) an energy- or temperature-controlled region at shallow water table depths, where lateral groundwater flow stabilizes soil moisture and removes any water limitation; (ii) a deep disconnected groundwater region where surface fluxes are dependent on precipitation (i.e., water-limited); and (iii) a groundwater-controlled region discussed in prior modeling (*8*) and observational (*10*) studies, where land-energy fluxes are correlated with water table depth.

Similar to *T* and *E*, *T/E* ratios (Fig. 2F) also show a clear groundwater dependence; however, they do not follow the same logistic curve behavior as their composite fluxes. Here a maximum *T/E* partitioning [up to 35 in some locations, which also agrees with recent global isotopically derived estimates of *T/E* (*4*)] occurs at medium

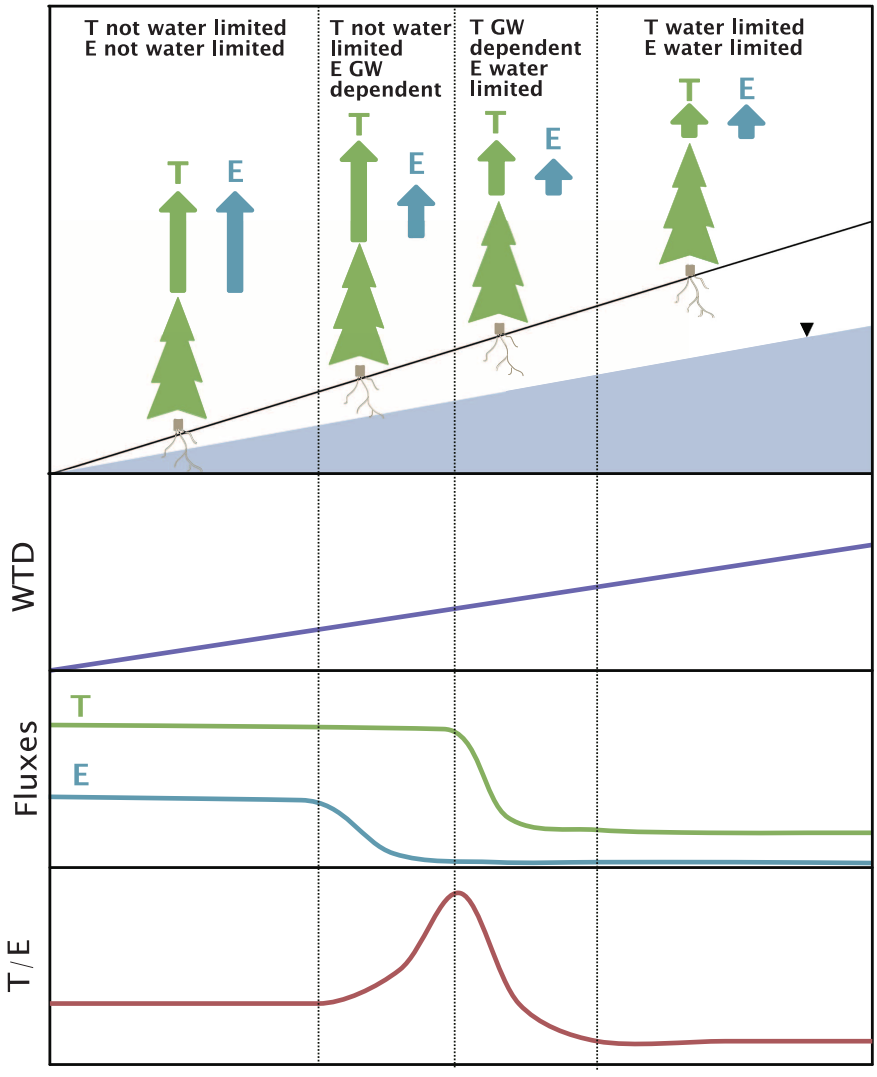

Fig. 3. The relationship between groundwater depth and land-energy fluxes for an idealized hillslope. On the left, groundwater (GW) is shallow and neither *T* or *E* is water-limited, because of lateral groundwater convergence, which stabilizes soil moisture. On the far right, groundwater is deep and disconnected from the land surface, resulting in lower *T* and *E* that are limited by precipitation. In the two center regions, *T* or *E* varies with groundwater depth, but *E* disconnects at shallower depths than *T*. As a result of these behaviors, *T/E* partitioning is sensitive to water table depth across both center regions. The peak in *T/E* reflects the differential in response to water table changes in *E* as compared to *T*. The roots as drawn here are not to scale and do not reflect potential changes in density due to water table depth, nor does this figure reflect the presence of subsurface heterogeneity.

groundwater depths (0.5 to 5 m). We showed that this change in *T/E* is due to different depths to available water for the separate *E* and *T* processes. *E* interfaces at the shallow soil surface, whereas *T* draws water deeper from within the root zone (*15*). A simple conceptual hillslope model (Fig. 3) shows that both *T* and *E* follow a similar logistic curve with respect to water table depth, but the depth range over which *E* is sensitive to water table depth is shallower than that for *T*. This shift creates a peak in *T/E* at groundwater depths where *E* is water-limited but *T* is not. This suggests that plants' access to deeper water allows them to draw water after the shallow soil is dry and can shift the balance of *T* partitioning in a manner not currently included in Earth system models.

These results indicate that integrated simulations of the terrestrial hydrologic cycle can provide insights into process interactions that are currently lacking from other approaches, and they further motivate the need to advance model development as well as observations in this area. For example, although the 1-km resolution used for this simulation is fine-scale over such a large extent, there are always processes below the grid scale that might be better represented with increased resolution. Additionally, these simulations do not include any anthropogenic influences, such as groundwater pumping, irrigation, surface water diversions, reservoirs, and urbanization. We envision a road map where these assumptions are systematically relaxed and the model is continuously reevaluated against all available observations [fig. S6 (*15*)].

Although there has been much recent debate regarding *ET* partitioning, our results suggest that lateral groundwater flow processes, currently overlooked in global approaches, may play an important role in characterizing evapotranspiration at large scales. Our integrated hydrologic simulation over most of the major river basins in continental North America suggests that groundwater not only moderates *E* and *T* over the continent, but may also increase the partitioning of *T* substantially. This underscores the importance of including lateral groundwater flow and storage in Earth system models (*22*), as well as developing careful multiscale observations of land surface fluxes and water table depth to better explore this relationship (*12*). Finally, the impact of groundwater on land-energy fluxes may have important implications for atmospheric simulation (*23*, *24*) and suggests that these feedbacks may go both ways: Changes in water table depth due to widespread worldwide pumping may have a profound influence on land-energy fluxes and climate (*25*, *26*).

REFERENCES AND NOTES

1. K. E. Trenberth, L. Smith, T. Qian, A. Dai, J. Fasullo, *J. Hydrometeorol.* **8**, 758–769 (2007).
2. K. E. Trenberth, J. T. Fasullo, J. Kiehl, *Bull. Am. Meteorol. Soc.* **90**, 311–323 (2009).
3. S. I. Seneviratne, D. Lüthi, M. Litschi, C. Schär, *Nature* **443**, 205–209 (2006).
4. S. P. Good, D. Noone, G. Bowen, *Science* **349**, 175–177 (2015).
5. J. S. Famiglietti, E. F. Wood, *Water Resour. Res.* **30**, 3061–3078 (1994).
6. G. D. Salvucci, D. Entekhabi, *Water Resour. Res.* **31**, 1725–1739 (1995).
7. S. J. Kollet, R. M. Maxwell, *Water Resour. Res.* **44**, W02402 (2008).
8. R. M. Maxwell, S. J. Kollet, *Nat. Geosci.* **1**, 665–669 (2008).
9. L. E. Condon, R. M. Maxwell, S. Gangopadhyay, *Adv. Water Resour.* **60**, 188–203 (2013).
10. J. Szilagyi, V. A. Zlotnik, J. Jozsa, *Ground Water* **51**, 945–951 (2013).
11. K. Wang, R. E. Dickinson, *Rev. Geophys.* **50**, RG2005 (2012).
12. P. D. Brooks *et al.*, *Water Resour. Res.* **51**, 6973–6987 (2015).
13. S. J. Sutanto *et al.*, *Hydrol. Earth Syst. Sci.* **18**, 2815–2827 (2014).
14. W. H. Schlesinger, S. Jasechko, *Agric. For. Meteorol.* **189–190**, 115–117 (2014).
15. Materials and methods are available as supplementary materials on *Science* Online.
16. S. J. Kollet, R. M. Maxwell, *Adv. Water Resour.* **29**, 945–958 (2006).
17. R. M. Maxwell, *Adv. Water Resour.* **53**, 109–117 (2013).
18. R. M. Maxwell, N. L. Miller, *J. Hydrometeorol.* **6**, 233–247 (2005).
19. R. M. Maxwell, L. E. Condon, S. J. Kollet, *Geosci. Model Dev.* **8**, 923–937 (2015).
20. S. Jasechko *et al.*, *Nature* **496**, 347–350 (2013).
21. A. M. J. Coenders-Gerrits *et al.*, *Nature* **506**, E1–E2 (2014).
22. M. P. Clark *et al.*, *Water Resour. Res.* **51**, 5929–5956 (2015).
23. R. M. Maxwell, F. K. Chow, S. J. Kollet, *Adv. Water Resour.* **30**, 2447–2466 (2007).
24. X. Jiang, G. Y. Niu, Z. L. Yang, *J. Geophys. Res.* **114**, D06109 (2009).
25. I. M. Ferguson, R. M. Maxwell, *Environ. Res. Lett.* **7**, 044022 (2012).
26. M. F. P. Bierkens, *Water Resour. Res.* **51**, 4923–4947 (2015).
27. J. F. Rihani, R. M. Maxwell, F. K. Chow, *Water Resour. Res.* **46**, W12523 (2010).

ACKNOWLEDGMENTS
This work was supported by the U.S. Department of Energy Office of Science, Offices of Advanced Scientific Computing Research and Biological and Environmental Sciences IDEAS project. All simulations were made possible through high-performance computing support from Yellowstone (ark:/85065/d7wd3xhc) provided by the National Center for Atmospheric Research's Computational and Information Systems Laboratory, sponsored by the National Science Foundation. The authors declare no financial conflicts. We thank M. M. Forrester for development and presentation of the graphics in figs. S1 and S6, L. Bearup for review comments, A. Bandler for assistance with surface water data processing, and D. Osei-Kuffuor for assistance with the analytical Jacobian. We also thank the anonymous reviewers for their constructive comments. All simulation data, models, and inputs are archived and are available. Specific versions of ParFlow are archived with complete documentation and may be downloaded at (http://inside.mines.edu/~rmaxwell/maxwell_software.shtml) or checked out from a commercially hosted, free SVN repository and GITHUB; r730 was the version used in this study. The input data and simulations presented here are available as supplementary materials on *Science* Online. R.M.M. and L.E.C. designed the study and prepared the input data; R.M.M. ran the numerical experiments; L.E.C. developed the model-observation comparison framework and metrics; and R.M.M. and L.E.C. synthesized the results, made the figures, and wrote the manuscript.

SUPPLEMENTARY MATERIALS
www.sciencemag.org/content/353/6297/377/suppl/DC1
Materials and Methods
Supplementary Text
Figs. S1 to S20
Tables S1 and S2
References (*28*–*68*)
Input Data
Model Output

30 March 2016; accepted 22 June 2016
10.1126/science.aaf7891

MICROBIOME

Cospeciation of gut microbiota with hominids

Andrew H. Moeller,[1,2] Alejandro Caro-Quintero,[3] Deus Mjungu,[4] Alexander V. Georgiev,[5,6] Elizabeth V. Lonsdorf,[7] Martin N. Muller,[8] Anne E. Pusey,[9] Martine Peeters,[10] Beatrice H. Hahn,[11] Howard Ochman[1]*

The evolutionary origins of the bacterial lineages that populate the human gut are unknown. Here we show that multiple lineages of the predominant bacterial taxa in the gut arose via cospeciation with humans, chimpanzees, bonobos, and gorillas over the past 15 million years. Analyses of strain-level bacterial diversity within hominid gut microbiomes revealed that clades of Bacteroidaceae and Bifidobacteriaceae have been maintained exclusively within host lineages across hundreds of thousands of host generations. Divergence times of these cospeciating gut bacteria are congruent with those of hominids, indicating that nuclear, mitochondrial, and gut bacterial genomes diversified in concert during hominid evolution. This study identifies human gut bacteria descended from ancient symbionts that speciated simultaneously with humans and the African apes.

Cospeciation is a hallmark of intimate and ancient symbiotic relationships (*1*, *2*). Humans and other mammals host communities of bacterial symbionts, which are essential for normal postnatal development and adult health. Gut bacterial community membership and abundance profiles are shaped by host genetics (*3*) and evolutionary history (*4*, *5*), but also by diet (*6*), geography (*7*), and medical intervention (*8*). External factors exert a strong influence on the composition of gut microbial communities, which are assembled anew in each host generation. It is unknown whether lineages of gut bacteria persist within individual host lineages over timescales long enough to lead to cospeciation. Here, we tested whether gut bacteria residing within present-day humans are descended from ancestral bacterial symbionts that cospeciated with humans and the African apes.

To test for cospeciation between hominids and their gut bacteria, we assessed the congruence between hominid and bacterial phylogenetic trees. Although DNA sequence data sets are available for gut microbiomes of hominids (*4*, *5*, *9*, *10*), these are based on short ribosomal RNA (rRNA) amplicons or shotgun-metagenomic data, which lack the resolution required to detect codiversification between bacterial and hominid lineages. Bacterial rRNA sequences diverge too slowly to track diversification over the time scale of hominid evolution (*11*, *12*), and shotgun metagenomic sequencing does not reliably capture orthologous genetic regions from related bacteria in different host species. Therefore, we used an amplicon sequencing approach that assays quickly evolving protein-coding regions in bacterial genomes (phyloTags) (*13*) to profile strain diversity within the gut microbiomes of humans, chimpanzees, bonobos, and gorillas. This fine-scale resolution allows inference of the phylogenies of closely related bacterial lineages, thereby enabling tests for cospeciation between gut bacteria and the Hominidae.

We amplified a variable region of the DNA gyrase, subunit B (*gyrB*) gene from bacteria present in fecal samples collected from humans living in Connecticut, USA (*Homo sapiens*; $n = 16$); wild chimpanzees from Gombe National Park, Tanzania (*Pan troglodytes*; $n = 47$); wild bonobos from three field sites in the Democratic Republic of the Congo (*Pan paniscus*; $n = 24$); and wild gorillas from two field sites in Cameroon (*Gorilla gorilla*; $n = 24$) (table S1 and fig. S1). We used multiple sets of primers, each designed to target one of three bacterial families prominent in the gut microbiome (*13*): the Bifidobacteriaceae, the Bacteroidaceae, or the Lachnospiraceae. Amplicons were sequenced on the Illumina MiSeq platform, generating 4,578,632 reads averaging 41,249 reads per sample. Sequences were screened for quality in QIIME (*14*) and filtered to eliminate sequencing errors (*15*) (data files S1 to S3), and the relative frequencies of Bacteroidaceae, Bifidobacteriaceae, and Lachnospiraceae strains recovered from each sample were recorded (tables S2 to S4). Phylogenetic analyses were performed separately for each bacterial family. Sequences were aligned with ClustalW as implemented in MEGA 6.0 (*16*), and maximum-likelihood trees were constructed with a general time-reversible plus invariant sites (GTR+I) model of nucleotide substitution. Relative node ages of maximum-likelihood trees were estimated in BEAST (*17*).

The phylogenetic relationships among the Bacteroidaceae strains from the Hominidae mirror the relationships of their host species (Fig. 1). Previous studies of the microbiota of the Hominidae compared the overall composition of their microbial communities (i.e., beta diversity) (*4*, *5*, *9*, *10*), but our phylogenetic analysis allowed us to trace the evolution of individual bacterial lineages. We recovered three well-supported clades (i.e., clades in which the relationships among the bacterial lineages derived from different host species were supported by more than 50% of bootstrap replicates) that contain strains from more than two host species (Fig. 1, A to C). The topology of each of these clades indicates ancient cospeciation between the Bacteroidaceae and the Hominidae: Within each of these clades, strains recovered from bonobos and chimpanzees form separate sister groups, which together form a clade that is sister to either gorilla-derived (Fig. 1, A and B) or human-derived (Fig. 1C) strains.

The dominant pattern of diversification has been the parallel cospeciation of multiple Bacteroidaceae lineages with their hominid host lineages (Fig. 1A). However, in one case along the branch leading to *Pan*, two Bacteroidaceae lineages arose

[1]Department of Integrative Biology, 2506 Speedway A5000, University of Texas at Austin, Austin, TX 78712, USA. [2]Miller Institute for Basic Research in Science, 2536 Channing Way, University of California, Berkeley, CA 94720, USA. [3]Corpoicá C.I Tibaitata, Santa Fe de Bogotá, Bogotá, Colombia. [4]Gombe Stream Research Center, Kigoma, Tanzania. [5]Department of Anthropology, Northwestern University, 1810 Hinman Avenue, Evanston, IL 60208, USA. [6]Department of Human Evolutionary Biology, Harvard University, 11 Divinity Avenue, Cambridge, MA 02138, USA. [7]Department of Psychology and Biological Foundations of Behavior Program, LSP 261B, Franklin and Marshall College, Lancaster, PA 17603, USA. [8]Department of Anthropology, University of New Mexico, MSC01-1040, Albuquerque, NM 87131, USA. [9]Department of Evolutionary Anthropology, 101 Biological Sciences Building, Duke University, Durham, NC 27708, USA. [10]Institut de Recherche pour le Développement, University of Montpellier, 34394 Montpellier, France. [11]Departments of Medicine and Microbiology, Perelman School of Medicine, 409 Johnson Pavilion, University of Pennsylvania, Philadelphia, PA 19104, USA.
***Corresponding author. Email: howard.ochman@austin.utexas.edu**

from a single ancestral lineage without a host split, and each subsequently codiversified with chimpanzees and bonobos (Fig. 1B). This instance of strain divergence within a single host lineage is analogous to a gene duplication event, in which a single ancestral gene gives rise to two distinct loci within a genome. In some cases (e.g., Fig. 1, A and B), bacterial lineages have been lost from the human population, consistent with previous observations that humans have a depleted microbiome relative to those in wild-living African apes (*5*). No close gorilla-derived relatives of the strains represented in Fig. 1C were detected. This bacterial group was either acquired on the lineage leading to humans, chimpanzees, and bonobos, or lost from the lineage leading to gorillas. The lack of detection of human-derived representatives from the clades depicted in Fig. 1, A and B, and of gorilla-derived representatives from the clade depicted in Fig. 1C is unlikely to be caused by primer bias, as the Bacteroidaceae primers used captured a broad diversity of human-derived and gorilla-derived Bacteroidaceae lineages from closely related clades (data file S4). Reanalysis of a previously reported data set (*18*) that includes the V4 region of 16*S* ribosomal DNA sequences recovered from sympatric chimpanzees (n = 9) and gorillas (n = 15) (10,028 to 110,324 reads per sample) living in Cameroon revealed no shared 99% Bacteroidaceae operational taxonomic units (OTUs) between these sympatric populations. Because *gyrB* phyloTAGs are hierarchically embedded within 16*S* OTUs (*13*), the observation that sympatric chimpanzees and gorillas harbor entirely nonoverlapping sets of 16*S* Bacteroidaceae OTUs indicates that sympatric chimpanzees and gorillas maintain distinct Bacteroidaceae *gyrB* lineages, although we cannot rule out the possibility that some lineages are shared at low, undetected abundances.

Other well-supported clades of Bacteroidaceae were recovered from more restricted (i.e., two or fewer) sets of host species; however, the relationships among these clades could not be resolved, and they could not be used to test for cospeciation. These included two clades from bonobos, three clades from chimpanzees, three clades from humans, four clades from gorillas, and three clades from humans and chimpanzees (data file S4). In all but two of these clades, strains derived from the same host species constitute monophyletic groups, confirming that bacterial strains have diversified within their respective host species. In the other two cases, unique strains recovered from chimpanzees fall within a clade recovered from humans (fig. S2), indicative of past rare strain transfers between humans and chimpanzees. The short branch lengths of the chimpanzee-derived Bacteroidaceae lineages of human origin imply that the transfers were relatively recent.

Results for the Bifidobacteriaceae resemble those for the Bacteroidaceae. The phylogeny of the 307 Bifidobacteriaceae strains recovered from the Hominidae also mirrors the phylogeny of the host species (Fig. 1D and data file S5). However, one clade of gorilla-derived Bifidobacteriaceae strains is sister to the clade of bonobo-derived strains. Hence, there appears to have been a transfer of a Bifidobacteriaceae lineage from *Pan* into gorillas (Fig. 1D). Branch lengths indicate that this transfer occurred soon after the divergence of chimpanzees and bonobos. Identical to what was observed for Bacteroidaceae, analysis of the previously reported data set (*18*) for sympatric chimpanzees and gorillas living in Cameroon revealed no shared 99% Bifidobacteriaceae OTUs between these sympatric populations.

For the Lachnospiraceae, the phylogenetic history contrasts with that observed in the Bacteroidaceae and the Bifidobacteriaceae. The present-day host associations of the 746 Lachnospiraceae strains indicate at least four between-host-species transfer events since the common ancestor of the Hominidae (fig. S3 and data file S6). These results corroborate previous observations that Lachnospiraceae 16*S* OTUs are shared across African ape species (*18*). The Lachnospiraceae, unlike Bacteroidaceae and Bifidobacteriaceae, are spore-forming and can survive outside the gut, which may enhance their ability to disperse and transfer among host species. The distinct evolutionary pattern of the Lachnospiraceae indicates that human and ape gut microbiomes are composites of cospeciating and independently diversifying bacterial lineages (fig. S4).

We expect, under a neutral model, the degree of sequence divergence between bacterial strains derived from different host species to be proportional to the divergence dates of their corresponding

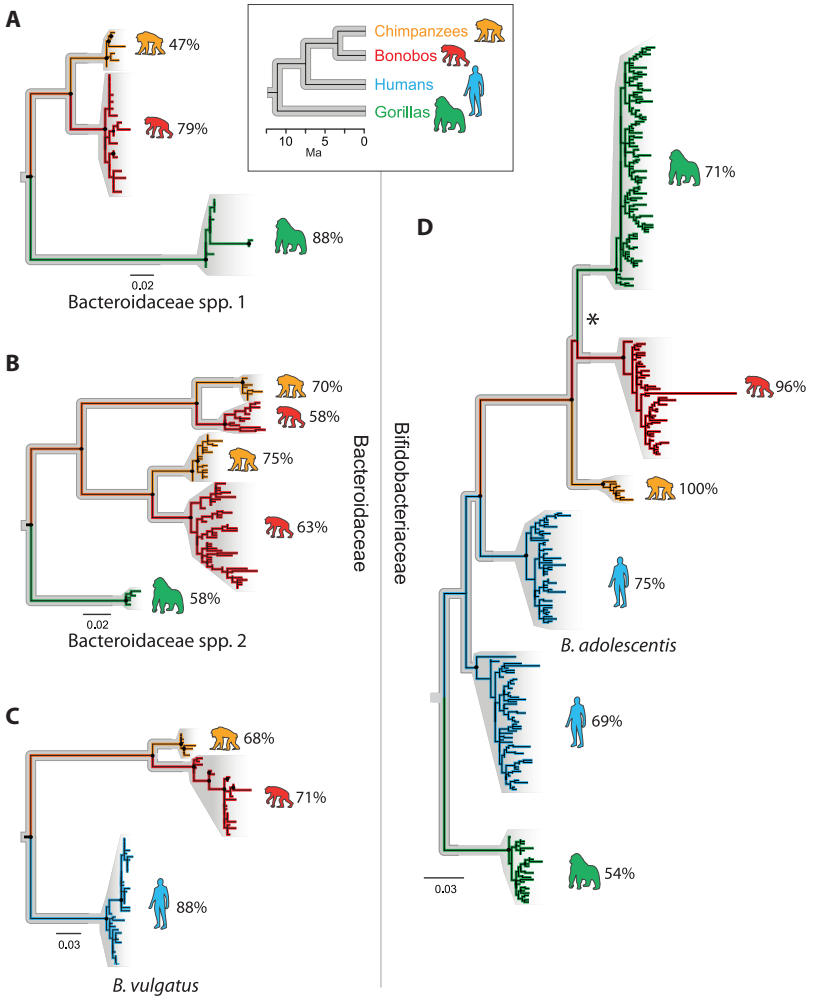

Fig. 1. Cospeciation between gut bacteria and hominids. Inset contains a phylogeny showing the relationships among humans and the African apes. (**A**) Maximum-likelihood phylogeny of a clade of Bacteroidaceae lineages that codiversified with the African apes but that was lost from the lineage leading to humans. In (A) and subsequent panels, black dots denote nodes supported in >50% of bootstrap replicates, colors correspond to the inset and denote the host species from which each bacterial lineage was recovered, and percentages indicate the percent of host individuals from which each clade was recovered. (**B**) Maximum-likelihood phylogeny of a clade of Bacteroidaceae lineages that codiversified with the African apes but that was lost from the lineage leading to humans. Note that this Bacteroidaceae lineage bifurcated in an ancestor of chimpanzees and bonobos, giving rise to two, paralogous cospeciating bacterial lineages. (**C**) Maximum-likelihood phylogeny of a Bacteroidaceae clade that cospeciated with humans, chimpanzees, and bonobos. No gorilla-derived representatives of this clade were recovered. (**D**) Inferred relationships among Bifidobacteriaceae *gyrB* sequences recovered from humans and African apes. Black asterisk indicates the transfer of a *Bifidobacterium adolescentis* relative from bonobos into gorillas.

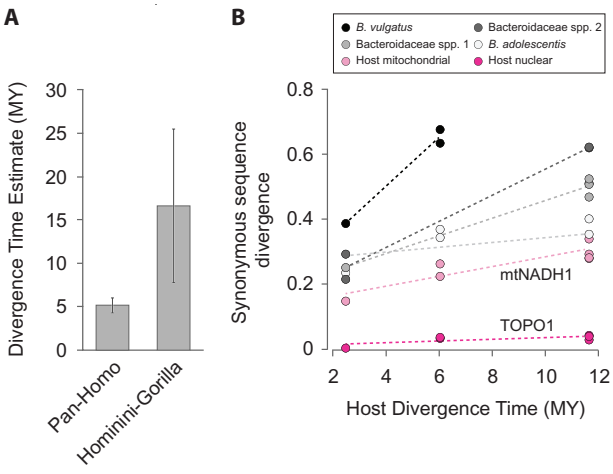

Fig. 2. Bacterial time scale for hominid evolution. (**A**) Divergence times of Hominidae species estimated from Bacteroidaceae and Bifidobacteriaceae *gyrB* sequences in BEAST. Error bars represent SDs of the mean divergence times estimated from each clade that cospeciated with Hominids. (**B**) Color-coded trend lines indicate rates of synonymous site divergence of *gyrB* in each bacterial clade displaying evidence of cospeciation, the host mitochondrial NADH1 (mtNADH1) gene, and the host nuclear topoisomerase I gene (TOPO1). Trend lines correspond to bacterial clades depicted in Figs. 1 and 2, and named bacterial species for each clade are shown when available.

host species. For the two bacterial families that displayed evidence of cospeciation with hominids, we estimated the divergence times within bacterial clades whose relationships recapitulated the host phylogeny (data files S7 and S8). For each bacterial clade, we estimated the divergence dates of *Homo*- and *Pan*-derived strains or of Hominini- (*Pan* + *Homo*) and *Gorilla*-derived strains based on the assumption that the nested chimpanzee- and bonobo-derived strains diverged 2.2 million years ago (Ma). Using the chimp-bonobo split as calibration, the mean estimated divergence dates of bacterial clades derived from the two deeper splits correspond closely to hominid divergence dates estimated from fossil and genomic evidence (Fig. 2). Based on the sequence divergence of gut bacteria, we date the split of humans and chimpanzees at 5.3 Ma (Fig. 2A), coincident with estimates based on host mitochondrial genomes (5.2 to 6.4 Ma) (*19*) but later than some recent estimates based on nuclear genomes (7 to 13 Ma) (*20*). In contrast, the human-gorilla split based on the sequence divergence of their gut bacteria is dated to 15.6 Ma (Fig. 2A), older than estimates based on mitochondrial genomes (7.1 to 9.2 Ma) (*19*) but within the range of estimates based on nuclear genomes (8 to 19 Ma) (*20*).

The history of cospeciation between the Hominidae and their gut bacteria provides robust host-derived calibration dates for estimating the rate of DNA sequence evolution in the Bacteroidaceae and Bifidobacteriaceae (Fig. 2B). Rates of molecular evolution are lowest in the mutualistic Bifidobacteriaceae, in which sequence divergence has accumulated at a rate of ~0.7 and 0.07% per million years at synonymous and nonsynonymous sites, respectively (Fig. 2B), estimates that agree well with those derived from comparisons of *Salmonella* and *Escherichia* gene sequences (*21*). In contrast, rates of molecular evolution are highest in the Bacteroidaceae clade containing the human-derived commensal and opportunistic pathogen *Bacteroides vulgatus* (displayed in Fig. 1C) at ~7.0 and 2.2% per million years at synonymous and nonsynonymous sites, respectively (Fig. 2B). This Bacteroidaceae clade also displayed the lowest GC content at 45%, compared with 50 to 56% GC in all other Bacteroidaceae clades. Together, fast rates of molecular evolution at both synonymous and nonsynonymous sites alongside relatively high AT content are indicative of an elevated mutation rate in the clade containing *B. vulgatus*.

Applying the same time calibration points for bacterial and host sequences, rates of synonymous site divergence of bacterial gyrase B genes (0.7 to 7%/Ma) are faster than those of host nuclear DNA (topoisomerase I, 0.2%/Ma) but similar to those of host mitochondrial DNA (e.g., NADH1, 1.4%/Ma). The observation that genes within cospeciating bacterial symbionts evolve faster than host genes may be useful for inferring the evolutionary and biogeographical relationships among recently diverged host species.

We next tested whether cospeciating gut bacterial lineages are also present in human populations living in Africa. We queried 23 previously reported gut metagenomes of humans from Malawi (*7*) with a representative *gyrB* sequence from each chimpanzee-derived clade. The top five *e*-value hits of each search were extracted and added to either the Bacteroidaceae, Bifidobacteriaceae, or Lachnospiraceae alignment, and phylogenetic analyses were reperformed (data files S9 to S11). The phylogenetic placements of all the Malawi-derived Bacteroidaceae and Bifidobacteriaceae *gyrB* sequences indicate a history of cospeciation. Among the bacterial strains detected, humans from Malawi harbor a cospeciating lineage of Bacteroidaceae not detected in humans from the USA (fig. S5), as well as distinct lineages within the cospeciating Bifidobacteriaceae clade depicted in Fig. 1 (fig. S6). The loss of bacterial lineages is in line with the general reduction in gut microbiome diversity that has been observed in USA humans (*5*, *7*). In contrast, the phylogenetic placements of the Malawi-derived Lachnospiraceae lineages are consistent with a history of transfer of Lachnospiraceae among host species (fig. S7).

Codiversification between the Hominidae and their gut bacteria shows that symbiotic associations arose in a common ancestor to all African great apes and have persisted over evolutionary time scales. Our comparisons only reveal the minimum age of these symbioses, and it is possible that diversification alongside ancestral bacterial lineages is common to all vertebrates. Evidence from experimental systems has revealed the roles that gut bacteria play in host development and immune-system function (*22*, *23*), indicating that hosts have evolved in response to their bacterial counterparts. Conversely, many bacterial taxa have adapted to their respective hosts (*24*, *25*). Our results represent a step toward understanding the coevolutionary history of vertebrates and their gut bacteria.

REFERENCES AND NOTES

1. M. A. Munson *et al.*, *J. Bacteriol.* **173**, 6321–6324 (1991).
2. N. A. Moran, D. B. Sloan, *PLOS Biol.* **13**, e1002311 (2015).
3. J. K. Goodrich *et al.*, *Cell* **159**, 789–799 (2014).
4. H. Ochman *et al.*, *PLOS Biol.* **8**, e1000546 (2010).
5. A. H. Moeller *et al.*, *Proc. Natl. Acad. Sci. U.S.A.* **111**, 16431–16435 (2014).
6. L. A. David *et al.*, *Nature* **505**, 559–563 (2014).
7. T. Yatsunenko *et al.*, *Nature* **486**, 222–227 (2012).
8. K. Forslund *et al.*, *Genome Res.* **23**, 1163–1169 (2013).
9. B. D. Muegge *et al.*, *Science* **332**, 970–974 (2011).
10. R. E. Ley *et al.*, *Science* **320**, 1647–1651 (2008).
11. N. A. Moran, M. A. Munson, P. Baumann, H. Ishikawa, *Proc. R. Soc. London Ser. B* **253**, 167–171 (1993).
12. H. Ochman, S. Elwyn, N. A. Moran, *Proc. Natl. Acad. Sci. U.S.A.* **96**, 12638–12643 (1999).
13. A. Caro-Quintero, H. Ochman, *Genome Biol. Evol.* **7**, 3416–3425 (2015).
14. J. G. Caporaso *et al.*, *Nat. Methods* **7**, 335–336 (2010).
15. Materials and methods are available as supplementary materials on *Science* Online.
16. K. Tamura, G. Stecher, D. Peterson, A. Filipski, S. Kumar, *Mol. Biol. Evol.* **30**, 2725–2729 (2013).
17. A. J. Drummond, A. Rambaut, *BMC Evol. Biol.* **7**, 214 (2007).
18. A. H. Moeller *et al.*, *Genome Res.* **23**, 1715–1720 (2013).
19. A. Bjork, W. Liu, J. O. Wertheim, B. H. Hahn, M. Worobey, *Mol. Biol. Evol.* **28**, 615–623 (2011).
20. K. E. Langergraber *et al.*, *Proc. Natl. Acad. Sci. U.S.A.* **109**, 15716–15721 (2012).
21. H. Ochman, A. C. Wilson, *J. Mol. Evol.* **26**, 74–86 (1987).
22. T. S. Stappenbeck, L. V. Hooper, J. I. Gordon, *Proc. Natl. Acad. Sci. U.S.A.* **99**, 15451–15455 (2002).
23. H. Chung *et al.*, *Cell* **149**, 1578–1593 (2012).
24. T. W. Cullen *et al.*, *Science* **347**, 170–175 (2015).
25. W. K. Kwong, P. Engel, H. Koch, N. A. Moran, *Proc. Natl. Acad. Sci. U.S.A.* **111**, 11509–11514 (2014).

ACKNOWLEDGMENTS

We thank N. Moran and A. Goodman for comments on the manuscript and K. Hammond for assistance with preparation of the figures. We also thank the staff of the Prevention of AIDS in Cameroon (PRESICA) project and the Bonobo Conservation Initiative, as well as J.-B. N. Ndjango for field work in Cameroon and the Democratic Republic of the Congo (DRC); field assistants in Gombe National Park for sample collection in Tanzania; the Cameroonian Ministries of Health, Forestry, and Wildlife and Scientific Research and Innovation for permission to collect samples in Cameroon; the Ministries of Health and Environment and the National Ethics Committee for permission to collect samples in the DRC; the Tanzania Commission for Science and Technology; the Tanzania Wildlife Research Institute for permission to conduct research in Gombe National Park; and the Bonobo Conservation Initiative and Vie Sauvage for assistance in the DRC. All human studies were conducted with approval from the Yale University Human Investigation Committee. This work was supported by funding from the NIH (grants R01 AI091595, R37 AI050529, R01 AI120810, P30 AI045008, R01 GM101209), NSF (Graduate Research Fellowship 2011119472 to A.H.M.), Agence Nationale de Recherche sur le Sida (ANRS 12125/12182/12255/12325), Jane Goodall Institute, Arthur L. Greene Fund, and Harvard University. A.H.M. performed analyses and wrote the paper. A.C.-Q. processed samples and prepared libraries for sequencing. D.M., E.V.L., M.N.M., A.V.G., A.E.P., M.P., and B.H.H. provided samples and commented on the manuscript. H.O. provided reagents and wrote the paper. Sequence data have been deposited in the European Nucleotide Archive under accession PRJEB13130.

SUPPLEMENTARY MATERIALS

www.sciencemag.org/content/353/6297/380/suppl/DC1
Materials and Methods
Figs. S1 to S7
Tables S1 to S4
Data Files S1 to S11

3 February 2016; accepted 2 June 2016
10.1126/science.aaf3951

MEMORY RESEARCH

Competition between engrams influences fear memory formation and recall

Asim J. Rashid,[1,2,3,4] Chen Yan,[1,2,3,4] Valentina Mercaldo,[1,2,3,4] Hwa-Lin (Liz) Hsiang,[1,2,3,4] Sungmo Park,[1,2,3,4] Christina J. Cole,[1,2,3,4] Antonietta De Cristofaro,[1] Julia Yu,[1] Charu Ramakrishnan,[5] Soo Yeun Lee,[5] Karl Deisseroth,[5] Paul W. Frankland,[1,2,3,4]* Sheena A. Josselyn[1,2,3,4]*

Collections of cells called engrams are thought to represent memories. Although there has been progress in identifying and manipulating single engrams, little is known about how multiple engrams interact to influence memory. In lateral amygdala (LA), neurons with increased excitability during training outcompete their neighbors for allocation to an engram. We examined whether competition based on neuronal excitability also governs the interaction between engrams. Mice received two distinct fear conditioning events separated by different intervals. LA neuron excitability was optogenetically manipulated and revealed a transient competitive process that integrates memories for events occurring closely in time (coallocating overlapping populations of neurons to both engrams) and separates memories for events occurring at distal times (disallocating nonoverlapping populations to each engram).

Memory of an event is thought to be represented by an ensemble of neurons, referred to as its memory trace or engram (*1*, *2*). Despite recent advances in localizing and manipulating single engrams, little is known about how multiple engrams interact to influence memory function. Two engrams may engage nonoverlapping neuronal populations, thus minimizing interference between distinct memory representations. Alternatively, engrams may engage overlapping neuronal populations to functionally link those memories. Here, we examined the rules governing engram interaction.

In lateral amygdala (LA), a region critical for conditioned fear memory (*3*–*5*), eligible neurons compete for engram allocation. Neurons with relatively higher function of transcription factor CREB or increased excitability at training preferentially win this competition and are allocated to an engram (*6*–*10*). Silencing these neurons prevents memory expression, whereas their activation artificially elicits memory expression, indicating that these allocated neurons are both necessary and sufficient for expression of that memory (*7*–*10*). Similar competition governs engram allocation in mice without experimental manipulation of CREB or excitability (*11*).

We asked if two fear-conditioning events that occur closely in time are coallocated to overlapping populations of neurons, thereby functionally linking these memories. Mice received two events (event 1, event 2) featuring distinct auditory conditioned stimuli (CS1 or CS2, Fig. 1A; see supplementary materials) separated by varying intertraining intervals (ITIs; 1.5, 3, 6, 18, or 24 hours). Event 2 (CS2+footshock) was the same across groups, but event 1 content and timing differed. Memory for event 1 was stable across ITIs (fig. S1B). However, event 2 memory was enhanced if event 1 (CS1+footshock) occurred shortly before (1.5 to 6 hours, but not 18 to 24 hours; Fig. 1B and fig. S2, B and C), even if event 1 consisted of light-footshock pairing (fig. S2A). Event 2 memory enhancement depended on previous fear conditioning (not sensitization); mice failed to show enhanced event 2 memory if event 1 consisted of CS1 alone or immediate footshock.

To examine if neural representations of events separated by short (not long) intervals are coallocated to overlapping neuronal populations, we used fluorescent in situ hybridization (FISH) for two activity-dependent genes. Nuclear *arc* mRNA labels neurons that were active in the preceding 5 min, whereas nuclear *homer1a* (*h1a*) mRNA labels neurons that were active in the preceding 30 to 40 min (*12*). Mice received event 1 and event 2 separated by 6 or 24 hours. During the memory test, CS1 was presented; then, 25 min later, CS2 was presented. Brains were removed 5 min later. arc^+ neurons were activated by CS2, $h1a^+$ neurons were activated by CS1, and $arc^+/h1a^+$ neurons were activated by both CSs (part of both engrams). Two control groups trained on event 1 only and tested under two conditions provided upper and lower overlap boundaries. During the test, the CS1-CS1 group was reexposed to CS1 twice ($h1a^+$ = first CS1 reexposure, arc^+ = second CS1 reexposure, "overlap ceiling"), whereas the CS1-CS3 group was reexposed to CS1 and novel CS3 ("floor"). The overlap observed in mice trained on event 1 and event 2 separated by 24 hours was not different from floor conditions, whereas the overlap observed in mice similarly trained with a 6-hour interval was higher, indicating coallocation (Fig. 1C and fig. S3, A to C).

To test whether coallocation functionally links memories, we extinguished event 2 memory (repeatedly presented CS2 without footshock) and examined the effect on event 1 memory. After CS2 extinction, all groups froze less to CS2. However, mice trained with short (6 hours), but not long (24 hours), ITIs also froze less in response to CS1, even though CS1 was not explicitly extinguished (Fig. 1D).

We next examined potential molecular and local circuit mechanisms governing engram interaction. Fear conditioning transiently (1.5 to 6 hours, but not 18 to 24 hours) increased the number of LA principal neurons with activated CREB (Fig. 2A), in agreement with reports showing that learning transiently increases neuronal excitability (*13*, *14*). CREB function cycles over time, in part, due to autoregulatory feedback (*15*) and, consistent with this, we observed that a depolarizing stimulus in cultured neurons first activated CREB, then increased an inhibitory CREB isoform (fig. S4).

The oscillation in CREB function and neuronal excitability provides a potential mechanism by which engrams supporting events occurring closely in time are coallocated, whereas events occurring at more remote time points are disallocated (Fig. 2B) (*16*). Although the size of an LA engram supporting a fear memory remains stable, a competitive process determines which neurons comprise each engram (*7*–*10*). If event 1 transiently increases CREB function and neuronal excitability in a population of LA neurons and event 2 occurs while these neurons are more excitable than their neighbors (within 6 hours), then overlapping neurons would be coallocated to both events. However, if event 2 occurs when event 1 neurons are no longer more excitable (e.g., 24 hours after event 1), the engram underlying event 2 is disallocated, thus functionally disambiguating these memories. We tested these predictions by manipulating LA neuronal excitability to control allocation. We sought to force coallocation to artificially link normally separated memories (24-hour interval) and force disallocation to artificially separate normally linked memories (6-hour interval).

To bidirectionally manipulate excitability in the same neuron, we constructed a replication-defective herpes simplex viral vector (HSV) expressing both channelrhodopsin-2 (ChR2, excitatory opsin) and halorhodopsin (NpHR3.0, inhibitory opsin) [HSV-NpACY (*17*, *18*)]. Blue light (via ChR2) increases excitability, whereas red light (via NpHR3.0) inhibits activity (Fig. 3A and figs. S5 and S7). HSV infects ~15% of LA principal neurons (*10*) (Fig. 3A and fig. S6). We verified this approach using one fear-conditioning event. To allocate HSV-infected neurons, we excited them (blue light, BL+) before training (*10*). To confirm their allocation, we tested mice under basal conditions (no red light, RL–) and while inhibiting infected neurons (red light, RL+). Mice trained immediately after activation of infected neurons froze less when these

[1]Program in Neurosciences and Mental Health, Hospital for Sick Children, 555 University Avenue, Toronto, ON M5G 1X8, Canada. [2]Department of Psychology, University of Toronto, Toronto, ON M5G 3G3, Canada. [3]Institute of Medical Sciences, University of Toronto, Toronto, ON M5S 1A8, Canada. [4]Department of Physiology, University of Toronto, Toronto, ON M5G 1X8, Canada. [5]Department of Psychiatry and Behavioral Sciences, Stanford University, Stanford, CA 94305, USA.
*Corresponding author. Email: sheena.josselyn@sickkids.ca (S.A.J.); paul.frankland@sickkids.ca (P.W.F.)

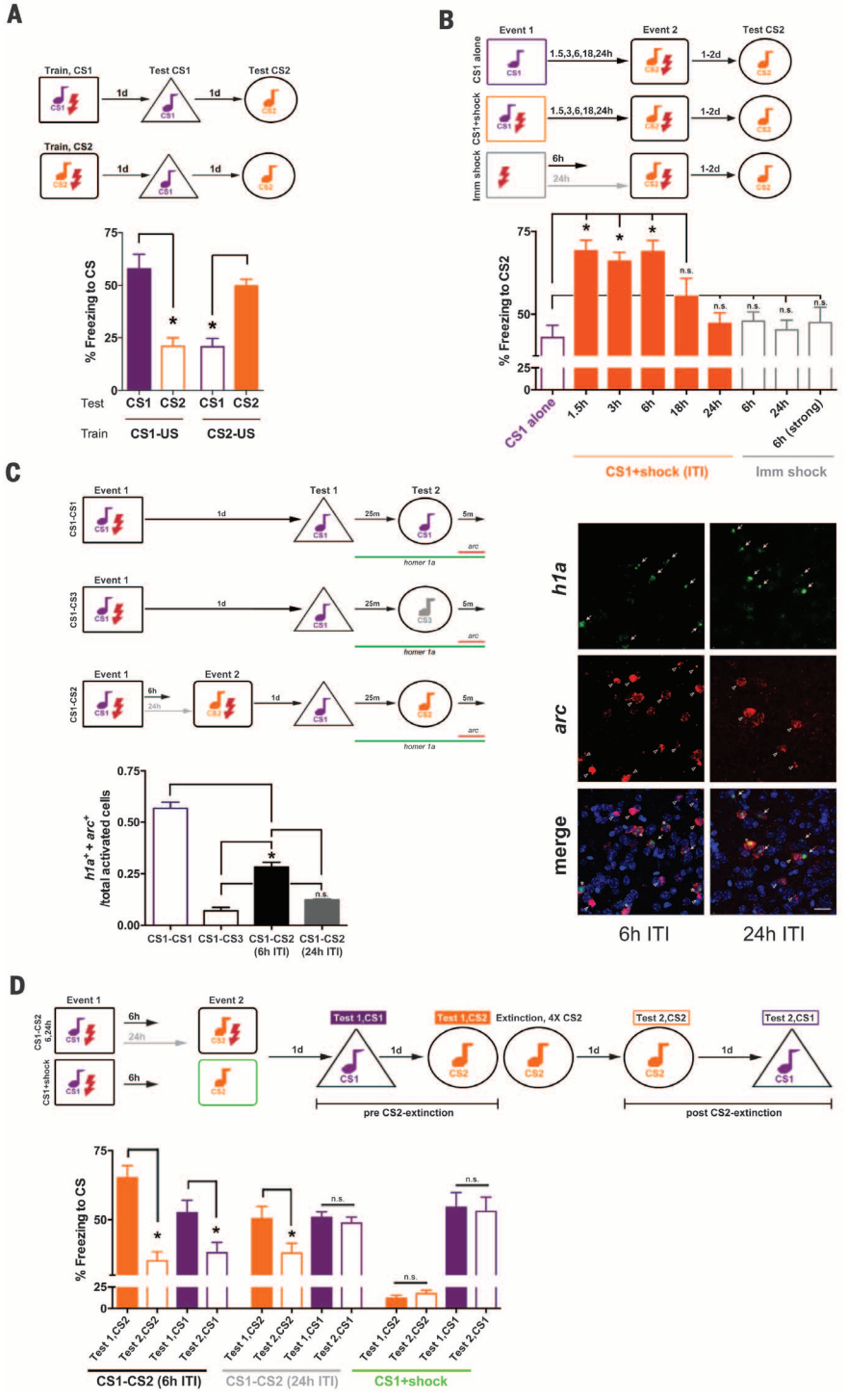

Fig. 1. Events occurring closely in time are coallocated to overlapping engrams, and memories become linked. (**A**) Mice distinguish conditioned stimuli (CS1, CS2), freezing more in response to trained, than untrained, auditory CS. ANOVA: Train-CS × Test-CS, $F(1,12) = 44.29$, $^*P < 0.001$. Means ± SEM. $n = 7$ mice per group. $^*P < 0.05$. (**B**) Event 2 memory was enhanced if event 1 (CS1+shock) occurred within a short intertraining interval (ITI). Enhancement was not due to CS1 alone or immediate shock (Imm shock) during event 1; $F(8,142) = 17.03$, $^*P < 0.001$. $n = 56$ for CS1 alone (see fig. S1A), $n = 5$ to 16 for other groups. n.s., not statistically different. (**C**) Engrams for events with a 6-hour (but not 24-hour) ITI coallocated to overlapping LA neurons; $F(3,8) = 119.01$, $^*P < 0.001$. (Right) Coallocation in 6-hour, but not 24-hour, ITI. arc^+ (CS2 reexposure, red), $homer1a^+$ ($h1a^+$, CS1 reexposure, green) neurons, 4′,6-diamidino-2-phenylindole (DAPI; blue, nuclear stain). Scale bar, 20 μm. $n = 3$ mice per group. (**D**) Extinguishing event 2 memory also decreased event 1 memory if a 6-hour (but not 24-hour) ITI was used. Group × CS-Freezing, $F(2,50) = 12.53$, $^*P < 0.001$. $n = 12$ mice, 6-hour, 24-hour groups; $n = 4$ mice, control group.

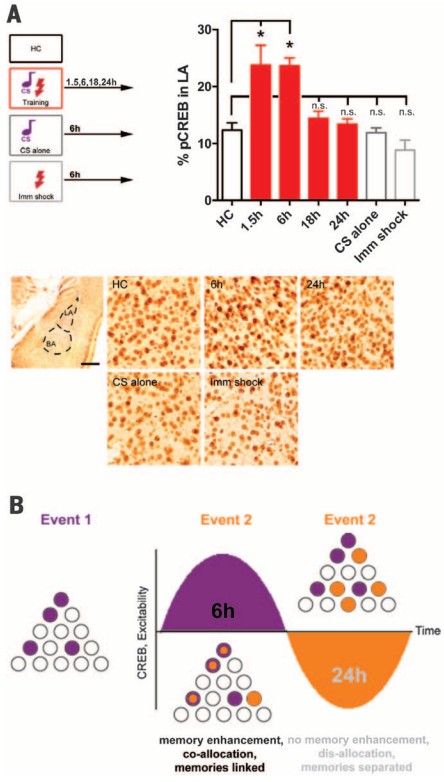

Fig. 2. Engram interaction may be governed by neuronal CREB function and excitability. (**A**) (Top) Fear conditioning transiently increases the percentage of LA neurons with activated CREB (pCREB) relative to home-cage (HC), CS alone (6h), or immediate shock (6h, Imm shock); $F(6,21) = 12.53$, $^*P < 0.001$. (Bottom) Left panel: LA. Scale bar, 400 μm. Right panels: pCREB staining, Scale bar, 25 μm. $n = 3$ to 5 mice per group. (**B**) Schematic of hypothesized engram interaction. Event 1 transiently increases CREB function and excitability in a population of LA neurons (purple). If event 2 occurs when these neurons have elevated CREB and excitability (6h), then engrams are coallocated, memories are linked (purple+orange neurons), and event 2 memory is enhanced. If event 2 occurs later (24h), neurons activated by event 1 are no longer more excitable (perhaps they are in a "refractory-like period"), engrams are disallocated to nonoverlapping neurons, and memories are distinct.

neurons were inhibited (Fig. 3B), indicating that optogenetically exciting neurons before training was sufficient for allocation. Inhibiting a similar number of neurons in control groups (BL–, BL+ 24 hours before training, BL+ but no opsin) did not affect memory expression, nor did BL+ affect training variables or function as a cue during the test (fig. S8B).

We confirmed time-limited coallocation of two events. Principal neurons expressing HSV-NpACY were excited immediately before event 1. Infected neurons were coallocated to event 2, if event 2 occurred 6 hours, but not 24 hours, later (Fig. 3C). To artificially link normally separated memories (24-hour interval), we excited the same population of HSV-infected neurons before event 1 and event 2, forcing coallocation. Inhibiting infected neurons

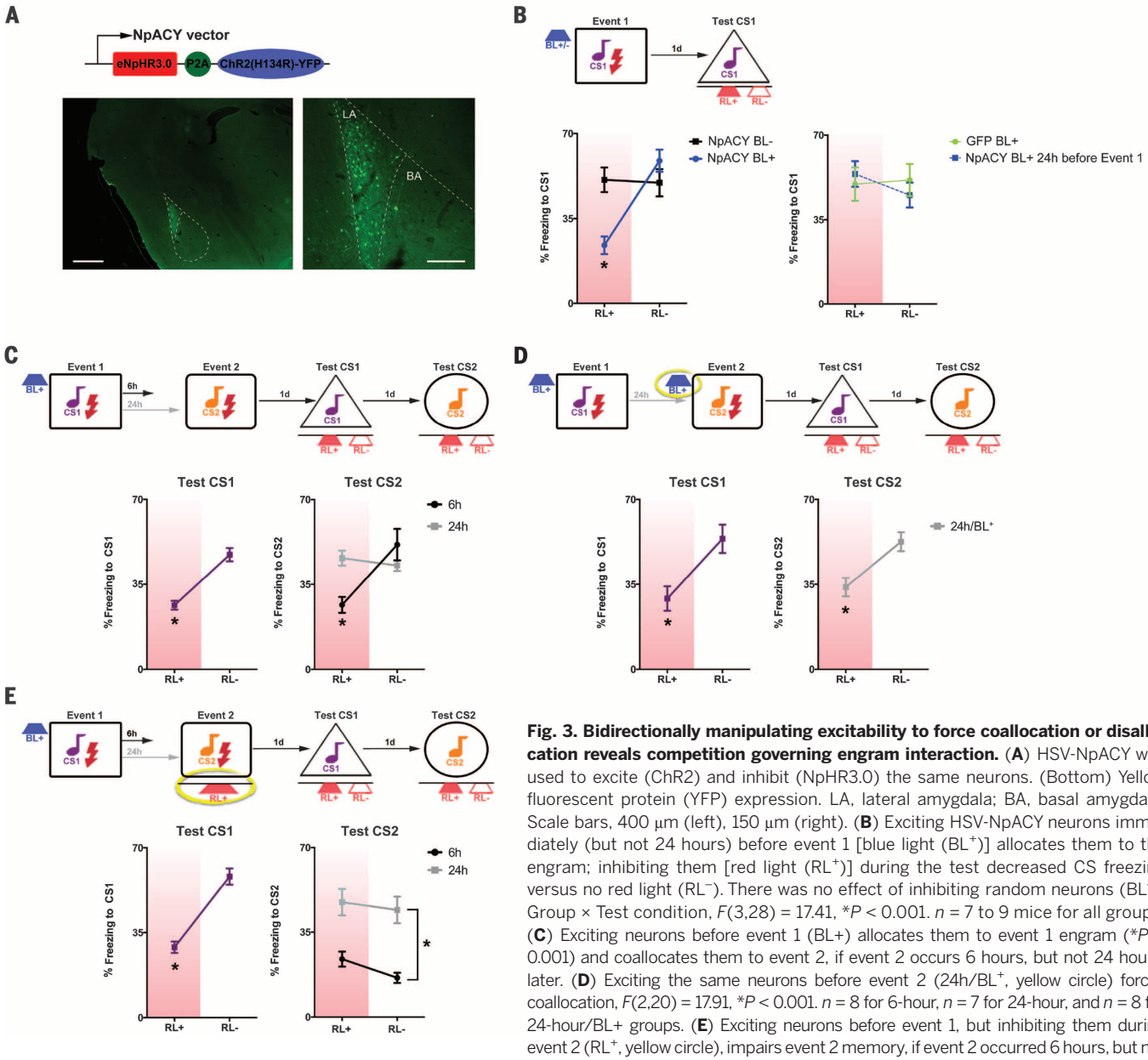

Fig. 3. Bidirectionally manipulating excitability to force coallocation or disallocation reveals competition governing engram interaction. (**A**) HSV-NpACY was used to excite (ChR2) and inhibit (NpHR3.0) the same neurons. (Bottom) Yellow fluorescent protein (YFP) expression. LA, lateral amygdala; BA, basal amygdala. Scale bars, 400 μm (left), 150 μm (right). (**B**) Exciting HSV-NpACY neurons immediately (but not 24 hours) before event 1 [blue light (BL^+)] allocates them to the engram; inhibiting them [red light (RL^+)] during the test decreased CS freezing versus no red light (RL^-). There was no effect of inhibiting random neurons (BL^-). Group × Test condition, $F(3,28) = 17.41$, $^*P < 0.001$. $n = 7$ to 9 mice for all groups. (**C**) Exciting neurons before event 1 (BL+) allocates them to event 1 engram ($^*P < 0.001$) and coallocates them to event 2, if event 2 occurs 6 hours, but not 24 hours, later. (**D**) Exciting the same neurons before event 2 (24h/BL^+, yellow circle) forces coallocation, $F(2,20) = 17.91$, $^*P < 0.001$. $n = 8$ for 6-hour, $n = 7$ for 24-hour, and $n = 8$ for 24-hour/BL+ groups. (**E**) Exciting neurons before event 1, but inhibiting them during event 2 (RL^+, yellow circle), impairs event 2 memory, if event 2 occurred 6 hours, but not 24 hours, later. $F(1,16) = 5.63$, $^*P < 0.05$. $n = 7$ for 24-hour and $n = 11$ for 6-hour groups.

impaired both event 1 and event 2 memory expression (Fig. 3D), indicating overlapping engrams of infected neurons. Similarly, we artificially linked normally separated memories (24-hour interval) by virally overexpressing CREB (vCREB) to excite the same neurons during event 1 and event 2. Silencing vCREB-infected neurons with the inhibitory DREADD receptor hM4Di [designer receptors exclusively activated by designer drug (*19*)] disrupted expression of both memories (fig. S9, A to D).

To artificially separate normally linked memories (6-hour interval), we excited infected neurons before event 1, then inhibited (RL+) these neurons during event 2. Surprisingly, event 2 memory was impaired, even when mice were tested without red light (Fig. 3E). Event 2 memory was also disrupted if we used vCREB to allocate neurons before event 1 and DREADDs to inhibit these neurons during event 2 (fig. S9E). In contrast, event 2 memory was intact in optogenetic experiments if the interval between events was increased to 24 hours (Fig. 3E). These results indicate that initially allocated neurons transiently prevent nonallocated neurons from being allocated to another engram (winning neurons inhibit losing neurons).

In neural networks, winner-take-all competition maintains sparse coding and is regulated by excitation and inhibition (*20*). Local LA inhibition is mediated predominantly by γ-aminobutyric acid (GABA)–releasing parvalbumin (PV) interneurons (*21*, *22*). PV interneurons in LA and basal amygdala (BA) form an inhibitory network receiving inputs from, and regulating, LA principal neuron activity by forming perisomatic synapses (*23*, *24*). Fear conditioning induced a transient increase in perisomatic PV immunolabeling (*24*) surrounding LA principal neurons (1.5 to 6 hours but not 18 to 24 hours, Fig. 4A).

To test whether PV interneurons suppress nonallocated principal neurons, we released LA and BA PV inhibition. Transgenic mice expressing Cre recombinase in PV interneurons (PV-Cre mice) were microinjected with adeno-associated virus (AAV) expressing Cre-dependent hM4Di. Control PV-Cre mice with intact PV function (vehicle-treated) similarly showed impaired event 2 memory (Fig. 3E) if HSV-infected neurons allocated to event 1 were optogenetically silenced during event 2 (6-hour interval, Fig. 4B). However, inhibiting PV neurons before event 2 [clozapine-*N*-oxide (CNO) to activate hM4Di receptors] permitted event 2 memory formation. Therefore, if principal neurons not allocated to the engram supporting event 1 (losers) are

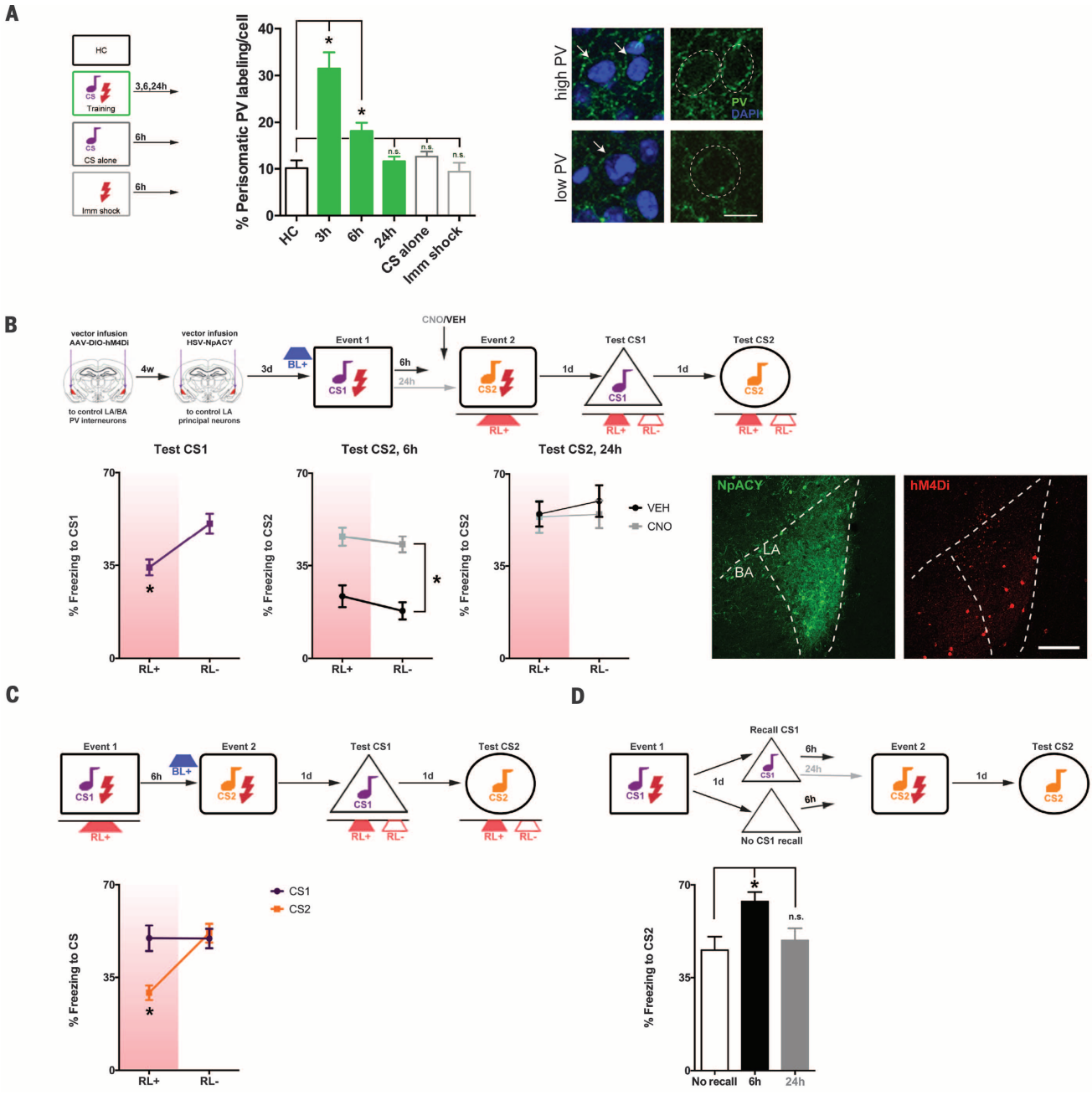

Fig. 4. Competition-mediating engram interaction depends on excitation-inhibition. (**A**) Fear conditioning transiently increases perisomatic PV immunolabeling (green) surrounding LA principal neurons relative to home-cage (HC), CS alone (6h), or immediate shock (6h, Imm shock); $^*P < 0.001$. (Right) High or low perisomatic PV, with or without DAPI-labeled nuclei (blue, perisomatic region outlined). Scale bar, 10 μm. $n = 3$ mice per group. Arrows indicate perisomatic PV immunolabel in example cells designated "high PV" or "low PV."(**B**) Event 2 memory is impaired (Fig. 3E) if events are separated by 6 hours and neurons allocated to event 1 are silenced (RL+) during event 2. Inhibiting PV interneurons (hM4Di+CNO) permits event 2 memory formation, group difference only, $F(3,23) = 22.61$, $^*P < 0.001$. (Right) HSV-NpACY (YFP, green), AAV-hM4Di (mCherry, red). Scale bar, 200 μm. $n = 4$ to 8 mice for all groups. (**C**) HSV-infected neurons inhibited (RL^+) during event 1 are not allocated to event 1 engram; $^*P > 0.05$. Exciting these neurons before event 2 (BL^+) allocates them to event 2 engram, $F(1,7) = 51.02$, $^*P < 0.001$. $n = 8$ mice. (**D**) Event 2 memory is enhanced if CS1 is recalled 6 hours, but not 24 hours, before event 2; $F(2,29) = 5.28$, $^*P < 0.05$. $n = 8$ to 12 mice for all groups.

released from PV inhibition, they may be allocated to an engram for an event occurring shortly after (become winners). Similarly, relieving PV inhibition before event 2 had no effect when events were separated by 24 hours, showing the time dependency of this competition (Fig. 4B).

We examined whether directly manipulating LA principal neuron excitability, rather than indirectly relieving PV inhibition, overcomes these competition effects. HSV-infected principal neurons were optogenetically inhibited during event 1 (these neurons were not allocated to event 1 engram; Fig. 4C). Event 2 occurred 6 hours later when neurons allocated to event 1 engram would also be coallocated to event 2 engram. However, immediately before event 2, we optogenetically excited HSV-infected neurons. These "loser" HSV-infected neurons became critical components of the engram supporting event 2, outcompeting previous winning neurons.

These results reveal that, in the LA, a transient competitive process governs the interaction between engrams to integrate memories for events occurring closely in time and distinguish memories

for events occurring farther apart in time. Coallocation is not limited to linking memories at encoding. Memory recall may engage a similar process to link new with old memories. We trained mice on event 1, 2 days before event 2. Event 2 memory was enhanced if event 1 was recalled 6 hours, not 24 hours, before event 2 (Fig. 4D). Here, we find that excitatory-inhibitory balance determines whether memories are bound or, alternately, segregated in the LA. More broadly, these principles provide a foundation for understanding how memories are organized within associative networks.

Note added in proof: During final preparation of this manuscript, a notable study showing time-limited coallocation of hippocampal memory traces was published (*25*).

REFERENCES AND NOTES

1. S. A. Josselyn, S. Köhler, P. W. Frankland, *Nat. Rev. Neurosci.* **16**, 521–534 (2015).
2. S. Tonegawa, X. Liu, S. Ramirez, R. Redondo, *Neuron* **87**, 918–931 (2015).
3. J. E. LeDoux, *Annu. Rev. Neurosci.* **23**, 155–184 (2000).
4. S. Maren, *Ann. N. Y. Acad. Sci.* **985**, 106–113 (2003).
5. S. Duvarci, D. Pare, *Neuron* **82**, 966–980 (2014).
6. D. Kim, D. Paré, S. S. Nair, *J. Neurosci.* **33**, 14354–14358 (2013).
7. J. H. Han *et al.*, *Science* **316**, 457–460 (2007).
8. J. H. Han *et al.*, *Science* **323**, 1492–1496 (2009).
9. Y. Zhou *et al.*, *Nat. Neurosci.* **12**, 1438–1443 (2009).
10. A. P. Yiu *et al.*, *Neuron* **83**, 722–735 (2014).
11. L. A. Gouty-Colomer *et al.*, *Mol. Psychiatry* **21**, 364–375 (2016).
12. J. F. Guzowski, *Hippocampus* **12**, 86–104 (2002).
13. M. M. Oh, A. G. Kuo, W. W. Wu, E. A. Sametsky, J. F. Disterhoft, *J. Neurophysiol.* **90**, 2171–2179 (2003).
14. L. T. Thompson, J. R. Moyer Jr., J. F. Disterhoft, *J. Neurophysiol.* **76**, 1836–1849 (1996).
15. L. Monaco, N. S. Foulkes, P. Sassone-Corsi, *Proc. Natl. Acad. Sci. U.S.A.* **92**, 10673–10677 (1995).
16. A. J. Silva, Y. Zhou, T. Rogerson, J. Shobe, J. Balaji, *Science* **326**, 391–395 (2009).
17. Y. Mei, F. Zhang, *Biol. Psychiatry* **71**, 1033–1038 (2012).
18. V. Gradinaru *et al.*, *Cell* **141**, 154–165 (2010).
19. B. N. Armbruster, X. Li, M. H. Pausch, S. Herlitze, B. L. Roth, *Proc. Natl. Acad. Sci. U.S.A.* **104**, 5163–5168 (2007).
20. P. A. Shoemaker, *Front. Comput. Neurosci.* **9**, 12 (2015).
21. P. Sah, E. S. Faber, M. Lopez De Armentia, J. Power, *Physiol. Rev.* **83**, 803–834 (2003).
22. S. B. Wolff *et al.*, *Nature* **509**, 453–458 (2014).
23. A. R. Woodruff, P. Sah, *J. Neurosci.* **27**, 553–563 (2007).
24. S. Trouche, J. M. Sasaki, T. Tu, L. G. Reijmers, *Neuron* **80**, 1054–1065 (2013).
25. D. J. Cai *et al.*, *Nature* **534**, 115–118 (2016).

ACKNOWLEDGMENTS

We thank B. Roth for reagents, N. Insel and B. Richards for comments on previous versions of this manuscript, and the Josselyn and Frankland labs for general comments. This work was supported by Canadian Institutes of Health Research (S.A.J., P.W.F.), Natural Sciences and Engineering Research Council of Canada (S.A.J., P.W.F.), Brain Canada (S.A.J., P.W.F.), and Brain and Behavior Research Foundation (S.A.J.) grants. K.D. is supported by the National Institute of Mental Health, National Institute on Drug Abuse, the Wiegers Family Fund, Howard Hughes Medical Institute, and the U.S. Army Research Laboratory and Defense Advanced Research Projects Agency (Cooperative Agreement no. W911NF-14-2-0013). Data are archived in the Dryad repository http://dx.doi.org/10.5061/dryad.5tp75.

SUPPLEMENTARY MATERIALS

www.sciencemag.org/content/353/6297/383/suppl/DC1
Materials and Methods
Figs. S1 to S9
References (*26*–*43*)

11 December 2015; accepted 17 June 2016
10.1126/science.aaf0594

BEHAVIORAL ECOLOGY

Reciprocal signaling in honeyguide-human mutualism

Claire N. Spottiswoode,[1,2]* Keith S. Begg,[3] Colleen M. Begg[3]

Greater honeyguides (*Indicator indicator*) lead human honey-hunters to wild bees' nests, in a rare example of a mutualistic foraging partnership between humans and free-living wild animals. We show experimentally that a specialized vocal sound made by Mozambican honey-hunters seeking bees' nests elicits elevated cooperative behavior from honeyguides. The production of this sound increased the probability of being guided by a honeyguide from about 33 to 66% and the overall probability of thus finding a bees' nest from 17 to 54%, as compared with other animal or human sounds of similar amplitude. These results provide experimental evidence that a wild animal in a natural setting responds adaptively to a human signal of cooperation.

In 1588, João dos Santos, a Portuguese missionary in Sofala (in present-day Mozambique), often noticed a small bird flying through cracks in the walls of his mission church and nibbling wax from the candlesticks within. This kind of bird, he wrote, had another peculiar habit of leading men to bees' nests by calling and flying from tree to tree. After the men harvested the honey, the birds would eat the wax combs left behind (*1*). We now know this species to have been the greater honeyguide *Indicator indicator* and dos Santos's description to have been accurate. Honeyguides eat beeswax and know where bees' nests are located; humans can subdue the bees and open the nest using fire and tools, thus exposing beeswax for the honeyguides and honey for the humans (*2*). This interaction remains an extremely rare example of mutualism between free-living wild animals and our own species. Here we show that it is also a specific example of reciprocal communication between birds and humans.

Greater honeyguides (Fig. 1A) seeking a human collaborator approach people and give a loud chattering call (audio S1). This call is distinct from their territorial song and is accompanied by referential gestures (*3*): the bird flies from tree to tree in the direction of the bees' nest until its human follower finds the nest (*2*, *4*). The honeyguide thus directs a signal of the bees' nest location toward humans, and the honey-hunters use this signal to their mutual advantage. In this study, we ask whether honeyguides in turn exploit specialized signals directed at them by humans. We studied greater honeyguides (hereafter "honeyguides") in the Niassa National Reserve in northern Mozambique. This region has been noted for its honey and beeswax production at least since Arab trading times centuries ago (*5*, *6*). The local Yao people still harvest wild honey using traditional methods, and this practice remains economically important.

[1]Department of Zoology, University of Cambridge, Downing Street, Cambridge CB2 3EJ, UK. [2]FitzPatrick Institute of African Ornithology, Department of Science and Technology–National Research Foundation (DST-NRF) Centre of Excellence, University of Cape Town, Rondebosch 7701, South Africa. [3]The Ratel Trust, Niassa Carnivore Project, Private Bag X18, Rondebosch 7701, South Africa.
*Corresponding author. Email: cns26@cam.ac.uk

First, we confirmed that in northern Mozambique, honeyguides give reliable information to human honey-hunters. To test whether guiding behavior accurately indicates the direction of bees' nests and leads to their successful discovery by humans, we trailed honey-hunters following honeyguides and tracked our movements via GPS. A guiding event was defined as a bout of guiding by an individual bird, sometimes involving consecutive journeys to different bees' nests. Each guiding event probably involved a different individual honeyguide, as the study area was 230 km^2, and the home ranges of individual honeyguides that we measured using radio telemetry did not exceed 1 km^2 and overlapped with one another (*7*) (fig. S1). 75.3% of guiding events led to the successful discovery by humans of at least one bees' nest [mean ± SE = 1.00 ± 0.08 nests; range = 0 to 3 nests; n = 97 events, excluding controls in the experiment discussed below (*7*)]. 94.6% of nests shown belonged to the honeybee *Apis mellifera*, and the rest to stingless bee species (*7*). Nests were located 0 to 832 m (median = 152 m, n = 84 nests, only considering the first nest per guiding event) from the point where guiding began. Figure 1B shows that the birds' initial flight direction accurately signaled the ultimate location of the bees' nest, corroborating a classic study from Kenya (*2*). Overall, 74.5% of bees' nests found by humans (n = 149) involved the help of a honeyguide.

Second, we asked whether the signals used by human honey-hunters provide reliable information to honeyguides. Honey-hunters seeking honeyguides often announce their presence with unspecialized sounds such as shouting and chopping wood (*4*, *8*). In some parts of Africa, however, humans also make specialized vocalizations used only when hunting honey. In the Niassa National Reserve (and, more widely, in northern Mozambique and adjacent southern Tanzania), Yao honey-hunters seeking and following honeyguides produce a loud trill followed by a grunt: "brrrr-hm" [audio S1; see (*9*) for a melodious whistle used in the same context by the Hadza people of northern Tanzania]. To confirm that "brrrr-hm" is a specialized honey-hunting sound, we interviewed 20 Yao honey-hunters, all of whom reported that they used this specific sound when hunting honey but in no other context. When

asked why, they reported that they learned it from their fathers and that it is the best way of attracting a honeyguide and maintaining its attention. Therefore, this sound has the potential to reliably signal to honeyguides that a prospective human partner is specifically seeking honey and has the tools, skills, and time to open a bees' nest, which many humans do not. A payoff to the bird reliably results from interacting with such a partner, because if a bees' nest is harvested then wax is left behind, either as combs containing no honey or as chewed lumps spat out by honey-hunters.

Finally, we examined whether honeyguides associated this vocal signal with a higher chance of a payoff from cooperation. If so, then honeyguides should be more likely to initiate collaboration with humans producing this honey-hunting sound rather than other sounds. To test this, we carried out 72 15-min experimental transects simulating honey-hunting forays, in which an author and two local honey-hunters walked while playing back one of three acoustic cues every 7 s at consistent amplitude using a calibrated speaker: (i) a control human sound (either the Yao words for "honeyguide" and "honey" or the honey-hunter's name, alternated among transects); (ii) a control animal sound (either the song or the excitement call of the ring-necked dove, *Streptopelia capicola*, alternated among transects); or (iii) the specialized "brrrr-hm" honey-hunting sound [see (*7*) for details and audio S2 to S4 for examples]. Each transect used a distinct playback exemplar recorded from a different individual person or bird. Honeyguides have never been confirmed to guide any species besides humans (*10*). We conducted this experiment during the hot dry season; the average shade air temperature at the end of each transect was 31°C (range = 23° to 38°C). Therefore, we also tested the effects of temperature, trial time relative to sunrise or sunset, and morning versus afternoon [details in (*7*)].

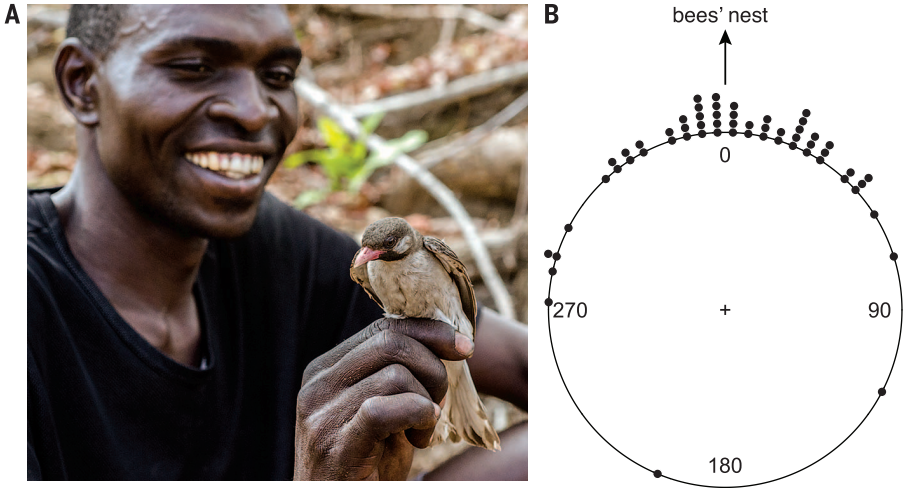

Fig. 1. Greater honeyguides accurately lead humans to bees' nests. (**A**) A Yao honey-hunter and a wild, free-living honeyguide. (This bird was captured using a researcher's mist-net and is neither tame nor habitually captive.) (**B**) Accuracy of honeyguide initial guiding behavior in relation to direction of successfully located bees' nests. Points represent the difference in bearing between initial guiding trajectory over the first 40 m of travel and the ultimate direction of the bees' nest (here set at 0) and are binned into 5° intervals. Each point represents a journey (n = 58 journeys) to a separate bees' nest that was at least 80 m away from the point where guiding began. Sometimes a honeyguide led humans to more than one nest consecutively (n = 50 guiding events). The circular distribution is unimodal (Rayleigh test, $P < 0.001$) with a mean of 1.7° (95% confidence interval includes zero: 352.3° to 11.1°), showing that honeyguide behavior offers reliable directional information to humans.

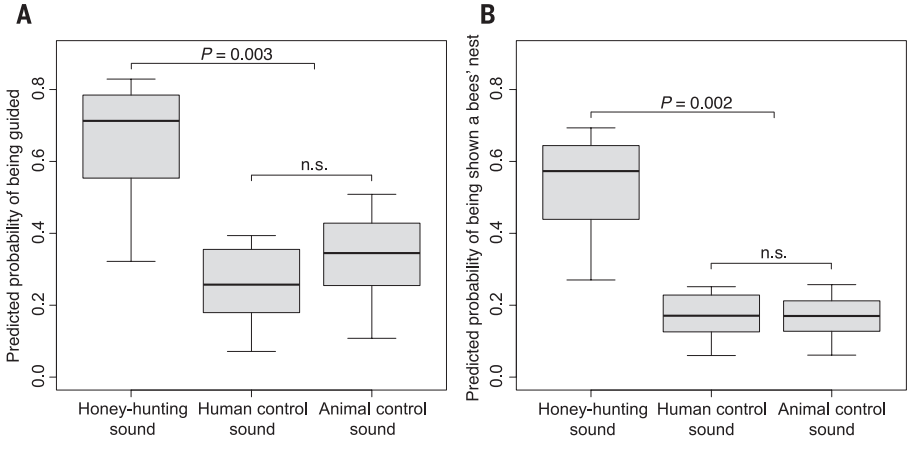

Fig. 2. Probability of a successful mutualistic interaction, in relation to experimentally given acoustic cues. Values are predicted probabilities of (**A**) being guided by a honeyguide and (**B**) being shown a bees' nest on a 15-min search, derived from a logistic model of data from experimental transects and accounting for time of day (minutes from sunrise to sunset). Boxes show medians and quartiles; whiskers show ranges (n = 24 trials per treatment group; P values show planned comparisons; n.s., not significant).

We were guided by a honeyguide on 30 of 72 transects. Transects accompanied by the honey-hunting call had a 66.7% probability of eliciting guiding from a honeyguide, which was significantly greater than that for transects accompanied by the human control sounds (25%) or animal control sounds (33.3%) (Fig. 2A; planned comparison with controls: estimate ± SE = 1.13 ± 0.38, Z = 2.96, P = 0.0031). The probability of guiding did not differ between the two control treatments (estimate ± SE = 0.25 ± 0.33, Z = 0.76, P = 0.45). The best model also included the time relative to sunrise or sunset as a covariate (probability of being guided weakly decreased closer to the middle of the day: estimate ± SE = −4.34 ± 0.20, Z = −2.13, P = 0.034) and, overall, explained 25% of the variance in probability of being led by a honeyguide.

Once a honeyguide initiated guiding behavior, we followed it while continuing to play back the acoustic treatment, while the honey-hunters searched visually for bees' nests [see (*7*) for measures taken to encourage and validate equal search effort]. This revealed that honeyguides tended to cease guiding behavior more often when either of the two control sounds was produced, resulting in no bees' nests being found. Of those transects on which we were led by a honeyguide, we found a bees' nest for 81.3% when accompanied by the honey-hunting sound, compared with 66.7 and 50.0% when accompanied by the human and animal control sounds, respectively. Overall, the honey-hunting sound resulted in a 54.2% predicted probability of finding a bees' nest (Fig. 2B; planned comparison with controls: estimate ± SE = 1.21 ± 0.39, Z = 3.14, P = 0.0017) compared with 16.7% for each of the control sounds (planned comparison between controls: estimate ± SE = 0.03 ± 0.39, Z = 0.08, P = 0.94). Thus, production of the honey-hunting sound more than tripled the probability of finding a bees' nest during a standardized 15-min search accompanied by an acoustic cue. This finding experimentally validates the honey-hunters' claims that the honey-hunting sound improves their foraging success.

Honeyguides might respond more to humans producing the honey-hunting sound either because they recognize and prefer it or because they are simply more likely to hear it versus control sounds. If the latter is true, then honeyguide behavior should be predicted by playback amplitude after attenuation in the environment. We measured the mean and maximum amplitudes (in units of A-weighted decibels) of every playback exemplar with a sound-level meter at a distance of 30 m in the natural habitat of these birds

(table S1) and tested whether the amplitudes explained any variance in guiding behavior, either in isolation or in the multivariate models above. In no case did these acoustic measures explain any variance in the probability of being guided or being shown a bees' nest (*7*). Therefore, the honeyguides' elevated response to the honey-hunting sound is unlikely to be explained by its audibility. Instead, the most parsimonious explanation is that honeyguides associate the honey-hunting sound with successful collaboration. Such partner choice should be adaptive by allowing honeyguides to improve their net benefit from interacting with humans.

These results show that a wild animal correctly attaches meaning and responds appropriately to a human signal of recruitment toward cooperative foraging, a behavior previously associated with only domestic animals, such as dogs (*11*). Although humans use many species as foraging partners, including falcons, dogs, and cormorants, these involve trained or domesticated individuals that are specifically taught to cooperate. The honeyguide-human relationship is notable in that it involves free-living wild animals whose interactions with humans have probably evolved through natural selection. To our knowledge, the only comparable relationship involves cooperation between artisanal fishermen and free-living dolphins. Several reports exist of men "calling" dolphins to hunt, starting with Pliny the Elder around 70 CE (*12*). Whether this reflects a similarly specialized communication system to that mediating the honeyguide-human mutualism in Mozambique remains unknown.

How might honeyguides acquire information about honey-hunters' signals of cooperation? Honeyguides are brood-parasitic and reared by insectivorous hosts (*4*), which suggests that their propensity to locate bees' nests and guide humans to them is likely to be innate. However, the "brrrr-hm" human signal studied here is confined to a specific geographical area, and a different cultural group living 1000 km away uses a different signal which is likely to have the same function (*9*). Local adaptation is unlikely to account for corresponding honeyguide specialization, given a lack of obvious genetic structure across its range (*13*). This implies that local refinements to guiding behavior are probably learned, which is supported anecdotally by the belief of many Yao honey-hunters that juvenile honeyguides [which have distinctive yellow plumage (*4*)] are a separate species (called "namandindi") that, despite beckoning humans in the manner of an adult honeyguide ("sego"), falls quiet in response to the honey-hunting sound. We propose that learning might occur socially from conspecifics in the vicinity of bees' nests, resulting in a local cultural tradition among honeyguides that reflects the customs of their human collaborators.

REFERENCES AND NOTES

1. J. dos Santos, *Ethiopia Oriental* (Convento de S. Domingos de Évora, Évora, 1609).
2. H. A. Isack, H. U. Reyer, *Science* **243**, 1343–1346 (1989).
3. A. L. Vail, A. Manica, R. Bshary, *Nat. Commun.* **4**, 1765 (2013).
4. H. Friedmann, in "The honey-guides" (U.S. National Museum Bulletin 208, Smithsonian Institution, 1955), pp. 1–292; https://repository.si.edu/handle/10088/10101.
5. G. D. Popplewell, T. E. Harcus, *Geogr. J.* **91**, 31–43 (1938).
6. E. Colson, M. Gluckman, *Seven Tribes of British Central Africa* (Manchester Univ. Press 1959).
7. Materials and methods are available as supplementary materials on *Science* Online.
8. H. A. Isack, thesis, University of Oxford, Oxford (1987).
9. B. M. Wood, H. Pontzer, D. A. Raichlen, F. W. Marlowe, *Evol. Hum. Behav.* **35**, 540–546 (2014).
10. W. R. J. Dean, W. R. Siegfried, I. A. W. MacDonald, *Conserv. Biol.* **4**, 99–101 (1990).
11. J. Kaminski, J. Call, J. Fischer, *Science* **304**, 1682–1683 (2004).
12. R.-G. Busnel, *Trans. N.Y. Acad. Sci.* **35**, 112–131 (1973).
13. C. N. Spottiswoode, K. F. Stryjewski, S. Quader, J. F. R. Colebrook-Robjent, M. D. Sorenson, *Proc. Natl. Acad. Sci. U.S.A.* **108**, 17738–17742 (2011).

ACKNOWLEDGMENTS

We thank O. Yassene, M. Muamedi, C. Augusto, E. Waiti, M. Marufo, R. Iassine, and A. Jorge for help with fieldwork and interviews; the honey-hunters of Mbamba village for their participation; Administração Nacional das Áreas de Conservação, Wildlife Conservation Society, and C. Miguel for research permission; Mariri Environmental Centre for logistical support; S. Hoy (Wild & Marr, Cape Town) for equipment loan; and N. Boogert, N. Davies, T. Flower, G. Jamie, R. Magrath, D. Rendall, G. Ruxton, M. Sorensen, B. Wood, and R. Wrangham for advice and comments. C.N.S. was supported by a Biotechnology and Biological Sciences Research Council David Phillips Research Fellowship (BB/J014109/1) and the DST-NRF Centre of Excellence at the FitzPatrick Institute. Data are deposited in Dryad (DOI: 10.5061/dryad.8c65s). All authors conceived the study; K.S.B. and C.M.B. facilitated the fieldwork; C.N.S. collected and analyzed the data and wrote the paper.

SUPPLEMENTARY MATERIALS

www.sciencemag.org/content/353/6297/387/suppl/DC1
Materials and Methods
Fig. S1
Table S1
References (*14–22*)
Audio S1 to S4

16 February 2016; accepted 28 June 2016
10.1126/science.aaf4885

PROTEIN DESIGN

Accurate design of megadalton-scale two-component icosahedral protein complexes

Jacob B. Bale,[1,2] Shane Gonen,[1,3]* Yuxi Liu,[4]* William Sheffler,[1] Daniel Ellis,[5] Chantz Thomas,[6] Duilio Cascio,[4,7,8] Todd O. Yeates,[4,7] Tamir Gonen,[3] Neil P. King,[1,5]† David Baker[1,5,9]†

Nature provides many examples of self- and co-assembling protein-based molecular machines, including icosahedral protein cages that serve as scaffolds, enzymes, and compartments for essential biochemical reactions and icosahedral virus capsids, which encapsidate and protect viral genomes and mediate entry into host cells. Inspired by these natural materials, we report the computational design and experimental characterization of co-assembling, two-component, 120-subunit icosahedral protein nanostructures with molecular weights (1.8 to 2.8 megadaltons) and dimensions (24 to 40 nanometers in diameter) comparable to those of small viral capsids. Electron microscopy, small-angle x-ray scattering, and x-ray crystallography show that 10 designs spanning three distinct icosahedral architectures form materials closely matching the design models. In vitro assembly of icosahedral complexes from independently purified components occurs rapidly, at rates comparable to those of viral capsids, and enables controlled packaging of molecular cargo through charge complementarity. The ability to design megadalton-scale materials with atomic-level accuracy and controllable assembly opens the door to a new generation of genetically programmable protein-based molecular machines.

The forms and functions of natural protein assemblies have inspired many efforts to engineer self- and co-assembling protein complexes (*1–24*). A common feature of these approaches, as well as the structures that inspire them, is symmetry. By repeating a small number of interactions in geometric arrangements that are consistent with the formation of regular structures, symmetry reduces the number of distinct interactions and subunits required to form higher-order assemblies (*2*, *3*, *25*). Symmetric complexes can be designed to form through self-assembly of a single type of protein subunit or co-assembly of two or more distinct types of protein subunits. Multicomponent materials possess several important advantages, including the potential to control the initiation of assembly by mixing independently prepared components. This property could allow,

[1]Department of Biochemistry, University of Washington, Seattle, WA 98195, USA. [2]Graduate Program in Molecular and Cellular Biology, University of Washington, Seattle, WA 98195, USA. [3]Janelia Research Campus, Howard Hughes Medical Institute, Ashburn, VA 20147, USA. [4]Department of Chemistry and Biochemistry, University of California–Los Angeles (UCLA), Los Angeles, CA 90095, USA. [5]Institute for Protein Design, University of Washington, Seattle, WA 98195, USA. [6]Department of Chemistry, University of Washington, Seattle, WA 98195, USA. [7]UCLA–Department of Energy (DOE) Institute for Genomics and Proteomics, Los Angeles, CA 90095, USA. [8]Department of Biological Chemistry and Molecular Biology Institute, UCLA, Los Angeles, CA 90095, USA. [9]Howard Hughes Medical Institute, University of Washington, Seattle, WA 98195, USA.
*These authors contributed equally to this work.
†Corresponding author. Email: neilking@uw.edu (N.P.K.); dabaker@uw.edu (D.B.)

for example, assembly to be performed in the presence of cargo molecules in order to package the cargo inside the designed nanomaterial. Thus far, only relatively small (24-subunit) two-component tetrahedra have been designed with high accuracy (*20*, *26*). Packaging substantial amounts of cargo requires larger assemblies; icosahedral symmetry is the highest of the point group symmetries and therefore generally results in the maximum enclosed volume for a symmetric assembly formed from a protein subunit of a given size (*27*, *28*).

We set out to design two-component icosahedral protein complexes capable of packaging macromolecular cargo through controlled in vitro assembly. The twofold, threefold, and fivefold rotational axes present within icosahedral symmetry provide three possible ways to construct

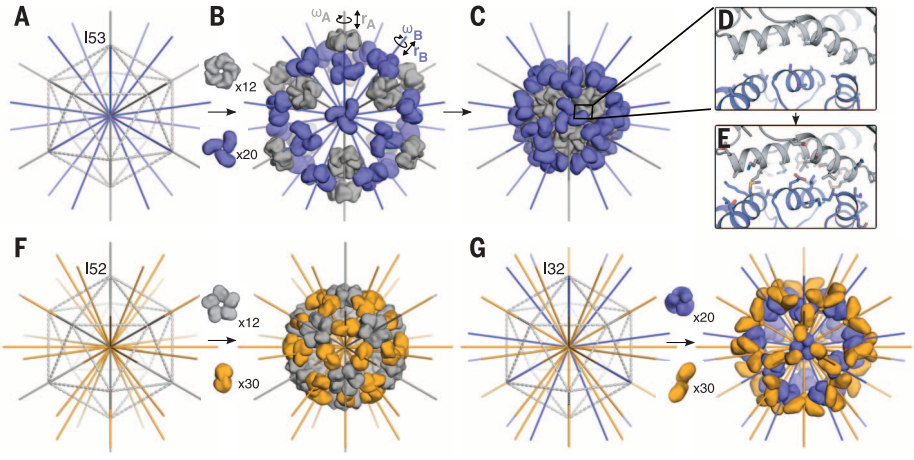

Fig. 1. Overview of the design method and target architectures. In (A) to (E), the design process is illustrated with the I53 architecture. (**A**) An icosahedron is outlined with dashed lines, with fivefold symmetry axes (gray) going through each vertex and threefold symmetry axes (blue) going through each face of the icosahedron. (**B**) Twelve pentamers (gray) and 20 trimers (blue) are aligned along the fivefold and threefold symmetry axes, respectively. Each oligomer possesses two rigid-body degrees of freedom, one translational (r) and one rotational (ω), that are systematically sampled to identify (**C**) configurations with (**D**) a large interface between the pentamer and trimer that makes them suitable for protein-protein interface design; only the backbone structure and beta carbons of the oligomers are taken into account during this procedure. (**E**) Amino acid sequences are designed at the new interface to stabilize the modeled configuration. (**F**) The I52 architecture comprises 12 pentamers (gray) and 30 dimers (orange) aligned along the fivefold and twofold icosahedral symmetry axes. (**G**) The I32 architecture comprises 20 trimers (blue) and 30 dimers (orange) aligned along the threefold and twofold icosahedral symmetry axes.

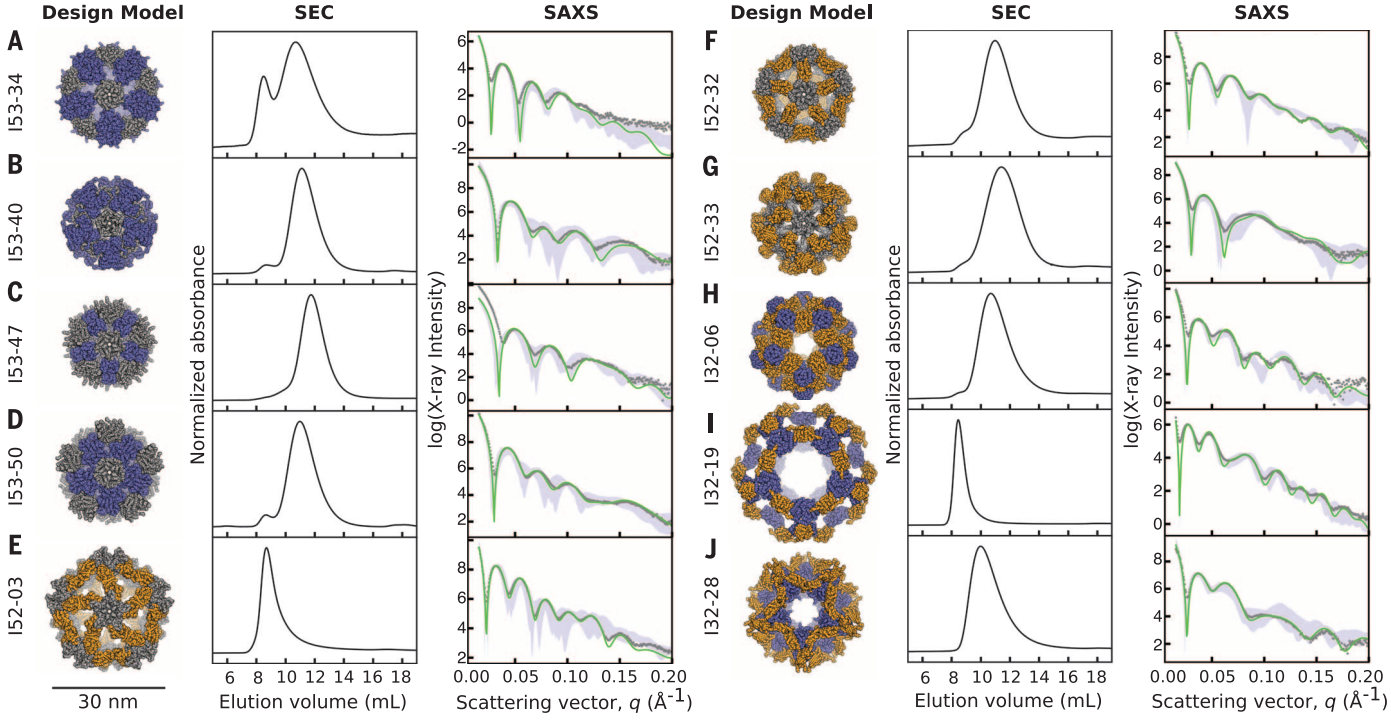

Fig. 2. Experimental characterization by SEC and SAXS. Computational design models (left), SEC chromatograms (middle), and SAXS profiles (right) are shown for (**A**) I53-34, (**B**) I53-40, (**C**) I53-47, (**D**) I53-50, (**E**) I52-03, (**F**) I52-32, (**G**) I52-33, (**H**) I32-06, (**I**) I32-19, and (**J**) I32-28. Design models (shown to scale relative to the 30-nm scale bar) are viewed down one of the fivefold symmetry axes, with ribbon-style renderings of the protein backbone (pentamers are shown in gray, trimers in blue, and dimers in orange). Co-expressed and purified designs yield dominant SEC peaks near the expected elution volumes for the target 120-subunit complexes and x-ray scattering intensities (gray dots) that match well with profiles calculated from the design models (green). Alternative configurations of the designs, generated by translating the oligomeric building blocks in the design models by ±10 Å and/or rotating them about their aligned symmetry axes by ±20°, generally fit worse with the SAXS data than the original design models do (the range of values obtained from fitting the alternative configurations is shown with light blue shading).

such complexes from pairwise combinations of oligomeric building blocks; we refer to these architectural types as I53, I52, and I32 (fig. S1). The I53 architecture is formed from a combination of 12 pentameric building blocks and 20 trimeric building blocks aligned along the fivefold and threefold icosahedral symmetry axes, respectively (Fig. 1, A to E; I53 stands for icosahedral assembly constructed from pentamers and trimers). Similarly, the I52 architecture is formed from 12 pentamers and 30 dimers (Fig. 1F), and the I32 architecture is formed from 20 trimers and 30 dimers, each aligned along their corresponding icosahedral symmetry axes (Fig. 1G). To generate novel icosahedral assemblies, 14,400 pairs of pentamers and trimers, 50,400 pairs of pentamers and dimers, and 276,150 pairs of trimers and dimers derived from x-ray crystal structures (tables S1 to S3) were arranged as described above, with each building block allowed to rotate around and translate along its fivefold, threefold, or twofold symmetry axis. These degrees of freedom were systematically sampled to identify configurations that would be suitable for interface design, as assessed by several parameters, including the size and secondary structure content of the newly formed interface and the relative orientation of backbone elements on the two sides of the interface. Protein-protein interface design calculations were then carried out on the resulting 66,115 designs of type I53, 35,468 designs of type I52, and 161,007 designs of type I32. The designs were filtered based on a variety of metrics, including interface area, predicted binding energy, and shape complementarity (*29*). Seventy-one designs of type I53, 44 of type I52, and 68 of type I32—derived from 23 distinct pentameric, 57 distinct trimeric, and 91 distinct dimeric protein scaffolds—were selected for experimental characterization (figs. S2 to S5 and table S4).

Codon-optimized genes encoding each pair of designed sequences were cloned into a vector for inducible coexpression in *Escherichia coli*, with a hexahistidine tag appended to the N or C terminus of one subunit in each pair. The proteins were expressed at a small scale and purified by immobilized metal-affinity chromatography (IMAC); clarified lysates and purification products were subjected to gel electrophoresis under denaturing conditions to screen for soluble expression and copurification of the hexahistidine-tagged and nontagged subunits (fig. S6A). Designs that appeared to copurify were subsequently analyzed by nondenaturing gel electrophoresis to screen for slowly migrating species as an additional indication of assembly into higher-order materials (fig. S6B). Those found to both copurify and assemble were expressed at a larger scale and purified by IMAC, which was followed by size exclusion chromatography (SEC; fig. S7). Ten designs—four I53 (I53-34, I53-40, I53-47, and I53-50), three I52 (I52-03, I52-32, and I52-33), and three I32 (I32-06, I32-19, and I32-28)—yielded major SEC peaks near the elution volumes expected based on the diameters of the design models (Fig. 2 and table S4). Two other designs, I53-51 and I32-10, also appeared to form large, discrete assemblies, but their structures could not be verified by subsequent experiments (supplementary text and figs. S8 and S9).

Small-angle x-ray scattering (SAXS) performed on the SEC-purified samples indicated that all 10 designs form assemblies similar to the intended three-dimensional configurations in solution. The experimentally measured SAXS profiles are feature-rich and distinct, with multiple large dips in scattering intensity in the region between 0.015 and 0.15 $Å^{-1}$, each of which is closely recapitulated in profiles calculated from the design models (Fig. 2) (*30*). To further evaluate how accurately and uniquely the design models match the experimental data, each was compared with a set of alternative models generated by systematically perturbing the radial displacements and/or the rotations of the building blocks in each design by ±10 Å and ±20°, respectively. The vast majority of alternative configurations were found to produce worse fits to the experimental data than the original design models (Fig. 2), suggesting that the materials assemble precisely in solution.

The information provided by SAXS about the overall ensemble of the structures observed in solution for each design was complemented and corroborated by visualization of individual particles by negative-stain electron microscopy (EM). Micrographs of I53-34, I53-40, I53-47, I53-50, I52-03, I52-33, I32-06, and I32-28 show fields of particles with the size and shape of the design models, and particle averaging yielded

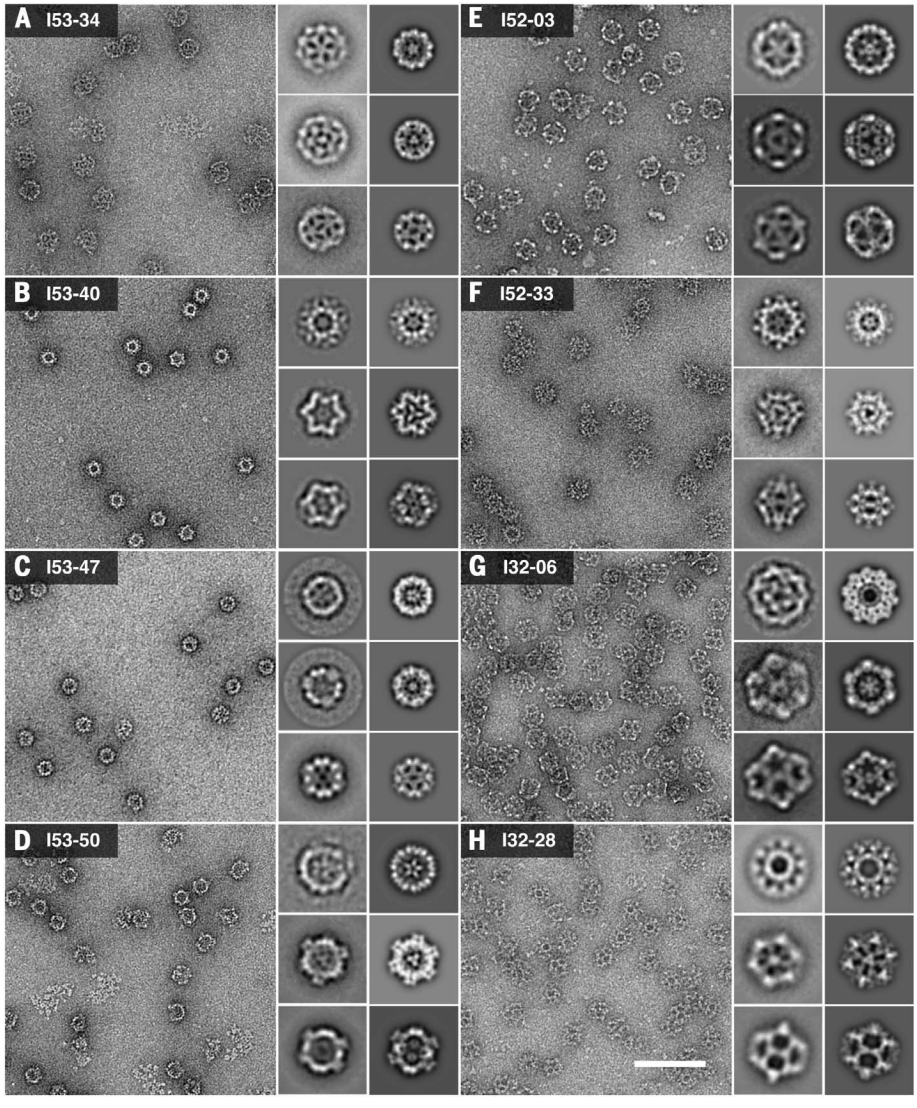

Fig. 3. Characterization of the designed materials by EM. Raw negative-stain electron micrographs of coexpressed and purified (**A**) I53-34, (**B**) I53-40, (**C**) I53-47, (**D**) I53-50, (**E**) I52-03, (**F**) I52-33, (**G**) I32-06, and (**H**) I32-28. All raw micrographs are shown to scale relative to the 100-nm scale bar in (H). The insets show experimentally computed class averages (roughly corresponding to the fivefold, threefold, and twofold icosahedral symmetry axes; left column in each inset), along with back projections calculated from the design models (right column in each inset). The width of each inset box is 55 nm.

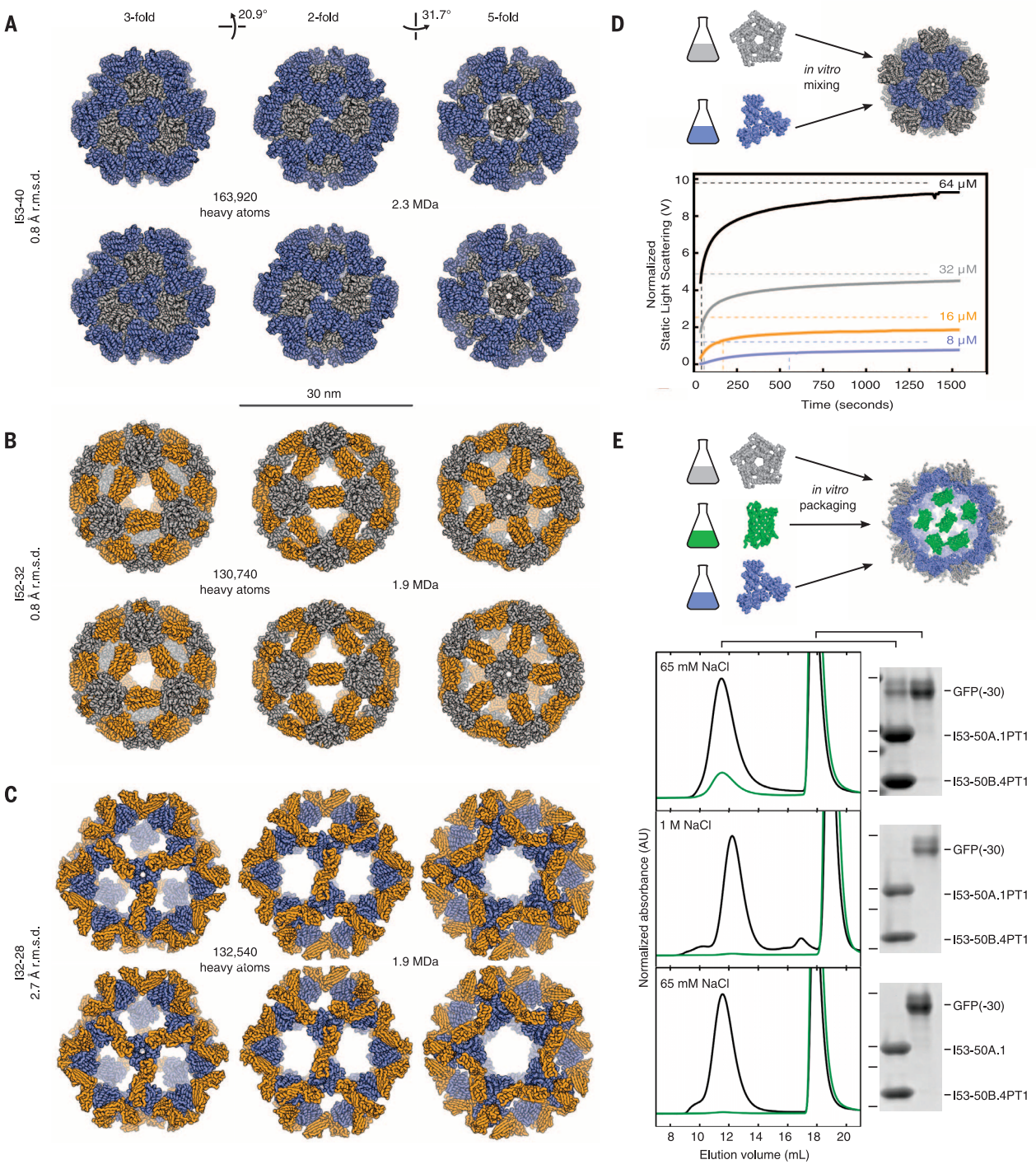

Fig. 4. Crystal structures, assembly dynamics, and packaging. Design models (top) and x-ray crystal structures (bottom) of (**A**) I53-40, (**B**) I52-32, and (**C**) I32-28. Views are shown to scale along the threefold, twofold, and fivefold icosahedral symmetry axes. Pentamers are shown in gray, trimers in blue, and dimers in orange. RMSDs are between crystal structures and design models over all backbone atoms in all 120 subunits. (**D**) In vitro assembly dynamics of I53-50. A schematic is shown in the upper panel. Below, normalized static light-scattering intensity is plotted over time after mixing independently expressed and purified variants of the I53-50 trimer and pentamer in a 1:1 molar ratio at final concentrations of 8, 16, 32, or 64 μM (blue, orange, gray, and black solid lines, respectively, representing detector voltage). Intensities measured from SEC-purified assembly at concentrations of 8, 16, 32, or 64 μM are indicated with dashed horizontal lines and used as the expected end point of each assembly reaction. The midpoint of each reaction is marked with a dashed vertical line. (**E**) Encapsulation of supercharged GFP in a positively charged I53-50 variant. A schematic is shown in the upper panel (bright green, GFP). SEC chromatograms and SDS-PAGE analyses of packaging and assembly reactions are shown below. The reactions were performed in either 65 mM NaCl (top and bottom) or 1 M NaCl (middle). I53-50A.1PT1 and I53-50B.4PT1 are variants of the trimeric and pentameric components of I53-50 bearing several mutations to positively charged residues; I53-50A.1 is a control variant of the trimeric component that lacks these mutations (supplementary text). In each case, the same buffer used in the packaging and assembly reaction was also used during SEC. Absorbance measurements at 280 nm (black) and 488 nm (green) are shown. Each SEC chromatogram was normalized relative to the 280-nm peak near 12 ml elution volume. Locations of 37-, 25-, 20-, and 15-kDa–molecular weight markers on SDS-PAGE gels are indicated by horizontal lines to the left of the gels.

distinct structures clearly matching the models (Fig. 3). The large trimeric and pentameric voids observed in the I52 and I32 averages, for instance, closely resemble the cavities in projections generated from the corresponding design models when viewed down the threefold and fivefold symmetry axes, respectively. The turreted morphology of the I53-50 and I52-33 design models and projections, resulting from pentameric and dimeric components that protrude away from the rest of the icosahedral shell, are also readily apparent in the corresponding class averages. Although the results from SEC and SAXS strongly indicate that I52-32 and I32-19 form assemblies closely matching the design models in solution, both appear to be unstable under the conditions encountered during grid preparation, yielding broken particles that were not suitable for further EM analysis (fig. S10).

To further evaluate the accuracy of our designs, x-ray crystal structures were determined for one material from each of the three architectural types: I53-40, I52-32, and I32-28 (Fig. 4 and table S5). Although the resolution of the structures (3.5 to 5.6 Å) is insufficient to permit detailed analysis of the side chains at the designed interfaces, backbone-level comparisons show that the building block interfaces were designed with high accuracy, giving rise to 120-subunit complexes that match the computational design models very well. Comparing pairs of interface subunits from each structure with the design models yields backbone root mean square deviations (RMSDs) between 0.2 and 1.1 Å, whereas the RMSD over all 120 subunits in each material ranges from 0.8 to 2.7 Å (Fig. 4, A to C, and table S6). With diameters between 26 and 31 nm, over 130,000 heavy atoms, and molecular weights greater than 1.9 MDa, these structures are comparable in size to small viral capsids and, to our knowledge, are the largest designed biomolecular nanostructures to date to be verified by x-ray crystallography (fig. S11).

The multicomponent composition of the materials presents the possibility of controlling their assembly through in vitro mixing of independently produced building blocks (*20*). Taking advantage of this feature, the assembly kinetics of an I53-50 variant (fig. S12A) with improved individual subunit stability were investigated by light scattering (supplementary materials). SEC-purified components were mixed at concentrations of 64, 32, 16, or 8 μM, and the change in light scattering was monitored over time (Fig. 4D). Assembly was roughly halfway complete within 1 min at 64 and 32 uM, within 3 min at 16 uM, and within 10 min at 8 uM. Similar assembly time scales have been observed for several viral capsids (*31*, *32*). Because our design process focused exclusively on structure without any consideration of kinetics, these results raise the interesting possibility that the rate of assembly of these viral capsids has not been highly optimized during evolution.

The ability to assemble the materials in vitro potentially enables the controlled packaging of macromolecular cargoes. To investigate this possibility, the trimeric and pentameric components of an I53-50 variant with several mutations to positively charged residues on its interior surface (supplementary materials) were successively mixed with a supercharged green fluorescent protein (GFP) with a net charge of –30 (*33*), and encapsulation was evaluated using SEC followed by SDS–polyacrylamide gel electrophoresis (PAGE) of relevant fractions (Fig. 4E and supplementary materials). When both the packaging reaction and SEC were performed in a buffer containing low (65 mM) NaCl, GFP(–30) and both I53-50 components coeluted from the column at the same elution volume previously observed for unmodified I53-50 (Fig. 2D). Mixtures of GFP(–30) with only one of the two components eluted at later volumes, indicating that the observed coelution requires assembly of I53-50 (fig. S12, B to D). When the packaging reaction was carried out in a buffer containing high (1 M) NaCl or using a variant of the trimeric component that lacked mutations to positively charged residues on the interior surface, little to no coelution was observed (Fig. 4E), suggesting that packaging is driven by the engineered electrostatic interactions between the I53-50 interior and GFP(–30). High-salt incubation resulted in disassociation of packaged GFP (fig. S12E), as has also been observed for an evolved variant of a naturally occurring protein container that packages cargo by means of electrostatic complementarity (*34*, *35*). Based on measurements of fluorescence intensity and ultraviolet–visible light absorbance, we estimate that about 7 to 11 GFPs are packaged per icosahedral assembly in 65 mM NaCl, occupying roughly 11 to 17% of the interior volume (supplementary materials).

How do the architectures of our designs compare to those of virus capsids and other icosahedral protein complexes found in nature? Our designs obey strict icosahedral symmetry, with the asymmetric unit in each case containing a heterodimer that comprises one subunit from each of the two components. The most similar naturally occurring structures of which we are aware are cowpea mosaic virus (CPMV) and related 120-subunit capsids with pseudo $T = 3$ symmetry [T refers to the triangulation number (*27*)]. Like our I53 designs, CPMV is composed of 60 copies each of two distinct protein subunits, with one type of subunit arranged around the icosahedral fivefolds and a second type of subunit arranged around the threefolds (fig. S13). However, the two subunits of CPMV are composed of three similar domains occupying spatially equivalent positions to those found in $T = 3$ assemblies formed from 180 copies of a single type of protein subunit (*36*, *37*). Our I53 designs display no such underlying pseudosymmetry and therefore cannot be considered to be pseudo $T = 3$. Furthermore, we are not aware of any natural protein complexes characterized to date that exhibit I52 or I32 architectures. Our designs thus appear to occupy new regions of the protein assembly universe, which either have not yet been explored by natural evolution or are undiscovered at present in natural systems.

The size and complexity of the materials presented here, together with the accuracy with which they assemble, push the boundaries of biomolecular engineering into new territory. The large lumens of our designed materials, combined with their multicomponent nature and the ability to control assembly through mixing of purified components, make them well suited for encapsulation of a broad range of materials including small molecules, nucleic acids, polymers, and other proteins. These features, along with the precision and modularity with which they can be engineered, make our designed nanomaterials attractive starting points for new approaches to targeted drug delivery, vaccine design, and bioenergy.

REFERENCES AND NOTES

1. Y. T. Lai, N. P. King, T. O. Yeates, *Trends Cell Biol.* **22**, 653–661 (2012).
2. N. P. King, Y. T. Lai, *Curr. Opin. Struct. Biol.* **23**, 632–638 (2013).
3. J. E. Padilla, C. Colovos, T. O. Yeates, *Proc. Natl. Acad. Sci. U.S.A.* **98**, 2217–2221 (2001).
4. P. Ringler, G. E. Schulz, *Science* **302**, 106–109 (2003).
5. S. Raman, G. Machaidze, A. Lustig, U. Aebi, P. Burkhard, *Nanomedicine* **2**, 95–102 (2006).
6. D. Grueninger *et al.*, *Science* **319**, 206–209 (2008).
7. S. Raman *et al.*, *Open Nanomed. J.* **2**, 15–26 (2009).
8. K. Usui *et al.*, *Protein Sci.* **18**, 960–969 (2009).
9. E. N. Salgado, R. J. Radford, F. A. Tezcan, *Acc. Chem. Res.* **43**, 661–672 (2010).
10. G. Grigoryan *et al.*, *Science* **332**, 1071–1076 (2011).
11. J. C. Sinclair, K. M. Davies, C. Vénien-Bryan, M. E. Noble, *Nat. Nanotechnol.* **6**, 558–562 (2011).
12. P. B. Stranges, M. Machius, M. J. Miley, A. Tripathy, B. Kuhlman, *Proc. Natl. Acad. Sci. U.S.A.* **108**, 20562–20567 (2011).
13. A. L. Boyle *et al.*, *J. Am. Chem. Soc.* **134**, 15457–15467 (2012).
14. J. D. Brodin *et al.*, *Nat. Chem.* **4**, 375–382 (2012).
15. B. S. Der *et al.*, *J. Am. Chem. Soc.* **134**, 375–385 (2012).
16. N. P. King *et al.*, *Science* **336**, 1171–1174 (2012).
17. Y. T. Lai, D. Cascio, T. O. Yeates, *Science* **336**, 1129 (2012).
18. C. J. Lanci *et al.*, *Proc. Natl. Acad. Sci. U.S.A.* **109**, 7304–7309 (2012).
19. J. M. Fletcher *et al.*, *Science* **340**, 595–599 (2013).
20. N. P. King *et al.*, *Nature* **510**, 103–108 (2014).
21. Y. T. Lai *et al.*, *Nat. Chem.* **6**, 1065–1071 (2014).
22. A. R. Voet *et al.*, *Proc. Natl. Acad. Sci. U.S.A.* **111**, 15102–15107 (2014).
23. S. Gonen, F. DiMaio, T. Gonen, D. Baker, *Science* **348**, 1365–1368 (2015).
24. Y. Hsia *et al.*, *Nature* **535**, 136–139 (2016).
25. D. S. Goodsell, A. J. Olson, *Annu. Rev. Biophys. Biomol. Struct.* **29**, 105–153 (2000).
26. J. B. Bale *et al.*, *Protein Sci.* **24**, 1695–1701 (2015).
27. D. L. Caspar, A. Klug, *Cold Spring Harb. Symp. Quant. Biol.* **27**, 1–24 (1962).
28. R. Zandi, D. Reguera, R. F. Bruinsma, W. M. Gelbart, J. Rudnick, *Proc. Natl. Acad. Sci. U.S.A.* **101**, 15556–15560 (2004).
29. M. C. Lawrence, P. M. Colman, *J. Mol. Biol.* **234**, 946–950 (1993).
30. K. N. Dyer *et al.*, *Methods Mol. Biol.* **1091**, 245–258 (2014).
31. A. Zlotnick, J. M. Johnson, P. W. Wingfield, S. J. Stahl, D. Endres, *Biochemistry* **38**, 14644–14652 (1999).
32. A. Zlotnick, R. Aldrich, J. M. Johnson, P. Ceres, M. J. Young, *Virology* **277**, 450–456 (2000).
33. M. S. Lawrence, K. J. Phillips, D. R. Liu, *J. Am. Chem. Soc.* **129**, 10110–10112 (2007).
34. B. Wörsdörfer, K. J. Woycechowsky, D. Hilvert, *Science* **331**, 589–592 (2011).
35. R. Zschoche, D. Hilvert, *J. Am. Chem. Soc.* **137**, 16121–16132 (2015).
36. T. Lin *et al.*, *Virology* **265**, 20–34 (1999).
37. T. Lin *et al.*, *J. Virol.* **74**, 493–504 (2000).

ACKNOWLEDGMENTS

We thank M. Sawaya and M. Collazo for their assistance with crystallography, conducted at the UCLA-DOE X-ray Crystallization and Crystallography Core Facilities, which are supported by DOE grant DE-FC02-02ER63421. We thank M. Capel, K. Rajashankar, N. Sukumar, J. Schuermann, I. Kourinov, and F. Murphy at Northeastern Collaborative Access Team beamlines 24-ID-E and 24-ID-C at the Advanced Photon Source (APS), which are supported by grants from the National Center for Research Resources (5P41RR015301-10) and the National Institute of General Medical Sciences (8 P41 GM103403-10) of the National Institutes of Health. Use of the APS is supported by DOE under contract no. DE-AC02-06CH11357. We thank the staff at the Advanced Light Source SIBYLS beamline at Lawrence Berkeley National Laboratory, including K. Burnett, G. Hura, M. Hammel, J. Tanamachi, and J. Tainer for the services provided through the mail-in SAXS program, which is supported by the DOE Office of Biological and Environmental Research Integrated Diffraction Analysis program and the NIH project MINOS (Macromolecular Insights on Nucleic Acids Optimized by Scattering; grant no. RO1GM105404). We also thank U. Nattermann for help with EM, Y. Hsia for assistance with light-scattering experiments, C. Stafford for mass spectroscopy assistance, B. Nickerson for assistance with in vitro assembly experiments, and G. Rocklin for providing scripts used in data analysis. This work was supported by the Howard Hughes Medical Institute (S.G., D.C., T.G., and D.B.) and its Janelia Research Campus visitor program (S.G.), the Bill and Melinda Gates Foundation (D.B. and N.P.K.), Takeda Pharmaceutical Company (N.P.K.), NSF (grant no. CHE-1332907 to D.B. and T.O.Y.), the Air Force Office of Scientific Research (grant no. FA950-12-10112 to D.B.), and the Defense Advanced Research Projects Agency (grant no. W911NF-14-1-0162 to D.B. and N.P.K.). Y.L. was supported by a Whitcome Fellowship through the UCLA Molecular Biology Institute, and J.B.B. was supported by a NSF graduate research fellowship (grant no. DGE-0718124). Coordinates and structure factors were deposited in the Protein Data Bank with accession codes 5IM5 (I53-40), 5IM4 (I52-32), and 5IM6 (I32-28). J.B.B., W.S., N.P.K., D.E., and D.B. have filed a nonprovisional U.S. patent application, no. 14/930,792, related to the work presented herein.

SUPPLEMENTARY MATERIALS

www.sciencemag.org/content/353/6297/389/suppl/DC1
Materials and Methods
Supplementary Text
Figs. S1 to S13
Tables S1 to S6
References (*38*–*60*)
Databases S1 to S3

15 April 2016; accepted 21 June 2016
10.1126/science.aaf8818

MITOCHONDRIA

Mitochondrial endonuclease G mediates breakdown of paternal mitochondria upon fertilization

Qinghua Zhou,[1]*† Haimin Li,[1]* Hanzeng Li,[1,2]* Akihisa Nakagawa,[1] Jason L. J. Lin,[3] Eui-Seung Lee,[1] Brian L. Harry,[1,4] Riley Robert Skeen-Gaar,[1] Yuji Suehiro,[5] Donna William,[6] Shohei Mitani,[5] Hanna S. Yuan,[3] Byung-Ho Kang,[7]‡ Ding Xue[1]‡

Mitochondria are inherited maternally in most animals, but the mechanisms of selective paternal mitochondrial elimination (PME) are unknown. While examining fertilization in *Caenorhabditis elegans*, we observed that paternal mitochondria rapidly lose their inner membrane integrity. CPS-6, a mitochondrial endonuclease G, serves as a paternal mitochondrial factor that is critical for PME. We found that CPS-6 relocates from the intermembrane space of paternal mitochondria to the matrix after fertilization to degrade mitochondrial DNA. It acts with maternal autophagy and proteasome machineries to promote PME. Loss of *cps-6* delays breakdown of mitochondrial inner membranes, autophagosome enclosure of paternal mitochondria, and PME. Delayed removal of paternal mitochondria causes increased embryonic lethality, demonstrating that PME is important for normal animal development. Thus, CPS-6 functions as a paternal mitochondrial degradation factor during animal development.

Mitochondria are critical for many cellular processes including cellular respiration, apoptosis, and metabolism, and they possess their own genome (mtDNA) (*1*, *2*). However, only maternal mitochondria are passed on to progeny. Although elimination of paternal mtDNA can occur at various developmental stages through different mechanisms (*3*), it is unclear why and how paternal mitochondria are selectively eliminated after fertilization during embryo development (*3*, *4*). To address these questions, we examined paternal mitochondria in *C. elegans* spermatozoa and embryos by electron microscopy (EM) and tomography.

Mitochondria in wild-type (N2) spermatozoa are spherical (fig. S1A), with an average diameter of 464 ± 68 nm (SD), and their cristae, formed by extensive infolding of the inner membrane, uniformly distribute in the matrix (Fig. 1A). Paternal mitochondria in N2 zygotes are readily distinguished from the tubular and thinner maternal mitochondria (with an average width of 238 ± 57 nm; fig. S1B). Notably, all paternal mitochondria in N2 zygotes have multiple dark aggregates (agg) in the matrix that form promptly after their entry into oocytes (Fig. 1, B and E, fig. S1, B to G, and movie S1). The double-layer membranes from autophagosomes have started to assemble around some paternal mitochondria at this stage (fig. S1B). We named paternal mitochondria containing small aggregates that lack nearby autophagosome membranes "small agg PM" (Fig. 1B). Those containing larger aggregates that are associated with autophagosome membranes are called "large agg PM" (Fig. 1C), and those with few cristae and enclosed in an autophagosome are called "ghost PM" (Fig. 1D). Many small agg PM arise independently of the autophagy machinery (Fig. 1, B and E, fig. S1, B to G, and movie S1). Large agg PM and ghost PM are observed in N2 zygotes but are mostly seen in two- or four-cell–stage embryos (Fig. 1, C to E).

In large agg PM, cristae are cleared from the central region as the aggregates enlarge in the matrix (Fig. 1C), which occurs before autophagosomes enclose paternal mitochondria. Once enclosed by autophagosomes, they lose matrix contents except for some remaining aggregates, but their outer membrane does not rupture until most of the cristae have disappeared (Fig. 1D and fig. S1H). These results suggest that paternal mitochondria are destroyed partly in embryos by self-initiated internal breakdown prior to autophagosome assembly and degradation.

To identify intrinsic mitochondrial factors involved in paternal mitochondrial elimination (PME), we performed an RNA interference (RNAi) screen against 217 *C. elegans* nuclear genes predicted to encode mitochondrial proteins (table S1), using a sensitive polymerase chain reaction (PCR)–based method and a 3053–base pair (bp) mtDNA deletion allele (*uaDf5*; Fig. 2A) to track the fate of mtDNA (*5*). *uaDf5* mtDNA was detected in cross-progeny at all developmental stages from mating of N2 males with *uaDf5/+* heteroplasmic hermaphrodites (fig. S2A) (*5*) but was detected only in early embryos, not in late embryos nor in larval cross-progeny from N2 hermaphrodites mated with *uaDf5/+* males (Fig. 2B); these findings indicate that PME is conserved in *C. elegans* (*5*–*7*). RNAi of the *cps-6* gene, which encodes a homolog of human mitochondrial endonuclease G (*8*, *9*), caused persistence of

[1]Department of Molecular, Cellular, and Developmental Biology, University of Colorado, Boulder, CO 80309, USA. [2]Department of Chemistry and Biochemistry, University of Colorado, Boulder, CO 80309, USA. [3]Institute of Molecular Biology, Academia Sinica, Taipei 11529, Taiwan. [4]Medical Scientist Training Program, University of Colorado, Aurora, CO 80045, USA. [5]Department of Physiology, Tokyo Women's Medical University, School of Medicine and CREST, Japan Science and Technology Agency, Tokyo 162-8666, Japan. [6]Department of Microbiology and Cell Science, University of Florida, Gainesville, FL 32611, USA. [7]School of Life Sciences, Centre for Cell and Developmental Biology and State Key Laboratory of Agrobiotechnology, Chinese University of Hong Kong, Hong Kong, China.
*These authors contributed equally to this work. †Present address: First Affiliated Hospital, Biomedical Translational Research Institute, Jinan University, Guangzhou 510630, China. ‡**Corresponding author. Email: ding.xue@colorado.edu (D.X.); bkang@cuhk.edu.hk (B.-H.K.)**

ACKNOWLEDGMENTS

We thank M. Sawaya and M. Collazo for their assistance with crystallography, conducted at the UCLA-DOE X-ray Crystallization and Crystallography Core Facilities, which are supported by DOE grant DE-FC02-02ER63421. We thank M. Capel, K. Rajashankar, N. Sukumar, J. Schuermann, I. Kourinov, and F. Murphy at Northeastern Collaborative Access Team beamlines 24-ID-E and 24-ID-C at the Advanced Photon Source (APS), which are supported by grants from the National Center for Research Resources (5P41RR015301-10) and the National Institute of General Medical Sciences (8 P41 GM103403-10) of the National Institutes of Health. Use of the APS is supported by DOE under contract no. DE-AC02-06CH11357. We thank the staff at the Advanced Light Source SIBYLS beamline at Lawrence Berkeley National Laboratory, including K. Burnett, G. Hura, M. Hammel, J. Tanamachi, and J. Tainer for the services provided through the mail-in SAXS program, which is supported by the DOE Office of Biological and Environmental Research Integrated Diffraction Analysis program and the NIH project MINOS (Macromolecular Insights on Nucleic Acids Optimized by Scattering; grant no. RO1GM105404). We also thank U. Nattermann for help with EM, Y. Hsia for assistance with light-scattering experiments, C. Stafford for mass spectroscopy assistance, B. Nickerson for assistance with in vitro assembly experiments, and G. Rocklin for providing scripts used in data analysis. This work was supported by the Howard Hughes Medical Institute (S.G., D.C., T.G., and D.B.) and its Janelia Research Campus visitor program (S.G.), the Bill and Melinda Gates Foundation (D.B. and N.P.K.), Takeda Pharmaceutical Company (N.P.K.), NSF (grant no. CHE-1332907 to D.B. and T.O.Y.), the Air Force Office of Scientific Research (grant no. FA950-12-10112 to D.B.), and the Defense Advanced Research Projects Agency (grant no. W911NF-14-1-0162 to D.B. and N.P.K.). Y.L. was supported by a Whitcome Fellowship through the UCLA Molecular Biology Institute, and J.B.B. was supported by a NSF graduate research fellowship (grant no. DGE-0718124). Coordinates and structure factors were deposited in the Protein Data Bank with accession codes 5IM5 (I53-40), 5IM4 (I52-32), and 5IM6 (I32-28). J.B.B., W.S., N.P.K., D.E., and D.B. have filed a nonprovisional U.S. patent application, no. 14/930,792, related to the work presented herein.

SUPPLEMENTARY MATERIALS

www.sciencemag.org/content/353/6297/389/suppl/DC1
Materials and Methods
Supplementary Text
Figs. S1 to S13
Tables S1 to S6
References (*38*–*60*)
Databases S1 to S3

15 April 2016; accepted 21 June 2016
10.1126/science.aaf8818

MITOCHONDRIA

Mitochondrial endonuclease G mediates breakdown of paternal mitochondria upon fertilization

Qinghua Zhou,[1]*† Haimin Li,[1]* Hanzeng Li,[1,2]* Akihisa Nakagawa,[1] Jason L. J. Lin,[3] Eui-Seung Lee,[1] Brian L. Harry,[1,4] Riley Robert Skeen-Gaar,[1] Yuji Suehiro,[5] Donna William,[6] Shohei Mitani,[5] Hanna S. Yuan,[3] Byung-Ho Kang,[7]‡ Ding Xue[1]‡

Mitochondria are inherited maternally in most animals, but the mechanisms of selective paternal mitochondrial elimination (PME) are unknown. While examining fertilization in *Caenorhabditis elegans*, we observed that paternal mitochondria rapidly lose their inner membrane integrity. CPS-6, a mitochondrial endonuclease G, serves as a paternal mitochondrial factor that is critical for PME. We found that CPS-6 relocates from the intermembrane space of paternal mitochondria to the matrix after fertilization to degrade mitochondrial DNA. It acts with maternal autophagy and proteasome machineries to promote PME. Loss of *cps-6* delays breakdown of mitochondrial inner membranes, autophagosome enclosure of paternal mitochondria, and PME. Delayed removal of paternal mitochondria causes increased embryonic lethality, demonstrating that PME is important for normal animal development. Thus, CPS-6 functions as a paternal mitochondrial degradation factor during animal development.

Mitochondria are critical for many cellular processes including cellular respiration, apoptosis, and metabolism, and they possess their own genome (mtDNA) (*1*, *2*). However, only maternal mitochondria are passed on to progeny. Although elimination of paternal mtDNA can occur at various developmental stages through different mechanisms (*3*), it is unclear why and how paternal mitochondria are selectively eliminated after fertilization during embryo development (*3*, *4*). To address these questions, we examined paternal mitochondria in *C. elegans* spermatozoa and embryos by electron microscopy (EM) and tomography.

Mitochondria in wild-type (N2) spermatozoa are spherical (fig. S1A), with an average diameter of 464 ± 68 nm (SD), and their cristae, formed by extensive infolding of the inner membrane, uniformly distribute in the matrix (Fig. 1A). Paternal mitochondria in N2 zygotes are readily distinguished from the tubular and thinner maternal mitochondria (with an average width of 238 ± 57 nm; fig. S1B). Notably, all paternal mitochondria in N2 zygotes have multiple dark aggregates (agg) in the matrix that form promptly after their entry into oocytes (Fig. 1, B and E, fig. S1, B to G, and movie S1). The double-layer membranes from autophagosomes have started to assemble around some paternal mitochondria at this stage (fig. S1B). We named paternal mitochondria containing small aggregates that lack nearby autophagosome membranes "small agg PM" (Fig. 1B). Those containing larger aggregates that are associated with autophagosome membranes are called "large agg PM" (Fig. 1C), and those with few cristae and enclosed in an autophagosome are called "ghost PM" (Fig. 1D). Many small agg PM arise independently of the autophagy machinery (Fig. 1, B and E, fig. S1, B to G, and movie S1). Large agg PM and ghost PM are observed in N2 zygotes but are mostly seen in two- or four-cell–stage embryos (Fig. 1, C to E).

In large agg PM, cristae are cleared from the central region as the aggregates enlarge in the matrix (Fig. 1C), which occurs before autophagosomes enclose paternal mitochondria. Once enclosed by autophagosomes, they lose matrix contents except for some remaining aggregates, but their outer membrane does not rupture until most of the cristae have disappeared (Fig. 1D and fig. S1H). These results suggest that paternal mitochondria are destroyed partly in embryos by self-initiated internal breakdown prior to autophagosome assembly and degradation.

To identify intrinsic mitochondrial factors involved in paternal mitochondrial elimination (PME), we performed an RNA interference (RNAi) screen against 217 *C. elegans* nuclear genes predicted to encode mitochondrial proteins (table S1), using a sensitive polymerase chain reaction (PCR)–based method and a 3053–base pair (bp) mtDNA deletion allele (*uaDf5*; Fig. 2A) to track the fate of mtDNA (*5*). *uaDf5* mtDNA was detected in cross-progeny at all developmental stages from mating of N2 males with *uaDf5/+* heteroplasmic hermaphrodites (fig. S2A) (*5*) but was detected only in early embryos, not in late embryos nor in larval cross-progeny from N2 hermaphrodites mated with *uaDf5/+* males (Fig. 2B); these findings indicate that PME is conserved in *C. elegans* (*5*–*7*). RNAi of the *cps-6* gene, which encodes a homolog of human mitochondrial endonuclease G (*8*, *9*), caused persistence of

[1]Department of Molecular, Cellular, and Developmental Biology, University of Colorado, Boulder, CO 80309, USA. [2]Department of Chemistry and Biochemistry, University of Colorado, Boulder, CO 80309, USA. [3]Institute of Molecular Biology, Academia Sinica, Taipei 11529, Taiwan. [4]Medical Scientist Training Program, University of Colorado, Aurora, CO 80045, USA. [5]Department of Physiology, Tokyo Women's Medical University, School of Medicine and CREST, Japan Science and Technology Agency, Tokyo 162-8666, Japan. [6]Department of Microbiology and Cell Science, University of Florida, Gainesville, FL 32611, USA. [7]School of Life Sciences, Centre for Cell and Developmental Biology and State Key Laboratory of Agrobiotechnology, Chinese University of Hong Kong, Hong Kong, China.
*These authors contributed equally to this work. †Present address: First Affiliated Hospital, Biomedical Translational Research Institute, Jinan University, Guangzhou 510630, China. ‡**Corresponding author. Email: ding.xue@colorado.edu (D.X.); bkang@cuhk.edu.hk (B.-H.K.)**

paternal *uaDf5* mtDNA until the late stages of embryogenesis—a finding not observed in RNAi of other genes (fig. S2B and supplementary materials). A 336-bp deletion *(tm3222)* in *cps-6*, which removes the catalytic site of CPS-6 (fig. S2C) (*10*), had the same effect as *cps-6(RNAi)*, leading to persistence of paternal *uaDf5* mtDNA throughout embryo development (Fig. 2C), whereas *uaDf5* was detected only in 64-cell or earlier embryos in crosses between *uaDf5*/+ males and N2 hermaphrodites (Fig. 2B). These results indicate that *cps-6* is associated with rapid removal of paternal mtDNA during early embryogenesis.

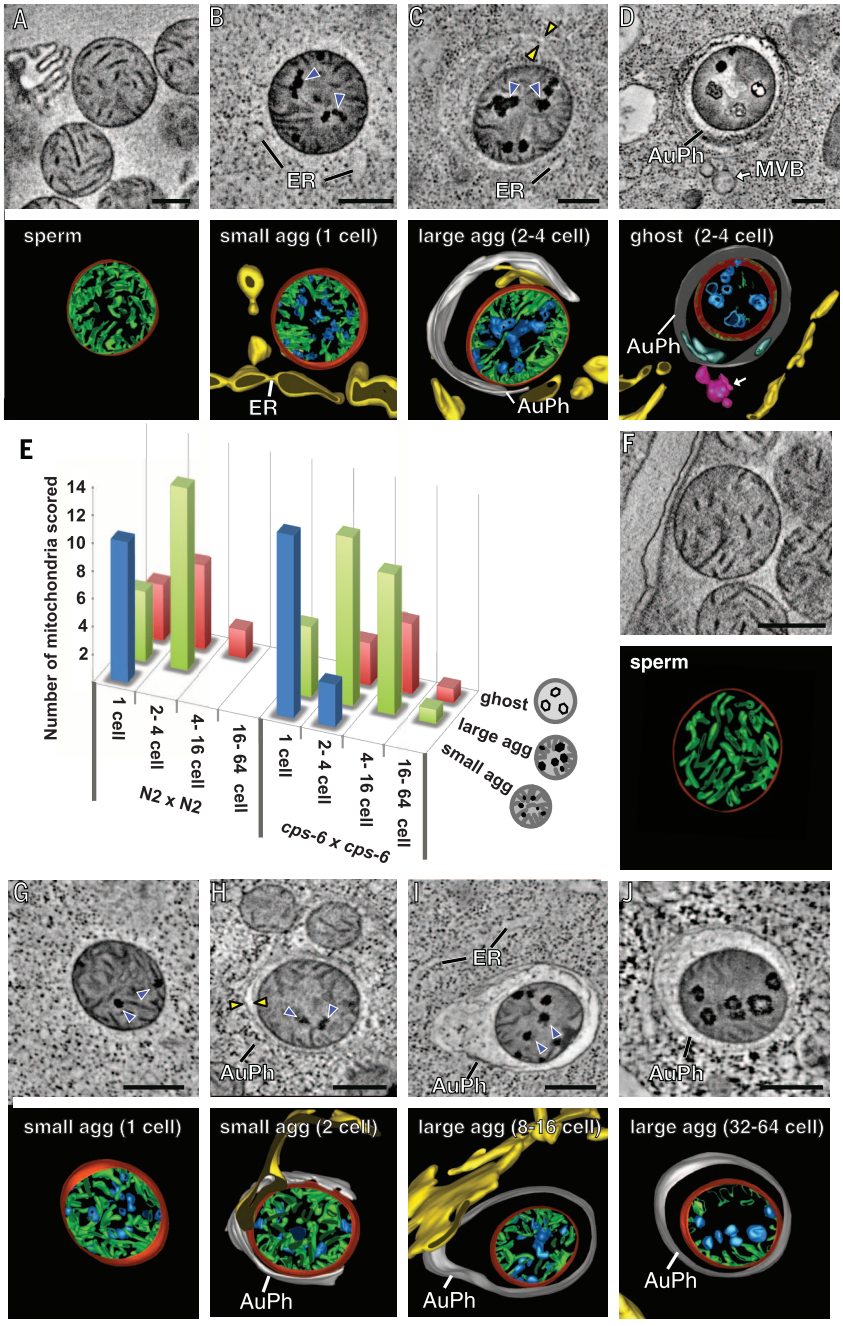

Fig. 1. Loss of *cps-6* delays internal breakdown of paternal mitochondria after fertilization. (**A** to **D**, **F** to **J**) Tomographic slice images and corresponding 3D models of a mitochondrion in an N2 (A) or *cps-6(tm3222)* (F) spermatozoon or a paternal mitochondrion in an N2 embryo [(B) to (D)] or a *cps-6(tm3222)* embryo [(G) to (J)] at the indicated stages. 3D models of autophagosomes (AuPh) and endoplasmic reticulum (ER) are shown. Mitochondrial membranes, cristae, and aggregates are colored red, green, and blue, respectively. Dark aggregates and autophagosome membranes are indicated with blue and yellow arrowheads, respectively. Scale bars, 300 nm. (**E**) Histogram showing three classes of paternal mitochondria in embryos of different stages from the indicated N2 cross (n = 45) or *cps-6(tm3222)* cross (n = 56).

We performed microscopic analysis to monitor the disappearance of paternal mitochondria stained by Mitotracker Red (MTR), a mitochondrion-specific dye (*5*). When MTR-stained N2 males were mated with unstained N2 hermaphrodites, MTR-stained paternal mitochondria were seen in embryos before the 64-cell stage (fig. S3, A to G), indicating that PME occurs in concert with paternal mtDNA elimination (Fig. 2B). Conversely, loss of *cps-6* resulted in persistence of MTR paternal mitochondria to around the 550-cell stage (fig. S3, H to N), confirming that CPS-6 promotes rapid clearance of paternal mitochondria.

CPS-6 was first identified as an apoptotic nuclease that translocates from mitochondria to the nucleus during apoptosis to mediate chromosome fragmentation (*8*, *9*). A nonapoptotic role of CPS-6 in *C. elegans* has not been reported. We used both the PCR assay and the microscopic assay to investigate whether CPS-6 is required paternally or maternally for PME (supplementary text) and found that a significant portion of paternal mitochondria and mtDNA persisted past the 64-cell stage when paternal *cps-6* was defective (Fig. 2, D and E, matings 3 and 4). By contrast, embryos without maternal *cps-6* displayed normal PME (Fig. 2, D and E, mating 2). These results indicate that paternal CPS-6 is required to promote PME.

CPS-6 is imported into mitochondria through a mitochondrial targeting sequence (amino acids 1 to 21), because CPS-6ΔN, lacking this targeting sequence, localizes to the nucleus (*8*). Expression of CPS-6, but not CPS-6ΔN, in *cps-6(tm3222)* males through the ubiquitously expressed *dpy-30* gene promoter rescued the defect in PME (Fig. 2F, matings 1, 2, and 5 to 7; see also supplementary text), indicating that localization of CPS-6 in paternal mitochondria is required to mediate PME. Because expression of the nuclease-deficient CPS-6(H148A) mutant in *cps-6(tm3222)* males failed to rescue the PME defect (Fig. 2F, matings 3 and 4), the nuclease activity of CPS-6 is essential for PME.

Using electron tomography, we examined how loss of *cps-6* affects PME. In *cps-6(tm3222)* zygotes, aggregates were still visible in paternal mitochondria but were smaller and fewer than in N2 zygotes, and no ghost PM were detected (Fig. 1, B, E, and G), indicating reduced and slower internal breakdown of paternal mitochondria. The autophagosome membranes started to assemble around paternal mitochondria in two- or four-cell *cps-6(tm3222)* embryos and completed enclosure by the 16-cell stage (Fig. 1, H and I), proceeding significantly slower than in N2 embryos, in which autophagosome assembly started earlier at the one-cell stage and was complete by the four-cell stage (Fig. 1, C to E). Even after autophagosome enclosure, internal breakdown of paternal mitochondria was clearly delayed (Fig. 1, I and J), because a significant portion of cristae remained superficially intact and fewer than 40% of paternal mitochondria transited into ghost PM in 16-cell

cps-6(tm3222) embryos (Fig. 1E). Some large agg PM even lingered on in 64-cell embryos (Fig. 1J), compared with 100% of paternal mitochondria either eliminated or becoming ghost PM by the four-cell N2 embryos (Fig. 1, D and E). Therefore, CPS-6 is important in mediating internal breakdown of paternal mitochondria and their enclosure by autophagosomes after fertilization.

Compromised mitochondria often show loss of membrane potential, which can be detected by tetramethylrhodamine ethyl ester (TMRE), a potential-sensitive mitochondrial dye. When N2 males prestained with TMRE and a nucleic acid dye (SYTO11)—which labeled sperm mitochondria and their mtDNA, respectively (fig. S4, A and B)—were mated with N2 hermaphrodites, paternal mitochondria were still labeled by SYTO11 in N2 zygotes, but their TMRE staining was completely lost (Fig. 3A). In comparison, staining of paternal mitochondria by potential-insensitive MTR persisted (fig. S4B). When we mated SYTO11-stained N2 males with N2 hermaphrodites in the presence of TMRE, only maternal mitochondria were stained by TMRE, and the SYTO11-positive paternal mitochondria were TMRE-negative (Fig. 3B). Therefore, paternal

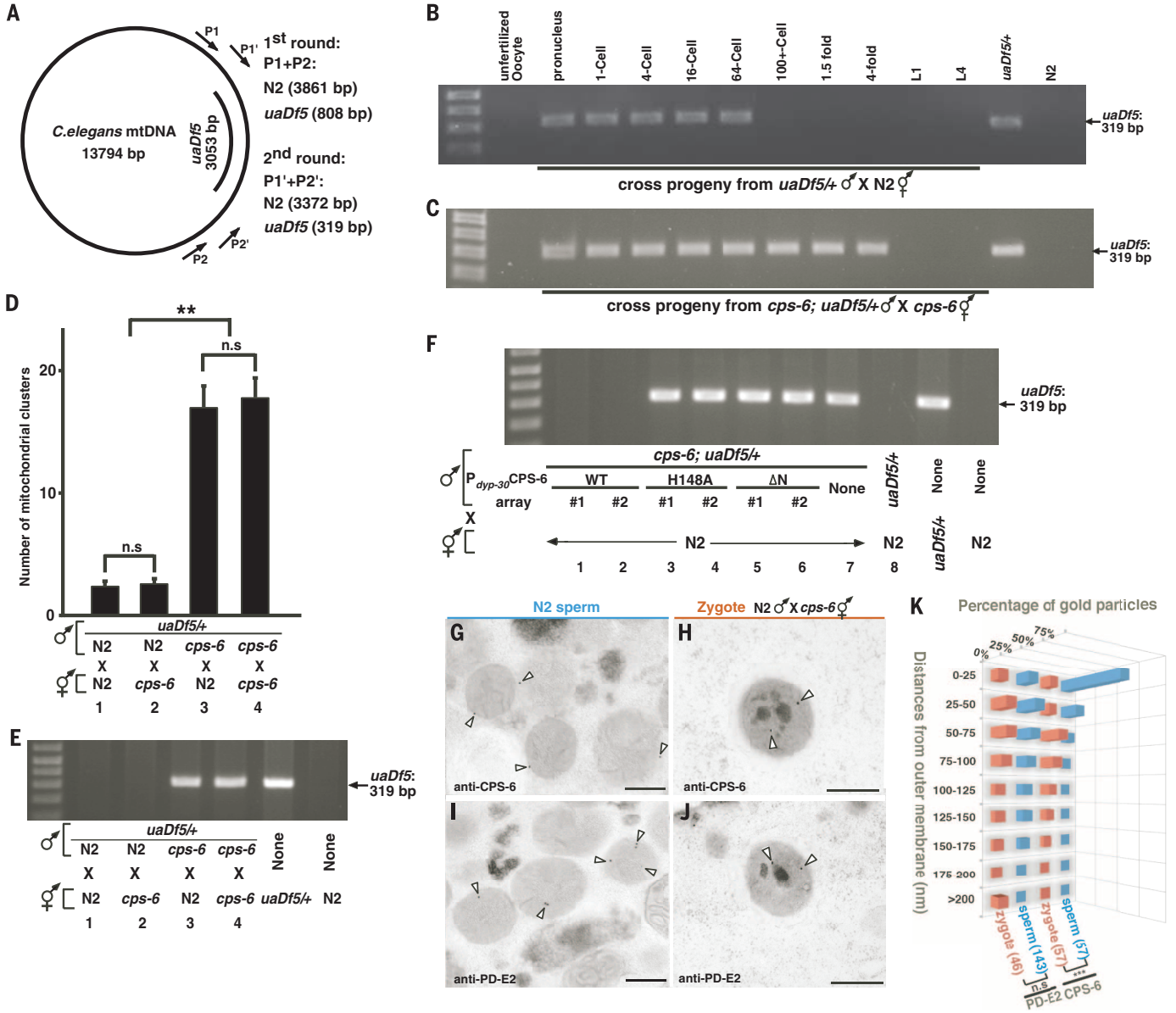

Fig. 2. CPS-6 relocates from the intermembrane space of paternal mitochondria to the matrix after fertilization to promote PME. (**A**) Diagram of *C. elegans* mtDNA, the *uaDf5* deletion, primers used in the nested PCR assays, and sizes of PCR products in N2 and *uaDf5/+* animals. (**B** and **C**) Hermaphrodites and MTR-stained males were mated as indicated. Males also carried *smIs42*, an integrated $P_{sur\text{-}5}$*sur-5::gfp* transgene used to track cross progeny (see fig. S2A). A single unfertilized oocyte and a single cross-fertilized embryo or larva (MTR- or GFP-positive) at the indicated stage was analyzed by PCR. *uaDf5/+* and N2 hermaphrodites were controls. (**D**) Quantification of MTR-stained paternal mitochondrial clusters in 64-cell embryos from the indicated crosses with MTR-stained males. Data are means ± SEM; n = 20 per cross. $^{**}P <$ 0.0001 (unpaired Student t test); n.s., not significant. (**E** and **F**) Five cross-fertilized embryos (E) or transgenic embryos (F) at approximately 100-cell stage from the indicated crosses were analyzed by PCR. (**G** to **J**) Representative immuno-EM images of mitochondria in N2 spermatozoa and paternal mitochondria in zygotes from the indicated cross. CPS-6–specific and PD-E2–specific immunogold particles are marked with arrowheads. Scale bars, 300 nm. (**K**) Histogram of the distances of 15-nm immunogold particles from the mitochondrial membrane, illustrating CPS-6's movement after fertilization. Numbers of immunogold particles scored are shown in parentheses. $^{***}P < 0.0001$ (Mann-Whitney U test). *cps-6(tm3222)* was used in all figures.

mitochondria are depolarized shortly after fertilization, preceding degradation of their mtDNA.

We used immuno-EM to determine the localization of CPS-6 in paternal mitochondria. CPS-6 immunogold particles were predominantly associated with the mitochondrial membrane in N2 spermatozoa (Fig. 2, G and K, and fig. S2G), in agreement with CPS-6's localization in mitochondrial intermembrane space. In zygotes from *cps-6(tm3222)* hermaphrodites mated with N2 males, CPS-6 immunogold particles were often located inside paternal mitochondria, away from the mitochondrial membrane (Fig. 2, H and K, and fig. S5). Because some paternal mitochondria had not been associated with autophagosomes (Fig. 2H), CPS-6 appeared to enter the matrix before the assembly of autophagosomes. The relocation of CPS-6 into the matrix after fertilization is clearly discerned when compared with the localization patterns of a mitochondrial matrix protein, the E2 subunit of pyruvate dehydrogenase (PD-E2, Fig. 2, I to K). Collectively, these different microscopy analyses provide strong evidence that paternal mitochondria are depolarized and damaged internally soon after fertilization, leading to the release of CPS-6 into the matrix to catalyze mtDNA degradation.

The autophagy and proteasome pathways promote PME in *C. elegans* (*5*–*7*). Both LGG-1, the worm LC3/Atg8 homolog necessary for autophagosome formation (*11*), and RAD-23, a ubiquitin receptor important for proteasomal degradation (*5*, *12*), act maternally to promote PME (fig. S6, A and B, and supplementary text). Analyses of the double and the triple mutants among *cps-6*, *lgg-1*, and *rad-23* indicate that *cps-6*, *lgg-1*, and *rad-23* use distinct mechanisms (mitochondrial self-destruction, autophagy, and proteasomes, respectively) to coordinate swift and efficient PME (fig. S6, C to F).

Because loss of *cps-6* slows down autophagosome formation and degradation of paternal mitochondria (Fig. 1), we further interrogated this issue by immunostaining; we found that in N2 zygotes, bright LGG-1 staining was seen clustering around MTR-stained paternal mitochondria near the site of sperm entry (fig. S4C), with 81% of paternal mitochondrial clusters colocalizing with LGG-1 autophagosomes (fig. S4E). By contrast, in *cps-6(tm3222)* zygotes, such colocalization dropped to 43% (fig. S4, D and E), indicating that loss of *cps-6* reduces autophagosome formation on paternal mitochondria. Analysis using superresolution structured illumination microscopy (SIM) revealed similar results. In N2 zygotes, the majority (77%) of paternal mitochondria were enclosed by LGG-1 autophagosomes, some (12%) were partially enclosed, and only 11% did not associate with (isolated) autophagosomes (Fig. 3, C and D, and fig. S4, F and H). By contrast, in *cps-6(tm3222)* zygotes, 51% of paternal mitochondria were isolated and only 29 and 20% of paternal mitochondria were enclosed and partially enclosed by autophagosomes, respectively (Fig. 3, E and F, and fig. S4, G and H). These findings indicate that the CPS-6 self-destruction process is important for efficient recruitment of autophagosomes to paternal mitochondria.

It has been suggested that the high rate of energy consumption during fertilization of an oocyte by many competing spermatozoa leads to increased oxidative damage and mutations in sperm mtDNA (*13*, *14*). Failure to remove paternal mitochondria with mutated mtDNA can cause incompatibility with maternal mitochondria and the nuclear genome and can adversely affect the fitness of animals (*15*–*17*). Comparison of N2 embryos with *uaDf5*/+ embryos, with four genes deleted in *uaDf5* mtDNA (*18*), revealed a factor of 23 increase in embryonic lethality from 0.4 to 9.4% (Fig. 4A, assays 1 and 3), indicating that the heteroplasmic presence of mtDNA mutations compromises embryo development. Delayed removal of *uaDf5* paternal mitochondria in embryos by loss of *cps-6* resulted in a lethality rate of 5.9%, higher by a factor of 5 to 7 than that of cross-fertilized *cps-6(tm3222)* embryos (0.7%) or that of embryos with no persistent paternal mitochondria (0.8 to 0.9%) (Fig. 4A, assays 4 to 7, and supplementary text). Moreover, delayed clearance of *uaDf5* paternal mitochondria slowed cell divisions, an energy-driven process, during *C. elegans* embryogenesis, because the average durations of cell divisions in two different cell lineages (MS and P) were significantly prolonged in *uaDf5*/+ embryos and by delayed removal of *uaDf5* paternal mitochondria (Fig. 4, B and C, fig. S7, and supplementary

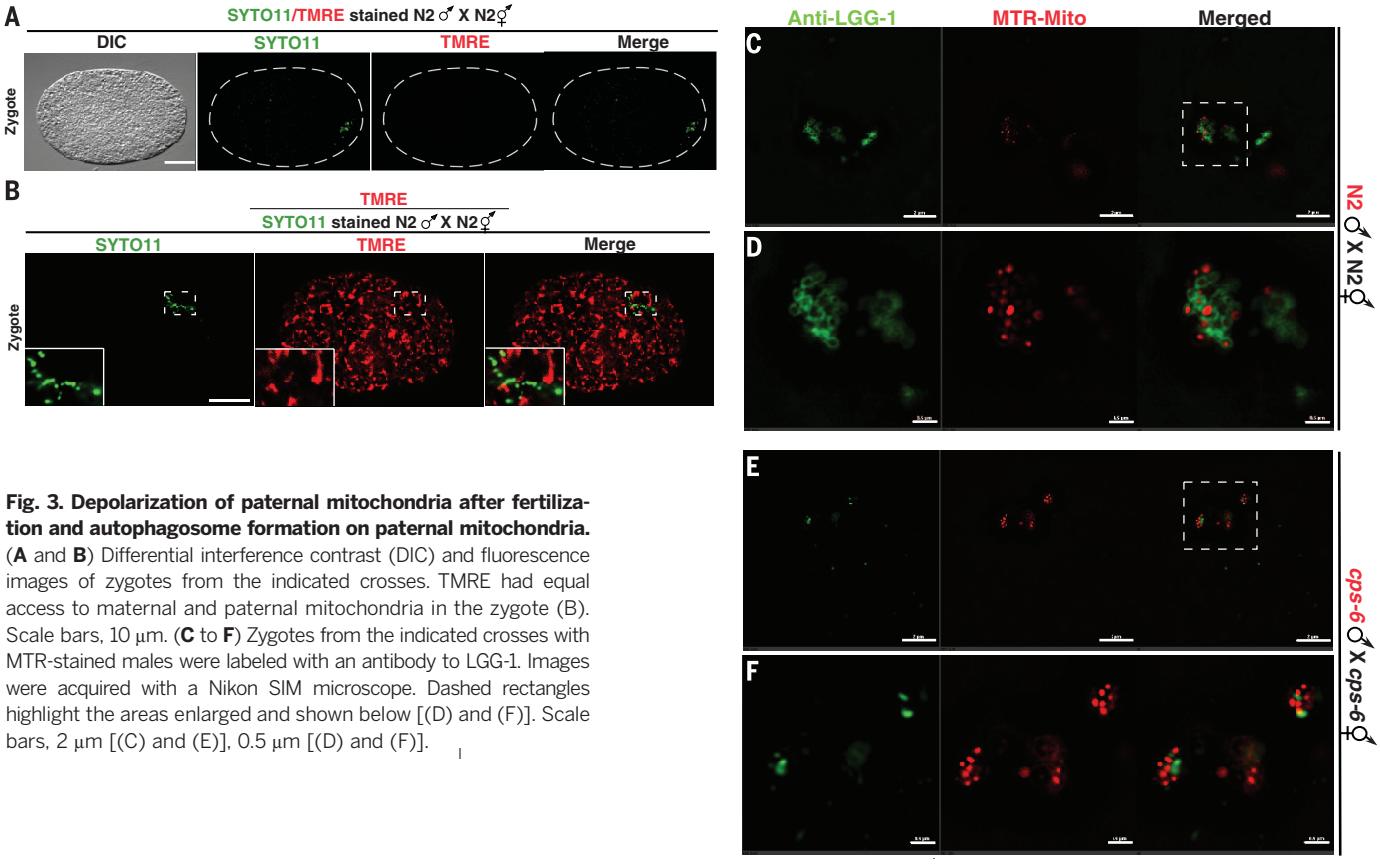

Fig. 3. Depolarization of paternal mitochondria after fertilization and autophagosome formation on paternal mitochondria. (**A** and **B**) Differential interference contrast (DIC) and fluorescence images of zygotes from the indicated crosses. TMRE had equal access to maternal and paternal mitochondria in the zygote (B). Scale bars, 10 μm. (**C** to **F**) Zygotes from the indicated crosses with MTR-stained males were labeled with an antibody to LGG-1. Images were acquired with a Nikon SIM microscope. Dashed rectangles highlight the areas enlarged and shown below [(D) and (F)]. Scale bars, 2 μm [(C) and (E)], 0.5 μm [(D) and (F)].

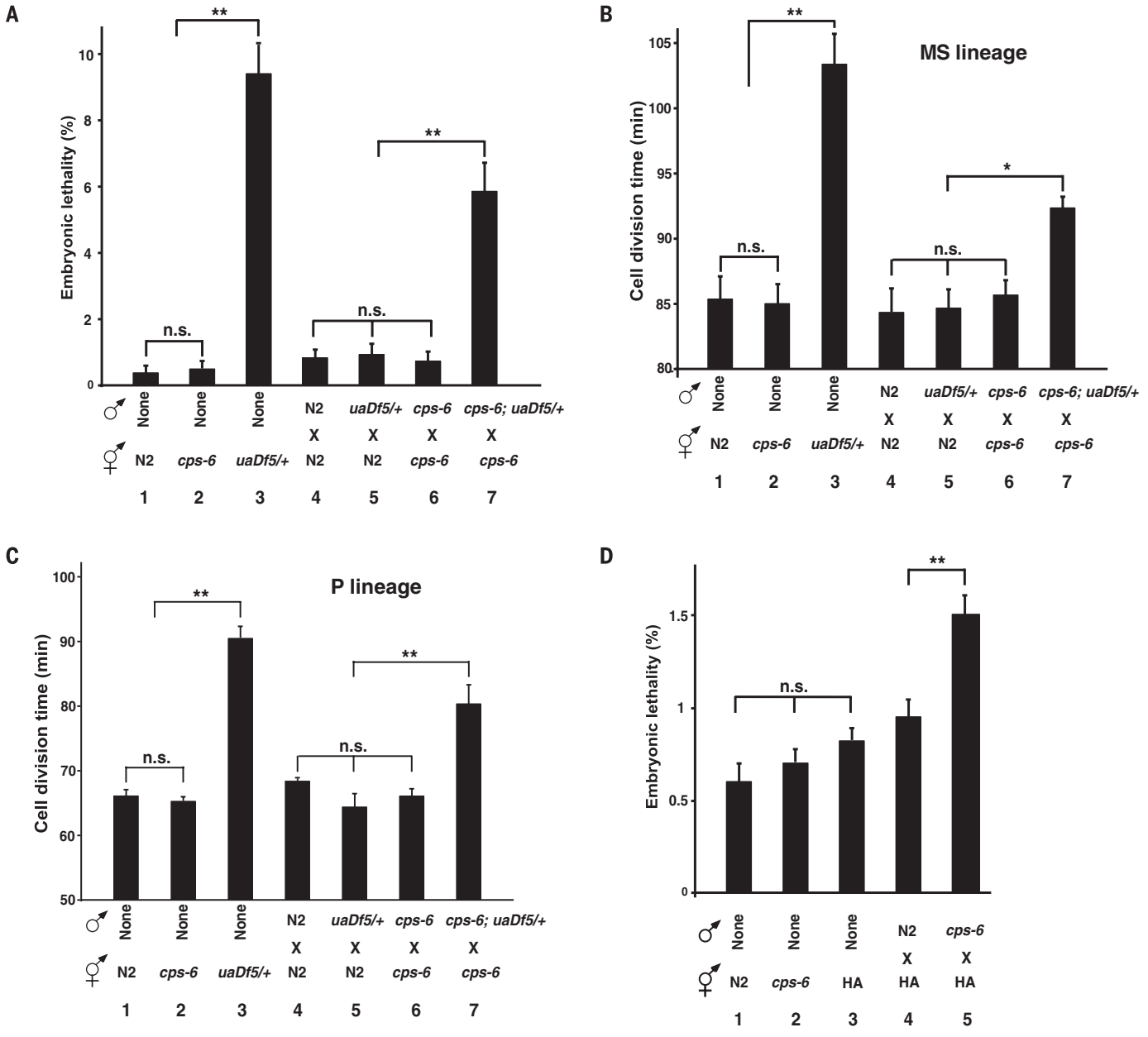

Fig. 4. Delayed removal of paternal mitochondria increases embryonic lethality and cell division durations. (**A** to **D**) The embryonic lethality rate [(A) and (D)] and durations of cell divisions in the MS lineage (B) and P lineage (C) were scored in self-fertilized embryos (1 to 3) or cross-fertilized embryos from crosses (4 to 7) of the indicated genotypes. All males carried *smIs42* and were stained with MTR to assist identification of zygotes [(B) and (C)]. Data are means ± SEM; $n > 1000$ embryos per cross at 25°C [(A) and (D)] and $n = 3$ embryos per cross at 20°C [(B) and (C)]. *$P < 0.05$, **$P < 0.001$ (unpaired Student t test).

text). These results provide evidence that delayed clearance of mutated paternal mitochondria leads to decreased fitness at the cellular and organismal levels and presents an evolutionary disadvantage.

Next, we examined the consequence of delayed removal of wild-type paternal mitochondria by mating two different *C. elegans* wild-type strains, the Bristol strain (N2) and the Hawaii strain (HA). Delayed removal of wild-type Bristol paternal mitochondria in HA embryos due to loss of paternal *cps-6* also resulted in a significantly higher percentage of embryonic lethality than that seen in HA embryos without persistent paternal mitochondria (Fig. 4D, assays 4 and 5, and fig. S6G, matings 2 and 4; see also supplementary text). Therefore, delayed clearance of wild-type paternal mitochondria slightly different from maternal mitochondria also compromises animal development, which suggests that transmission of paternal mitochondria among different wild-type variants is evolutionarily disadvantageous.

Our results show that soon after fertilization, paternal mitochondria are depolarized and lose their inner membrane integrity, which apparently marks them for degradation by autophagy (*19*, *20*). The inner membrane breakdown probably triggers the entry of the intermembrane CPS-6 into the matrix of paternal mitochondria to degrade mtDNA, which encodes 12 mitochondrial proteins, two rRNAs, and 22 tRNAs that are essential for normal functions and maintenance of mitochondria (*1*, *13*, *18*). Degradation of mtDNA is detrimental, which accelerates breakdown of paternal mitochondria and could promote externalization of signals recognized by the autophagy or proteasome machinery (*19*, *20*), leading to PME (fig. S8). Consistent with this model, loss of paternal *cps-6* delays internal breakdown of paternal mitochondria and their enclosure and degradation by the autophagy

machinery. Interestingly, delayed removal of either mutant or slightly different wild-type paternal mitochondria results in increased embryonic lethality in heteroplasmic animals, likely due to incompatibility in cellular signaling between the mitochondrial and nuclear genomes (*15*, *17*). This provides evidence that persistence of paternal mitochondria compromises animal development and may be the impetus for maternal inheritance of mitochondria. DeLuca and O'Farrell showed that endonuclease G mediated the degradation of sperm mitochondrial DNA during *Drosophila* spermatogenesis before fertilization and hypothesized that this degradation helped prevent paternal mtDNA transmission (*21*). In contrast, we find in *C. elegans* that CPS-6 acts after fertilization to mediate degradation of both paternal mitochondria and mtDNA to facilitate their autophagic degradation. These findings imply a conserved role of endonuclease G in paternal mtDNA elimination and expand the roles of this nuclease beyond apoptosis and mitochondrial maintenance (*8*, *9*, *22*).

REFERENCES AND NOTES

1. S. E. Calvo, V. K. Mootha, *Annu. Rev. Genomics Hum. Genet.* **11**, 25–44 (2010).
2. X. Wang, *Genes Dev.* **15**, 2922–2933 (2001).
3. M. Sato, K. Sato, *Biochim. Biophys. Acta* **1833**, 1979–1984 (2013).
4. B. Levine, Z. Elazar, *Science* **334**, 1069–1070 (2011).
5. Q. Zhou, H. Li, D. Xue, *Cell Res.* **21**, 1662–1669 (2011).
6. S. Al Rawi *et al.*, *Science* **334**, 1144–1147 (2011).
7. M. Sato, K. Sato, *Science* **334**, 1141–1144 (2011).
8. J. Parrish *et al.*, *Nature* **412**, 90–94 (2001).
9. L. Y. Li, X. Luo, X. Wang, *Nature* **412**, 95–99 (2001).
10. J. L. Lin *et al.*, *J. Biol. Chem.* **287**, 7110–7120 (2012).
11. K. Jia, B. Levine, *Adv. Exp. Med. Biol.* **694**, 47–60 (2010).
12. K. Madura, *Trends Biochem. Sci.* **29**, 637–640 (2004).
13. D. C. Wallace, *Environ. Mol. Mutagen.* **51**, 440–450 (2010).
14. J. M. Cummins, *Hum. Reprod.* **15** (suppl. 2), 92–101 (2000).
15. M. S. Sharpley *et al.*, *Cell* **151**, 333–343 (2012).
16. M. Schwartz, J. Vissing, *N. Engl. J. Med.* **347**, 576–580 (2002).
17. N. Lane, *BioEssays* **33**, 860–869 (2011).
18. W. Y. Tsang, B. D. Lemire, *Biochem. Cell Biol.* **80**, 645–654 (2002).
19. G. Ashrafi, T. L. Schwarz, *Cell Death Differ.* **20**, 31–42 (2013).
20. K. Wang, D. J. Klionsky, *Autophagy* **7**, 297–300 (2011).
21. S. Z. DeLuca, P. H. O'Farrell, *Dev. Cell* **22**, 660–668 (2012).
22. C. McDermott-Roe *et al.*, *Nature* **478**, 114–118 (2011).

ACKNOWLEDGMENTS

We thank T. Blumenthal, R. Poyton, and K. Krauter for comments and H. Zhang for strains and antibodies. Supported by March of Dimes grant 1-FY14-300 and NIH grants GM59083, GM79097, and GM118188 (D.X.) and Research Grants Council of Hong Kong grant AoE/M-05/12 (B.-H.K.).

SUPPLEMENTARY MATERIALS

www.sciencemag.org/content/353/6297/394/suppl/DC1
Materials and Methods
Supplementary Text
Figs. S1 to S8
Table S1
Movie S1
References (*23*–*37*)

14 February 2016; accepted 15 June 2016
Published online 23 June 2016
10.1126/science.aaf4777

CANCER IMMUNOTHERAPY

Cdk5 disruption attenuates tumor PD-L1 expression and promotes antitumor immunity

R. Dixon Dorand,[1,2] Joseph Nthale,[2,3] Jay T. Myers,[2,3] Deborah S. Barkauskas,[2,3] Stefanie Avril,[1,4] Steven M. Chirieleison,[1] Tej K. Pareek,[2,3] Derek W. Abbott,[1,4] Duncan S. Stearns,[2,3,4] John J. Letterio,[2,3,4] Alex Y. Huang,[1,2,3,4]*† Agne Petrosiute[2,3,4]*†

Cancers often evade immune surveillance by adopting peripheral tissue–tolerance mechanisms, such as the expression of programmed cell death ligand 1 (PD-L1), the inhibition of which results in potent antitumor immunity. Here, we show that cyclin-dependent kinase 5 (Cdk5), a serine-threonine kinase that is highly active in postmitotic neurons and in many cancers, allows medulloblastoma (MB) to evade immune elimination. Interferon-γ (IFN-γ)–induced PD-L1 up-regulation on MB requires Cdk5, and disruption of Cdk5 expression in a mouse model of MB results in potent $CD4^+$ T cell–mediated tumor rejection. Loss of Cdk5 results in persistent expression of the PD-L1 transcriptional repressors, the interferon regulatory factors IRF2 and IRF2BP2, which likely leads to reduced PD-L1 expression on tumors. Our finding highlights a central role for Cdk5 in immune checkpoint regulation by tumor cells.

Cyclin-dependent kinase 5 (Cdk5) is a nonstereotypical Cdk whose activity depends on coactivators, p35 and/or p39. A proline-directed serine-threonine kinase (*1*), Cdk5 is essential in central nervous system (CNS) development (*2*, *3*). Cdk5 also contributes to angiogenesis, apoptosis, myogenesis, vesicular transport, and senescence in nonneuronal cells, including tumors (*4*–*6*), which makes Cdk5 a potential therapeutic target in cancers (*7*–*9*). We explored whether Cdk5 plays a role in medulloblastoma (MB), a common malignant pediatric CNS tumor.

MB cell lines and clinical specimens expressed Cdk5, p35, and p39 (Fig. 1A and fig. S1A). Cdk5-specific kinase activity could be abolished in vitro by roscovitine, a nonselective inhibitor against Cdks 1, 2, 5, 7, and 9 (fig. S1B) (*10*). To interrogate Cdk5-specific functions, we disrupted Cdk5 in wild-type murine MB cells (MM1 WT) by short hairpin–mediated RNA interference (MM1 shCdk5) and clustered regularly interspaced short palindromic repeats (CRISPR)–Cas9–targeted mutation (MM1 crCdk5), with nontargeting constructs as controls (MM1 shNS and MM1 crNeg). A reduction in Cdk5 was confirmed at the transcript (fig. S1C) and protein levels (fig. S1D). In vitro, there were no significant differences in cell proliferation among all constructs (fig. S1, E and F) (*1*).

[1]Department of Pathology, Case Western Reserve University School of Medicine, Cleveland, OH 44106, USA. [2]Division of Pediatric Hematology-Oncology, Department of Pediatrics, Case Western Reserve University School of Medicine, Cleveland, OH 44106, USA. [3]Angie Fowler Adolescent and Young Adult Cancer Institute and University Hospitals Rainbow Babies and Children's Hospital, Cleveland, OH 44106, USA. [4]Case Comprehensive Cancer Center, Case Western Reserve University School of Medicine, Cleveland, OH 44106, USA.
*These authors contributed equally to this work. **†Corresponding author. Email: ayh3@case.edu (A.Y.H.); axp125@case.edu (A.P.)**

To assess MB growth in vivo, 5×10^4 Cdk5-deficient or control cells were inoculated subcutaneously (s.c.) into the flanks of immunodeficient mice. All mice developed comparable-sized tumors by day 14 (fig. S2, A to C). However, 78 to 50% of C57BL/6 mice injected s.c. with Cdk5-deficient MB cells showed tumor-free survival (TFS) at 19 and 42 days, whereas mice injected with WT and control tumors exhibited 0 and 7% TFS after 19 days, respectively (Fig. 1B and fig. S3A). Mice injected with Cdk5-deficient MB cells developed significantly smaller tumors (0.02 ± 0.04 g) than mice injected with WT (0.91 ± 0.39 g) or NS (0.51 ± 0.21 g) cells (fig. S3B). These data suggest a T cell–dependent rejection mechanism of Cdk5-deficient MM1 cells. This interpretation is supported by the observation that Cdk5 expression inversely correlated with T cell infiltration in human MB (Fig. 1C and fig. S2D).

To identify T cell populations mediating this potent rejection, we depleted $CD8^+$ T cells, $CD4^+$ T cells, or both subsets in mice inoculated with MM1 crCdk5 or crNeg cells (5×10^4 s.c.). By day 11, 100% of mice injected with MM1 crNeg and 80% of mice receiving MM1 crCdk5 developed measurable tumors (Fig. 1B), although MM1 crNeg tumors were 8 times the size of MM1 crCdk5 tumors (808.8 ± 382.1 versus 101.1 ± 92.9 mm^3) (Fig. 1D). Depletion with CD4-specific (αCD4) antibody alone or with both αCD4 and αCD8 antibodies resulted in 100% MM1 crCdk5 tumor incidence accompanied by rapid tumor growth, whereas CD8 depletion alone yielded 30% TFS, similar to isotype control (Fig. 1D). Among mice receiving isotype antibody, three of eight crCdk5 tumor outgrowths regressed starting on day 17, whereas three of nine crCdk5 tumor outgrowths among mice depleted of $CD8^+$ T cells regressed starting on day 25; these outgrowths contributed

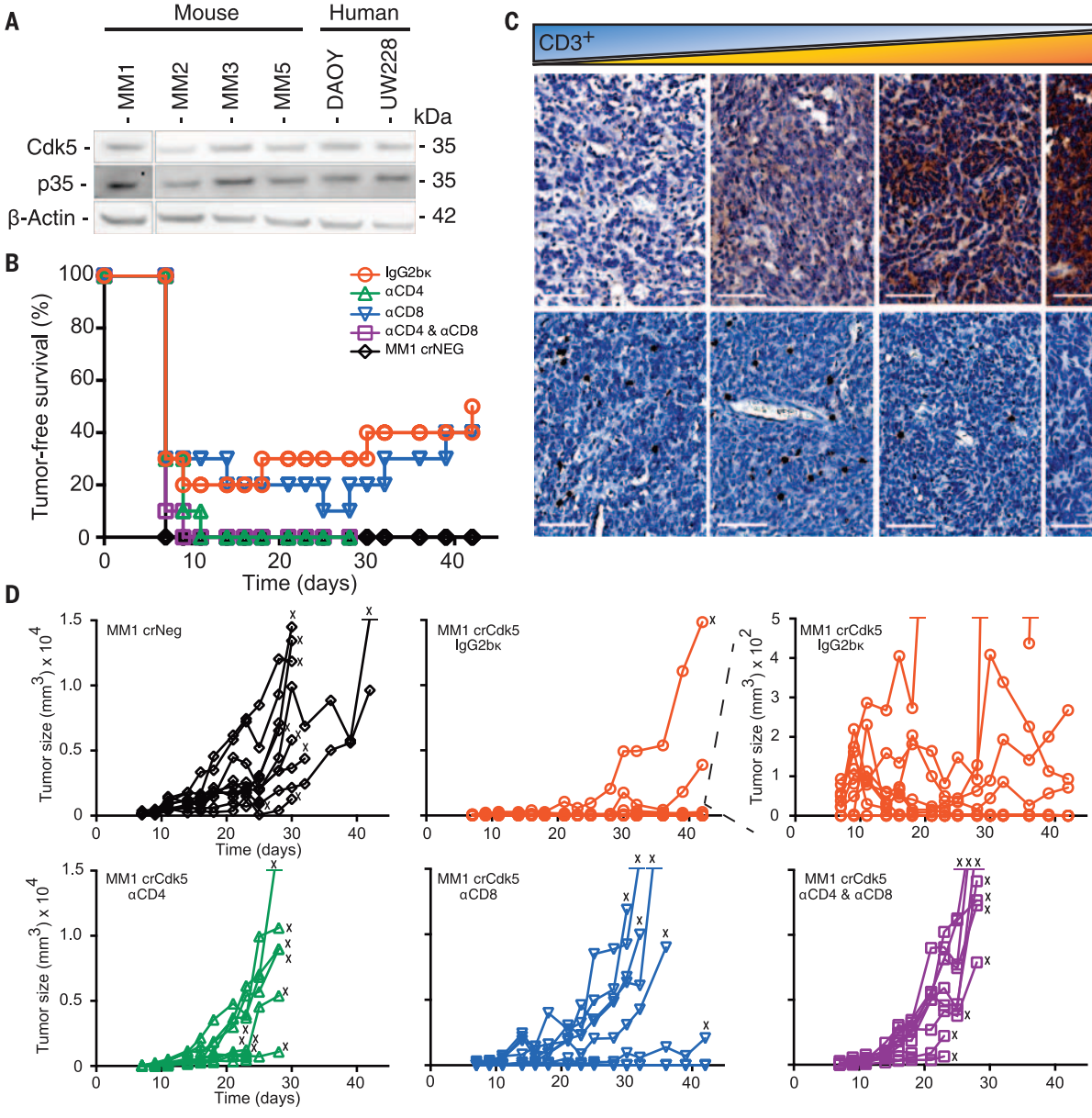

Fig. 1. Targeted deletion of Cdk5 in MB results in rejection by CD4$^+$ T cells. (**A**) Cdk5 and p35 proteins are expressed in murine and human MB cell lines in vitro. (**B**) TFS in C57BL/6J mice injected with MM1 crNeg or crCdk5 cells with various depleting antibodies (n = 10 per group). (**C**) Immunohistochemistry of six clinical MB samples reveals an inverse correlation between tumor Cdk5 expression (top) and CD3$^+$ T cell infiltration (bottom). Pearson correlation = −0.91 (fig. S2D). Scale bars, 100 μm. (**D**) Tumor-growth kinetics for individual animals in each group from (B). The top right-hand graph shows the center one with an expanded scale. X indicates that an animal was killed because of tumor size or ulceration.

to a total TFS of 50 and 40%, respectively (Fig. 1, B and D). Tumors harvested from MM1 crCdk5-bearing mice remained Cdk5$^-$ without evidence of Cdk5$^+$ escape (fig. S4A). Similar results were seen in mice receiving MM1 shCdk5 and shNS inoculations, with a dependency on CD4$^+$ T cells for tumor rejection (fig. S3C). Cdk5-deficient tumors also grew aggressively in mice deficient in major histocompatibility complex class II (MHC-II) (fig. S3D). Finally, 60 to 75% of mice that rejected Cdk5-deficient tumors remained tumor free after rechallenge with a lethal dose of MM1 WT cells (fig. S3E). Collectively, these studies point to a CD4$^+$ T cell–dependent rejection of Cdk5-deficient tumors with robust antitumor immune memory generation.

Interferon-γ (IFN-γ) is a major CD4$^+$ T cell effector cytokine (*11*) and was abundant in Cdk5-deficient tumor mass (fig. S5A). IFN-γ induces p35 (*12*), which results in enhanced Cdk5 activity (fig. S5B). IFN-γ is known to induce PD-L1 (*13*), whose expression on infiltrating immune cells is evidence of an ongoing intratumoral immune response (*14*). We examined whether disruption of Cdk5 expression in MB impaired PD-L1 induction in response to IFN-γ stimulation. We analyzed human tumor databases and found a cooccurrence of Cdk5 and PD-L1 mRNA expression in many tumor types (fig. S6). In Cdk5-deficient MM1, we observed a 37.58 ± 14.28% reduction in basal PD-L1 mRNA level (Fig. 2A). Note that Cdk5-deficient MM1 cells exhibited a blunted PD-L1 up-regulation in response to IFN-γ stimulation in vitro (Fig. 2, A and B, and fig. S4B). Other IFN-γ–responsive proteins, such as MHC H-2K^b and H-2D^b (fig. S7A), were not significantly affected in the Cdk5-deficient tumors, which indicated that a global disruption of the IFN-γ receptor (IFNGR) signaling was not responsible for failed PD-L1 up-regulation or enhanced immune sensitivity. Disrupting Cdk5 in rhabdomyosarcoma also led to a blunted

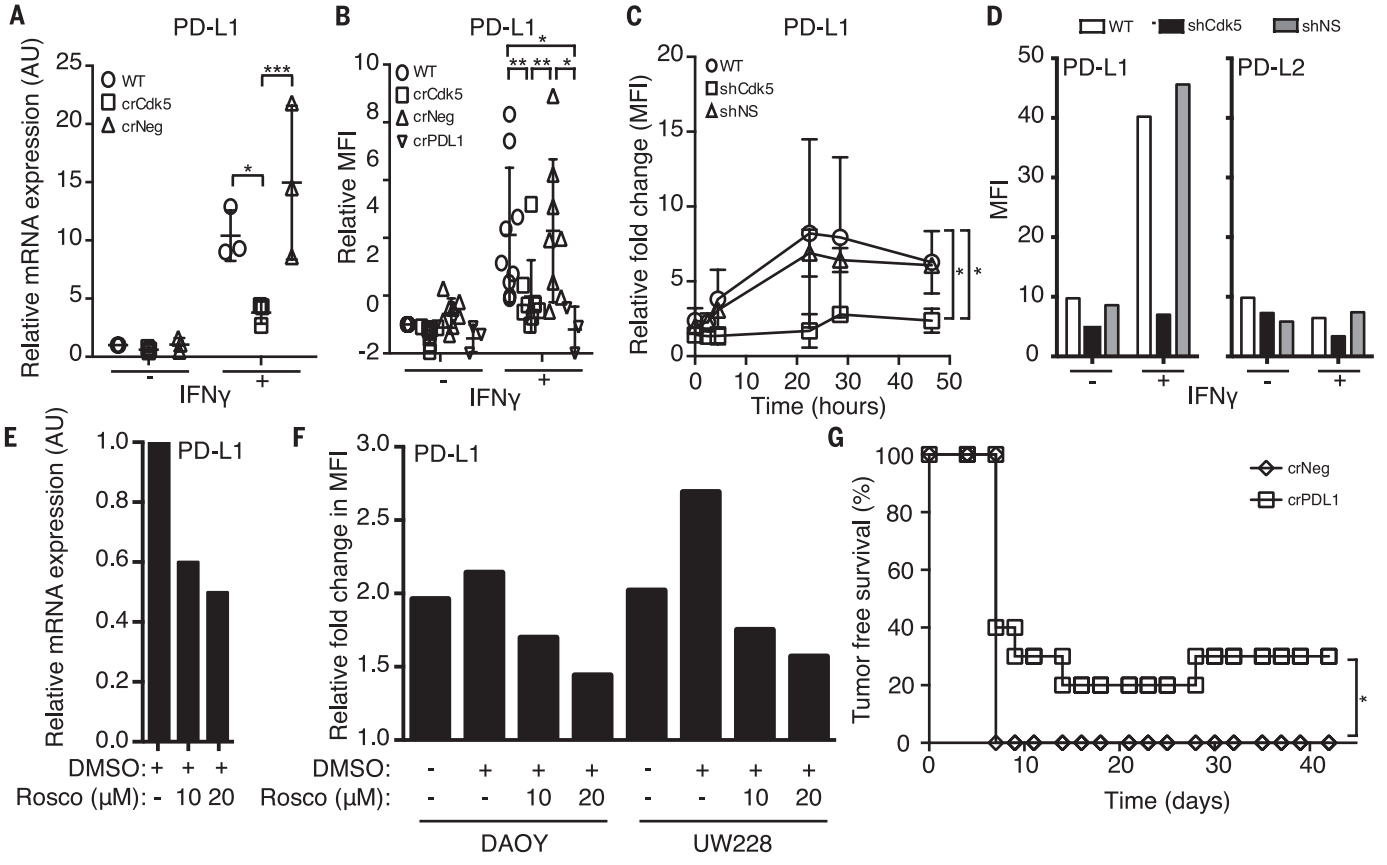

Fig. 2. Disruption of either Cdk5 gene expression or Cdk5 activity suppresses PD-L1 expression that cannot be overcome with IFN-γ stimulation in both human and murine MBs. (**A**) In vitro mRNA expression in arbitrary units (AU) of *PD-L1* by MM1 WT, crCdk5, and crNeg cells with or without 24 hours of IFN-γ stimulation. Values represent the average of three biological replicates ± SD. (**B**) In vitro PD-L1 surface staining of MM1 WT, crCdk5, crNeg, and crPDL1 cells with or without 24 hours of IFN-γ stimulation. Values represent the average mean fluorescence intensity (MFI) ± SD compared with unstimulated MM1 WT cells over seven or eight replicates. (**C**) Fold change of surface PD-L1 expression in MM1 WT, shCdk5, and shNS cells over the course of 48 hours of IFN-γ stimulation. (**D**) MFI of PD-L1 and PD-L2 expressed in MM1 WT, shCdk5, and shNS cells. (**E**) *PD-L1* mRNA expression in MM1 WT cells when treated with roscovitine and stimulated with IFN-γ for 24 hours. AU relative to untreated. DMSO, dimethyl sulfoxide. (**F**) DAOY and UW228 human MB lines treated with roscovitine and stimulated with IFN-γ for 24 hours. MFI relative to untreated samples. (**G**) TFS of MM1 crNeg and crPDL1 injected mice over 36 days (n = 10 mice per group). *P < 0.05; **P < 0.01; ***P < 0.001. Significance was determined by two-way ANOVA with Bonferoni posttest (A) and (B), Student's t test (C), or log-rank test (G). Representative experiments are shown in (D) and (E).

IFN-γ–induced PD-L1 up-regulation (fig. S4, C to E), which indicated that the link between Cdk5 and PD-L1 regulation by IFN-γ is not MB-specific. Twenty-four hours after IFN-γ exposure, surface PD-L1 expression reached a peak of 8.2- and 6.8-fold above baseline in WT and NS cells, respectively (Fig. 2C), whereas Cdk5-deficient cells only up-regulated PD-L1 2.8-fold, so it reached a peak level similar to the basal levels in unstimulated WT and NS controls. The blunted response to IFN-γ is specific for PD-L1 but not PD-L2 (Fig. 2D). To further corroborate the link between Cdk5 and PD-L1 synthesis, we treated MM1 WT cells with roscovitine and observed a dose-dependent decrease in PD-L1 transcripts (Fig. 2E). In vitro treatment of human MB with roscovitine also diminished surface PD-L1 up-regulation with IFN-γ in a dose-dependent manner (Fig. 2F). Finally, to establish a functional link between PD-L1 and in vivo rejection of Cdk5-deficient MM1, we disrupted the PD-L1 gene (*CD274*) in MM1 cells (MM1 crPDL1). Similar to MM1 crCdk5 experiments, 30% of mice inoculated with MM1 crPDL1 remained tumor-free for more than 4 weeks (Figs. 2G and 1B).

Next, we interrogated the IFNGR signaling pathway. Western blot analysis of various MM1 cells failed to show differences, after IFN-γ exposure, in STAT1, STAT2, or STAT3 (members of the family of signal transducers and activators of transcription) (Fig. 3A and fig. S7B), in agreement with the robust MHC class I induction in Cdk5-deficient MM1 cells (fig. S7A). To further dissect this STAT1-independent signaling, we examined interferon regulatory factor–1 (IRF1) and interferon regulatory factor–2 (IRF2), which are implicated as positive and negative regulators of PD-L1 transcription, respectively (*13*, *15*). IRF1 protein was rapidly induced by IFN-γ and remained elevated for up to 48 hours regardless of Cdk5 expression (Fig. 3A and fig. S7C). We observed a rapid loss of the PD-L1 transcription repressor, IRF2, in WT and crNeg cells. In contrast, IRF2 and its corepressor IRF2BP2 (*16*) were elevated at baseline in Cdk5-deficient cells and persisted for up to 48 hours after IFN-γ exposure (Fig. 3A and fig. S7C). This protein expression difference cannot be accounted for at the transcriptional level (fig. S7D). Phosphoproteomic analysis identified 77 distinct phosphopeptides in the shCdk5 versus WT or shNS screen (tables S1 and S2), and 798 phosphopeptides in the crCdk5 versus WT or crNeg screen (tables S3 and S4). Between these two data sets, 22 common proteins were differentially phosphorylated in Cdk5-deficient cells, with IRF2BP2 among the highest phosphorylated peptide species (Fig. 3B).

Finally, we introduced Cdk5-deficient MM1 cells orthotopically into C57BL/6 mice. Gross inspection revealed a 50% tumor incidence in mice injected with Cdk5-deficient MM1, mirroring s.c. tumors. In contrast, 100% of mice injected with WT or NS MM1 cells developed gross brain tumors by day 14 (fig. S8A). Intracranial (i.c.) Cdk5-deficient tumor outgrowth remained devoid of Cdk5 expression without the emergence of a Cdk5^{+} escape variant (fig. S8B). Histological analysis showed increased accumulation of IBA-1^{+} cells, which marks microglia and infiltrating monocytes, and PD-L1^{+}

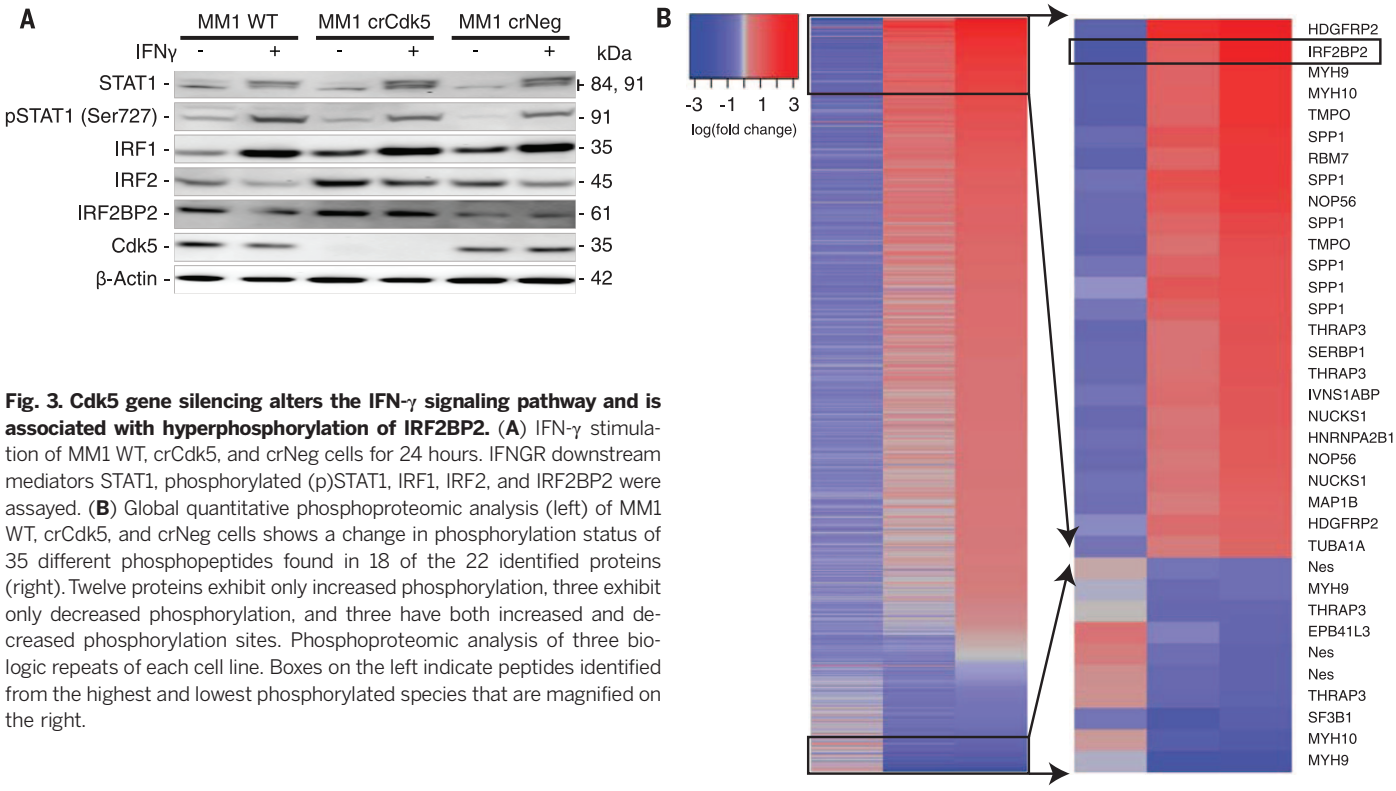

Fig. 3. Cdk5 gene silencing alters the IFN-γ signaling pathway and is associated with hyperphosphorylation of IRF2BP2. (**A**) IFN-γ stimulation of MM1 WT, crCdk5, and crNeg cells for 24 hours. IFNGR downstream mediators STAT1, phosphorylated (p)STAT1, IRF1, IRF2, and IRF2BP2 were assayed. (**B**) Global quantitative phosphoproteomic analysis (left) of MM1 WT, crCdk5, and crNeg cells shows a change in phosphorylation status of 35 different phosphopeptides found in 18 of the 22 identified proteins (right). Twelve proteins exhibit only increased phosphorylation, three exhibit only decreased phosphorylation, and three have both increased and decreased phosphorylation sites. Phosphoproteomic analysis of three biologic repeats of each cell line. Boxes on the left indicate peptides identified from the highest and lowest phosphorylated species that are magnified on the right.

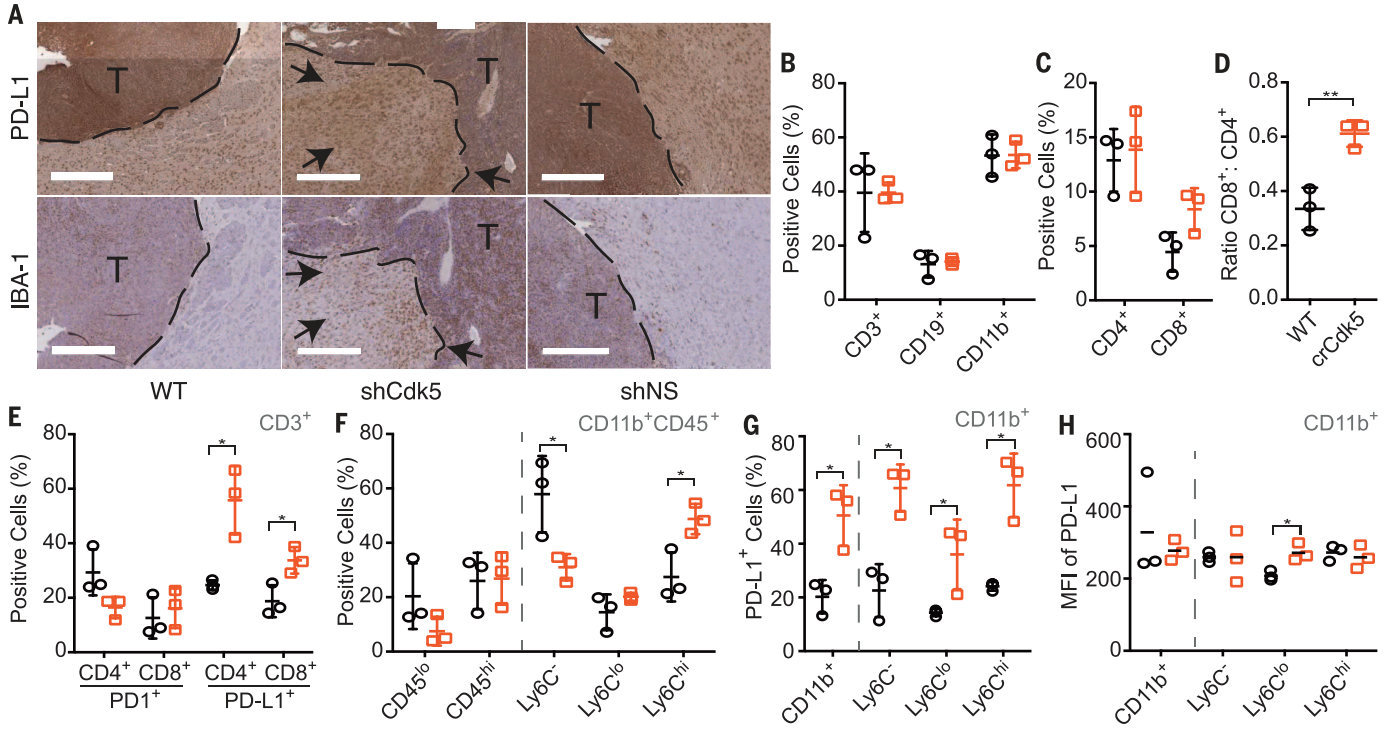

Fig. 4. Orthotopic Cdk5-deficient tumors exhibit increased PD-L1 staining, CD4$^+$ tumor–infiltrating lymphocytes (TILs), and accumulating infiltrates of CD11b$^+$ populations. (**A**) Tumors extracted 14 days postinoculation from MM1 WT, shCdk5, or shNS mice stained for PD-L1 expression. Dashed line represents margin between tumor (T) and stroma. Black arrows point to increased PD-L1$^+$ and IBA-1$^+$ cells in the tumor stroma. Scale bars, 400 μm. (**B** and **C**) Fluorescence-activated cell sorting (FACS) analysis of MM1 WT (black circle) and MM1 crCdk5 (orange square) tumor infiltrate by percentage of cell type. (**D**) Ratio of total CD8$^+$:CD4$^+$ cell infiltrate. (**E**) FACS analysis of the percentage of PD-1$^+$ or PD-L1$^+$ cells in the CD4$^+$ or CD8$^+$ populations. (**F**) FACS analysis of the percentage of myeloid cells in tumor infiltrate based on differential CD45 staining (left) or Ly6C staining among CD11b$^+$CD45$^+$ cells (right). (**G**) Percent of total CD11b$^+$ population (left) and subpopulations (right) present in tumor infiltrate that express PD-L1. (**H**) MFI of PD-L1 expression among CD11b$^+$ total population (left) and subpopulations (right). (B), (C), (D), (E), (F), and (G) were graphed as means ± SD. (H) was graphed as individual MFI with mean indicated. n = 9 per group. Each data point represents pooled samples from three mice. *P < 0.05; ** P < 0.01. Significance was determined using the Student's t test.

staining in the Cdk5-deficient MM1 tumor margin and surrounding stroma (Fig. 4A). Immune cell composition analysis showed a modest increase in $CD3^+$ T cells, similar to that shown by immunohistochemical data (Fig. 1C and fig. S8, C and D). However, the percentages of $CD3^+$ cells were equivalent in crCdk5 and WT tumor samples by flow cytometry (Fig. 4B). Cdk5-deficient tumors elicited an increased ratio of $CD8^+$ to $CD4^+$ T cell infiltrate, lower PD-1 expression in $CD4^+$ T cells, and higher PD-L1 expression in both T cell subsets (Fig. 4, C to E). Although $CD8^+$ T cells are not the primary antitumor effector cells in this model, their increased recruitment likely reflects an overall inflammatory tumor milieu as evidenced by increased PD-L1 expression and overall tissue IFN-γ levels (Fig. 1B and figs. S3C, S5A, and S9, A to E). The myeloid infiltrate in i.c. tumors shifted from a $Ly6C^-$ to a $Ly6C^{hi}$ population with an increased percentage of PD-$L1^+$ cells in bulk $CD11b^+$ cells and in each Ly6C subset (Fig. 4, F to H), accompanied by a decrease in the percentage of microglia ($CD11b^+CD45^{lo}$) (Fig. 4F). The $Ly6C^{lo}$ subset expressed a higher density of surface PD-L1 in the Cdk5-deficient tumors (Fig. 4H). Again, this finding was recapitulated in s.c. tumors, which showed a significant increase in the percentage of PD-$L1^+$ immune cells, with a trend toward increased density of PD-L1 staining in the crCdk5 tumor microenvironment (fig. S9, F to I). The observed increase in PD-$L1^+$ populations and staining density aligns with histologic analyses (Fig. 4A and fig. S9B), which suggests a state of global immune activation in response to ongoing IFN-γ stimulation. This finding is in good agreement with reports showing increased PD-$L1^+$ immune cells in MB stroma undergoing active immune checkpoint blockade (*17*).

Here, we showed that Cdk5 disruption sensitizes MB to $CD4^+$ T cell–dependent rejection via posttranslational modification of IRF2BP2, which increases IRF2 and IRF2BP2 abundance and sustains PD-L1 transcriptional repression after IFN-γ stimulation. Downstream IFN-γ signaling induces interferon-stimulated genes, including *IRF1* (*18*), which activates secondary-response genes, including *PD-L1* (*13*, *19*, *20*). IRF2 acts as a repressor that competes with IRF1 for binding to the same promoter element (*15*). Constitutively present, IRF2 is up-regulated in response to either type I IFNs or IRF1 (*15*, *20*) and provides a negative-feedback loop by binding to its own promoter to block transcription (*15*). The prolonged half-life of IRF2 (8 hours) relative to IRF1 (0.5 hours) provides a mechanism for IRF2 antagonism (*20*). IRF2BP2 was recently identified as a corepressor with IRF2 (*16*), and low IRF2BP2 expression was correlated with high PD-L1 expression in breast cancer (*21*). Our data provide a direct link between disruption of Cdk5 activity and IRF2BP2 hyperphosphorylation at sites that are distinct from previously described sites that affect nuclear localization, vascular endothelial growth factor A, or MHC-I expression (*22*–*24*), which suggests that Cdk5 either directly or indirectly inhibits other kinase(s) that phosphorylate IRF2BP2 (fig. S10).

PD-L1 and PD-1 play a critical role in tumor immune evasion, with ~30% of tumors responding to immune checkpoint blockade (*25*, *26*). High Cdk5 expression correlates with worse clinical outcome in multiple cancers (fig. S11). In our studies, both Cdk5- and PD-L1–deficient MB cells exhibit similar TFS (Figs. 1B and 2G). More $CD4^+$ T cells with lower PD-1 expression were found in the Cdk5-deficient CNS tumors, whereas $CD11b^+$ cells accumulate in larger quantities with higher PD-$L1^+$ expression (Fig. 4, C to G). Myeloid PD-L1 up-regulation may be a response to overall increased IFN-γ (*13*, *27*). Alternatively, these cells may play a distinct role modulating infiltrating T cell function, which are present in most human MB specimens (*28*). Last, as Cdk5 directly phosphorylates MYC on Ser^{62} (*29*), it remains to be determined whether Cdk5 plays a role in MYC-regulated PD-L1 expression (*30*).

REFERENCES AND NOTES

1. R. Dhavan, L. H. Tsai, *Nat. Rev. Mol. Cell Biol.* **2**, 749–759 (2001).
2. T. Ohshima *et al.*, *Proc. Natl. Acad. Sci. U.S.A.* **93**, 11173–11178 (1996).
3. E. Utreras, A. Futatsugi, T. K. Pareek, A. B. Kulkarni, *Drug Discov. Today Ther. Strateg.* **6**, 105–111 (2009).
4. E. Contreras-Vallejos, E. Utreras, C. Gonzalez-Billault, *Cell. Signal.* **24**, 44–52 (2012).
5. A. Arif, *Biochem. Pharmacol.* **84**, 985–993 (2012).
6. T. K. Pareek *et al.*, *J. Exp. Med.* **207**, 2507–2519 (2010).
7. F. N. Hsu *et al.*, *J. Biol. Chem.* **286**, 33141–33149 (2011).
8. G. Feldmann *et al.*, *Cancer Res.* **70**, 4460–4469 (2010).
9. R. Liu *et al.*, *Proc. Natl. Acad. Sci. U.S.A.* **105**, 7570–7575 (2008).
10. H. S. Khalil, V. Mitev, T. Vlaykova, L. Cavicchi, N. Zhelev, *J. Biotechnol.* **202**, 40–49 (2015).
11. H. J. Kim, H. Cantor, *Cancer Immunol. Res.* **2**, 91–98 (2014).
12. J. H. Song *et al.*, *J. Biol. Chem.* **280**, 12896–12901 (2005).
13. S. J. Lee *et al.*, *FEBS Lett.* **580**, 755–762 (2006).
14. J. M. Taube *et al.*, *Sci. Transl. Med.* **4**, 27ra37 (2012).
15. H. Harada *et al.*, *Cell* **58**, 729–739 (1989).
16. K. S. Childs, S. Goodbourn, *Nucleic Acids Res.* **31**, 3016–3026 (2003).
17. C. D. Pham *et al.*, *Clin. Cancer Res.* **22**, 582–595 (2016).
18. L. C. Platanias, *Nat. Rev. Immunol.* **5**, 375–386 (2005).
19. S. Yao *et al.*, *Mucosal Immunol.* **8**, 746–759 (2015).
20. T. Taniguchi, A. Takaoka, *Nat. Rev. Mol. Cell Biol.* **2**, 378–386 (2001).
21. H. Soliman, F. Khalil, S. Antonia, *PLOS ONE* **9**, e88557 (2014).
22. A. C. Teng *et al.*, *PLOS ONE* **6**, e24100 (2011).
23. A. C. Teng *et al.*, *FASEB J.* **24**, 4825–4834 (2010).
24. K. W. Jarosinski, P. T. Massa, *J. Neuroimmunol.* **122**, 74–84 (2002).
25. D. M. Pardoll, *Nat. Rev. Cancer* **12**, 252–264 (2012).
26. W. Zou, L. Chen, *Nat. Rev. Immunol.* **8**, 467–477 (2008).
27. J. Liu *et al.*, *Blood* **110**, 296–304 (2007).
28. V. S. Salsman *et al.*, *PLOS ONE* **6**, e20267 (2011).
29. H. R. Seo, J. Kim, S. Bae, J. W. Soh, Y. S. Lee, *J. Biol. Chem.* **283**, 15601–15610 (2008).
30. S. C. Casey *et al.*, *Science* **352**, 227–231 (2016).

ACKNOWLEDGMENTS

We thank F. Scrimieri, G. Valdivieso, A. Awadallah, A. Kresak, D. Schlatzer, and the Case Western Reserve University Center for Proteomics for technical assistance; M. Couce for constructing human MB tissue microarray; and M. Chieppa, D. Askew, and B. Benson for careful review of the manuscript. The data reported in this manuscript are tabulated in the main paper and in the supplementary materials. This work was supported by NIH F31CA196265 (R.D.D.), NIH T32GM007250 (R.D.D. and S.M.C.), NIH T32AI089474 (S.M.C.), NIH R01GM086550 (D.W.A.), NIH R01CA154656 (A.Y.H.), NIH R21CA181875 (A.Y.H. and J.J.L.), NIH R01HL111682 (A.Y.H. and J.J.L.), NIH P30CA043703 (A.Y.H. and A.P.), Wolstein Research Scholarship (R.D.D.), St. Baldrick's Foundation (A.P., J.J.L., and A.Y.H.), Hyundai "Hope-on-Wheels" Program (A.P., D.S.S., and A.Y.H.), Marc Joseph Fund (A.Y.H.), Alex's Lemonade Stand Foundation (A.P. and A.Y.H.), the Angie Fowler Adolescent and Young Adult Cancer Research Initiative at the Case Comprehensive Cancer Center (A.P., J.J.L., D.S.S., S.A., and A.Y.H.), and Theresia G. and Stuart F. Kline Family Foundation in Pediatric Oncology (A.Y.H.). This work was supported by the Clinical and Translational Science Collaborative of Cleveland UL1TR000439 (A.P.), and KL2TR000440 (S.A.) from the National Center for Advancing Translational Sciences (NCATS) component of the NIH. Authors declare no competing financial interests. All phosphoproteomics data are available in the supplementary materials.

SUPPLEMENTARY MATERIALS

www.sciencemag.org/content/353/6297/399/suppl/DC1
Materials and Methods
Figs. S1 to S11
Tables S1 to S4
Reference (*31*)

9 December 2015; accepted 31 May 2016
10.1126/science.aae0477

NEW ENGLAND BioLabs® Inc.

Migrate to Monarch®.

Environmentally-friendly Nucleic Acid Purification Kits from New England Biolabs

Want to feel good about your choice in DNA purification? With our fast and reliable Monarch Nucleic Acid Purification Kits, you can achieve optimal purification while creating less waste. Available for plasmid minipreps, DNA gel extraction and enzymatic cleanup (including PCR), our products use up to 44% less plastic and are packaged using responsibly-sourced, recyclable materials. Make the change and migrate to Monarch today.

> *These kits might be the best I have used for the price. The best part is that it uses less plastic for production!! Thank you for caring about our environmental impacts, NEB!!!*
>
> – NEB customer

Request your free sample at **www.NEBMonarch.com**

myIDP: A career plan customized for you, by you.

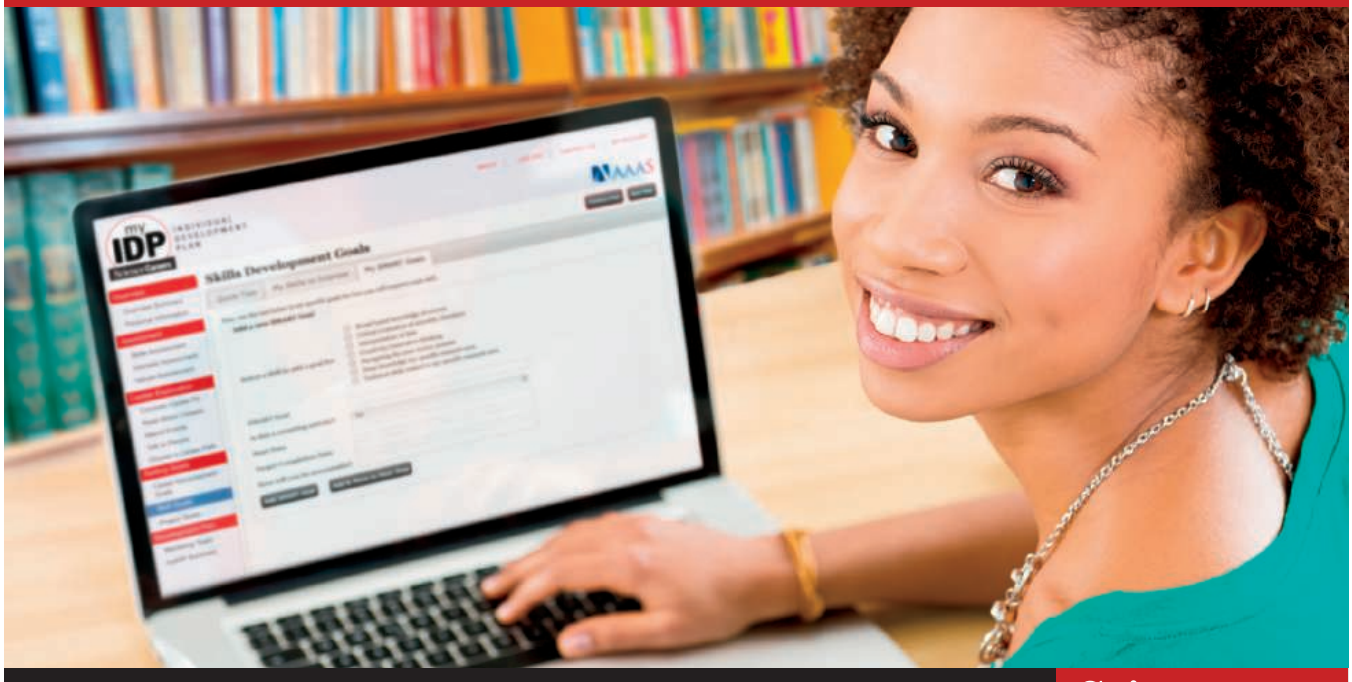

For your career in science, there's only one Science

my IDP
Science Careers

Recommended by leading professional societies and the NIH

Features in myIDP include:

- Exercises to help you examine your skills, interests, and values.
- A list of 20 scientific career paths with a prediction of which ones best fit your skills and interests.
- A tool for setting strategic goals for the coming year, with optional reminders to keep you on track.
- Articles and resources to guide you through the process.
- Options to save materials online and print them for further review and discussion.
- Ability to select which portion of your IDP you wish to share with advisors, mentors, or others.
- A certificate of completion for users that finish myIDP.

Visit the website and start planning today!
myIDP.sciencecareers.org

Science Careers In partnership with:

advancing the life sciences 1912-2012 FASEB Federation of American Societies for Experimental Biology

UCSF University of California San Francisco

Medical College of Wisconsin

Burroughs Wellcome Fund

want new technologies?

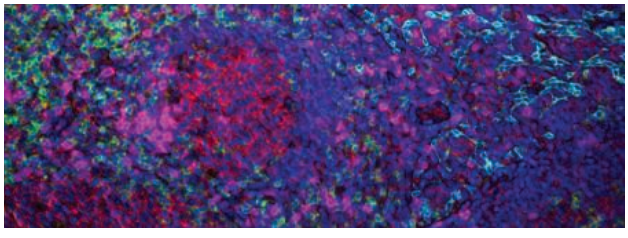

antibodies
apoptosis
biomarkers
cancer
cytometry
data
diseases
DNA
epigenetics
genomics
immunotherapies
medicine
microbiomics
microfluidics
microscopy
neuroscience
proteomics
sequencing
toxicology
transcriptomics

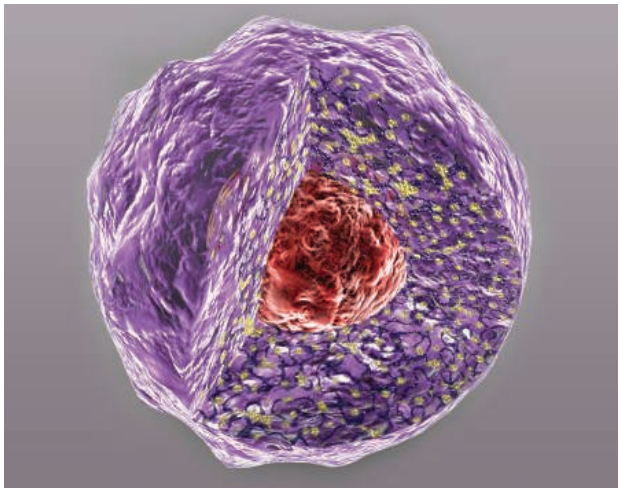

watch our webinars

Learn about the latest break-throughs, new technologies, and ground-breaking research in a variety of fields. Our expert speakers explain their quality research to you and answer questions submitted by live viewers.

VIEW NOW!
webinar.sciencemag.org

Science
AAAS

Brought to you by the *Science*/AAAS Custom Publishing Office

@SciMagWebinars

Air-Bearing Rheometer

The Thermo Scientific HAAKE Viscotester iQ Air rheometer extends the capabilities and measurement range of the HAAKE Viscotester iQ product line to enable monitoring of very low-viscosity materials. Built-in Connect Assist technology provides real-time feedback that reduces operator errors and makes it easier for users to set up sample tests. The HAAKE Viscotester iQ Air rheometer is designed to acquire simple viscosity curves and complex rheological investigations in rotation or oscillation, covering measurements ranging from low-viscosity liquids to highly viscous pastes. It also provides a touchscreen interface for stand-alone routine measurement and a USB flash drive for extended capabilities; all modes are operated with full software control from a computer. Thermo Fisher Scientific offers a complete portfolio of rheology testing solutions. The Viscotester range has been specifically developed to meet the demands of rheological tasks in quality control, combining fast, reliable, and precise measurements with maximum ease of use.

Thermo Fisher Scientific
For info: 800-955-6288
www.thermofisher.com/vtiq

Metal Catalyst Reaction Monitoring Probe

The inert Atmospheric Solids Analysis Probe (iASAP) enables chemists and chemistry students to ionize liquid and solid samples for analysis by mass spectrometer without the need for sample preparation. The technique allows a synthetic chemist to perform real-time reaction monitoring by simply dipping the iASAP into the reaction mixture and inserting the probe into the atmospheric pressure chemical ionization source of the compact mass spectrometer (CMS). Mass spectral data is presented within seconds. For air-sensitive compounds, such as metal catalysts, iASAP is a viable technique to prevent oxidization during the assay. The iASAP protects the compounds in inert gas as they are transferred to the CMS, enabling such measurements without the traditional need for glove boxes. Researchers led by Charles McEwen, Ph.D, at the University of Pennsylvania, and Ingo Krossing, Ph.D., at the Albert-Ludwig University of Freiburg, developed the iASAP.

Advion
For info: 607-266-9162
www.advion.com

Confocal Laser Scanning Microscope

The FLUOVIEW FV3000 confocal laser scanning microscope combines high-performance imaging capabilities with ease of use, so scientists in such fields as cell biology, cancer research, and stem cell research can collect relevant imaging data quickly. The FV3000 offers flexibility for all live-cell imaging applications and provides high-resolution images of structures and dynamic intracellular processes. The FV3000 is controlled via a new, intuitive software interface so even novices can generate high-quality data and images. Objectives range from 1.25X to 150X magnification. Users can choose the FV3000 with the galvanometer scanner or the hybrid resonant/galvanometer scanner. The high-speed resonant scanner acquires high-resolution images at up to 438 frames per second, so scientists can observe fast-changing processes. Users have the freedom to select the exact wavelength range that they wish to capture in every detection channel at nanometer precision, and to change the scanning range or laser light midway through an experiment with millisecond precision.

Olympus
For info: 704-877-8801
www.olympus-lifescience.com

Differential Scanning Calorimeters

A new line of differential scanning calorimeters (DSCs)—the Discovery DSC 2500, DSC 250, and DSC 25—features enhanced sensing technologies, resulting in unprecedented performance in baseline flatness, sensitivity, resolution, and reproducibility. At the core of every new Discovery DSC is the exclusive TA Fusion Cell, which incorporates design concepts from the Q-Series and first-generation Discovery DSCs, patented Tzero technology, and new proprietary manufacturing processes. All models come with an app-style user interface, TRIOS software, and automated calibration and verification routines that work seamlessly to improve laboratory workflows. Discovery DSCs are used for many applications, including materials science, pharmaceuticals, and chemistry. The DSC 2500 comes standard with all options, which include T4P heat-flow technology and a linear autosampler that assigns sample and reference pans to any combination of the available 54 positions. The DSC 250 is a configurable, research-grade DSC. The DSC 25 is a cost-effective, easy-to-use, general purpose DSC.

TA Instruments
For info: 302-427-4000
www.tainstruments.com

Seed Germination

Phytotc seed germination pouches are an inexpensive, space-saving alternative to pots and other containers. Phytotc has two parts: a plastic see-through pouch and a paper wick that fits inside the pouch. Seeds are placed in the trough formed by the paper wick. Water or nutrient substrates are then added. The pouch is finally placed in an upright position and the seeds are left to grow. An optional stand can hold multiple pouches. Most seeds grow in days. The pouches are available in small (14-cm high × 12.5-cm wide) for plants with fibrous or shorter roots; medium (18-cm high × 12.5-cm wide) for plants with tap roots or longer roots; and large (30-cm high × 25-cm wide) for plants needing longer growing times. All pouches come sterilized. They can be used in plant nematology, physiology, and pathology applications as well as for legume inoculation and tissue transfer.

Eikonix
For info: +44-(0)-1223-515440
www.eikonix.com

Electronically submit your new product description or product literature information! Go to www.sciencemag.org/about/new-products-section for more information.

Newly offered instrumentation, apparatus, and laboratory materials of interest to researchers in all disciplines in academic, industrial, and governmental organizations are featured in this space. Emphasis is given to purpose, chief characteristics, and availability of products and materials. Endorsement by *Science* or AAAS of any products or materials mentioned is not implied. Additional information may be obtained from the manufacturer or supplier.


上海工程技术大学
Shanghai University of Engineering Science

The Sincere Recruitment of Global Talents in *Shanghai University of Engineering Science*

1. Introduction

Shanghai University of Engineering Science (SUES) is a widely recognized university specializing in applied technologies and engineering sciences, focusing on interdisciplinary integration of economics and management, and art design, etc. and promoting a well-coordinated development of undergraduate, graduate and higher vocational education. The main campus of SUES is located in the Songjiang University Town, covering an area of 1500 mu. SUES now boasts 4 first-accredited and 22 second-accredited master's degree programs and 2 professional master's degree programs with 82 majors for undergraduates and junior college students. SUES is home to about 20,000 undergraduates and junior college students, and about 1,800 postgraduates and over 1,100 full-time teachers.

SUES in one of the first-batch experimental universities for outstanding engineer education and cultivation plan of the Ministry of Education. Its disciplines and majors are closely connected with Shanghai modern industries, filling with brilliant characteristics.

SUES has carried out extensive exchanges and cooperation with dozens of universities in the US, the UK, France, Germany, Japan, Sweden, Korea, Canada, Australia, New Zealand and so on.

And this university is now warmly welcome talents in various fields to join its university construction.

2. Applicants

1) High-level Talents

Academicians of the Chinese Academy of Sciences and Chinese Academy of Engineering, National High-level Talents Special Support Plan (Thousands of People Plan), National Thousand Talents Program, Changjiang Scholars Program, Shanghai Thousand Talents Plan, Shanghai Orientalist, etc.

2) Talents Action Plan in Shanghai University of Engineering Science

·Zhihong Scholars: Applicants are required to have a doctor's degree and under the age of 45; being the associate professor of high-level university and above or other rather positions.

·Soaring Plan: Applicants are required to have a doctor's degree and under the age of 36; being the associate professor and above or other rather positions.

·Winging Plan: Applicants are required to have a doctor's degree and under the age of 32; with higher academic level and strong teaching and scientific research abilities and prominent achievements.

3) Teaching Faculties and Scientific Researchers

4) Excellent Fresh Ph.D Graduates

Note: Please refer to www.sues.edu.cn for detailed recruitment content.

3. Positions (including but not limited to the following majors)

Engineering: Mechanical Engineering, Control Science and Engineering, Electrical Engineering and Automation, Aerospace Propulsion Theory and Engineering, Vehicle Engineering, Rail Transit Information and Control, Materials Science and Engineering, Textile Science and Engineering, Design,etc.

Management: Marketing, Industrial Engineering, Public Management, Management Science and Engineering, International Economics and Trade, etc.

Science: Mathematics, Physics, etc.

4. Applying Channels

1) Please e-mail your application materials and job intention to jsk@sues.edu.cn.

2) Please post via our official talent recruitment system (http://zhaopin.sues.edu.cn)

5. Contact

Address: No. 333 Longteng Road,
Songjiang District, Shanghai, China
Contact Person: Teacher Miao, Teacher Zhu
E-mail: jsk@sues.edu.cn
Phone: (86-21) 67791252 67791249

Science Careers Advertising

For full advertising details, go to ScienceCareers.org and click For Employers, or call one of our representatives.

Tracy Holmes
Worldwide Associate Director
Science Careers
Phone: +44 (0) 1223 326525

THE AMERICAS

E-mail: advertise@sciencecareers.org
Fax: +1 (202) 289 6742

Tina Burks
Phone: +1 (202) 326 6577

Nancy Toema
Phone: +1 (202) 326 6578

Online Job Posting Questions
Phone: +1 (202) 312 6375

EUROPE / INDIA / AUSTRALIA / NEW ZEALAND / REST OF WORLD

E-mail: ads@science-int.co.uk
Fax: +44 (0) 1223 326532

Sarah Lelarge
Phone: +44 (0) 1223 326527

Kelly Grace
Phone: +44 (0) 1223 326528

Online Job Posting Questions
Phone: +44 (0) 1223 326528

JAPAN

Katsuyoshi Fukamizu (Tokyo)
E-mail: kfukamizu@aaas.org
Phone: +81 3 3219 5777

Hiroyuki Mashiki (Kyoto)
E-mail: hmashiki@aaas.org
Phone: +81 75 823 1109

CHINA / KOREA / SINGAPORE / TAIWAN / THAILAND

Ruolei Wu
E-mail: rwu@aaas.org
Phone: +86 186 0082 9345

Danny Zhao
E-mail: dzhao@aaas.org
Phone: +86 131 4114 0012

ScienceCareers
FROM THE JOURNAL SCIENCE AAAS

ScienceCareers.org

PURDUE UNIVERSITY

THREE ASSISTANT PROFESSOR TENURE-TRACK POSITIONS

The College of Agriculture at Purdue University, West Lafayette, Indiana, invites applications from outstanding basic scientists for three academic year tenure-track assistant professor positions as part of a college-wide cluster hire in fundamental plant biology. Candidates addressing important fundamental questions in plant biology are encouraged to apply. We are interested in individuals working on molecular, organismal or ecosystem levels, and in model systems, crops, or natural systems. This hiring initiative is part of the Plant Sciences Research and Education Pipeline, through which are being developed high-throughput controlled environment imaging, field-scale phenotyping, and a plant commercialization incubator.

Each successful candidate will be expected to develop an internationally recognized research program, interact with diverse faculty, staff and students across campus, and contribute to the further development of plant science as an area of excellence on the Purdue University campus. Each such candidate will also teach graduate and/or undergraduate courses, and function as an active member of the departmental and university faculty. Applicants should have a Ph.D. in biological, computational, or physical sciences, preferably with at least two years of post-doctoral experience or its equivalent, a strong publication record, the potential to develop a vigorous, extramurally funded research program, and a commitment to both hypothesis-driven research and teaching excellence. Applications should be submitted electronically to **molecularag@purdue.edu** and should include in a single pdf file a cover letter, curriculum vitae, two page summary of research interests, a one-page teaching statement, and the names and contact information for three references. Applicants may learn more about the departments involved in this search at https://ag.purdue.edu/plantsciences/center-for-molecular-agriculture-2/ and indicate in their application up to two departments of greatest interest. Screening of applications will begin **August 31, 2016**, and will continue until the positions are filled. A background check is required for employment in these positions.

Purdue University is an EOE/AA Employer. All individuals, including minorities, women, individuals with disabilities, and veterans are encouraged to apply.

UNIVERSITY OF MICHIGAN

BIOLOGICAL SCIENCES SCHOLARS PROGRAM
For Junior, Tenure Track Faculty

The University of Michigan Medical School announces recruitment for the Biological Sciences Scholars Program (BSSP) to enhance the institution's strengths in the biological and biomedical research areas.

Now entering its 18th year, the BSSP has led recruitment of outstanding scientists pursuing research in genetics, microbiology, immunology, virology, structural biology, biochemistry, molecular pharmacology, stem cell biology, cancer biology, physiology, cell and developmental biology, bioinformatics, and the neurosciences. The Program seeks individuals with PhD, MD, or MD/PhD degrees, at least two years of postdoctoral research experience, and who have not previously held a tenure-track faculty position. Candidates will show evidence of superlative scientific accomplishment and scholarly promise. Successful candidates will be expected to establish a vigorous, externally-funded research program, and to become leaders in departmental and program activities, including teaching at the medical, graduate, and/or undergraduate levels. Primary departmental affiliation(s) will be determined by the applicant's qualifications and by relevance of the applicant's research program to departmental initiatives and themes. All faculty recruited via the BSSP will be appointed at the Assistant Professor level.

APPLICATION INSTRUCTIONS: Please apply to the Scholars Program through the BSSP website at: **http://bssp.med.umich.edu**. A curriculum vitae (including bibliography), a three page research plan, an NIH biosketch, and three original letters of support should all be submitted through the BSSP website. More information about the Scholars Program, instructions for applicants and those submitting letters of recommendation, and how to contact us is located on the BSSP web site: **http://bssp.med.umich.edu**. The deadline for applications is **Friday, September 30, 2016**.

The University of Michigan is an Affirmative Action/Equal Opportunity Employer.

MICHIGAN STATE UNIVERSITY

MSU-DOE PLANT RESEARCH LABORATORY
Michigan State University
East Lansing, MI 48824
http://www.prl.msu.edu

Faculty Position in the Biology of Photosynthetic Organisms

The MSU-DOE Plant Research Laboratory (PRL) has a tenure-track, twelve-month faculty position available at the Assistant Professor level. We seek to recruit individuals who investigate fundamental questions in the biology of plants, algae, or photosynthetic bacteria. Relevant research areas and approaches include, but are not limited to: biophysical/biochemical mechanisms and regulation of photosynthesis, plant synthetic biology, metabolism and metabolic engineering, signaling and regulatory networks, structural biology, phenomics, and computational biology.

The PRL, with long-standing funding from the U.S. Department of Energy, provides a highly collaborative environment for conducting creative, fundamental research on photosynthetic organisms, with an emphasis on energy-related, interdisciplinary research. PRL faculty are full members of the MSU tenure-stream faculty. Successful candidates will be jointly appointed in an appropriate academic department. Applicants should have a PhD and postdoctoral research experience with evidence of productivity and potential for independent research. Applications must include a cover letter, curriculum vitae, summary of research accomplishments, a 3-5 page plan for future research, a statement of teaching philosophy, and names and contact information of three references. Application materials should be submitted as a single PDF file through the MSU applicant page at **https://jobs.msu.edu** (**position # 3603**). Questions regarding this position should be directed to the chair of the search committee, Jianping Hu (huji@msu.edu). Consideration of applicants will begin on **November 15, 2016**.

MSU is an Affirmative-Action, Equal-Opportunity Employer and is committed to achieving excellence through diversity. The University actively encourages applications of women, persons of color, veterans, and persons with disabilities, and we endeavor to facilitate employment assistance to spouses or partners of candidates for faculty and academic staff positions.

FRED HUTCH
CURES START HERE™

Senior Faculty Leadership Position in Global Oncology at Fred Hutchinson Cancer Research Center

Fred Hutchinson Cancer Research Center seeks exceptional applicants for a full-time senior faculty leadership position in the Global Oncology Program at the Full Member level (comparable to Professor). The primary responsibility of this position will be to lead the development and execution of Fred Hutch's global oncology research agenda, encompassing basic and translational research, innovative prevention and treatment, and implementation science. The leader will be expected to conduct groundbreaking scientific research with global impact and to foster scientific collaborations involving multiple investigators across Fred Hutch and external, international partners. The ideal candidate will have a well-established and funded research portfolio with international recognition for scientific excellence and have a demonstrated record in mentoring faculty and partners to pursue an international research portfolio.

The Fred Hutch has established a broad international footprint to enable the conduct of innovative basic and clinical research in cancer, and particularly in infectious disease-related cancers. In May 2015, the Fred Hutch and the Uganda Cancer Institute (UCI) opened the world-class UCI-Fred Hutch Cancer Centre in Kampala, Uganda. This 25,000 square-foot facility supports research, outpatient care and training, as well as clinical laboratory and specialized laboratories for molecular diagnostics, biorepository, histopathology and immunology. This first comprehensive cancer center holds promise for accelerating groundbreaking scientific cancer and infectious research. Additional opportunities for global oncology pathogen-associated research are afforded with in-country partners at our state-of-the-art 10,000 square-foot freestanding immunology laboratory in Cape Town, South Africa. Through our long-term China collaborative research initiative, the FH has joint research and training partnerships for clinical and epidemiologic studies linked to pathogen-associated and environmentally-linked cancer development.

The Global Oncology Leader will guide the collaboration with the Uganda Cancer Institute, lead the Global Oncology program staff and will oversee Fred Hutch's international operations. Applicants must have an MD and/or PhD (or foreign equivalent) and board eligibility in clinical oncology is preferred. Expertise in cancer biology and pathogen-mediated cancers are also desirable characteristics. Selection criteria include excellence in clinical care, scholarship, creativity in research, success in developing and advancing collaborations, and demonstrated leadership in the profession. Ideal candidates will have experience working in international settings.

The Global Oncology leader will be based in Seattle, Washington, at Fred Hutch in the Vaccine and Infectious Disease Division (VIDD) and have opportunities for cross-divisional appointments based on research expertise. Fred Hutch offers a vibrant intellectual environment within a beautiful, lakeside campus in Seattle's South Lake Union biotech hub. VIDD occupies a new building that is connected by walking trails to Seattle Cancer Care Alliance and the other four Fred Hutch Divisions and by trolley to major partners such as the University of Washington School of Medicine, Seattle Children's Research Institute, Center for Infectious Disease Research, and the Infectious Disease Research Institute.
Salary DOE + excellent benefits.

Interested candidates should submit a CV, a concise statement of their research interests, and the names and contact information for three (3) references to **fredhutch.org/job/7959**. Specific inquiries can be directed to **Dr. Julie McElrath** at **206-667-1858**.

Applications should be received by **September 1, 2016** to assure consideration and will be evaluated as received.

The Fred Hutchinson Cancer Research Center is an Affirmative Action, Equal Opportunity Employer. All qualified applicants will receive consideration for employment without regard to, among other things, race, religion, color, national origin, sex, age, status as protected veterans, or status as qualified individuals with disabilities. We strongly encourage applications from women, minorities, individuals with disabilities and covered veterans.

CHINA
聚焦"双一流"

Talent is the Key to "the World-class University and the First-class Discipline"

Welcome to Join us in the Chinese University Construction

On October 24, 2015, "the Overall Plan about Pushing Forward World-class University and First-class Discipline Construction " has been issued by the State Council, which is another important project of Chinese government to promote the development of colleges and universities after "211" and "985" project. Unlike the past projects, it has put forward the concept of disciplines for the first time in addition to the concept of universities, which is building the world-class university and the first-class discipline simultaneously, and this will give more opportunity to colleges and universities, which can help them win by their features.

No matter the construction of first-class discipline or the construction of world-class university, it will eventually need to rely on the excellent talents to complete. We can foresee that, the construction of "the double tops" will further promote the demand for high-level talents in Chinese universities, especially the needs of oversea Chinese scholars and high level scholars.

Dr. Li Zhimin
Director of the Ministry of Education of Science and Technology Development Center

Li Zhimin said that "The main task of the construction of the world-class university and first-class discipline is to strengthen the construction of talent team and improve the ability of independent innovation." In 2016 Chinese Universities Talent Peak BBS Which Focusing on "Double Tops", Dr. Li said, the construction of world-class university depends on the first-class talents, and the world-class university cannot leave the first-class discipline. At the same time, the top discipline need the support of the first-class scholar team, as these are complementary and indispensable.

Director Li considers that, the world-class university is a fuzzy concept, it will be more reflected in the world recognized level, status and outstanding achievements. It will own first-class schooling capability, long history and culture, cultivate the talents who can make the contribution in politics, economy and social development, and will also have distinguished professors who have made the significant contribution in several areas of science and technology and enjoy high academic reputation.

Dr.Lijun Wan
The president of the University of Science and Technology of China

Dr.Lijun Wan said that if "211" and "985" Project are the "assembly" for Chinese university concentrating education resources and upgrading the education and research capacity, promoting "two tops" will be the "bugle call" for Chinese universities marching to the international forefront and building top universities.

Dr. Jun Hu
The president of Jinan University

Dr.Jun Hu said that with a history of more than 100 years, JNU is striving for its goal to be a first-class university in China and a world-famous institution of higher education. We are looking forward to realizing this goal with collective wisdom and wit of talents around the world.

Dr. Shuguo Wang
The president of Xi`an Jiaotong University

Dr.Shuguo Wang said that outstanding talents are the driving force for sustainable development of Xi'an Jiaotong University. The university welcomes all kinds of talents to join us, and commits itself to employing talents without overstressing qualifications. Great efforts will be made to create an exceptional environment where first-class talents can gather.

Dr.Jianguo Xia
The president of Shanghai University of Engineering Science

Jianguo Xia said that overseas topnotch talents are the important intellectual support to help the development of Shanghai University of Engineering Sciences. The university will take the advantage of locating in Shanghai, an international metropolis, and provide the good living condition and career development prospect for talents both from domestic and abroad.

To help China's top-ranked universities attract high-level talent from overseas, CERNET has partnered with *Science* to launch a print and online media campaign. Many of China's top universities are recognized as world-class and are doing first-class research but the aim is to build on this and establish worldwide acclaim for all of China's top universities in both institute and discipline rankings.

Researchers, interested in working in China, are invited to consider applying for jobs published in the following special section "Opportunities in China" and online at http://jobs.sciencecareers.org/

Further information can also be located at - http://www.edu.cn/syl/

Faculty Positions in the Department of Biomedical Engineering at SUSTC

南方科技大学
SOUTHERN UNIVERSITY OF SCIENCE AND TECHNOLOGY

South University of Science and Technology of China (SUSTC) is seeking applicants for multiple tenure-track or tenured faculty positions at all ranks in the Department of Biomedical Engineering. The newly formed Department of Biomedical Engineering at SUSTC is supported by faculty in the Department of Biomedical Engineering at Columbia University. We are interested in candidates with expertise in the broad areas of biomedical engineering, including but not limited to, biomechanics, cellular and tissue engineering, biomedical imaging and biosignal analysis, neural engineering, auditory physiology and information processing, etc. Applicants are expected to manage an independent research program in their fields and be committed to excellence in teaching at both undergraduate and graduate levels. Candidates for tenured positions must be established scholars with national and international recognitions.

We offer internationally competitive salaries and benefits. We also provide ample start-up resources for equipment and personnel. Qualified candidates for Thousand Talent Program, the Peacock Program or other talent programs will receive additional support from the central and municipal governments.

A PhD degree in related fields, an excellent track record in research and good communication skill are required. Application must be submitted online to http://talent.sustc.edu.cn. Applicants should also submit the following documents to zhoub@sustc.edu.cn.

(1) Curriculum vitae, including full publication list
(2) Research interests and a statement of research plan
(3) Teaching interests
(4) Copies of three representative publications
(5) Three reference letters

About us

SUSTC is a publicly funded new university in Shenzhen, Guangdong Province, China. By providing generous funding, Shenzhen municipality is fully committed to the development of SUSTC as a world-class research university that excels in research and the cultivation of innovative talent. The university features a 1:10 faculty/student ratio and emphasizes international standards, advanced interdisciplinary studies, innovation and entrepreneurship.

At present, the Department of Biomedical Engineering at Columbia University is to fully support SUSTC establish BME department. The BME department at SUSTC engages in a broad scope of advanced biomedical engineering research, including auditory physiology and information processing, biological tissue and material mechanics, medical imaging and biomedical analysis. The department aims to build a world-class center for biomedical engineering research and education with high quality, we are actively recruiting faculty members at ranks of the assistant professor, associate professor, and full professor.

"JINAN DOUBLE HUNDRED TALENTS PLAN"

Recruiting Members (Candidates) Of the "Thousand Young Talents Program"

暨南大學 JINAN UNIVERSITY

About Jinan University

Jinan University is one of China's "One Hundred Key Universities of 21st Century"(the "211 Project") and is operated under the leadership of the Overseas Chinese Affairs Office of State Council. As the first university established by the State for overseas Chinese students, JNU currently has the largest number of overseas and foreign students and is honored as the "top university for overseas Chinese". Abiding by the motto of "loyalty, sincerity, integrity and respect", the university is committed to cultivating talents with the excellent traditional Chinese moralities and culture. In June 2015, JNU was selected into the "High-level University Construction Program" by Guangdong provincial government. The University has 27 colleges, comprising 62 departments, 188 research institutions, 77 laboratories and offering 89 undergraduate majors, 189 master degree programs in 38 Level-I and 5 Level-II disciplines as well as 74 doctoral degree programs in 15 Level-I and 4 Level-II disciplines. Besides, we have 4 national key disciplines (industrial economics, aquatic biology, finance and literary theory) , 8 key disciplines at the level of the Overseas Chinese Affairs Office of the State Council, 20 provincial Level-I key disciplines, and 4 provincial Level-II key disciplines. The University has the following teaching and research bases: a key research base of national humanity & social sciences, a teaching & research base for Chinese language & literature of the Education Ministry, a base for national university cultural quality education, a national base for teaching Chinese as a foreign language, an educational base for overseas Chinese education of the Overseas Chinese Affairs Office of the State Council and a key research base of humanity & social science of Guangdong Province. It also has one national engineering center, 14 ministerial and provincial engineering centers and 13 key ministerial and provincial laboratories.

To achieve the goal of building a high-level university, JNU continues to implement the strategy of "strengthening universities with more talented people" in order to greatly enhance the core competitiveness of talent and sustainable development capacity and to further strengthen the support for the introduction and training of outstanding personnel. For this purpose, the university is now recruiting members or candidates of the "High-level Overseas Young Talents Program" (referred to as the Thousand Young Talents Program) from home and abroad.

Disciplines Open for Recruitment

Optical engineering, information and communication engineering, electronic science and technology, science of Chinese pharmacology, pharmacy, biology, biomedical engineering, ecology, environmental science and engineering, basic medicine, clinical medicine, integration of traditional Chinese and western medicine, traditional Chinese medicine, oral medicine, public health and preventive medicine, nursing, mechanics, cyberspace security, computer science and technology, software engineering, mathematics, chemistry, materials science and engineering, food science and engineering and physics.

Basic Requirements

1. Members of the "Thousand Young Talents Program".

2. Candidates of the "Thousand Young Talents Program" (candidates of the discipline of finance not included). Applicants should meet the following requirements:

(1) Applicants should consciously adhere to China's laws and regulations, and have good academic ethics;

(2) Applicants whose research fields are in natural science and engineering technology should be under 40 years old (up to June.1, 2016, the same below);

(3) Applicants should have acquired a doctoral degree, and have over three years' overseas research and working experience (not including working experience abroad with employment relations remained in China). Applicants who received a doctoral degree in China should not exceed the age limit of 40. Applicants who have received a doctoral degree abroad may be waived from the age limit of 40 if they have outstanding research performance and other great achievements. In such cases, a waiver letter with explanation and proofs is required.

(4) Applicants should have a permanent teaching or research position in overseas universities, research institutions and enterprises of high prestige.

(5) Generally, applicants should not have a full-time position in China at the time of application. However, if applicants are already holding a position in China, it should be less than one year that they returned from abroad.

(6) Applicants should work full time in China once employed.

(7) Applicants should be the top performers among their peers in the same research field and have potentials to become the leading persons of their field.

Package of Salary & Benefits

JNU will provide recruited members and candidates of "Thousand Young Talents Program" with a competitive package of salary and benefits based on the job position.

1. **For members of "Thousand Young Talents Program":**

(1) Salary: no less than ￥500,000 per year(pre-tax).

(2) Supporting funds for research: ￥1,000,000-3,000,000.

(3) Housing/settling allowance: no less than ￥2,000,000(pre-tax).

(4) Recruited members will be directly employed as a senior professional.

(5) Recruited members will have the priority to recruit PhD students, post-doctors and research assistants.

(6) The university will provide applicants assistance in their children's entry into kindergarten, primary school and middle school in Guangzhou.

(7) Members will enjoy the one-stop service for high-level talents.

(8) The university will give priority to solve the job transfer of spouse of members.

(9) Each new recruit is entitled to a central finance subsidy of ￥500,000and a research fund ranging from ￥1,000,000 to ￥3,000,000, which, once ratified, will be allocated according to schedule. The Guangdong provincial finance will also grant the recruit a living allowance of ￥250,000 and a supportive fund of ￥500, 000.

2. **Candidates having successfully passed the university review process can sign an employment contract of intent, and apply for the "Thousand Young Talents Program" membership in the name of Jinan University. Candidates who have entered into the defense session are entitled to the following salary and benefits:**

(1) Salary: no less than ￥400,000 per year(pre-tax).

(2) Supporting funds for research: no less than ￥1,000,000.

(3) Housing/settling allowance: no less than ￥1,000,000(pre-tax).

(4) Recruited members will have the priority to recruit PhD students and research assistants.

(5) The university will provide applicants assistance in their children's entry into kindergarten, primary school and middle school in Guangzhou.

(6) Recruited members will enjoy the one-stop service for high-level talents.

(7) If recruited members are enrolled into the "Thousand Talents Program", they are entitled to all the pay and benefits offered by the university to members of this program.

This advertisement is valid permanently. Electronic copies of your related materials are also required when applying. Please send them to the official email: otalents@jnu.edu.cn.

Contact Information

Home page of Personnel Department, Jinan University
(http://personal.jnu.edu.cn/)
Tel: 0086-20-85227283 (fax available), 0086-20-85223525
Contacts: Mr. Tong, Mr. Liu
Email: otalents@jnu.edu.cn
Address: No. 601, Huangpu Avenue West, Guangzhou, Guangdong, PRC
Post Code: 510632

東北林業大學
Northeast Forestry University

Northeast Forestry University Invites Talents Offering Millions of Annual Salary

Introduction: Northeast Forestry University offers "1 Million+1 Million+5 Million" to leading talents. That is to say, 500 thousand to 1 million annual salary, 500 thousand to 1 million house purchase subsidies and 3 to 5 million scientific research funds for natural science, 500 thousand to 1 million for human society. Offer job opportunities to spouses, and children will have guaranteed admission to schools.

-University Profiles

Established in 1952 and located in Harbin – beautiful "Ice City", Northeast Forestry University is in national "211 Project" directly under the Ministry of Education of the People's Republic of China and key construction projects of "Advantage Discipline Innovation Platform". It is a multidisciplinary university integrating agriculture, science, industry, economics, management, culture, law, medicine and art with forestry science as advantage and forestry engineering as specialty.
To further improve the overall level of teaching staff and achieve a research university with international view, we are hereby looking for talents sincerely and mainly introducing excellent domestic and foreign talents with important assisting and guiding functions for the construction of subjects and talent team.

-Subject Areas for Recruitment

Acoustics,Agricultural Economics & Policy,Agriculture, Dairy & Animal Science,Agriculture,Multidisciplinary,Agriculture, Multidisciplinary,Biochemistry & Molecular Biology,Biodiversity Conservation,Biology,Biophysics,Biotechnology & Applied Microbiology,Cell & Tissue Engineering,Cell Biology,Chemistry, Analytical,Chemistry, Applied,Chemistry, Inorganic & Nuclear,Chemistry, Medicinal,Chemistry, Multidisciplinary,Organic,Computer Science, Cybernetics,Hardware & Architecture,Information Systems,Interdisciplinary Applications,Interdisciplinary Applications,Theory & Methods,Developmental Biology,Developmental Electrochemistry,Energy & Fuels Engineering, Biomedical Engineering, ,Chemical,Civil,Electrical & Electronic,Environmental,Geological,Industrial,Manufacturing,Mechanical,Multidisciplinary,Entomology, Environmental Sciences,Food Science & Technology,Food Science & Technology,Genetics & Heredity,Geography, Physical,Horticulture,Immunology,Materials Science, Biomaterials,Ceramics, Characterization & Testing,Coatings & Films, Composites,Multidisciplinary,Paper & Wood,Paper & Wood,Mathematical & Computational Biology,Mathematical & Computational Biology,Mathematics,Applied,Interdisciplinary Applications,Mechanics,Microbiology,Multidisciplinary Sciences,Nanoscience & Nanotechnology,Nanoscience & Nanotechnology,Oncology,Physics, Applied,Atomic, Molecular & Chemical,Plant Sciences,Polymer Science,Remote Sensing,Remote Sensing,Soil Science,Statistics & Probability,Telecommunications,Transportation Science & Technology,Veterinary Sciences,Virology,Water Resources,Zoology

-Recruitment Plan

1. Leading Talents or Teams: Introduce leading talents or teams at international advanced level with competitiveness in distinctive preponderant disciplines of the university and national key disciplines.
2. Distinguished Young Scholars: Have published highly cited academic paper in the peer-reviewed journals of related field, with the potential to be selected into talent projects such as Thousands Talents Program, National Science Fund for Distinguished Young Scholars, Thousand Youth Talents Plan and Tens of Thousands of People Plan, or personnel with academic title of associate professor in overseas famous universities or personnel equivalent to the level of researchers in overseas famous research institutes.
3. Excellent Young Scholars: Have published highly cited academic paper in the peer-reviewed journals of related secondary discipline, with the potential to be selected into talent projects such as Provincial Science Fund for Distinguished Young Scholars, Longjiang Scholars and Provincial Excellent Young and Middle-aged Experts.
4. Young Backbone: Have published highly cited academic paper in the peer-reviewed journals of related secondary discipline, with the ability of winning National Science Foundation of China and Philosophy and Social Science Foundation of China and great development potential in academy and scientific research.

-Treatment

1. Leading Talents: appointed to the post of professor;
2. Distinguished Young Scholars: appointed to the post of professor;
3. Excellent Young Scholars: appointed to the post of professor or associate professor;
4. Young Backbone: appointed to the post of associate professor or lecturer;
The university will provide salary, scientific research start-up fund and house purchase subsidies according to the level of talent.

-Further Details and Contact Information

1. Please check the following links for more details about the recruitment plan:
http://gkzp.nefu.edu.cn
2. Contact Person:
Ni Songyuan(Tel:+86-451-82191327)
Zhang Chunlei (Tel: +86-451-82190165)
Email: nefumoe@163.com
3. For official website, please check:
http://www.nefu.edu.cn

Dongguan University of Technology Recruitment for High-Level Talents

Dongguan University of Technology (DGUT) was initially built in 1992 in Dongguan city, Guangdong province. In 2015, with a five-year 3.5 billion RMB investment plan jointly approved by Guangdong province and Dongguan city, Dongguan University of Technology is to be built into a high level university of science and technology. Dongguan University of Technology has ushered in a new stage of extraordinary development. With our most sincere heart, we look forward to you joining us for a prosperous future!

東莞理工學院
DONGGUAN UNIVERSITY OF TECHNOLOGY

I. Positions Available

1. Exceptional talents
(1) Academicians of the Chinese Academy of Sciences and Chinese Academy of Engineering: salary, housing subsidies, research start-up funds and other benefits will be subject to individual negotiations.
(2) Recipients of "The National Science Fund for Distinguished Young Scholars", "The Chang Jiang Scholars" of Ministry of Education or "The National One Thousand Talents Plan": 1-1.3 million RMB for basic annual salary and 2.2-2.5 million RMB for house subsidies.
(3) Recipients of "The National Natural Science Foundation for Outstanding Youth", "The National One Thousand Young Talents Plan", or "The Chang Jiang Young Scholars" of Ministry of Education: 0.5 million RMB for basic annual salary and 1 million RMB for house subsidies.
(4) Introduced leading talents of Guangdong province, leaders of introduced innovative teams of Guangdong province: 0.8 million RMB for basic annual salary and 1.8 million RMB for house subsidies.
In addition, talents listed in the aforesaid categories (2)-(4) can enjoy a start-up research fund of up to 50 million RMB.
2. Leading talents and excellent talents
(1) Leading talents (position A and position B)
Salary package:
Position A: 0.6 million RMB for basic annual salary and 1 million RMB for house subsidies
Position B: 0.5 million RMB basic annual salary and 0.8 million RMB for house subsidies
A qualified leading talent will be provided with suitable experiment places, research start-up funds and lab-construction funds up to 20 million RMB.
(2) Excellent talents
Salary package:
0.4 million RMB for basic annual salary and 0.6 million RMB for house subsidies
A qualified excellent talent will be provided with research start-up fund above 1 million RMB.
3. Industrial elites
Salary package: The basic annual salary is 0.5 million RMB and the house subsidies is 1 million RMB plus over 3 million RMB start-up funds.
4. Innovative teams
Benefits: The team shall receive a scientific research fund of over 10 million RMB.
5. Entrepreneur teams
Benefits: The team shall receive a venture fund of 5 million to 10 million RMB.
6. President-appointed talents
The position for president-appointed talents will be the president's independent decision.

II. Applicable Fields of Study

1. Electronic science and technology.
2. Chemical engineering and technology.
3. Computer science and technology.
4. Mechanical engineering.
5. Optical engineering.
6. Economics, management, law and other fields of study related to the intelligent manufacturing.
For overseas high-level talents, and those from Hongkong, Macau and Taiwan, please refer to the standard above.
All salary package, benefit and funds listed above are pretax and paid in RMB.

III. Contacts Us

High-Level Talent Service Center
Dongguan University of Technology
Email: hr@dgut.edu.cn
Ms. Yao, Ms. Chen
Phone: (86)769-22862996
Address: No.1, Daxue Rd. Songshan Lake, Dongguan, Guangdong Province, P.R. China
School website: www.dgut.edu.cn

西南交通大學
Southwest Jiaotong University

Southwest Jiaotong University, Chengdu, China Invites Applications for the Academic Positions

Southwest Jiaotong University (SWJTU), founded in 1896 and located in Chengdu, the capital of Sichuan province--China's dynamically growing West. SWJTU is an elite university with national key multidisciplinary "211" and "985 Feature" projects directly managed by the Ministry of Education.SWJTU is currently on the strategic "Developing and Strengthening the University by Introducing and Cultivating talents" campaign. Thus, you are cordially invited to apply for the following academic positions. More information is available at http://www.swjtu.edu.cn/

Positions and Requirements

A. High-level Talented Leaders: Candidates should be qualified to be listed in national top talents programs such as Program of Global Experts, Top Talents of National Special Support Program, "Chang Jiang Scholars", China National Funds for Distinguished Young Scientists and National Award for Distinguished Teacher.

B. Young Leading Scholars: Candidates are preferable to be listed or qualified for the following programs: National Thousand Young Talents Program,The Top Young Talents of National Special Support Program (Program for Supporting Top Young Talents), Science Foundation for the Excellent Youth Scholars.

C. Excellent Young Academic Backbones

D. Excellent Doctors and Post Doctoral Fellows

Please contact Mr. Yu Wang, Ms. Ye Zeng,Ms.Qing Ya Wang

Telephone number: +86-28-66367238/ 66366202

Email: talent@swjtu.edu.cn

Address: Human Resources Department, SWJTU, Western Park of High-Tech Zone, Chengdu, Sichuan, China, 611756

南昌大学 江西医学院 医学部
Jiangxi Medical College, Nanchang University

PI Positions Available in Nanchang University Jiangxi Medical College

Nanchang University Jiangxi Medical College (NCU-JXMC), which was founded in 1921, is a comprehensive medical education center in Jiangxi Province. The college consists of 10 schools: School of Basic Medical Science, School of Public Health, School of Pharmacy, School of Nursing, Queen Mary School, 1st Clinical Medical School, 2nd Clinical Medical School, 4th Clinical Medical School, School of Stomatology and School of Optometry.

The college is now recruiting **Principal Investigators (PIs)** worldwide in the following fields: Medical science (Gastroenterology, Cardiovascular Medicine, Neuroscience, Cell and molecular biology, Biochemistry, Microbiology, Physiology, Immunology, Pathology, Oncology), Public Health, Pharmacy, and Nursing.

Competitive candidates should hold PhD (or MD) and have an outstanding education and research background, with strong publication records in related fields. Leadership capability in establishing and managing innovative research group is more than welcomed. Qualified candidates will be offered negotiable and competitive salaries and funding packages.

For application, please send your CV and three reference letters, along with five representative publications, to Ms Yun He (Email: yunhe1210@ncu.edu.cn) at the following address:

Jiangxi Medical College,Nanchang University,461 Bayi Avenue,Nanchang 330006,China

Phone: +86-791-86362537

For further information, please visit http://www.jxmu.edu.cn/

or visit "Wechat ID: NCU_JXMC"

Harbin Engineering University Sincerely Invites talents to Apply for "The Recruitment Program for Professionals"

哈爾濱工程大學
HARBIN ENGINEERING UNIVERSITY

Basic Qualifications

1. Applicants engaged in scientific researches or Engineering technology and below the age of 40.
2.Have obtained a doctorate degree and have no less than three years of overseas working experience.
3. With formal teaching and researching positions in overseas prestigious universities, institutions or enterprises.
4. The applicants should be the top-notch talents in their research fields, and have the potential to become future leaders in relevant areas.
5.The applicants will be able to work full time in China. For those who have worked in China, they should be no more than one year.

Outstanding PHD students can be recruited in exceptional cases.

Preferential Policies and Treatments

What we offer for entrants of "The Recruitment Program for Professionals":

1. Employed as professor or doctoral tutor
2.Support to form academic team
3.A lump sum of 500,000 RMB shall be granted by the central budget
4.Research subsidies, varying from 1 million to 3 million RMB, shall be allocated in batches throughout the process of the program according to the level and quality of the program.
5.Provide no less than 400,000 RMB annual salary and 300,000 RMB setting-in allowance.
6.Provide an apartment no less than 80 square meters or 1 million to 1.5 million RMB housing benefit.
7.Offer job opportunities to spouses, and children will have guaranteed admission to schools.

If interested in applying for "The Recruitment Program for Professionals", please send your resume to rencai@hrbeu.edu.cn.

For more information, please contact :

Contact Persons: Gao shan, Bai yun.

Tel:+86-451-82518061

E-mail:rencai@hrbeu.edu.cn

北京理工大學
BEIJING INSTITUTE OF TECHNOLOGY

Faculty Recruitment - Beijing Institute of Technology

Beijing Institute of Technology (BIT) was founded in 1940, being one of the first groups of national higher education projects- "Project 211" and "Project 985". In 2002, BIT was ranked among Top 100 in QS Asian Universities Ranking and Top 500 in QS World Universities Ranking, which was the 13rd among the 19ranked Chinese universities. The recent nation-wide evaluation on disciplines shows that 8 subjects at BIT are ranked in top 10 in Chinese universities. 5 fields of BIT entered global top 1% as Engineering, Materials, Chemistry, Physics, and Mathematics. BIT now has 8 national key laboratories and engineering research centers; 43 provincial key laboratories and engineering research centers. During the past 5 years, the research funding of BIT has been amounted to more than10 billion RMB.

Recently, BIT attaches great importance to the recruitment and cultivation of outstanding faculty, which facilitates the founding of "Advanced Research Institute for Multidisciplinary Science (ARIMS)". In order to attract more excellent talents home and abroad, BIT gives ARIMS great priority and names it as a "Special Zone for Talents". That is to say, BIT will offer a great platform and good facilities and services for the development of the recrutied talents.

I. Positions and Requirements

1. National "Youth Thousand Talents Program"

(1) Areas: Natural Science or Technology Engineering.
(2)PhD degree; more than three years' oversea experience in scientific research. The applicants should have a formal teaching position or equivalent positions in famous universities, research institutes, or famous companies overseas.
(3) Under the age of 40. Work full time at BIT once recruited.

2. Outstanding Youth Teachers Program (Tenure-tracked Associate Professor and Assistant Professor)

(1) PhD degree; more than 2 years' learning and working experience in prestigious oversea universities or research institutes.
(2) Has a good understanding of the academic development trend in his/her own field; has certain academic influence with highly recognized research achievements and presents great potential for future academic development; has the ability to develop new research directions; has published high-level research papers as the first author or corresponding author.
(3) Under the age of 35 for associate professor and under the age of 32 for assistant professor.

3. Post Doctor

(1) Generally, the applicant should be PHD graduate student under the age of 35at prestigious universities or research institutes overseas.
(2) Has good academic background; has the ability to conduct research independently; has published high-level research papers as the first author or corresponding author.

II. Application Materials and Contact Information

Applicants should send CVs and 5 representative papers (the whole paper) to the HR Office of BIT.
For "Youth Thousand Talents" and "Outstanding Youth Teachers" relevant matters, please contact Mr.GanZhenkun.
Tele.: +86-10-68918577 Email: bitrcb@bit.edu.cn
For "Post Doctor" relevant matters, please contact Mr.ChenXiaoyan.
Tele.: +86-10-68912334 Email: bitzhaopin@bit.edu.cn
For more information about "Thousand Talents" and "Chang Jiang Scholars" programs, please visit: http://renshichu.bit.edu.cn/

上海理工大學
University of Shanghai for Science and Technology

High-end Talents Recruitment in University of Shanghai for Science and Technology

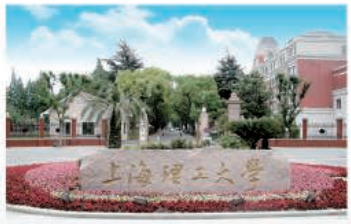

1. Introduction

University of Shanghai for Science and Technology (USST), with a long history of over one hundred years, is a key municipal research-oriented university specializing in engineering, focusing on interdisciplinary integration of engineering, science, management, economics, arts, laws and so on.

2. Recruitment Disciplines

Optical Engineering, System Science, Power Engineering and Engineering Thermophysics, Management Science and Engineering, Biomedical Engineering, Mechanical Engineering or other related interdiscipline.

3. Scope of Talents Recruitment

(1)**Level One**: Academicians of the Chinese Academy of Sciences and Chinese Academy of Engineering.
(2)**Level Two**: Distinguished professor of Changjiang Scholars Program; Selected candidate of innovation project of National "1000 Talents Plan"; Winner of National Science Fund for Outstanding Young Scholars; Outstanding talents of Thousands Talents Program; Selected candidate of Leading Talents, etc.
(3)**Level Three**: Selected candidate of Thousands Talents Program for Young Top-notch Talent; Winner of "Top University Teacher in Teaching Award" issued by Chinese Ministry of Education.
(4)**Level Four**: Selected candidate and young selected candidate of "1000 Talents Plan" issued by the Organization Department of the Central Committee of the CPC; Candidate from the "National Millions of Talents Projects".
(5)**Level Five**: Selected candidate of Shanghai "1000 Talents Plan" (Innovation Project); Selected candidate of "Hundred Talent Plan" of Chinese Academy of Sciences; Shanghai Leading Talents; Distinguished Professor of Shanghai "Orientalist".

4. Treatment

(1)USST will provide competitive salaries, house purchase and renting subsidies and settlement allowance (one-off payment).
Talents of Level One: Salary negotiable according to personal details;
Talents of Level Two:
Annual salary: RMB700,000-800,000Yuan.
House Purchase and Renting Subsidies: RMB1,200,000-2,400,000Yuan

Talents of Level Three:
Annual salary: RMB500,000-600,000Yuan,
House Purchase and Renting Subsidies:
RMB600,000-1,200,000Yuan.

Talents of Level Four:
Annual salary: RMB400,000-500,000Yuan,
House Purchase and Renting Subsidies:
RMB400,000-800,000Yuan.

Talents of Level Five:
Annual salary: RMB300,000-400,000Yuan,
House Purchase and Renting Subsidies:
RMB300,000-600,000Yuan.

(2)Besides the above treatment, USST will also provide makeshift shelter and corresponding scientific research allowance (RMB200,000-2,000,000Yuan)

5. Contact:

Contact Person: Weijia Li, Dong An
Phone: 86-21-55271605
E-mail: liweijia@usst.edu.cn
andong@usst.edu.cn
Address: Room 207, Gezhi Hall, University of Shanghai for Science and Technology, No. 516 Jungong Road, Shanghai, China
Zip code: 200093

10 ways that *Science* Careers can help advance your career

1. Register for a free online account on **ScienceCareers.org**.
2. Search thousands of job postings and find your perfect job.
3. Sign up to receive e-mail alerts about job postings that match your criteria.
4. Upload your resume into our database and connect with employers.
5. Watch one of our many webinars on different career topics such as job searching, networking, and more.
6. Download our career booklets, including Career Basics, Careers Beyond the Bench, and Developing Your Skills.
7. Complete an interactive, personalized career plan at "my IDP."
8. Visit our Career Forum and get advice from career experts and your peers.
9. Research graduate program information and find a program right for you.
10. Read relevant career advice articles from our library of thousands.

Visit **ScienceCareers.org** today — all resources are free

ScienceCareers

FROM THE JOURNAL SCIENCE AAAS

SCIENCECAREERS.ORG

THE UNIVERSITY OF RHODE ISLAND

GEORGE & ANNE RYAN INSTITUTE FOR NEUROSCIENCE

Cluster Hire
Assistant, Associate and Full Professor

The George & Anne Ryan Institute for Neuroscience at the University of Rhode Island invites applications for tenure-track or tenured academic year/calendar year positions at the rank of Assistant, Associate, and Full Professor.

The George & Anne Ryan Institute for Neuroscience is a multidisciplinary research center focused on discovering and developing disease-modifying therapies for neurodegenerative diseases. As the University of Rhode Island undergoes major expansion in the neurosciences, we are building a faculty with a strong record of successful laboratory and/or clinical research that supports our mission of integrating discovery science, translational medicine, education and community engagement to identify and deliver tomorrow's treatments today.

Successful candidates will have dual appointments in the George & Anne Ryan Institute for Neuroscience and academic departments at the University. A determination on the status of the position (Academic Year or Calendar Year) will be made at the time of hire. Candidates must maintain an active and productive research program and demonstrate meaningful contributions to the literature through publication and other scholarly activities. Junior faculty are expected to develop an internationally recognized research program that is supported by extramural funding, while senior faculty must demonstrate a record of consistent productivity and funding. The Institute is especially interested in research that considers novel contributions to the pathogenesis of neurodegenerative disease and in research that seeks to link scientific discoveries to disease-modifying therapies. Preference will be given to applicants who have demonstrated a strong commitment to interdisciplinary research and whose research interests complement the programs of existing faculty.

The George & Anne Ryan Institute for Neuroscience has become an integral and essential partner in the growing neuroscience community in the State of Rhode Island. The Institute has established formal relationships with Brown University and the State's major health care systems to encourage and support active collaborations in neuroscience. Institute faculty have access to top-level laboratory and core facilities throughout the State and are eligible to receive seed/pilot grant funds for innovative research.

The University of Rhode Island is located near the picturesque Narragansett Bay and renowned beaches on Rhode Island Sound. Average housing and other living expenses are well below the Boston, New York and San Francisco metro areas, with comparable access to cultural and arts events and highly-rated schools.

In addition to its own robust scientific and healthcare communities, Rhode Island is also near thriving scientific and entrepreneurial enterprises in Boston, Cambridge, New York, and beyond, with easy access by road, rail or air.

All candidates must have a Ph.D., M.D., M.D./Ph.D. or equivalent degree and qualify for a tenure track or tenured faculty position at the University of Rhode Island. Candidates for the Assistant Professor position must have at least one year of postdoctoral training in an area related to neuroscience and a record of research productivity as evidenced by publications and/or patents and presentations at national and international meetings. Candidates for the Associate and Full Professor position must have an established research program and a history of extramural funding. All candidates are expected to demonstrate excellence in oral and written communication and the ability to teach in neuroscience, cell/molecular biology or a related field.

To Apply: Visit the URI jobs website at: https://jobs.uri.edu to apply and view complete details for job postings: (**Assistant Professor - SF00284**); (**Associate Professor – SF00285**); (**Full Professor – SF00286**). Please attach 3 (PDF) documents to your online Faculty Employment Application: (#1) Cover letter, (#2) Curriculum Vitae that should include the names and contact information of three professional references, and (#3) "Other Document" to include a statement of research accomplishments and goals.

APPLICATION DEADLINE: Search will remain open until the positions are filled. First consideration will be given to applications received by August 31, 2016. Second consideration may be given to applications received by October 31, 2016. Applications received subsequent to the second consideration date (October 31, 2016) may not be given full consideration.

Only electronic applications will be accepted.

The University of Rhode Island is an AA/EEOD Employer. Women, persons of color, protected veterans, individuals with disabilities, and members of other protected groups are encouraged to apply.

By **Nathan L. Vanderford**

Alternatives within academia

When I started graduate school, I wanted to become a professor at a small teaching college. I envisioned myself helping students develop a passion for science and guiding them in the pursuit of their chosen careers. But as I progressed through my own academic training, I felt tremendous pressure from faculty members to pursue the more "traditional" research-focused faculty path. That path and its requirements—constant pressure to publish, obtain grant funding, and jump through other hoops to obtain tenure—were not at all what I wanted. By the end of graduate school, I was also burned out on my own research in pancreatic β cell biology. I figured that my best option was to pursue "alternative" career paths. And after a few hurdles and unexpected opportunities, I did find an alternative niche—which has brought me full circle back to academia.

As I reached the end of my time in grad school, I applied to dozens of nonresearch positions where I felt that I could apply my scientific background to the greater biomedical enterprise, including in policy, writing, and project management. But I didn't even get a phone interview. I think one reason for my lack of success was that my applications didn't highlight the transferable skills I had gained during my training. I didn't think I could claim to have experience in project management, for example, because I had never had that job title. I didn't realize that, in many ways, earning a Ph.D. is one long project management task.

But even without that knowledge, my first break finally came: I was hired for a science writing and editing position in the cancer center at the University of Kentucky, my alma mater for both my bachelor's degree and my Ph.D. The résumé and cover letter I submitted still did not emphasize my nonresearch skills, but I later found out that professors from my grad school days convinced the hiring manager that I was a good communicator and a hard worker. I then leveraged those two traits, along with my other transferable skills, to move up the administrative ladder. I helped create and manage a larger communications office aimed at enhancing faculty productivity, and then moved into a research administration and operations management position in the cancer center. I found that I loved fostering research by helping manage it.

My passion for conducting research also returned once I had some distance from the lab, and I have enjoyed the freedom to pursue scholarly work in my administrative positions. The difference is that now I get to work on research areas that I have very personal connections to, including improving Ph.D. training and studying the molecular biology and epidemiology of lung cancer, which caused my father's death. I have also put together a professional development course in which I leverage my own experience to better prepare trainees for the workforce.

"I did find an alternative niche—which has brought me full circle."

Now, ironically, my skills as an administrator who can also conduct research and teach have earned me a nontraditional faculty position. It started as non–tenure-track, but beginning this month I'll be working toward tenure. The bulk of my effort is dedicated to research administration, with a much smaller portion focused on teaching and scholarly activity. As a result, I don't face the pressures associated with typical faculty positions, which played a big part in driving me away from this path earlier in my career.

While slogging away as a frustrated trainee dead set on running as fast as I could from becoming a faculty member in a research-intensive university, I would have never imagined that is exactly where I would happily end up. It thrills me to be involved in managing the research enterprise—and to be teaching, my original career goal. Helping trainees discover and plan for the vast career options available to them—including those within academia—gives me a great sense of satisfaction. ■

Nathan L. Vanderford is an assistant professor in the Department of Toxicology and Cancer Biology and the Markey Cancer Center at the University of Kentucky in Lexington. Send your story to SciCareerEditor@aaas.org.

ILLUSTRATION: ROBERT NEUBECKER